2023

MITOCHONDRIAL DIVISION: SYNERGIZING IN MITOCHONDRIAL DIVISOME

Ao Liu
Dartmouth College, ao.liu.gr@dartmouth.edu

MITOCHONDRIAL DIVISION: SYNERGIZING IN MITOCHONDRIAL DIVISOME

A Thesis
Submitted to the Faculty
in partial fulfillment of the requirements of the
degree of

Doctor of Philosophy
in
Biochemistry and Cell Biology
By
Ao Liu
Guarini School of Graduate and Advanced Studies
Dartmouth College
Hanover, New Hampshire

December 2023

Examining Committee:

_____
(Chair) ***Henry N. Higgs, Ph.D.***

_____
James B. Moseley, Ph.D.

_____
Michael J. Ragusa, Ph.D.

_____
Halil Aydin, Ph.D.

_____
F. Jon Kull, Ph.D.
Dean of the Guarini School of Graduate and Advanced Studies

Abstract

Mitochondria are the energy factories of the cell. The dynamic nature of cells demands routine changes in mitochondrial morphology by fusion and division. The dynamin GTPase Drp1 is a central mitochondrial division protein, driving constriction of the outer mitochondrial membrane via oligomerization. At least four regulatory factors control Drp1 activity on the outer mitochondrial membrane (OMM): 1) receptor proteins (Mff, MiD49, MiD51, and Fis1); 2) actin filaments; 3) the mitochondrial phospholipid cardiolipin (CL); and 4) Drp1 post-translational modifications, of which two phosphorylation sites (S579 and S600) are the most well studied. However, the molecular mechanism of how these factors work together in Drp1 activation is unknown.

In this thesis, I take biochemical and cellular approaches to understand how these regulatory factors work individually and together, showing that:

1) Mff oligomerizes in both solution and cells in a concentration-dependent manner through its C-terminal coiled-coil. The dynamic oligomerization of Mff is crucial for activating Drp1. In the solution, oligomerization-defective Mff fails to activate Drp1 and loses its capacity to recruit Drp1 in U2OS cells. Biochemically, actin filaments work synergistically with Mff to enhance Drp1 activity by reducing the effective concentration of Mff.
2) The activation of MiD49 and MiD51 occurs through long-chain acyl coenzyme A (LCACA), leading to their oligomerization and subsequent activation of DRP1 GTPase activity. A point mutation in the LCACA binding pocket diminishes LCACA binding, resulting in reduced MiD51 oligomerization and impaired Drp1 activation both in solution and HeLa cells. Finally, MiD49 or MiD51 oligomers collaborate with Mff, rather than actin filaments, in DRP1 activation.
3) Phosphorylation at S579 and S600 sites maintain basal GTPase activity, but eliminate GTPase stimulation by actin and decrease GTPase stimulation by cardiolipin, Mff, and MiD49. The oligomerization state of both phospho-mimetic mutants is shifted toward smaller oligomers.

Taken together, I propose that mitochondrial division is a multifaceted process involving various factors, and the synergy of these factors may serve distinct purposes for specific mitochondrial division events.

Acknowledgements

I first want to express my gratitude to my supervisor, Dr. Henry N. Higgs for his constant encouragement and support throughout my graduate studies. I would like to appreciate his patience, expertise and vast knowledge about all the subjects, which facilitated the completion of this work. His guidance helped me in evolving better research skills as well as in developing better communication abilities. Apart from being a great supporter he also played a role of an excellent critic, which only propelled the work to be better. Over the past 6.5 years, Harry has been more than just a scientific mentor; he's been a guiding presence, helping me navigate numerous challenges. He has created a nurturing environment for my growth and has consistently been my steadfast supporter, no matter the circumstances. Joining Higgs lab has undoubtedly been one of the best decisions I've ever made.

Secondly, I want to thank my advisory committee members James Moseley and Michael Ragusa who have kindly shared their time to provide feedback and guidance on my project and life. I want to thank my outside examiner Halil Aydin not only for traveling to Dartmouth for my defense, but also for his kind help and insightful discussion for my project. Also, I want to extend my heartfelt gratitude to the entire BioMT core team, with special mention to Zdenek Svindrych, Andreia Verissimo, Emilie Shipman, Angela Kull, Noor Taher, and Susu He. Your assistance truly lightens the path of this journey. Zdenek, I have enjoyed working and learning from you, Thanks for your generous assistance—I'll always have confidence conducting experiments with you nearby.

My lab mates in the Higgs lab are amazing. Thank you for creating a comfortable environment in the lab, and I appreciate that you've become trustworthy partners for each other. You're not just my colleagues, but also my friends. Thank you for bringing so many wonderful moments together. Many thanks to Frieda Kage, Miriam Lee, Sukrut Kamerkar, Ziwei She, Siddhi Bramhe, William King, and Julia Patterson. I would also like to recognize the alumni of Higg's lab: Casey Latario, Lincoln Howarth, Marlena Bartkus, Lorna Young, and Lori Schoenfeld. I truly appreciated the time we spent together. Casey, I can't imagine completing this journey without you.

Last but not least, I would like to thank my parents and friends. Without their confidence and encouragement, none of this would be possible.

TABLE OF CONTENT

List of illustrations

List of tables

Glossary

OMM	Mitochondrial outer membrane
IMS	Intermembrane space
TOM	The outer membrane
IMM	Inner mitochondrial membrane
ETC	Electron transport chain
mtDNA	Mitochondrial DNA
EM	Electron microscopy
MDVs	Mitochondrially-derived vesicles
MDCs	Mitochondrially-derived compartments
Drp1	Dynamin-related protein 1
BSE	Bundle signaling elements
PH	Pleckstrin homology
VD	Variable domain
Mff	Mitochondrial fission factor
CC	Coiled-coil domain
TM	Transmembrane domain
AMPK	Adenosine monophosphate (AMP)-activated protein kinase
MiD49	Mitochondrial dynamics protein of 49 kDa
MiD51	Mitochondrial dynamics protein of 51 kDa
Ntase	Nucleotide transferase
ADP	Adenine diphosphate
GDP	Guanosine diphosphate
Fis1	Mitochondrial fission protein 1
Cdk1	Cyclin dependent kinase 1
ERK1/2	Extracellular signal-regulated kinases
PKCδ	Protein kinase C δ
ROCK	Rho-associated protein kinase
CaMKII)	Ca^{2+}/calmodulin-dependent protein kinase II
DUSP6	Dual-specificity phosphatase 6
cAMP	Cyclic AMP
PKA	Protein kinase A (PKA)

CaMKIα	Ca^{2+}/calmodulin-dependent protein kinase Iα
PKD	Protein kinase D
PP2A	Protein phosphatase 2A
PGAM5	Phosphoglycerate mutase 5
CIA	Calcium-induced actin
CL	Cardiolipin
PA	Phosphatidic acid
MitoPLD	Mitochondria-localized phospholipase D
TGN	Trans-Golgi network
ERMCs	ER-mitochondria contact sites
PI4KIIIβ	Phosphatidylinositol 4-kinase IIIβ
LCACA	Long-chain acyl coenzyme A
ER	Endoplasmic reticulum
vAUC	Velocity analytical ultracentrifugation
SEC	Size exclusion chromatography
TIRF	Total internal reflection fluorescence
KO	Knock out
IDT	Integrated DNA Technologies
DTT	Dithiothreitol
EDTA	Ethylenediaminetetraacetic acid
CV	Column volumes
HEPEs	4-(2-hydroxyethyl)-1-piperazineethanesulfonic acid
EGTA	Ethylene glycol tetraacetic acid
IEX	Ion exchange
GST	Glutathione Sepharose
PVDF	Polyvinylidine difluoride
CPT1	Carnitine O-palmitoyltransferase 1
ACC	Acetyl-CoA carboxylase
MCS	Multiple cloning site

NOTE ON THE FORMATE OF THIS THESIS

Portions of the text and figurers in Chapter II-IV have been previously published or submitted in the following journals:

Chapter II: Mff oligomerization is required for Drp1 activation and synergy with actin filaments during mitochondrial division

Liu A, Kage F, Higgs HN. Mff oligomerization is required for Drp1 activation and synergy with actin filaments during mitochondrial division. *Molecular Biology of the Cell* 2021, DOI: 10.1091/mbc.E21-04-0224.

Chapter III: Long-chain fatty acyl-coenzyme A activates the mitochondrial fission factors MiD49 and MiD51 by inducing their oligomerization

Liu A*, Kage F*, Sapp G, sAydin H, Higgs NH. Long-chain fatty acyl-coenzyme A activates the mitochondrial fission factors MiD49 and MiD51 by inducing their oligomerization. *Under revision at Nature Cell Biology*. 2023

DOI: 10.1101/2023.07.31.551267

*: These authors contributed equally to this work

Chapter IV: Effects of phosphorylation on Drp1 interaction with actin filaments, cardiolipin, and Drp1 receptors

Liu A*, Hatch A*, Higgs NH. Effects of phosphorylation on Drp1 interaction with actin filaments, cardiolipin, and Drp1 receptors. *Under review at Molecular Biology of the Cell* 2023

DOI: 10.1101/2023.08.20.554022

*: These authors contributed equally to this work

Chapter I:

Introduction

1.1 Mitochondrion: a dynamic organelle

Mitochondria are known as the powerhouse of the cell: using fuel sources (pyruvate, fatty acids, or amino acids) and oxygen to produce energy-rich ATP. However, mitochondria have many other functions outside of ATP production, such as calcium storage, reactive oxygen species (ROS) dynamics, and cellular homeostasis control[1]. In addition, mitochondria can have cell type-specific functions, such as steroid hormone synthesis or heat production[2].

Consistent with the theory of natural selection proposed by Darwin, mitochondrial genomes and proteomes differ substantially across eukaryotes and in differing environments[3]. For example, in eukaryotes adapted to a low-oxygen environment, mitochondrial number is drastically reduced and functionally altered[4]. The number of mitochondria in a cell is closely related to the need for mitochondrial activity. In humans, for example, a normal sperm cell has fewer than 100 mitochondria, a liver cell can contain 1000 to 2000 mitochondria, while a human heart muscle cell has 5000 to 8000 mitochondria[5,6]. Despite this diversity, all mitochondria are thought to derive from an evolutionary process named as endosymbiosis: integration of an *alpha proteobacterium* into a host cell[7]. Indeed, since Lynn Margulis proposed this idea at 1967[8], accumulating phylogenetic analyses has confirmed that mitochondrial provenance is remarkably distinct from their "host" eukaryotic lineage[9,10].

During evolution from an endo-symbiotic organism to a fully integrated organelle, mitochondria have adapted to their hosts while maintaining their structure and function. Mitochondria consist of a double-membrane structure. The mitochondrial outer membrane (OMM) separates the intermembrane space (IMS) from the cytosol **(Figure 1-1A)**. The OMM is quite porous to small molecules (largely through the low-selectivity VDAC protein) but mediates protein import through the transporter of the outer membrane (TOM) complex. Compared with the OMM, the inner mitochondrial membrane (IMM), flanked by the IMS and the mitochondrial matrix, is tighter and has stricter control over the flow of metabolites. The IMM is highly folded to form numerous tubular invaginations called cristae. Electron transport chain (ETC) complexes and ATP synthase enriched in cristae, with the cristae lumen being a region of low pH due to ETC-mediated proton transport. The inner mitochondrial compartment is the matrix, which is filled with molecules required for macromolecule synthesis, as well as the enzymes of the Krebs cycle (also known as the citric acid cycle or tricarboxylic acid cycle). Also within the matrix is mitochondrial DNA (mtDNA), a circular genome which is compacted into a spherical structure approximately 100 nm

in diameter. In humans the mitochondrial genome is 16.6 kilo-bases and includes 37 genes: 13 protein-coding (all coding for subunits of ETC complexes or ATP synthase), 22 tRNA-coding, and 2 rRNA-coding[11]. Mitochondrially-encoded proteins are transcribed and translated in the matrix. However, more than 1000 nuclear-encoded proteins are imported, thus mitochondria cannot be synthesized *de novo*[12].

Early observations of mitochondria relied on thin-section transmission electron microscopy (EM). Although this technique provides high-resolution of mitochondrial sub-compartments, the thin sectioning (<100 nm thick) causes longer mitochondria to appear as several shorter mitochondria, which is why mitochondria are often depicted in the form of pills in textbooks **(Figure 1-1B)**. 3D-reconstitution from EM micrographs[13] (**Figure 1-1C**) and light microscopy (**Figurer 1-1D**) make clear that there is extensive variation in the length and morphology of mitochondria, as well as the potential for mitochondrial branching[13] **(Figure 1-1C, D)**. In cultured cells, peripheral and perinuclear mitochondria can appear morphologically different, with perinuclear mitochondria having larger diameters[14,15] **(Figure 1-1D)**.

In mammals, differences in mitochondrial morphology are not only influenced by cell type, gender, and age, but also can be influenced by week-to-week variation of mitochondrial activities[16]. A prerequisite for mitochondria to respond to this variation is the ability to undergo acute mitochondrial fusion and division **(Figure 1-1E).** These two opposing processes are often referred to as mitochondrial dynamics[17]. The balance between mitochondrial division and fusion regulates mitochondrial number, size and positioning within the cell. Defects in mitochondrial dynamics link to several neurological diseases[18,19].

1.1.1 Why are mitochondria dynamic?

There is not one reason why mitochondria undergo dynamics. Both division and fusion can be triggered by a variety of situations. Indeed, one of the goals of my thesis has been to transition the thinking in mitochondrial dynamics away from a focus on a single mechanism and towards context-specific mechanisms for division. Here, I describe the reasons for which mitochondria divide and fuse.

1.1.1.1 Mitochondrial division

Mitochondrial division, also known as mitochondrial fission, refers to the process by which a single mitochondrion divides into two separate mitochondria. There are several reasons why mitochondrial division is necessary **(Figure 1-2A)**.

Firstly, mitochondrial division is important for proper mitochondrial distribution. Most mitochondria have multiple genomes, with a typical culture cell containing hundreds of mitochondrial genomes[20,21]. In dividing cells, mitochondrial division ensures that each daughter cell receives an appropriate number of genome-containing mitochondria[22,23]. Even in non-dividing cells, mitochondrial division allows for efficient movement and distribution within the cells, which is especially important for polarized cells like neurons. Neurons consist of a cell body (soma), a long axon and multiple branched dendrites. Although axons and dendrites have high demands for ATP, it is thought that most new mitochondria are generated in the soma[24]. Thus, neurons require efficient transportation of mitochondria to meet ATP demands along the length of these long structures (up to 1,000,000 microns in length). Mitochondrial division creates smaller mitochondria which are more efficiently transported. In cultured hippocampal neurons, defects in mitochondrial division results in the accumulation of elongated mitochondria in the soma and reduced dendritic mitochondrial numbers, suggesting that highly interconnected mitochondria may not be able to be efficiently transported to distal neuronal processes[25]. Mitochondrial division also is important for maintaining the content of mitochondria near neuromuscular junctions[26].

Second, mitochondrial division plays a crucial role in the removal of defective mitochondrial from the cell. Mitochondria are susceptible to damage from various factors, such as oxidative stress or mutations to the mitochondrial genome. Mitochondrial damage is often accompanied by mitochondrial depolarization (loss of the ETC-created proton gradient). The process of removal of unhealthy mitochondria is known as mitophagy[27], and proper compartmentalization of damaged mitochondrial segments, followed by mitochondrial division of those unhealthy segments, is an important precursor to mitophagy. Inhibition of mitochondrial division leads to the aggregation of oxidized mitochondrial proteins and reduces the efficiency of oxidative phosphorylation[28]. Division at the ends of mitochondria enables damaged material to be shed into smaller mitochondria destined for mitophagy, which suggests a distinct division signature for mitochondrial degradation[28,29].

Third, some components of the mitochondrial division machinery are also involved in apoptosis, or programmed cell death. Activation of caspase proteases is a key step in apoptosis[30]. Cytochrome *c* and other pro-apoptotic proteins resides in the IMS of healthy mitochondria. When the apoptotic

program is initiated, cytochrome *c* is released from mitochondria to activate caspase 9 in the cytoplasm[31,32]. The release of cytochrome *c* has been shown to depend on mitochondrial division proteins such as Drp1[30], although actual division does not necessarily occur in this process. Inhibition of mitochondrial division proteins delays the release of cytochrome *c*, caspase activation, and cell death[33,34].

Fourth, mitochondrial division is associated with cell metabolism, although the mechanisms by which this occurs are not fully understood. One observation is that mitochondrial division might be associated with lower mitochondrial ATP generation, in the following manner. Dimerization of the ATP synthase is known to increase its activity[35]. Thus, regulation of the distance between individual ATP synthases alters ATP production efficiency. Fragmentation of mitochondria decreases mitochondrial cristae number in some cases, which is associated with lower levels of the ATP synthase dimer and thus lower ATP synthesis activity[35]. In contrast to this association of mitochondrial division with lower mitochondrial activity, a recent study shows that mitochondrial division can be associated with higher mitochondrial oxidative activity in specific circumstances. In particular, nutrient excess (like high level of fat or glucose), obesity or type 2 diabetes are commonly accompanied by mitochondrial division in cells like brown adipocytes, pancreatic beta cells, and certain cancers[36–40]. A very recent study shows that the mitochondrial division that takes place in response to fatty acid exposure is necessary for increased mitochondrial fatty acid oxidation, probably by activating mitochondrial fatty acid import[38]. This finding provides interesting potential significance for my work in Chapter III.

A last function of the mitochondrial division machinery is the production of small mitochondrial fragments called mitochondrially-derived vesicles (MDVs) in mammals[41] or mitochondrially-derived compartments (MDCs) in yeast[42]. MDVs and MDCs have diameters of 70-150nm and are often found around mitochondria[41,43,44]. Current information suggests that MDVs and MDCs have similar features, but it is unclear if they represent similar functional structures.

One function of MDVs appears to be transport of small amounts of mitochondrial components to lysosomes or peroxisomes for clearance and degradation[45]. As such, MDVs may represent a less all-or-nothing mechanism than mitophagy to maintain mitochondrial homeostasis. MDVs can contain OMM only or both OMM and IMM and, in the latter case, the MDV can maintain IMM polarity. The final step of MDV/MDC formation uses mitochondrial division proteins, including Drp1 and its receptors Mff, MiD49, and MiD51[46,47].

1.1.1.2 Mitochondrial fusion

Mitochondrial fusion is the process by which two or more mitochondria fuse to form a single, interconnected mitochondrion. As a complement of division, mitochondrial fusion is equally critical to cellular and organismal physiology[48,49].

As with division, mitochondrial fusion serves several purposes. One function of mitochondrial fusion is the exchange of substances between mitochondria. As mentioned earlier, most mitochondrial components are encoded by the nuclear genome, so that mitochondrial proteins must be imported. Such a process tends to lead to uneven distribution of the proteome in individual mitochondria. Fusion solves this problem by allowing rapid exchange and redistribution of mitochondrial proteins. Matrix proteins re-distribute quickly after fusion[50,51]. In addition to exchange of proteins, mitochondrial fusion also ensures efficient distribution of mtDNA, ions, lipids, and other metabolites[52–54].

Mitochondrial fusion can also serve to distribute harmful substances between healthy mitochondria and dysfunctional mitochondria, buffering the degree of toxicity and facilitating the recovery of damaged mitochondria[54].

Another role of mitochondrial fusion is to protect mitochondria from phagophore engulfment. Elongated mitochondria are spared from autophagic degradation. Under nutrient starvation, mitochondria become significantly elongated and interconnected[55].

Finally, it is believed that elongated mitochondria increase cristae number in the IMM, which enhances ATP synthase activity[35], This potential connection between mitochondrial shape and bioenergetics, however, remains controversial[54].

1.1.1.3 Balancing division and fusion

To respond to different physiological conditions, mitochondria must alter fusion and division rates. Loss of mitochondrial fusion or division can lead to detrimental effects on mitochondrial function[56–59]. Interestingly, cells are healthier when both fusion and division are inhibited, as opposed to inhibition of division or fusion alone, suggesting that the balance of the two processes is at least as important as the individual process[54].

One form of balance in mitochondrial dynamics is 'Kiss-and-Run', in which fusion and division occur in rapid succession, preserving the original mitochondrial morphology[28,50]. During this short process, mitochondria can exchange soluble IMS and matrix proteins. Mitochondrial kiss-and-run is reported to play important roles in the regulation of mitochondrial membrane potential, mitophagy and autophagy.

Overall, the delicate regulation of mitochondrial fusion and division is essential for maintaining a healthy mitochondrial network and cellular function. My thesis focuses on mitochondrial division, so I will only discuss this process in detail.

1.1.2 The difficulty in elucidating mechanisms of mitochondrial division.

Mitochondrial division can be simply understood as the division of one mitochondrion into two, but even this seemingly simple process has been the subject of a wide range of proposed mechanisms, especially in mammalian cells. My opinion is that several issues underly our incomplete understanding of mitochondrial division:

1) Technical issues with quantifying mitochondrial division. There are multiple factors that complicate the quantitative assessment of mitochondrial division:
    a. Mitochondria often overlap in space when observed by even the highest resolution fluorescence microscopy, making it difficult to determine whether one is observing a single large/branched mitochondrion or several overlapping/independent mitochondria. This is especially problematic in the ''peri-nuclear' region of the cell, where mitochondria are often enriched.
    b. The potential for mitochondrial heterogeneity. It is clear that distinct mitochondrial populations can exist in the same cell[14], meaning that picking a 'region of interest' (ROI) in a cell for quantification might not provide the whole story.
    c. The use of mitochondrial matrix markers (MitoTracker or the majority of transfected mitochondrial markers) provides a measure of IMM dynamics but not complete mitochondrial division. It is clear that IMM dynamics can take place in the absence of complete OMM division[60].
    d. Fixed-cell assays rely on the assumption that the only reason that mitochondria become small/rounded is because they divided. We feel that this assumption has

led to the widely-held belief that mitochondrial depolarization (through treatment with CCCP or FCCP) leads to mitochondrial 'fragmentation'[61–63]. A number studies that have carefully observed the process find that mitochondria appear shorter because they 'circularize' through IMM remodeling, without division[13,64,65]. We have also observed this circularization, which requires the IMM protein Oma1 but does not require Drp1[66,67]. While mitochondrial division may increase at later time points after depolarization, it does not appear to be stimulated in the short-term (< 30 min).

e. Live-cell assays suffer from low throughput and problematic analytical techniques. Essentially, it is difficult to train a program to differentiate between division and just changes in mitochondrial overlap (see the first issue above).

f. Traditional thin section transmission electron microscopy suffers from the thinness of the section, making it, in my opinion, the worst technique for assessing mitochondrial division. This problem can be circumvented by electron tomography, but this technique requires additional equipment/expertise, and reduces throughput.

2) As described above, mitochondria divide for a variety of reasons. This heterogeneity in division stimuli almost certainly results in differences in division machinery. A recent study defined two types of mitochondrial division, midzone and peripheral division, which have substantially different properties[29] (**Figure 1-2B**). Midzone division is a hallmark of healthy mitochondrial division. By contrast, peripheral division occurs when the tip of the organelle lacks membrane potential, indicating unhealthy mitochondria. Indeed, the authors report that cellular stress increases peripheral division, while midzone division increased after stimulation of cell proliferation. Some of the components of the division machinery differ between midzone and peripheral division. I feel that this publication represents the tip of the iceberg, and that there are likely multiple variations on a common theme of mitochondrial division, with all using a common protein, Drp1.

I will now discuss the known molecular players in mitochondrial division, sometimes known as the 'divisome'[68].

1.2 Mitochondrial divisome

The seemingly simple process of mitochondrial division actually requires precise control of a number of proteins, lipids, and even other organelles. These factors must work in sequence to conduct a series of synergistic actions. During these actions, two membranes must undergo division without leakage of components, which could trigger apoptosis (see earlier discussion). I start with detailed discussion of a central factor, Drp1.

1.2.1 The dynamin-like GTPase Drp1

The master regulator of mitochondrial division is the dynamin-related protein 1 Drp1 (called Dnm1 in budding yeast). Drp1 is a cytoplasmic protein which can be recruited to the OMM by 'receptor' proteins. In the cytoplasm, Drp1 exists in multiple oligomeric states, with the fundamental subunit being a dimer[69,70]. Drp1 oligomerizes extensively on the OMM to form a ring-like structure, in a process we refer to as oligomeric maturation[71]. Upon GTP hydrolysis, the Drp1 ring constricts, leading to mitochondrial division (**Figure 1-3A**). Drp1 is not only essential for mitochondrial division, but also mediates peroxisome division[72]. Drp1 knockout or expression of dominant-negative mutants leads to elongated mitochondrial morphology, and Drp1-null mice die after embryonic day 12.5 as a result of brain hypoplasia with apoptosis[73–76].

1.2.1.1 Drp1 structure

Drp1 is a highly conserved protein throughout eukaryotes, including animals, plants, fungi, and protists[74,77–79]. Four years after its initial discovery in budding yeast[80], three research groups simultaneously reported a role in mitochondrial division in yeast and mammals[78,81,82].

Drp1 has a typical dynamin superfamily architecture comprised of three distinct structural domains: GTPase domain, the bundle signaling elements (BSE), and the stalk region[70] (**Figure 1-3B)**. The GTPase domain is responsible for nucleotide binding and hydrolysis. Adjacent to the G domain, the BSE plays a role to transmit conformational changes from the GTPase domain to the stalk domain. The stalk domain is essential for Drp1 dimer formation. While other cytoplasmic dynamins (dynamin 1 and 2) contain a phospholipid-binding pleckstrin homology (PH) domain, Drp1 has an unstructured 'variable domain' (VD) in this region (**Figure 1-3B**). Even though the VD lacks a bona fide lipid binding domain, it is important for membrane interaction[70,83]. The stalk domain links the BSE domain to the VD.

Crystallographic and EM structural studies show that the basic functional unit of Drp1 is a dimer[70]. Drp1 dimerization is mediated through interface 2 located in the stalk domain. Subsequent dimers incorporate into large oligomers through interfaces 1 and 3 (**Figure 1-3B-D**). The Drp1 crystal structure reveals a fourth interface resides at the stalk domain, opposite of interface 2, allowing Drp1 to form a two-star helix with stacking interactions between strands. In the presence of GTP, Drp1 presents an additional interaction between adjacent GTPase domains, which is important for GTPase activity[84].

In humans, Drp1 is encoded by the DNM1L gene (chromosome 12) and contains 21 exons. Alternative splicing of three of these exons gives rise to nine possible isoforms[85,86] (**Figure 1-3E**). It is reported that Drp1 isoforms are functionally distinct and can have profound impacts on the cellular function of Drp1[85,87–89]. For example, certain Drp1 isoforms are associated with microtubules in HeLa cells[85]. However, how different Drp1 isoforms interact with other molecules, such as Drp1 receptors, remains unclear. In addition, the exact number of alternately spliced exons/isoforms is still unclear because Drp1 from mouse has been reported to have four alternately-spliced exons and 10 isoforms[90].

1.2.1.2 Oligomerization

In cells, Drp1 appears as 'puncta' of varying size, overlaying a uniform cytoplasmic background (**Figure 1-4A**). These puncta likely represent oligomers in varying stages of assembly. Almost all of these puncta appear associated with membranes, with 63-70% on mitochondria, ~15% on peroxisomes, and ~15% on endoplasmic reticulum[71,91]. In the cytoplasm, Drp1 appears to be in equilibrium between dimers and tetramers[92]. Purified Drp1 exists in multiple oligomeric states in the nucleotide-free state, and oligomer size increases with Drp1 concentration in the micro-molar range[69]. In the presence of GTP, purified Drp1 self-assembles into rings composed of 13-18 monomers, and has an outer and inner ring diameter of ~30 nm and ~20 nm, respectively. This Drp1 ring can tubulate isolated mitochondria or model membranes[93–98], and can even cause membrane division[96]. Assembly of large Drp1 oligomers from smaller assemblies can also be observed in live cells[71,91] (**Figure 1-4B**). Several factors besides GTP have been shown to influence Drp1 oligomerization, including ionic strength, anionic lipids[69,70,99–101]. My work also shows the oligomerization of Drp1 receptors is able to shift Drp1 towards oligomer assembly.

Drp1 oligomerization is important for efficient GTP hydrolysis. Neither Drp1 monomers nor dimers show high GTPase activity under stimulation[84]. In addition, the interaction between two Drp1 dimers via GTPase domain also play an essential role for Drp1 activity stimulation. Mutations of Gln34, Ser35, and Asp190 in the interface of dimerization of the GTPase domain led to a loss of the lipid-stimulated GTPase activity[84], suggesting the interaction of two GTPase domain contributes to the high-level GTPase activity in Drp1 oligomerization processes.

1.2.1.3 Special role of the Variable Domain

In contrast to the rest of the protein, the variable domain (VD, also called B-insert)[87,102,103], displays high sequence variability across species and is structurally not resolved in the current structures[70,97]. Also, two of the alternately spliced exons are in the VD, adding to its variability. However, the VD contains a conserved cassette of four lysines that is present in all splice variants. Mutating these lysines to alanines results in dimeric Drp1 that is unable to further oligomerize, suggesting an essential role of the VD in Drp1 oligomerization[70]. In addition, the VD harbors two phosphorylation sites and eight SUMOylation sites which have been implicated in Drp1 regulation[104–108].

Interestingly, expression of Drp1 lacking the VD (Drp1ΔVD) causes mitochondrial fragmentation in HeLa cells, which is consistent with biochemical data showing that Drp1ΔVD is more prone towards oligomer formation in solution[85,109,110]. These results suggest that the VD suppresses Drp1 activation. However, similar to the PH domain in dynamin 1 or 2, VD binding to membranes containing cardiolipin results in Drp1 activation[87]. A recent study shows that cardiolipin/VD interaction may screen repulsive Arg-Arg forces to allow intermolecular VD-VD interaction on the membrane[111]. Another group shows that the VD undergoes a disorder-to-ordered structural transition to penetrate the membrane bilayer when it binds cardiolipin[112]. Together, these results suggest that the VD is a key region for Drp1 regulation.

1.2.2 Drp1 receptors

During Drp1-mediated mitochondrial division, one of the important steps is the recruitment of cytosolic Drp1 to the OMM. Four OMM proteins have been identified as Drp1 receptors in mammals: Mff, MiD49, MiD51, and Fis1.

1.2.2.1 Mitochondrial fission factor (Mff)

Mitochondrial Fission Factor (Mff) is a tail anchored membrane protein only found in metazoans, with the majority of the protein facing the cytoplasm and only two C-terminal amino acids in the IMS (**Figure 1-5A, B**). In addition to mitochondria, Mff is found on peroxisomes[113] and ER[71]. Mff was first identified as a factor affecting mitochondrial and peroxisomal morphology in a genetic screen using siRNA in *Drosophila* S2 cells[113,114]. Loss of Mff leads to Drp1 recruitment defects and elongation of mitochondria and peroxisomes, similar to Drp1 depletion[113,115,116]. In contrast, Mff overexpression leads to fragmentation of mitochondria and peroxisomes, suggesting an important role of Mff in division[115].

Mammalian Mff can exist as nine distinct alternately spliced variants[113]. All Mff isoforms contain the following sequence regions: two short repeat motifs near the N-terminus, a coiled-coil domain (CC) and a transmembrane domain (TM). The two short repeat motifs are required for recruiting Drp1[110,115]. The highly conserved CC region (100% amino acid identity over a wide range of metazoans) consists of three heptads (21 residues). Mff appears as puncta on the OMM (**Figure 1-5C**), suggesting Mff may form oligomers (**Figure 1-5C**). Two phosphorylation sites immediately N-terminal to the CC have been associated with increased mitochondrial division, and can be phosphorylated by adenosine monophosphate (AMP)-activated protein kinase (AMPK), suggesting a possible role of Mff in energy-sensing[117]. Chapter II of my thesis examines the significance of Mff oligomerization through the CC.

Although the role for Mff in Drp1 recruitment has been clearly shown in cells, the mechanism by which Mff-Drp1 interaction causes Drp1 activation remains unclear. In biochemical assays, multiple studies have shown that the cytoplasmic region of Mff alone either stimulates Drp1 weakly or not at all[91,101,109,118]. Two studies show that Mff cannot bind and activate Drp1 unless the Drp1 variable domain (VD), which inhibits Drp1, is removed[109,110]. How the inhibitory effects of the VD are overcome *in vivo* is unknown. In cells, Drp1 does not coimmunoprecipitate with Mff unless chemical cross-linking is employed prior to lysis, suggesting that the interaction is relatively low affinity after cell extraction[109,113,115,119]. Chapter II of my thesis addresses some of these issues.

1.2.2.2 Mitochondrial dynamics protein of 49 kDa /51 kDa (MiD49/MiD51)

MiD49 and MiD51 (also called MIEF2 and MIEF1, respectively) are single-pass membrane proteins, with a short N-terminal region reaching into the IMS[120,121] (**Figure 1-5A, B)**. Knock-down or knock-out of MiD49 and MiD51 causes mitochondrial elongation, although the extent of the effect is variable between studies and there are differing reports of the redundancy between MiD49

and 51[116,122]. Unlike Mff and Fis1, MiD49/51 are only found on mitochondria (not peroxisomes)[120,121]. Similar to Mff, both MiD49 MiD51 form puncta on mitochondria (**Figure 1-5C**), suggesting that oligomerization might occur[51,120,121,123] . Interestingly, the purified cytoplasmic regions of either MiD49 or MiD51 behave as monomers and cannot stimulate Drp1 activity, suggesting that oligomerization may be regulated[124–126]. Another interesting characteristic of MiD49/51 is that over-expression of either protein causes extensive DRP1 recruitment to mitochondria and leads to mitochondrial elongation[120,121], suggesting that the mechanisms by which these two Drp1 receptors influence mitochondrial division might be more complex than simply bringing Drp1 to the OMM.

Both MiD49 and MiD51 assume structures similar to nucleotide transferase (NTase) proteins, which bind nucleotides[124–126]. MiD51 binds adenine diphosphate (ADP) and guanosine diphosphate (GDP), while MiD49 displays no binding to these nucleotides[126]. Interestingly, MiD51 still recruits Drp1 in the absence of nucleotide binding, but does not activate Drp1 significantly[124,125]. In Chapter III, I show that both MiD49 and MiD51 bind long chain fatty acyl-CoA, which induces MiD oligomerization, in turn activating Drp1 GTPase activity.

1.2.2.3 Mitochondrial fission protein 1 (Fis1)

Mitochondrial fission protein 1 (Fis1) is a tail-anchored protein found on peroxisomes and mitochondria, exposing a 15 kDa region to the cytoplasm (**Figure 1-5A, B)**. Unlike the other Drp1 receptors discussed above, Fis1 is broadly expressed in eukaryotes, including in yeast. Also, Fis1 is more homogenously distributed on mitochondria than the other receptors[127] (**Figure 1-5C).** Detailed characterization of Fis1 has been conducted in budding yeast, where it was initially discovered by complementation screens designed to identify genes that could regulate mitochondrial morphology[78,128]. The loss of Fis1 in yeast induces defects in mitochondrial Dnm1 recruitment and contributes to failed division[129]. Drp1 binding by Fis1 requires an adaptor protein, either Mdv1 or Caf4[130–133].

The role of Fis1 in mammalian mitochondrial division is more controversial. Discovered shortly after the discovery of Fis1 in yeast, initial reports were that mammalian Fis1 participated in mitochondrial division[34,88,134–136]. Several later studies, however, found that ablation of Fis1 did not elongate mitochondria as expected[115,116,122,137,138]. Similarly, the role of Fis1 in peroxisome division has been controversial[115,139,140]. In addition, no obvious Mdv1/Caf4 homologs are present in mammals and there is no clear evidence showing that Fis1 directly interacts with Drp1[120]. These

conflict observations suggest that Fis1 might not be involved in mammalian mitochondrial division, or may be involved in a specific type of division event, perhaps one that is stress-induced. Corresponding to this idea, a recent study shows that Fis1 regulates peripheral mitochondrial division, which is related to lysosomal-related mitochondrial degradation[29,141].

Despite the controversial role in mitochondrial division, Fis1 has been found to interact with other proteins to regulate several cellular processes. 1) It was reported that Fis1 inhibits mitochondrial fusion by interacting with mitochondrial fusion protein Opa1 and Mfn1/2 and inhibiting their GTPase activities[142]. 2) Fis1 also plays a role in in mitophagy by recruiting TBC1D15 and TBC1D17 to constrain autophagosome formation. In addition, Fis1 also interacts with Syntaxin 17 to delay mitophagy during acute cellular stress[88,137,143]. 3) Fis1 overexpression leads to the clustering of mitochondria at perinuclear region and to induce ER calcium release[134,136]. In sum, the direct role of Fis1 in mammalian mitochondrial division is still unclear.

1.2.3 Drp1 regulatory mechanisms

Besides Drp1 receptors on the OMM, several other mechanisms for Drp1 regulation have been demonstrated, as discussed below.

1.2.3.1 Drp1 phosphorylation

Protein phosphorylation/dephosphorylation is a common regulatory mechanism that involves the post-translational addition or removal of a phosphate moiety to serine, threonine, or tyrosine residues, performed by enzymes called kinases/phosphatases. Drp1 phosphorylation is thought to play important regulatory roles in mitochondrial division. There are, however, some confusing aspects to the existing literature, as discussed below.

Drp1 can be phosphorylated at multiple sites, with two phosphorylation sites in the variable domain being the best studied: S579[105] and S600[104,106] (**Figure 1-6A**)(amino acid positions given for Drp1 isoform 3, see **Figure 1-6B** for the corresponding positions in all Drp1 isoforms). Although several tyrosines (Y266, Y368, Y449) have been reported to be phosphorylated by c-Abl kinase in an activating manner[144], these sites have not been widely reported and are therefore not discussed further here.

Drp1 S579 was first discovered to be phosphorylated by the cyclin dependent kinase 1 (Cdk1/cyclin B)[105], but subsequent studies have shown that this site can also be phosphorylated by the extracellular signal-regulated kinases (ERK1/2)[145–147], protein kinase C δ (PKCδ)[148], Rho-associated protein kinase (ROCK)[149], Ca^{2+}/calmodulin-dependent protein kinase II (CaMKII)[150,151] and Cdk5[85,152]. Recently, this site was also found to be a substrate of PINK1, suggesting a novel mechanism of mitochondrial division independent of parkin and autophagy[153]. The phosphatase mediating S579 dephosphorylation is not well studied, although dual-specificity phosphatase 6 (DUSP6) might play this role[154]. Drp1 S600 is phosphorylated by cyclic AMP (cAMP)-dependent protein kinase A (PKA)[104,106], ROCK1[155], Ca^{2+}/calmodulin-dependent protein kinase Iα (CaMKIα)[156], adenosine monophosphate (AMP)–activated protein kinase (AMPK)[157] and protein kinase D (PKD)[158], and can be dephosphorylated by protein phosphatase 2A (PP2A), calcineurin, and phosphoglycerate mutase 5 (PGAM5)[106,159–161].

Due to the close structural proximity between S579 and S600, there may be crosstalk between the two phosphorylation sites. Although a recent study has shown that Drp1 phosphorylation at S600 promotes phosphorylation at the S579 site, with phosphorylation of both sites being required for maximal mitochondrial fragmentation[162], other studies have reported that increasing phosphorylation of S579 site either does not change the phosphorylation of S600 site or corresponds to a reduction of P-S600[150,152,154,163,164]. These conflict results might suggest that the phosphorylation of these two sites is controlled by different mechanisms in different cell lines.

An accepted view in the field is that S579 phosphorylation increases Drp1-mediated mitochondrial division, while S600 phosphorylation decreases division (**Figure 1-6C**). For S579, this association is uniformly supported in the literature, with phosphorylation of S579 is associated with increased mitochondrial division in many cellular circumstances[85,105,145–150,153]. In contrast, the function of S600 phosphorylation on Drp1 activity remains controversial. While PKA has been shown to phosphorylate S600 and hamper mitochondrial division[104,106,157,159], phosphorylation by other kinases (CaMKIα-, ROCK1-, PKD-associated) leads to the opposite effect: fragmented mitochondria[155,156,158]. These results suggest that additional factors might be involved in this regulation under physiological conditions.

Apart from the observations of phosphorylation effects in cells, detailed studies of phosphorylation effects on Drp1 properties have not been conducted. Theoretically, phosphorylation may influence

three aspects of Drp1 function: 1) translocation from the cytosol to the outer mitochondrial membrane; 2) interaction with Drp1 receptors; 3) Drp1 self-oligomerization and GTPase activity.

1) Drp1 translocation

   The VD domain of Drp1 is reported to regulate the interaction between Drp1 and the mitochondrial lipid cardiolipin[112], thus PTMs in this region might influence binding of Drp1 to OMM. Consistent with view, phosphorylation of S579 unvaryingly promotes the recruitment of Drp1 to mitochondria regardless of upstream kinase doing the phosphorylation[105,148–150]. There is, however, seemingly contradictory data on the functional consequences of Drp1 phosphorylation at S600. Whereas several studies report that phosphorylation of Drp1 at S600 site by PKA decreases mitochondrial Drp1 recruitment[106,159,165], other studies demonstrate that phosphorylation of the same site by other kinases have the opposite effect[155,156]. Interestingly, another publication reports that S600 phosphorylation is not a determinant controlling mitochondrial Drp1 recruitment[166].

2) Interaction with Drp1 receptors

   Another possibility is that phosphorylation of Drp1 regulates mitochondrial division through regulating its interaction with receptors. Research in this area is mainly conducted through the co-immunoprecipitation or interactions between purified proteins. *In vitro*, while purified S579D phosphomimetic mutant does not display increased binding to Mff[110], purified S600D decreases the Drp1-Mff interaction. This finding is consistent with co-IP results from HEK293 cells, which show that the association of Mff with the phosphomimetic Drp1-S600D is reduced compared with Drp1-WT and Drp1-S600A[116,166]. There are less reports regarding the effects of S579 phosphorylation on MiD49/51 interaction, with most studies examining the S600 site. One study shows that the phosphomimetic mutant S600D binds better to MiD49 and MiD51, and overexpression of MiD49 or MiD51 in turn increases the phosphorylation level of Drp1 at the S600 site[116]. Another study, however, suggests that S600D fails to co-assemble with MiD49[97].

3) Drp1 self-oligomerization and GTPase activity.

   How phosphorylation regulates Drp1 oligomerization and GTPase activity has not been studied in any detail. My work shows that phosphorylation of either site reduces Drp1 oligomerization and decreases the stimulatory effects on GTPase activity for all Drp1 activators tested. These findings will be discussed in Chapter IV.

1.2.3.2 Actin filaments

Actin has a wide range of functions in eukaryotic cell, including around mitochondria[17,167]. The interaction between actin and dynamin proteins is well known[168–170]. Drp1 has also been shown to be able to directly interact with actin, with regulatory consequences for mitochondrial division, as described below.

Pioneering work from the Higgs laboratory showed evidence for the Drp1/actin filament interaction during mitochondrial division[91,171]. In these studies, an ER-bound splice variant of the formin INF2 nucleates a network of actin filaments (**Figure 1-7A**). This actin polymerization is also referred as calcium-induced actin (CIA), because a transient increase in cytosolic calcium activates INF2[60,91,172,173]. Biochemically, Drp1 can directly bind and bundle actin filaments, and actin filaments have a 4-fold stimulatory on Drp1 activity[69,91]. INF2 depletion decreases mitochondrially-associated Drp1 and inhibits mitochondrial division[69,91,171](**Figure 1-7B**). Besides INF2, other actin-binding proteins also play roles in this division process, such as SPIRE1C and myosin II[14,174] (**Figure 1-7A**). How these factors work together is still unclear. A recent review provides some insights on this process[17].

One important question specifically draws our attention: once Drp1 is recruited by actin filaments, how does it transfer to the OMM to directly drive mitochondrial division? I found evidence that actin-recruited DRP1 oligomers might be passed to Mff. These findings will be discussed in Chapter II.

1.2.3.3 Phospholipids: Cardiolipin and phosphatidic acid

Phospholipids are fundamental building blocks of mitochondrial membranes. There is some evidence that the predominately mitochondrial lipid cardiolipin (CL) is involved in mitochondrial division. Although CL is more enriched on the IMM (~25 mol%) than on the OMM (<10 mol%), local OMM CL content can approach to 25 mol % at IMM-OMM contact sites under certain conditions[175–180]. In the IMM, CL is synthesized from phosphatidic acid (PA). In contrast, in the OMM, CL can be converted back to PA by mitochondria-localized phospholipase D (MitoPLD)[181]. The balance between PA and CL appears to have an effect on mitochondrial division[181] (**Figure 1-7C**).

CL is thought to contribute to mitochondrial division in several ways (**Figure 1-7D**):

1) Membrane Curvature:

   CL affects membrane curvature due to its unique shape, charge and properties[182–184]. Using supported lipid membrane tube assays, it was shown Drp1 displays an intrinsic preference for binding CL-containing membranes of high curvature, and could readily sever lipid tubes of diameters up to 400 nm[96].

2) Drp1 localization and stabilization

   Studies using purified Drp1 have shown that Drp1 interacts directly with CL[70,87,99,185]. A recent study shows that Drp1 VD is necessary and sufficient for specific CL interactions *in vitro*, with the VD undergoing a disordered-to-ordered structural transition upon binding CL-containing membranes[112]. This stabilization is also shown to be involved in VD-dependent Drp1 oligomerization and phase separation[111].

3) Regulation of Drp1 GTPase activity

   GTPase activity is essential for Drp1 function in membrane constriction and mitochondrial division. CL potently stimulates Drp1 GTPase activity[87,99,185]. However, a critical amount of CL is necessary for stimulation. Liposomes containing 10 mol % CL have no effect on Drp1 activity, while maximal stimulation is achieved at 25 mol %[87]. The extent to which CL can stimulate GTP hydrolysis could be isoform dependent, with Drp1 isoform 3 shows highest stimulation and Drp1 isoform 6 being stimulated to a lower level[87].

   As mentioned previously, PA and CL can be inter-converted, and this inter-conversion might regulate mitochondrial division through altering Drp1 GTPase activity. Overexpression of MitoPLD converts CL to PA, leading to the accumulation of Drp1 oligomers on mitochondria without productive division. Although PA is able to interact with Drp1, it has been proposed that PA blocks the GTPase activity of Drp1 after oligomerization[186]. Thus, regulation CL level by MitoPLD might regulate mitochondrial dynamics.

Overall, these results suggest that CL and PA could play roles in Drp1 recruitment and mitochondrial division. However, questions regarding how CL synergizes with other Drp1 regulatory factors is still unclear.

1.2.3.4 Mitochondrial division-related organelles

Mitochondria communicate extensively with other organelles, including ER, lysosomes, and Trans-Golgi network (TGN)-derived vesicles. The interaction between mitochondria with these organelles during mitochondrial division has recently been studied.

1) ER

   ER-mitochondria contact sites (ERMCs) serve many purposes, including mitochondrial division[187]. Actin polymerization might play a key role in ERMC-mediated mitochondrial division, with two important proteins being the ER-bound formin INF2 and the OMM-bound protein Spire1C, which facilitate assembly of actin filaments for Drp1 recruitment[91,171,174]. ERMCs also facilitate calcium transfer from ER to mitochondria, triggering mitochondrial IMM division prior to OMM division[60,188]. ERMCs are also associated with division of the mitochondrial genome, which often precedes mitochondrial division[189].

2) Lysosomes

   Mitochondria can also associate with lysosomes during mitochondrial division[190], with mitochondria-lysosome contact sites marking mitochondrial division sites[141]. Release of the contact, a process required for mitochondrial division, occurs following Rab7 GTP hydrolysis, mediated by Fis1-dependent recruitment of TBC1D15 to mitochondria[141].

3) Trans-Golgi network (TGN) vesicles

   Another interaction regulating mitochondrial division is the contact between mitochondria and TGN vesicles. At the Golgi apparatus, the GTP-bound form of Arf1 regulates the formation of TGN-derived vesicles by recruiting the PI4P kinase to form PI4P[191]. Mechanistically, it has been shown that PI4P is required downstream of Drp1 recruitment to mediate a late step in mitochondrial division. The TGN vesicles carry PI4P to mitochondria-ER-lysosome contact sites. Suppression of either Arf1 or phosphatidylinositol 4-kinase IIIβ (PI4KIIIβ) leads to mitochondrial elongation[192–194].

Although all of these organelles appear to play roles in mitochondrial division, it is unclear how these roles relate to the other regulatory roles discussed above.

1.3 Crosstalk in mitochondrial divisome

In general, the 'crosstalk' between any two regulatory mechanisms in mitochondrial division is poorly understood. Do each of these represent independent means of regulating division, or do they work together in a single, unified mechanism? My feeling is that the truth is somewhere between these two possibilities, with some regulatory mechanisms working together whereas others regulating division in response to distinct stimuli.

1.3.1 Drp1 receptors

As described earlier, four Drp1 receptors Mff, MiD49, MiD51, and Fis1 are expressed in mammals, often simultaneously in the same cell. Among these receptors, Mff, MiD49 and MiD51 are able to independently interact with and recruit Drp1 to the OMM. This seems to imply a redundant mode of action for the Drp1 receptors in mammals, but this redundancy might be explained by two possible mechanisms:

1) Cooperative effects of receptors on Drp1

   It was reported that 90-98% of MiD51 is found in foci with a partner protein: MiD49, Mff or Drp1[195]. Another report shows that MiD49/51 might facilitate the binding of Mff to Drp1 by serving as a molecular adapter in a trimeric Drp1-MiD49/51-Mff complex at the OMM[196–198]. Taken together, these studies suggest that MiD49/51 might act together with Mff in the same division event. In my work, I have found that MiD49/51 oligomers synergized with Mff to stimulate Drp1 activity, be discussed in Chapter III.

2) Roles for Drp1 receptors in distinct fission events

   Another possibility for the existence of multiple receptors is that each receptor might be regulated by different signals and thereby control distinct mitochondrial division events.

   As mentioned earlier, a recent study identified two types of mitochondrial division: midzone and peripheral division[29]. Although both types of division are mediated by Drp1, Mff and actin polymerization appear to be important only in midzone division. Interestingly, Fis1 was shown to play a role in peripheral division. MiD49/51 were not examined in this study.

   My recent work has revealed that long-chain acyl coenzyme A (LCACA) is an activator of MiD49 and MiD51, inducing their oligomerization and activating Drp1 activity. These results suggest that MiD49 and MiD51 might function in a pathway that mediates mitochondrial fatty

acid oxidation, although it is not clear whether they are the only Drp1 receptors involved in this pathway. I will discuss the details in Chapter III.

1.3.2 Interaction between the two Drp1 phosphorylation sites

As mentioned above, Drp1 can be phosphorylated at two phosphorylation sites: S579 and S600. The effects of phosphorylation on each site have been widely discussed. However, studies regarding combined effects on these two sites is limited. Two studies generated mutants of Drp1 mimicking constitutive phosphorylation (S→D/E) or dephosphorylation (S→A) on the two Drp1 phosphorylation sites and studied the combo effects in either HeLa cells or in mice[159,162]. In Hela cells, the S579A/S600A mutant fragmented mitochondria, while S579D/S600D elongated mitochondria, suggesting that S600 site is the dominant site regulating mitochondrial morphology[159]. Consistent with this observation, Drp1 phosphorylation at S600 acts as an upstream event for S579 phosphorylation in mouse cells and tissues, leading to mitochondrial fragmentation[162]. Although these two studies have investigated the combo effects in two different models, the mechanism of how the combo phosphorylation of Drp1 directly influences its activity is still unknown. In my work, I have examined the combo effects biochemically, and discuss my findings in Chapter IV.

1.4 Other questions concerning mitochondrial division

1.4.1 Is Drp1-mediated constriction the final event in division?

Although the ability of Drp1 to constrict OMM is well described, its capacity to mediate full division (including the final scission step) has frequently been questioned. Some studies propose that Drp1 does not sever but rather constricts the OMM, based on three observations: 1) recombinant Drp1 leads to liposome tubulation but not to their scission[93]; 2) in the presence of GTP, the diameter of Dnm1-lipid tubes is ~ 50-60 nm[95], indicating Drp1 does not have the dynamic range to complete membrane division *per se*; 3) depletion of the ubiquitously-expressed classical dynamin 2 causes mitochondrial "super-constrictions" but not full division, suggesting dynamin 2 is required for the final step of mitochondrial division[199].

A recent study puts forward a different view, showing that Drp1 is sufficient to cause mitochondrial division and dynamin 2 is dispensable for peroxisomal and mitochondrial division[96]. Division

events were observed in mouse embryonic fibroblasts lacking Dnm1, 2 and 3. In addition, using reconstitution experiments on pre-formed membrane tubes, the authors show that Drp1 alone both constricts and severs membrane tubes. Indeed, another study has revealed that Drp1 is able to form rings with an inner diameter of 16 nm, which should constrict the underlying tube to a lumen size of 6 nm[97]. This extreme constriction is enough to cause mitochondrial division[200]. However, other studies suggest that trans-Golgi network (TGN)-derived vesicles are involved in the last step of mitochondrial division[194]. Thus, there is still no clear answer regarding whether Drp1-mediated constriction is the final event in mitochondrial division.

1.4.2 What factors play a role in IMM division?

It has been an open question whether both OMM and IMM are divided simultaneously, or whether additional proteins exist to support inner membrane division. Recent studies suggest the division of IMM involves machinery different from OMM division.

The first clue is from the observation that mitochondria undergo pre-constriction at ERMC prior to Drp1 recruitment[60,188,201]. It was found that increased mitochondrial calcium is necessary for pre-constriction[60,188], and that actin and myosin II involve in in stimulating the calcium transfer[14,202,203].

A second clue is the identification of a new role for Atg44 in mitochondrial division. Atg44 (also known as Mdi1 or mitofissin) is a small protein of 73 amino acids, located in the IMS. Deletion of Atg44 in *Saccharomyces cerevisiae* or *Schizosaccharomyces pombe* leads to net-like mitochondria, resembling Dnm1 mutants[68,204]. In yeast, Atg44 assembles into punctate structures that frequently co-localize with Dnm1, indicating the linkage between OMM and IMM division. Based on structure analysis and *in vitro* biochemical evidence, Atg44 could interact with lipid membrane and preferentially binds to sites with high positive curvature, with the ability to affect division of lipid nanotubes[205]. In addition, overexpression of Atg44 induces mitochondrial fragmentation in Dnm1-deficient cells. These data suggests that Atg44 activity does not require Dnm1, and is able to trigger Drp1-indepenent mitochondrial division[205]. While these findings are suggestive that Atg44 might play a role in IMM division, more work will be required to test this hypothesis. In addition, finding the metazoan homologue of Atg44 is essential for identification of a similar mechanism in human cells.

1.5 Concluding comments

Elucidating the mechanism of mitochondrial division is complicated by numerous regulators, participation in multiple processes, and overlapping functions in space and time. In my opinion, there are certainly more regulation mechanisms in mitochondrial division than those reported here. In this thesis, I will describe my efforts to further our understanding of three different topics in mammalian mitochondrial division.

Figures

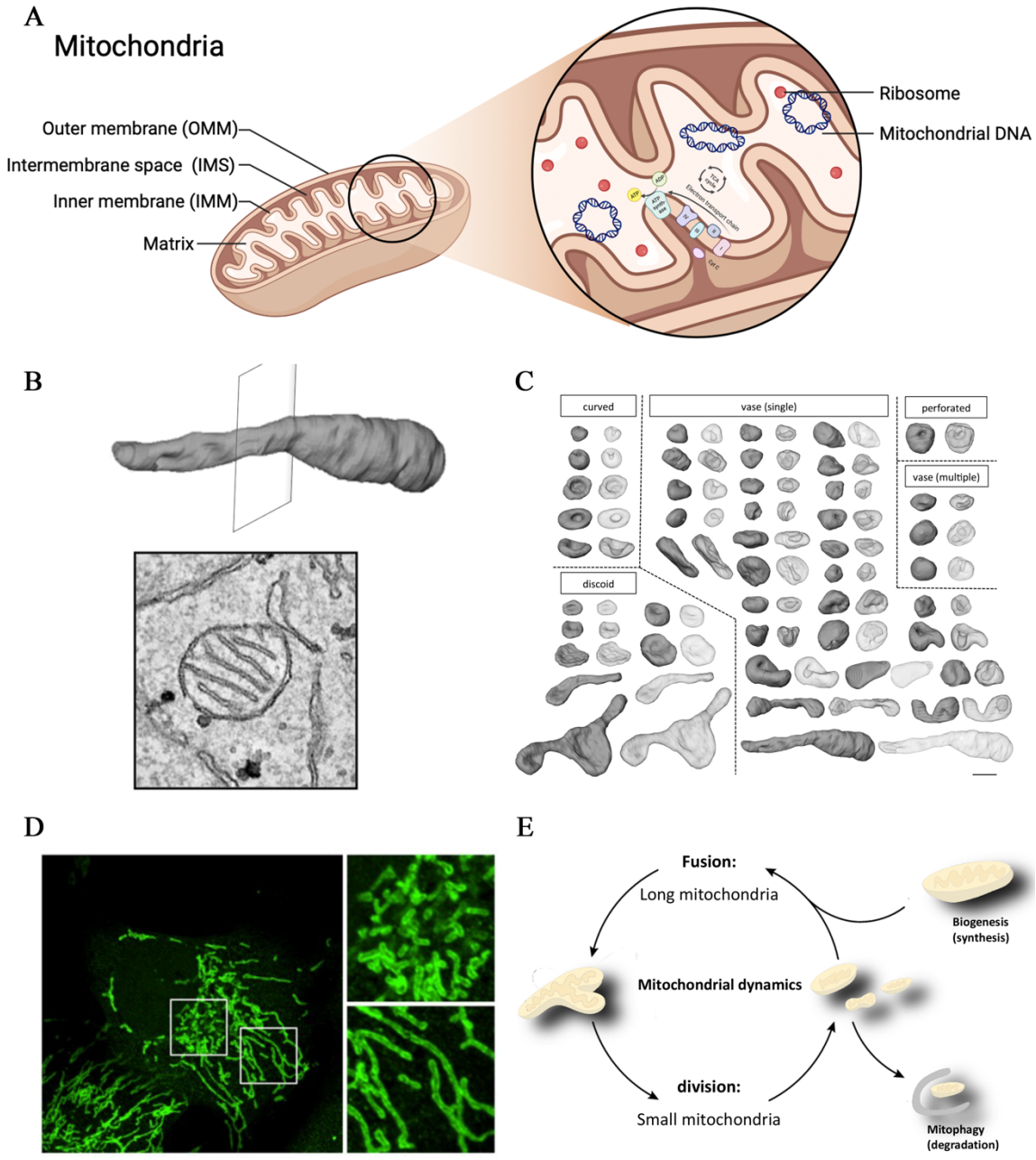
A
Mitochondria
Outer membrane (OMM)
Intermembrane space (IMS)
Inner membrane (IMM)
Matrix
Ribosome
Mitochondrial DNA
B
C
curved
vase (single)
perforated
vase (multiple)
discoid
D
E
Fusion:
Long mitochondria
Biogenesis
(synthesis)
Mitochondrial dynamics
division:
Small mitochondria
Mitophagy
(degradation)

Figure 1-1: Mitochondrial structure and dynamics.

A) Mitochondrial structure. The double-membrane structure, outer mitochondrial membrane (OMM) and inner mitochondrial membrane (IMM) results in two aqueous compartments: the inter-membrane space (IMS) and matrix. The IMM is segregated into the cristae membrane and inner-boundary membrane. The four complexes of the electron transport chain enrich on the side of the cristae, whereas ATP synthase enriches at the cristae tip. Nucleoid, containing compacted mitochondrial DNA, might attach to the cristae side.

B) The distorted view of mitochondria, from thin section electron microscopy. A long mitochondrion was cross-sectioned during thin sectioning, resulting in an image of a circular mitochondrion[13].

C) Different morphologies of mitochondria. The shape of the mitochondria was categorized into seven groups, with adjacent images showing solid and translucent views of the surface rendering to observe invaginations. Figure is modified from[13]. Scale bar, 1 μm.

D) Immunofluorescence of U2OS cell mitochondria, two boxes highlight the difference between peri-nuclear and peripheral mitochondria.

E) Mitochondrial dynamics. Mitochondria undergo fusion and division. Small mitochondria fuse into large mitochondria, while long mitochondria divide into small mitochondria. Mitochondrial dynamics are essential for biogenesis, mitophagy and other cellular process.

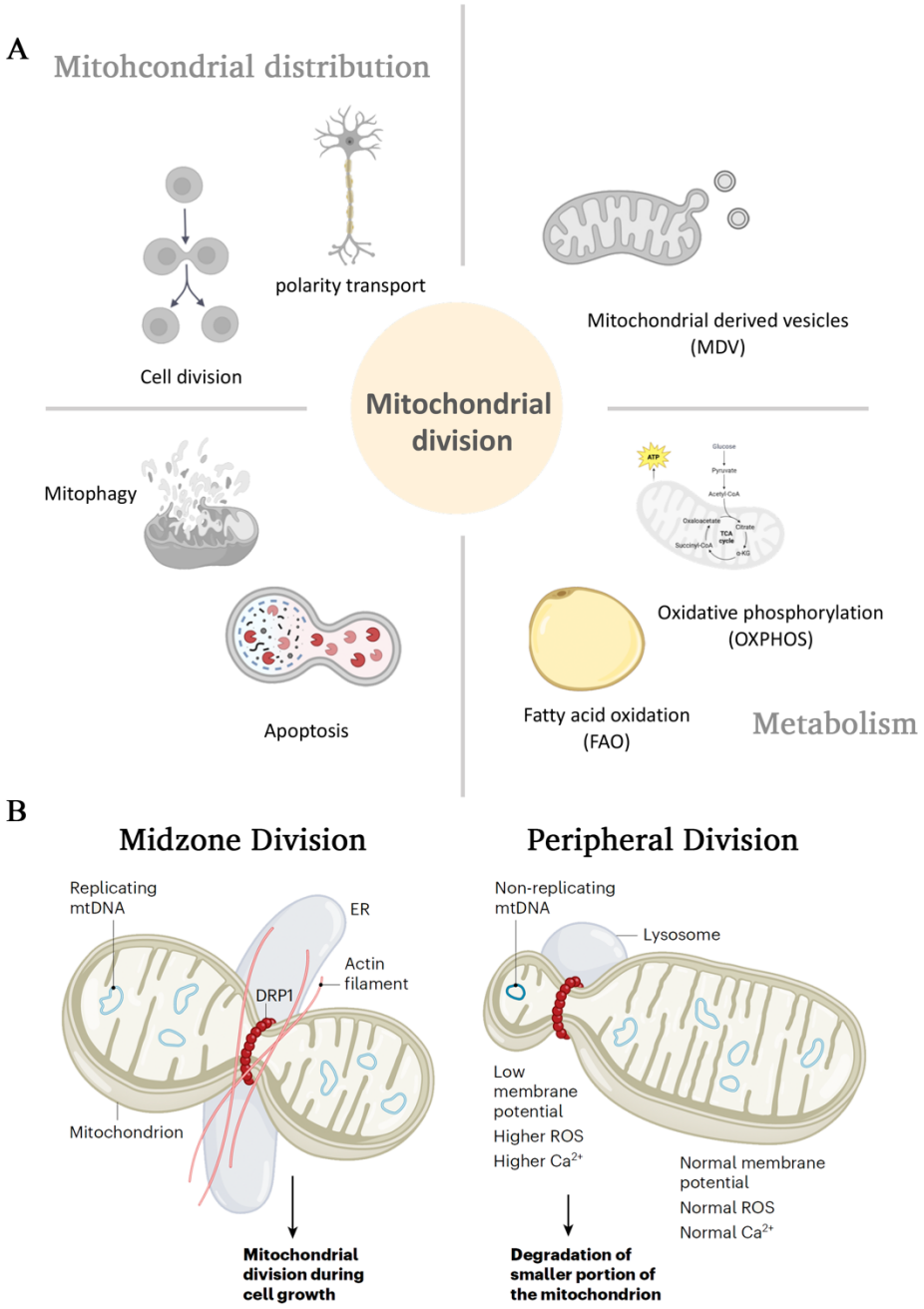

Figure 1-2: Cellular and physiological importance of the mitochondrial division.

A) Mitochondrial division alters the global mitochondrial network and affects a variety of cellular processes.

B) Two pathways for mitochondrial division. Midzone division is associated with mitochondrial division during cell growth. Peripheral division is associated with damaged mitochondria. Figure is adapted from[206].

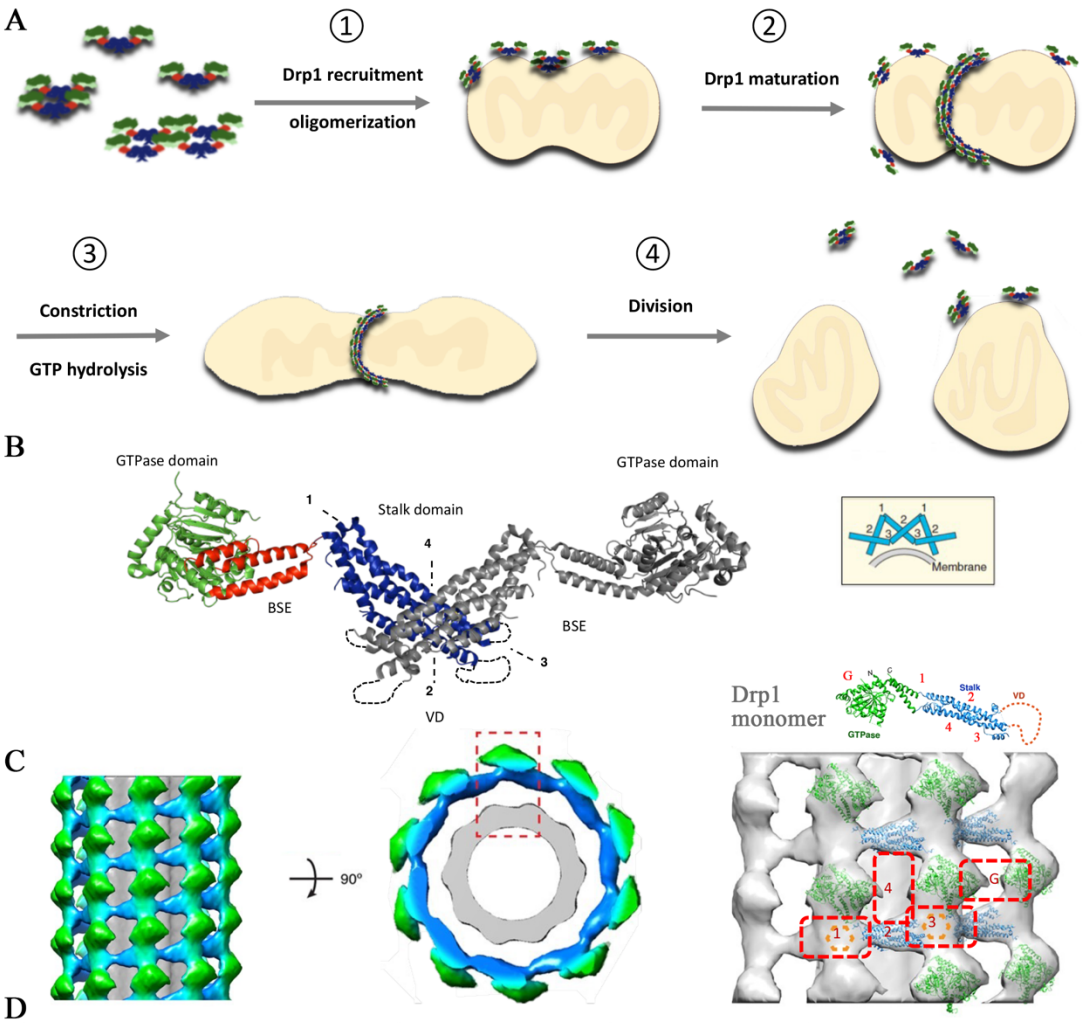

Isoform name*	Binary nomenclature**	UniProtKB	Protein length (amino acids)
isoform 1	0 1 1	o0042-1	736
isoform 2	0 0 1	o00429-3	710
isoform 3	0 0 0	o00429-4	699
isoform 4	0 1 0	o00429-2	725
isoform 5	0 x 0	o00429-5	710
isoform 6	1 1 1	o00429-6	749
isoform 7	x 1 1	o00429-7	533
isoform 8	1 1 0	o00429-8	738
isoform 9	1 0 0	o00429-9	712

Figure 1-3: Drp1 structure and role in mitochondrial division.

A) Model for assembly of division-productive Drp1 on mitochondria. Step1: Recruitment. Drp1 exists as multiple oligomeric species in the cytosol and can be recruited to the mitochondrial OMM. Step2: Maturation. Mitochondrially-bound Drp1 oligomers grow through incorporation of other mitochondrially-bound oligomers, progressively encircling the OMM in the process. Step3: Activation of Drp1 ring. Upon GTP hydrolysis, Drp1 changes and constricts its conformation and constrict mitochondria OMM at mitochondrial division site. Step 4: mitochondrial division. Drp1 synergizes with several mitochondrial division factors to drive mitochondrial division.

B) Schematic of Drp1 binding interface. Structural model of Drp1 dimer from (PDB ID: 4BEJ)[207]. Four major interfaces were identified based on the crystal structure of Drp1 fit into the cryo-electron microscopy structure of Dnm1 assembled on a lipid tube. Interface 1 is on the upper left side of Drp1 dimer and interacts with another interface1, while interface 3 binds to another interface 3 in the same way. Drp1 monomers interact with each other by the interface 2 on the stalk domain. On the lipid membrane, two Drp1 dimers interacts parallelly by interface 4 on the stalk domain.

C) 3D structure of Drp1 associated with a phosphatidylserine (PS) lipid template[207].The tertiary structure (PDB ID: 4BEJ) of Drp1 highlights conserved domains: G domain (green), middle domain (blue), variable domain (orange) and GTPase effector domain (GED, blue). The four interfaces are highlighted by red.

D) Table of the nine human Drp1 isoforms listed in Uniprot, following isoform designation given by[86] and binary nomenclature used by[85]. Binary nomenclature based on presence (1) or absence (0) of the three alternatively spliced inserts, with ‘x’ denoting a variation of the indicated site (described in [86]).

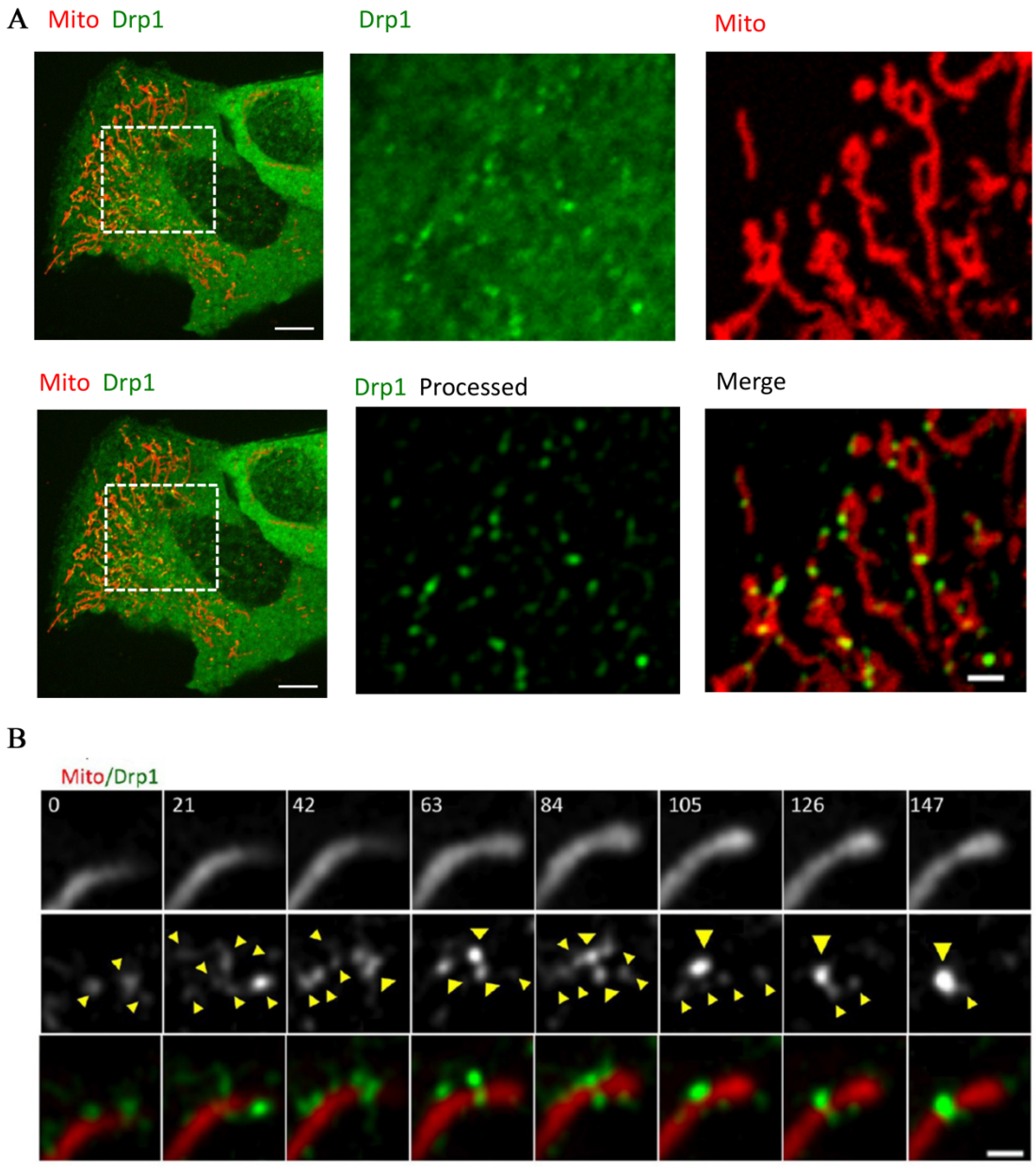

Figure 1-4: Drp1 distribution and maturation.

A) Drp1 exists in multiple oligomeric species in U2OS cells. Images of GFP-Drp1-KI U2OS cells reveal that Drp1 (green) is a cytosolic protein (upper panel). The processed image (lower panel) demonstrates that Drp1 has the ability to oligomerize, forming puncta of different sizes, with some Drp1 puncta overlapping with mitochondria (red) [71].

B) Super-resolution Airyscan live-cell images showing Drp1 maturation (yellow arrowheads)[71].

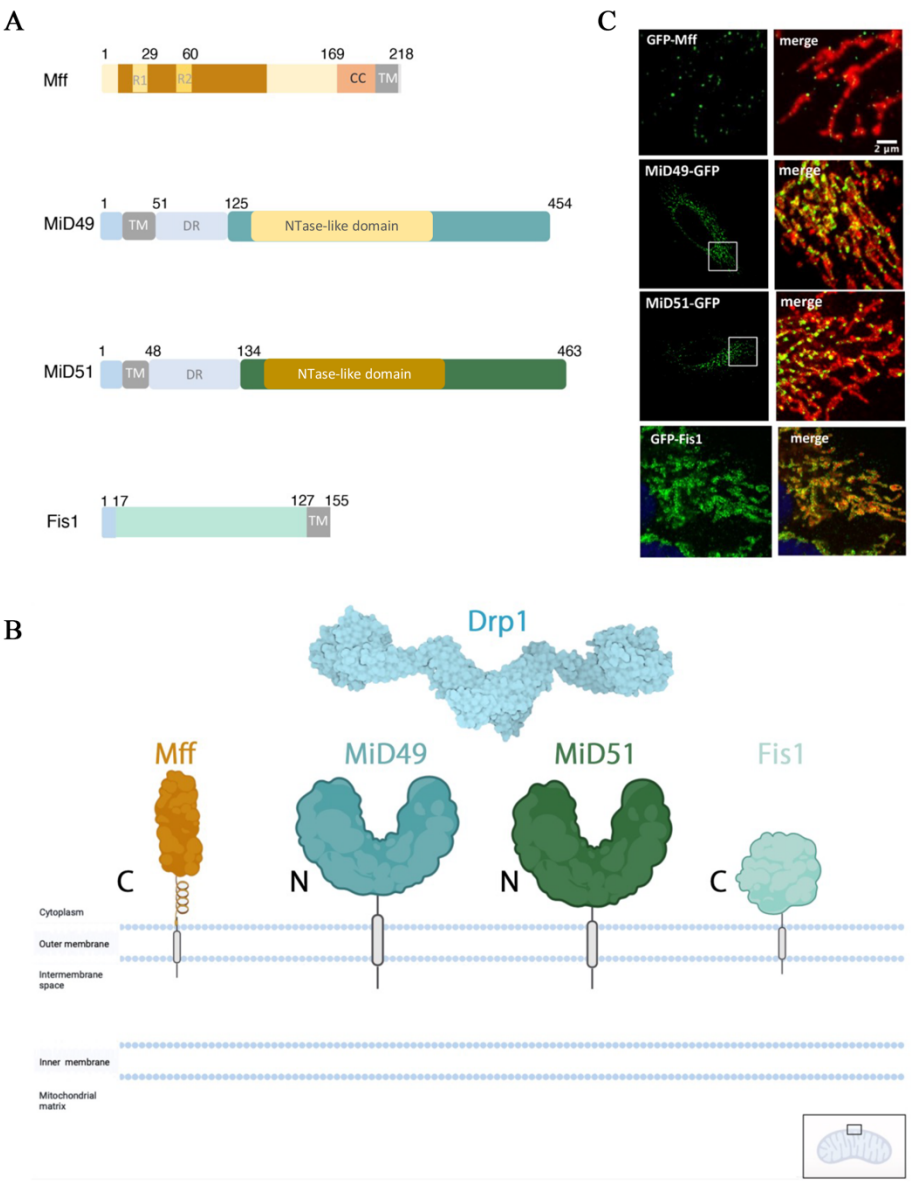

Figure 1-5: Drp1 receptors in mammalian cells.

A) Bar diagrams of Mff, MiD49, MiD51 and Fis1. Mff contains three regions: two repeats at the N-terminus (where Drp1 binds), a coiled-coiled region and a C-terminus transmembrane domain. MiD49 and MiD51 have similar structure, both contains a N-terminus transmembrane domain, followed by a disordered domain (DR) and a NTase-like (Nucleosidase-like) domain.

B) Schematic of Drp1 receptors. Mff and Fis1 insert into OMM by N-terminus transmembrane domain, while MiD49 and MiD51 by C-terminus transmembrane domain.

C) Subcellular distribution of Drp1 in mammalian cells. Images of Fis1 is adapted from[127].

A

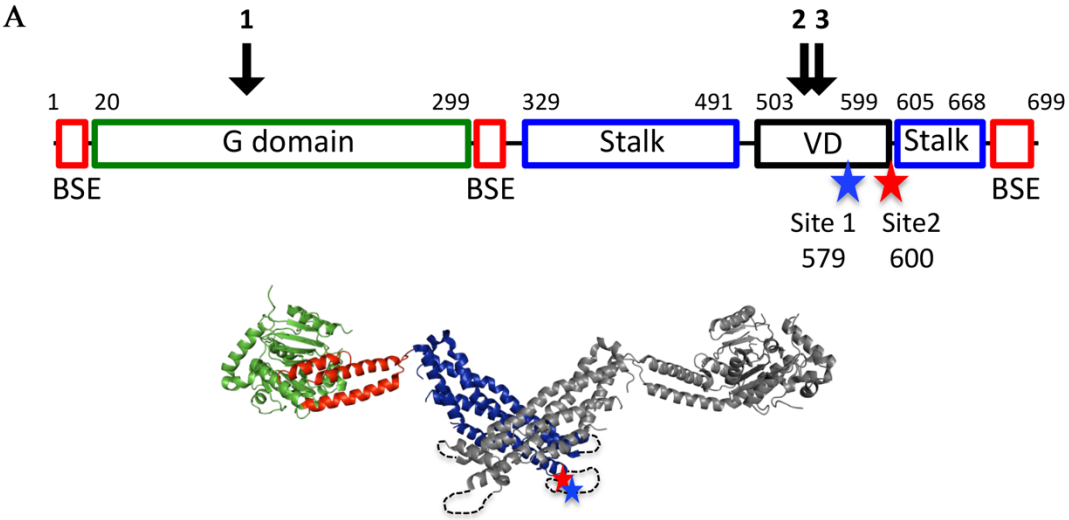

B

Isoform name*	Binary nomenclature**	UniProtKB	Protein length (amino acids)	Phosphorylation site 1	Phosphorylation site 2
isoform 1	0 1 1	o00042-1	736	616	637
isoform 2	0 0 1	o00429-3	710	590	611
isoform 3	0 0 0	o00429-4	699	579	600
isoform 4	0 1 0	o00429-2	725	605	626
isoform 5	0 x 0	o00429-5	710	590	611
isoform 6	1 1 1	o00429-6	749	629	650
isoform 7	x 1 1	o00429-7	533	413	434
isoform 8	1 1 0	o00429-8	738	618	639
isoform 9	1 0 0	o00429-9	712	592	613

C

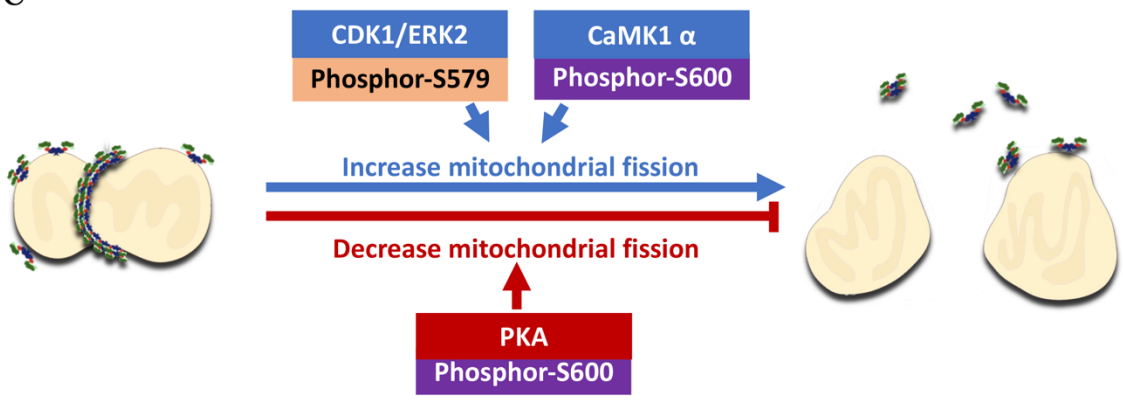

Figure 1-6: Drp1 phosphorylation sites.

A) Domain organization of Drp1 isoform 3 (also called Drp1-000): GTPase domain (green), Bundle Signaling Element (BSE, red), stalk (blue), Variable Domain (VD, black, also called the B-insert in some publications). Blue and red stars indicate phosphorylation sites S579 (site 1) and S600 (site 2), respectively. Black arrows indicate locations of the three alternatively spliced inserts.

B) Structural model of Drp1 dimer (PDB 4BEJ) showing positions of phosphorylation sites S579 (blue star) and S600 (red star) on one subunit (color coded similar to panel A). Dashed loops for Variable Domain denote that this was not resolved in PDB 4BEJ.

C) Table listing positions of the phosphorylation sites corresponding to S579 (Site 1) and S600 (Site 2) in this paper for the nine human Drp1 isoforms listed in UniProt, following isoform designation given by[86] and binary nomenclature used by [85]. Binary nomenclature based on presence (1) or absence (0) of the three alternatively spliced inserts, with 'x' denoting a variation of the indicated site[86].

D) Classical view of phosphorylation at S579 site by CDK1/ERK2 activates Drp1, S600 site by PKA inhibits Drp1 activity, while contradicting results show that phosphorylation at S600 site activates Drp1 and stimulates mitochondrial division.

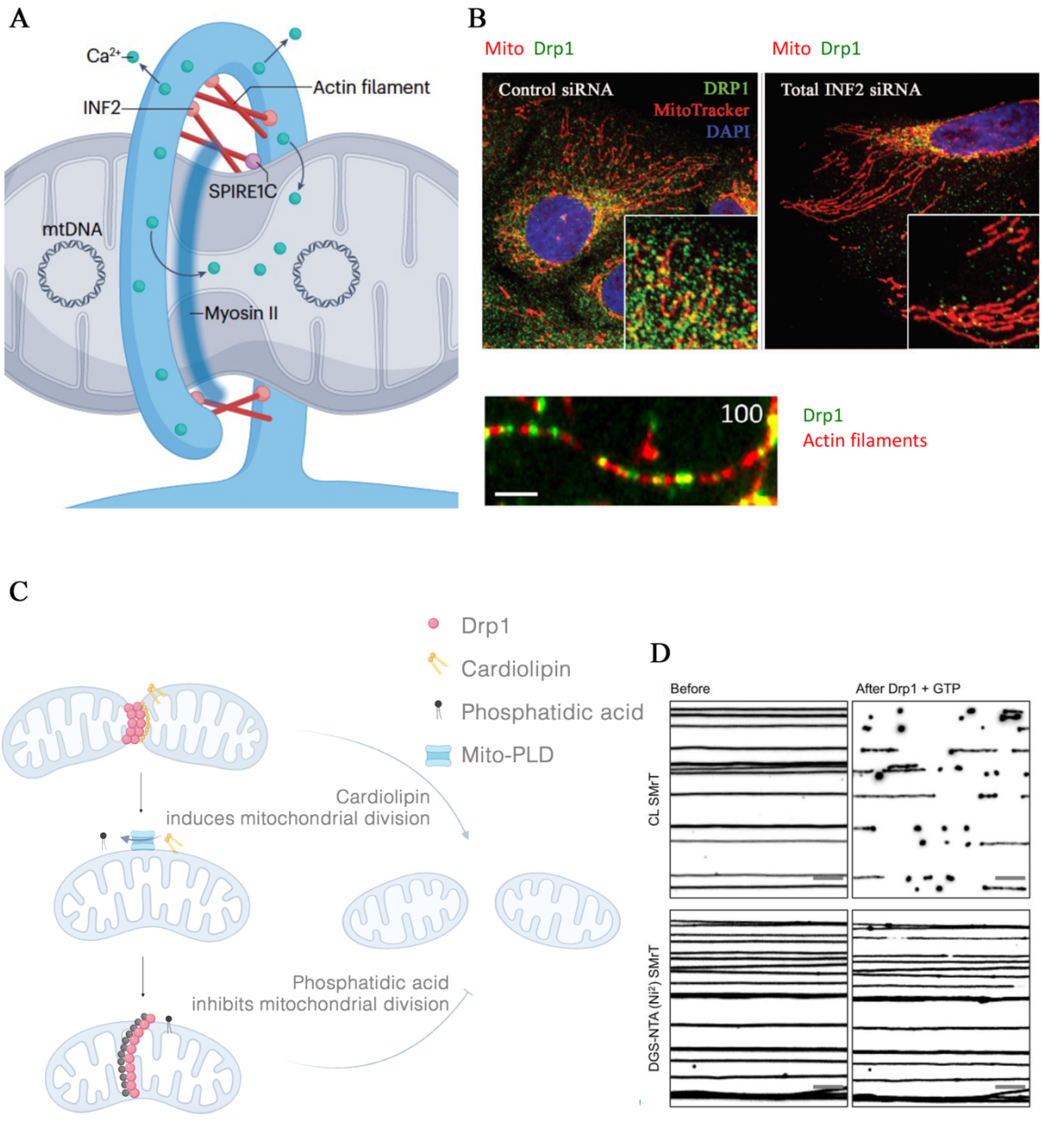
A
Ca2+
Actin filament
INF2
SPIRE1C
mtDNA
Myosin II
B
Mito Drp1
Mito Drp1
Control siRNA
DRP1
MitoTracker
DAPI
Total INF2 siRNA
100
Drp1
Actin filaments
C
Drp1
Cardiolipin
Phosphatidic acid
Mito-PLD
Cardiolipin
induces mitochondrial division
Phosphatidic acid
inhibits mitochondrial division
D
Before
After Drp1 + GTP
CL SMrT
DGS-NTA (Ni2) SMrT

Figure 1-7: Other factors involved in mitochondrial division.

A) Model for actin involvement at mitochondrial division. Actin polymerized by ER-bound INF2 leads to enhanced ER-mitochondrial contact in a myosin II-dependent manner. Enhanced ER-mitochondria contact allows more efficient calcium transfer from ER to mitochondria, leading to pre-constriction of both in IMM and OMM[17].

B) Drp1 recruitment to mitochondria by actin filaments. INF2 KD reduces Drp1 recruitment and mitochondrial elongation (upper panel), the lower panel shows that purified Drp1 (green) direct interacts with actin filaments (red) by TIRF microscopy[69].

C) Regulation of mitochondrial division by phosphatidic acid and cardiolipin. Cardiolipin synthesized in the IMM is transported to the OMM where it interacts directly with Drp1 through its variable domain. At the OMM, cardiolipin can be transformed back into phosphatidic acid by the mitochondrial OMM-localized enzyme, phospholipase D (MitoPLD). Phosphatidic acid inhibits Drp1-oligomerization-induced GTP hydrolysis, although it does not prevent Drp1 from forming its classic ring structure around the mitochondria.

D) Representative fluorescence micrographs of supported membrane nanotubes (SMrT) containing 30 mol% CL (top) and 10 mol% DGS-NTA ($Ni2^{+}$) (bottom) imaged before and after addition of Drp1 with GTP. Fission is seen as severing of the nanotubes. Images are inverted in contrast and scale bars = 10 μm. Figure is adapted from[208].

Chapter II:

Mff oligomerization is required for Drp1 activation and synergy with actin filaments during mitochondrial division

Chapter II

Mff oligomerization is required for Drp1 activation and synergy with actin filaments during mitochondrial division

Ao Liu[1], Frieda Kage[1], and Henry N. Higgs[1]

[1]Department of Biochemistry and Cell Biology, Geisel School of Medicine at Dartmouth College, Hanover, NH 03755

The text and data here are adapted or reproduced in full from the manuscript published in

Molecular Biology of the Cell

(DOI: https://doi.org/10.1091/mbc.E21-04-0224)

This work was supported by National Institutes of Health Grants NIH GM122545 and DK088826 to H.N.H. and P20 GM113132 to the Institute for Biomolecular Targeting Centers of Biomedical Research Excellence (COBRE). This work was also supported by the German Research Foundation grant KA 5106/1-1 to F.K.

2.1 Abstract

Mitochondrial division is an important cellular process in both normal and pathological conditions. The dynamin GTPase Drp1 is a central mitochondrial division protein, driving constriction of the outer mitochondrial membrane. In mammals, the outer mitochondrial membrane protein Mff is a key receptor for recruiting Drp1 from the cytosol to the mitochondrion. Actin filaments are also important in Drp1 recruitment and activation. The manner in which Mff and actin work together in Drp1 activation is unknown. Here, we show that Mff is an oligomer (most likely a trimer) that dynamically associates and disassociates through its C-terminal coiled-coil, with a K_d in the range of 10 μM. Dynamic Mff oligomerization is required for Drp1 activation. While not binding Mff directly, actin filaments enhance Mff-mediated Drp1 activation by lowering the effective Mff concentration 10-fold. Total internal reflection microscopy assays using purified proteins show that Mff interacts with Drp1 on actin filaments in a manner dependent on Mff oligomerization. In U2OS cells, oligomerization-defective Mff does not effectively rescue three defects in Mff knock-out cells: mitochondrial division, mitochondrial Drp1 recruitment, and peroxisome division. The ability of Mff to assemble into puncta on mitochondria depends on its oligomerization, as well as on actin filaments and Drp1.

2.2 Introduction

Mitochondrial division is important for mitochondrial stress response, correct mitochondrial distribution in polarized cells, and mitochondrial partitioning during cell division [22,201,209–211]. Defects in mitochondrial division lead to a number of diseases, particularly in the nervous system [212–214]. A key player in mitochondrial division is the dynamin family GTPase Drp1, which is recruited from the cytosol to the outer mitochondrial membrane (OMM), where it oligomerizes and hydrolyzes GTP to constrict the OMM en route to division [98]. Whole-body deletion of Drp1 is lethal in mice [76], with tissue-specific deletions causing major defects [75]. Mutations in Drp1 are linked with severe neurological and other conditions in humans [215–217].

Mitochondrial recruitment of Drp1 relies on Drp1 'receptor' proteins on the OMM [211,218]. Budding yeast uses the OMM protein Fis1p, which binds the dimeric cytosolic protein Mdv1p to recruit Drp1[130,185,219]. Mammals do not use this mechanism, but have several OMM proteins that can act as Drp1 receptors. One such receptor is the tail-anchored protein Mff (mitochondrial fission factor). Knock-down or knock-out of Mff results in a dramatic decrease in mitochondrial division in multiple cell types, and an almost complete absence of punctate Drp1 accumulation on mitochondria, indicative of Drp1 oligomerization [71,113,115,116,122]. Patients with Mff deficiency display developmental and neurological abnormalities [220,221]. Two other proteins, MiD49 and MiD51 (also called MIEF2 and MIEF1, respectively) can also act as Drp1 receptors [97,120,121,124]. However, the effects of Mff depletion on mitochondrial division are generally greater [115,116]. In addition, Mff is the sole receptor required for Drp1-mediated peroxisomal division, suggesting its central importance in Drp1 recruitment [71,113].

The mechanisms by which Mff activates Drp1, however, are unclear. In biochemical assays, multiple studies have shown that the cytoplasmic region of Mff alone either stimulates Drp1 weakly or not at all [91,101,109,118]. Two studies show that Mff is insufficient to bind and activate Drp1 unless an inhibitory region of Drp1, the variable domain (VD), is removed [109,222]. How the inhibitory effects of the VD are overcome *in vivo* is unknown. In cells, Drp1 does not co-immunoprecipitate with Mff unless chemical crosslinking is employed prior to lysis, suggesting that the interaction is relatively low-affinity [109,113,115,119].

Another area of uncertainty is Mff's oligomeric state. While several studies show that Mff oligomerizes through its coiled-coil region, the nature of this oligomer is unclear, with one report

suggesting a tetramer and another report suggesting a dimer [101,109]. In addition, a cellular study shows evidence that mutation of the coiled-coil region has minimal effect on Mff's cellular function [115].

These results suggest that other factors must be present to assist Mff, and there has been evidence for multiple such factors. Phosphorylation of both Drp1 and Mff modulate mitochondrial division, with Drp1 subjected to both activating and inhibitory phosphorylation while Mff phosphorylation is activating [104,106,117]. Drp1 is subject to a number of other post-translational modifications that modulate mitochondrial division [107,223–226]. Phospholipids also influence Drp1 activity, with phosphatidic acid being inhibitory and cardiolipin activating [99,186,227]. Finally, interaction between mitochondria and endoplasmic reticulum (ER) stimulates mitochondrial Drp1 recruitment [71,228].

We have shown that the mechanism for ER-mediated stimulation may be through actin polymerization, through the ER-bound formin INF2-CAAX [171]. Inhibition of INF2, or of actin polymerization in general, inhibits Drp1 puncta assembly in cells [91,171]. INF2 activation increases mitochondrial Drp1 puncta accumulation [91], and this effect requires Mff [71]. Drp1 binds directly to actin filaments, and actin binding increases Drp1 GTPase activity 6-fold [69,91]. These results suggest that INF2-mediated actin polymerization on ER stimulates Drp1 oligomerization, and that actin polymerization works with Mff in this process. One possibility is that actin binding might enhance the relatively weak interaction between Mff and full-length Drp1, to drive Drp1 oligomerization forward.

We show here that a key element of Mff's ability to activate Drp1 is its own oligomerization, which is of low affinity. Actin filaments increase Mff-mediated Drp1 activation by reducing the Mff concentration needed for activation. This effect of actin requires Mff oligomerization. Mff oligomerization is needed in cells for Drp1 recruitment and mitochondrial division. These results provide a mechanistic explanation for actin's role in Drp1 activation.

2.3 Results

2.3.1 Mff stimulates Drp1 activity and oligomerization in a concentration-dependent manner.

Previous studies have shown that the cytosolic region of Mff has modest effects on Drp1 GTPase activity [91,101,109,118]. We re-examined these properties, using the cytoplasmic region of human Mff isoform 4 (also called 0000) as a C-terminally 6His-tagged construct expressed in *E. coli* and purified the protein to apparent homogeneity (Mff-ΔTM) (**Figure 2-1A, B**). We then tested the effect of Mff-ΔTM on Drp1 GTPase activity, using full-length Drp1 000 (containing none of the alternative splice inserts) expressed and purified as previously described [69].

At 100 μM, Mff-ΔTM stimulates Drp1 GTPase activity 10-fold (**Figure 2-1C**), from a baseline of 1.55 ± 0.05 μM/min/μM to 15.53 ± 1.04 μM/min/μM. We then assessed the concentration dependence of this stimulation. Mff-ΔTM stimulates Drp1 GTPase activity poorly at low concentrations similar to those tested previously, and has an EC_{50} of 19.7 μM (**Figure 2-1D**).

We also examined the ability of Mff-ΔTM to mediate Drp1 oligomerization, as assessed by high-speed pelleting assay. In the presence of 1mM GTP, only a small fraction of Drp1 pellets at 1.3 μM. Increasing concentrations of Mff-ΔTM result in increasing amounts of both Drp1 and Mff in the pellet, with Mff concentrations > 10 μM necessary for observable effects (**Figure 2-1E, F**).

These results show that Mff engages in low-avidity interaction with Drp1, resulting in activation of its GTPase activity and oligomerization. The low binding and activation of Drp1 observed in previous assays is likely due to the low concentrations of both proteins used in these assays.

2.3.2 Mff undergoes reversible oligomerization, dependent on the coiled-coil region

We next asked why such a high concentration of Mff-ΔTM is needed to stimulate Drp1 activity. One possibility is that Mff oligomerization is necessary for Drp1 binding, and that this oligomerization is of relatively low affinity. Mff has been reported to be an oligomer [101,109] through a coiled-coil (CC) region at the C-terminus of the cytoplasmic segment. However, the nature of the oligomer is unclear, being reported as a dimer in one study [101] and a tetramer in another study [109]. To resolve this discrepancy, we analyzed the CC in detail.

The CC region consists of three heptads (21 residues) N-terminal to the transmembrane (TM) domain (**Figure 2-1A**). The amino acid sequence conservation of the CC is impressive, with 100% sequence identity over a broad range of vertebrates (**Figure S2-1A**), suggesting functional relevance. Analysis by LOGICOIL [229] predicts that the CC is likely trimeric, followed by parallel dimeric, anti-parallel dimeric, and tetrameric in order of likelihood (**Figure S2-1B**).

We produced two constructs postulated to disrupt Mff oligomerization (**Figure S2-1A**): 1) a construct lacking the CC and helical region (Mff-ΔCC), and 2) a construct in which we mutated the d positions of two of the three predicted heptad repeats in the CC (Mff-L2P, **Figure S2-1C**) [230]. We then compared the hydrodynamic properties of these constructs with those of Mff-ΔTM. By velocity analytical ultracentrifugation (vAUC), 100 μM of Mff-ΔTM has a sedimentation coefficient of 2.7 (**Figure 2-2A**), with a resulting calculated mass of 65.6 kDa (**Figure S2-2A**). In contrast, Mff-ΔCC and Mff-L2P sediment at 1.2 and 1.4 S respectively (**Figure 2-2A**), with calculated masses of 21.8 and 25.5 kDa respectively (**Figure S2-2A, Table S2-1**). The formula-calculated masses of these constructs are 23.6, 19.7, and 23.5 kDa respectively. Conducting vAUC at a higher Mff-ΔTM concentration (250 μM) produces similar results (3.0 S, 60.2 kDa, **Figure 2-2A, Figure S2-2A, Table S2-1**). These results suggest that Mff-ΔTM is a trimer, whereas Mff-ΔCC and Mff-L2P are monomers.

We examined the concentration dependence of Mff-ΔTM oligomerization using size exclusion chromatography (SEC). At 100 and 600 μM, Mff-ΔTM elutes in an early fraction, but lower concentrations elute progressively later (**Figure 2-2B**). Plotting the calculated Stokes radii versus concentration results in an apparent half-maximal concentration for the change in Stokes radius of 4.8 μM (**Figure 2-2C**). In contrast, 100 μM of both Mff-ΔCC and Mff-L2P elute considerably later than Mff-ΔTM (**Figure 2-2D**), and do not vary as a function of concentration (**Figure 2-2C**).

To determine whether the CC region is sufficient for oligomerization, we examined a fusion protein of the Mff CC on the C-terminus of GFP (GFP-CC), as well as the L2P mutant of this construct (GFP-L2P, **Figure 2-3A**). By vAUC, GFP-CC at 250 μM sediments primarily as a 4.9 S particle, corresponding to a mass of 100.3 kDa (**Figure 2-3B, Figure S2-2B, Table S2-1**), whereas the calculated monomer mass is 34.8 kDa. In contrast, GFP-L2P sediments at 2.7 S, corresponding to a mass of 29.3 kDa (**Figure 2-3B, Figure S2-2B, Table S2-1**). By SEC, a dilution series of GFP-CC results in steadily decreasing Stokes radii, with a half-maximal concentration of 15 μM, while

GFP-L2P displays similar Stokes radii at low and high concentrations (**Figure 2-3C-E**). GFP-CC itself has no ability to stimulate Drp1 GTPase activity (**Figure S2-2C**) or to cause the pelleting of Drp1 (**Figure S2-2D**), showing that the Mff-CC alone is not capable of Drp1 activation.

These results suggest that the cytoplasmic portion of Mff is oligomeric, and that its oligomerization is in dynamic equilibrium in the range of 5-15 μM in solution. The oligomer is most likely a trimer, although definitive resolution awaits structural analysis (see Discussion). Oligomerization is mediated by the coiled-coil region.

2.3.3 Mff oligomerization is necessary for productive Drp1 interaction

We next tested the effect of Mff oligomerization on its ability to influence Drp1, using Mff-ΔCC or Mff-L2P as non-oligomeric constructs. In GTPase assays, neither Mff-ΔCC nor Mff-L2P increases Drp1 GTPase activity at any concentration tested, in contrast to the effect of Mff-ΔTM (**Figure 2-1D**). In Drp1 pelleting assays, these monomeric mutants do not cause an increase in Drp1 pelleting in the presence of GTP (**Figure 2-1E, F**).

We also used total internal reflection fluorescence (TIRF) microscopy to assess the binding of Mff to Drp1 oligomers. In the presence of the nonhydrolyzable GTP analogue GMPPCP, Cy5-labeled Drp1 appears as heterogeneous punctae (**Figure 2-4A**), representing oligomeric rings [101]. Introduction of fluorescein-labeled Mff-ΔTM causes fluorescein accumulation on Drp1 puncta (**Figure 2-4A, B**). Significant fluorescein label remains on the puncta after washout, suggesting stable binding between Mff-ΔTM and Drp1. In contrast, Mff-L2P displays 5-fold less binding than Mff-ΔTM and is removed after wash (**Figure 2-4A, B**).

These results suggest that Mff oligomerization is required for productive Drp1/Mff interaction, stimulating Drp1 GTP hydrolysis. The fact that oligomerization-competent Mff persists on Drp1 oligomers after wash-out of free Mff suggests that Drp1 binding stabilizes the Mff oligomerization interaction.

2.3.4 Actin filaments synergize with oligomeric Mff to stimulate Drp1 activity

We have previously shown that actin filaments stimulate Drp1 GTPase activity in a bi-phasic manner, with maximal stimulation occurring at 0.5 μM actin and then descending back to the level of Drp1 alone at higher actin concentrations [69]. Here, we examined the combined effects of Mff-ΔTM and actin on Drp1 GTPase activity. Either actin or Mff-ΔTM alone stimulate Drp1, but a high concentration of Mff-ΔTM is required for stimulation, with an EC_{50} of 17.4 μM (**Figure 2-5A**). However, addition of 0.5 μM actin filaments greatly increases the potency of Mff's effect on Drp1 by shifting the EC_{50} of Mff-ΔTM to 2.2 μM (**Figure 2-5A**). Mff-ΔTM does not affect the maximal effective concentration of actin (**Figure 2-5B**). The maximum combined effect of Mff-ΔTM and actin is approximately 16 μM GTP hydrolyzed/min/μM Drp1. In contrast to its effect on Mff-ΔTM, actin has no effect on the ability of Mff-L2P to activate Drp1, which is not able to enhance actin-induced Drp1 GTPase activity at any concentration tested (**Figure 2-5A**). Finally, the ability of Mff-ΔTM and actin to stimulate Drp1 GTPase activity depends upon Drp1's ability to oligomerize, since an oligomerization-defective mutant (Drp1 401-404 AAAA) [69,70] is not activated by the Mff/actin combination (**Figure S2-3A**).

The ability of actin to enhance the efficiency of the Drp1 GTPase activity stimulation by Mff-ΔTM is not due to a direct affinity of Mff-ΔTM for actin filaments. In high-speed pelleting assays, Mff-ΔTM does not sediment appreciably with actin filaments (**Figure S2-3B, C**). In TIRF assays, fluorescein-Mff-ΔTM does not accumulate on actin filaments at any concentration tested (**Figure 2-5C**). In pyrene-actin polymerization assays, Mff-ΔTM does not influence the polymerization of actin alone or in the presence of the formin protein INF2 (**Figure 2-5D**). These results suggest that actin increases Mff's ability to stimulate Drp1 activity through an effect on the Mff/Drp1 interaction.

We next examined the effect of Mff-ΔTM on actin bundling by Drp1. In a previous study, we showed that Drp1 is a weak bundler of actin filaments, requiring at least 1 μM Drp1 for effective bundling [69]. At 0.2 μM Drp1, no actin bundles are observed (**Figure 2-6A**). Mff-ΔTM addition results in the appearance of actin bundles, with increasing Mff resulting in increasing bundle thickness (**Figure 2-6A, B**), and increasing Drp1 intensity in these bundles (**Figure 2-6C**). In contrast, Mff-L2P has minimal effect on Drp1-mediated bundling (**Figure 2-6A-C**).

We also evaluated Mff binding to Drp1-bundled actin filaments, using TIRF assays in which fluorescein-labeled Mff (1 μM) was added to actin filaments (0.1 μM) pre-bundled by 2.5 μM Cy5-Drp1. We did not label actin filaments in this experiment, because the slight bleed-through of the

bright actin filaments into the fluorescein channel decreased detection sensitivity for fluorescein-Mff binding. In the absence of GTP, 1 μM Mff-ΔTM is able to bind Drp1/actin bundles, and ~50% of Mff-ΔTM remains after wash (**Figure 2-6D, E**). GTP significantly increases Mff-ΔTM binding to the bundles, and maintains Mff-ΔTM on the bundles after wash (**Figure 2-6D, E**). In contrast, 1 μM Mff-L2P displays no detectable binding to Drp1/actin bundles in the absence of GTP, and low apparent binding to bundles in the presence of GTP. Increasing the Mff-L2P concentration causes detectable binding to Drp1/actin bundles in the absence of GTP, but Mff-L2P is removed by wash (**Figure S2-4**). We also tested the possibility that Mff can directly bind to bundled actin in general by using fascin-assembled actin bundles. In contrast to Drp1-mediated bundles, Mff-ΔTM displays no detectable binding to fascin/actin bundles (**Figure 2-6F**).

These results show that Mff and actin synergize in Drp1 activation in a manner dependent on Mff oligomerization. Mff does not interact with actin itself, but can interact with actin-bound Drp1. The presence of GTP strengthens this interaction.

2.3.5 Mff oligomerization is required for its role in mitochondrial division

To test the importance of Mff oligomerization in mitochondrial division, we expressed either full-length Mff-WT or Mff-L2P as GFP-fusions in Mff-knock out (KO) U2OS cells. Expression levels of the GFP fusions were controlled by varying the concentration of transfected plasmid, to obtain expression levels close to those of endogenous Mff, with 25 and 50 ng being used in further experiments for GFP-Mff-WT and GFP-Mff-L2P, respectively (**Figure S2-5A**).

We have previously reported that Mff-KO U2OS cells are strongly defective in mitochondrial division [71], similar to studies in other cell types [115,116,122,123,231] This defect is characterized by increased mean mitochondrial size, and a decreased number of individual mitochondria (**Figure 2-7A-C**). GFP-Mff-WT expression in Mff-KO U2OS cells largely rescues the KO phenotype, with an increase in mitochondrial number and a decrease in mitochondrial size (**Figure 2-7A-C**). In contrast, expression of Mff-L2P at comparable levels causes significantly reduced recovery of these parameters (**Figure 2-7A-C**).

We next examined the effect of Mff-WT and Mff-L2P on peroxisome size, since Mff is also required for peroxisome division [71,113,232]. Mff-KO cells display elongated peroxisomes (**Figure 2-7D**), with mean peroxisomal area 8.4-fold larger than that of WT cells (**Figure 2-7E**). Expression

of Mff-WT partially rescues the peroxisome size defect, with 1.6-fold larger area than WT (**Figure 2-7D, E**). In contrast, Mff-L2P is much less effective at reducing peroxisomal size, with 5.9-fold larger area than WT (**Figure 2-7D, E**). Interestingly, while Mff-WT clearly enriches on the majority of peroxisomes, Mff-L2P does not appear to display peroxisomal enrichment (**Figure 2-7F**).

We also examined the distribution of Mff and Drp1 under these conditions. The two Mff constructs display clear differences in distribution, with GFP-Mff-WT displaying a punctate pattern on mitochondria while Mff-L2P is evenly distributed on mitochondria (**Figure 2-7A**). In addition, some GFP-Mff-L2P appears to be present in the cytosol, similar to previous observations for an Mff construct with deletion of the CC [115]. We quantified the distribution of Mff-WT and Mff-L2P through blinded classification into three categories: uniform distribution, few puncta within a background of uniform distribution, and puntate (**Figure S2-5B**). Mff-WT displays punctate distribution in over 70% of the cells, whereas Mff-L2P is punctate in less than 10% of cells (**Figure S2-5C**).

We also examined the effect of Mff on mitochondrial Drp1 puncta, which presumably reflects Drp1 oligomerization. Our previous work has shown that Mff-KO or knock-down U2OS cells decreases Drp1 puncta [71], similar to other studies [115,116]. GFP-Mff-WT expression in the Mff-KO U2OS cells results in recovery of larger Drp1 puncta (**Figure S2-6A**), as quantified by puncta area and mean intensity (**Figure S2-6B, C**). In contrast, GFP-Mff-L2P induces ~30% smaller Drp1 puncta (**Figure S2-6A-C**), suggesting that Mff oligomerization increases cellular Drp1 oligomerization.

We have previously shown that the punctate pattern of Mff is dependent on Drp1, similar to another study [71,123]. We find the same result here, with Drp1 knock-down resulting in a uniform distribution of GFP-Mff-WT on mitochondria (**Figure S2-7A**). We also tested whether actin filaments are required for the punctate pattern of GFP-Mff-WT. WT U2OS cells were treated with the actin monomer sequestering drug latrunculin A (LatA) for 15 min, then stained with anti-Mff to detect the endogenous protein. As observed previously [171], LatA treatment results in mitochondrial elongation (**Figure S2-7B**). LatA treatment also results in a change in mitochondrial Mff staining pattern from punctate to more uniform (**Figure S2-7B**). We quantified this effect by measuring the % mitochondrial area covered by Mff, with an increase in coverage denoting a less punctate Mff pattern. The Mff area increases 2-fold in LatA-treated cells (**Figure S2-7C**). These results

suggest that Drp1 and Mff reciprocally enhance each other's oligomerization in cells, and that actin filaments are important for this effect.

2.4 Discussion

We show here that oligomerization of Mff plays an important role in its ability to recruit and activate Drp1. Without the capacity to oligomerize, Mff does not efficiently affect Drp1 oligomeric recruitment or mitochondrial division in cells. Furthermore, Mff and actin filaments act synergistically in Drp1 activation, and this synergy also depends on Mff oligomerization. Actin filaments lower the concentration of Mff needed to activate Drp1.

Our results suggest a fundamentally similar requirement for Drp1 receptor oligomerization in mammalian and yeast mitochondrial division, although the Drp1 receptors are quite different. In yeast, Fis1p is the relevant OMM receptor, but does not bind Drp1 directly. Instead, Fis1p recruits the cytoplasmic adaptor protein Mdv1 to the OMM, with Mdv1 in turn recruiting Drp1 [130,185,219]. Mdv1 forms a dimer through a coiled-coil interaction, and this dimerization is essential for both Drp1 recruitment and mitochondrial division [130,185,219]. Yeast has a second protein, Caf4, with similar properties to Mdv1 [131,132]. Although mammals have a Fis1p homologue, they do not have a Caf4/Mdv1 homologue, and it is becoming increasingly clear that Fis1p has distinct functions from mitochondrial division [115,142].

We show that Mff oligomerization is important for three cellular effects: Drp1 puncta assembly on mitochondria, mitochondrial division, peroxisomal division. In addition, oligomerization-deficient Mff itself does not display a punctate appearance on mitochondria, unlike wild-type Mff. We suspect that these cellular Mff puncta are structures that we have observed previously to co-localize with Drp1 puncta [71]. It is not clear whether they represent solely the coiled-coil mediated oligomerization or a larger oligomer. The fact that puncta of Mff-WT are reduced by either actin depolymerization or Drp1 KD suggest that the three entities (Mff, Drp1 and actin filaments) are all required to promote oligomeric Drp1-containing assemblies capable of driving mitochondrial division.

Previous results suggested that oligomerization was not required for Mff's cellular function, because an Mff construct in which the coiled-coil is deleted rescues the mitochondrial phenotype of Mff-depleted cells nearly to the same degree as wild-type Mff [115]. We found similar effects when our non-oligomerizable Mff mutant was expressed at levels much higher than endogenous Mff, but at levels closer to that of endogenous Mff the functional difference between WT Mff and non-oligomerizable Mff are clear. High Mff expression levels likely can overcome defects in Mff

oligomerization through crowding on the OMM. This effect has been suggested by biochemical results showing that monomeric Mff alone has no ability to stimulate Drp1, but can stimulate Drp1 when attached to liposomes [109,122], although the relative surface concentrations of monomeric and oligomerization-competent Mff necessary for this effect were not assessed. It is also possible that additional factors such as phosphorylation of Drp1 or Mff [104,106], cardiolipin levels (Bustillo-Zabalbeitia *et al.*, 2014; Macdonald *et al.*, 2014), or the presence of MiD proteins [120,121] might allow some Drp1 recruitment by oligomerization-defective Mff.

It has been unclear as to whether the many factors that can activate Drp1 act together in the same pathway, or as independent mechanisms for inducing mitochondrial division [233]. Our results strongly suggest that Mff and actin filaments operate in the same pathway. Previously, we have shown that increasing cytosolic calcium causes a 4-fold increase in mitochondrial division and an increase in mitochondrial Drp1 oligomerization, and that these responses require actin polymerization through the formin protein INF2 [91,171] as well as Mff [71]. Drp1 binds directly to actin filaments, and this binding increases Drp1 GTPase activity [69,91]. How actin and Mff work together, however, has been unclear.

In this paper, we show a mechanism for this actin/Mff synergy. Mff is a poor Drp1 activator unless Drp1's variable domain (VD) is removed [109,222]. The VD acts to inhibit aberrant interaction between Drp1 dimers [103], and oligomerization-deficient Drp1 mutants cannot be activated by Mff [109,222]. We show here that high concentrations of Mff alone can activate Drp1 even with the VD present. Actin filaments synergize by lowering the effective concentration of Mff for Drp1 activation. The inhibitory effects of the VD on Drp1 oligomerization might be overcome by Drp1 binding to actin filaments, allowing pre-assembly of Drp1 oligomers which can bind Mff more effectively. Another possibility, not mutually exclusive with the first, is that Drp1 oligomer assembly on the actin filament enhances Mff oligomerization by providing a multi-valent binding site that stabilizes Mff oligomers, allowing Mff to exert its full stimulation of Drp1 at lower concentration. Others have shown that Drp1 must be oligomerization-competent for activation by Mff [109,222], and we show similar results here for Drp1 activation by Mff and actin. In either case, it is clear that Mff's effect on Drp1 is greater than that of actin, suggesting that Mff allows a more productive Drp1 assembly for GTP hydrolysis.

The coiled-coil region, consisting of three heptad repeats, is required for Mff oligomerization. Mutation of two of the three heptad repeats is sufficient to disrupt this oligomerization. Given that

Mff is a tail-anchored protein on the OMM, with the CC only eight residues from the trans-membrane domain, it is highly likely that the oligomerization is parallel.

From the ensemble of the techniques used here, we conclude that Mff is most likely a trimer. Our rationale are: 1) that both the full cytoplasmic region of Mff and the CC alone as a GFP fusion sediment as trimers by vAUC, and 2) that prediction software gives the highest probability for a trimer. Our results differ to published results suggesting two different oligomeric states for Mff: a dimer [101,103] or a tetramer [109]. The dimerization prediction made from an eAUC study [101] may have been influenced by the slow speeds used, which did not provide sufficiently broad curves for high-confidence analysis. A second prediction of dimerization [103] as well as a prediction of tetramerization [109] were based on SEC-MALS measurements. These discrepancies are likely due to the low affinity nature of Mff oligomerization, and the fact that most of the Mff polypeptide is not predicted to adopt a stable fold [222]. Definitive determination of the oligomerization stoichiometry for Mff awaits more detailed structural analysis.

Regardless of the stoichiometry, our data clearly show that Mff oligomerization is relatively low affinity in solution, with dissociation constants in the range of 10 μM. On membranes, oligomerization would be significantly more favored by the reduction in dimensionality and generally confined membrane area of the OMM. Still, we find that the oligomerization-deficient mutant has a low tendency to display a punctate mitochondrial appearance when expressed at concentrations similar to endogenous, suggesting that assembly of these mitochondrial aggregates of Mff requires oligomerization.

At present, it is not possible to determine if these puncta themselves represent the Mff oligomers determined biochemically, but we believe that the puncta are considerably bigger than trimers of Mff. Our model is that Mff oligomerization is a necessary step in the assembly of higher-order structures consisting of Drp1 oligomers and multiple Mff trimers. An additional required step is nucleation of Drp1 oligomers, which we postulate occurs here through actin binding. We and others have shown that knockdown of Drp1 disrupts Mff puncta [71,115,123], suggesting that Drp1 oligomerization is necessary for Mff puncta. In addition, others have shown that Mff binds preferentially to Drp1 oligomers, suggesting that this actin-mediated nucleation is necessary to increase the affinity of Mff for Drp1[222]. It is possible that other Drp1 stimuli, such as cardiolipin and MiD49/51, serve the same purpose as actin in different contexts.

Overall, our understanding of actin's role in mitochondrial division is evolving as we learn more about its functional interactions with other division factors. Previously, we postulated that actin and myosin II mediated a "mitokinetic ring" to cause outer mitochondrial membrane pre-constriction prior to Drp1 action [171,233]. Subsequent studies from our lab and others revealed that this pre-constriction is due to calcium-induced constriction of the inner mitochondrial membrane, and that actin/myosin II are necessary for the increase in mitochondrial calcium [60,188,234]. In parallel, however, actin plays a second role in mitochondrial division: direct binding to Drp1, which initiates Drp1 assembly. Mff is then able to recruit these actin-nucleated Drp1 oligomers to assemble the functional constrictive ring [69,71,91]. This paper provides biochemical evidence for the model. We still do not know how myosin II or other proteins might enhance this process but, since myosin II is necessary for both the calcium effect [60] and Drp1 recruitment [203], we postulate that its ability to organize/constrict the actin filaments assembled by INF2 create a higher affinity interface for Drp1 nucleation.

2.5 Materials and Methods

Plasmids. For bacterial expression, full-length of human Drp1 isoform 3 (NP_055681.2, UniProt ID O00429-4) and truncated human Mff isoform 4 (UniProt ID Q9GZY8-4) (Mff-ΔTM) have been described previously [69,122]. Mff-L2P double mutant (L179P and L186P) was created in Mff-ΔTM construct by Quick Change mutagenesis (Stratagene, Santa Clara, CA). For Mff-ΔCC, hMff-isoform 4 lacking coiled-coil domain and transmembrane segment was cloned with a C-terminal HRV3C protease site into the pET28a vector using *Nco1* and *Xho1* sites followed by a 6-His affinity tag, a cystine was inserted between Mff-ΔCC and HRV3C site for labeling purpose. For GFP-CC, DNA coding for the coiled-coil domain of hMff-isoform 4 (amino acids 149 to 197) flanked by linkers (N-terminal SGGG, C-terminal GGGS) was synthesized by Integrated DNA Technologies (IDT) and inserted into a modified GFP-fusion pGEX-KT vector as previously described [235]. The GFP contains the A206K mutation, which reduces the ability to dimerize [236]. Quick Change mutagenesis was performed to make GFP-L2P double mutant. For cellular assays, full length hMff-isoform 4 was inserted into GFP-C1 vector as previously described [119].

Protein Expression, Purification.

Drp1 was expressed and purified as previously described with modifications [69]. Briefly, Drp1 construct was expressed in One Shot BL21 Star (DE3) *Escherichia coli* (C6010-03; Life Technologies, Carlsbad, CA) in LB broth, induced by isopropyl-β-D-thiogalactoside (IPTG) at 16 °C for 16 h when OD reached to 1.5. Cell pellets were resuspended in lysis buffer (100 mM Tris-Cl, pH 8.0, 500 mM NaCl, 1 mM dithiothreitol [DTT], 1 mM Ethylenediaminetetraacetic acid [EDTA], 2 µg/ml leupeptin, 10 µg/ml aprotinin, 2 µg/ml pepstatin A, 2 mM benzamidine, 1 µg/ml calpain inhibitor I [ALLN], and 1 µg/ml calpeptin) and lysed using a high-pressure homogenizer (M-110L Microfluidizer Processor; Microfluidics, Newton, MA). The lysate was cleared by centrifugation at 40,000 rpm (type 45 Ti rotor; Beckman, Brea, CA) for 1 h at 4°C. Avidin (20 µg/ml; PI-21128; Thermo Fisher Scientific, Waltham, MA) was added to the supernatant, and then was loaded onto Strep-Tactin Superflow resin (2-1206-025; IBA, Göttingen, Germany) by gravity flow. The column was washed with 20 column volumes (CV) of lysis buffer without protease inhibitors. To elute Drp1, 0.01 mg/ml HRV3C protease in lysis buffer without protease inhibitors was added for 16 h at 4°C. The Strep-Tactin Superflow eluate was further purified by size exclusion chromatography on Superdex200 (GE Biosciences, Piscataway, NJ) with Drp1-S200 buffer (20 mM 4-(2-hydroxyethyl)-1-piperazineethanesulfonic acid [HEPES]-[KOH] pH 7.5, 150 mM KCl,

2 mM $MgCl_2$, 1 mM DTT, 0.5 mM ethylene glycol tetraacetic acid [EGTA]), spin concentrated, frozen in liquid nitrogen, and stored at −80°C.

Mff-ΔTM and Mff-L2P were expressed in Rosetta™2 BL21-(DE3) *Escherichia coli* (71400; EMD Millipore Corporation, Burlington, MA) in LB broth, induced by 1M IPTG at 30 °C for 4 h when OD reached to 1.5. Cell pellets were resuspended in lysis buffer (50 mM Tris-HCl, pH 7.5, 500 mM NaCl, 20 mM imidazole, pH 7.5, 1 mM DTT, 1 mM EDTA, 2 µg/ml leupeptin, 10 µg/ml aprotinin, 2 µg/ml pepstatin A, 2 mM benzamidine, 1 µg/ml calpain inhibitor I [ALLN], and 1 µg/ml calpeptin) and lysed using M-110 microfluidizer processor. The lysate was cleared by centrifugation at 40, 000 rpm (type 45 Ti rotor; Beckman, Brea, CA) for 40 minutes at 4°C, the supernatant was saved. Affinity capture was performed using FPLC and a HiTrap IMAC column (17-5248-01, GE Healthcare, Chicago, IL). Prepacked HiTrap IMAC column was equilibrated with IMAC-A buffer (50 mM Tris-HCl pH 7.5, 0.1 M NaCl, 20 mM imidazole). Cleared lysate was loaded onto the column with a rate of 3 mL/min and washed to baseline with IMAC-A. Mff was eluted from the column with gradient step washes by IMAC-B buffer (50 mM Tris-HCl pH 7.5, 0.1 M NaCl, 500 mM imidazole): step1 10% IMAC-B for 5CV, step2 20% IMAC-B for 5CV, step3 100% for 5CV. Fractions from step3 were pooled and diluted 10-fold in ion exchange (IEX)-A buffer (50 mM Tris-HCl pH 7.5, 1 mM DTT). Diluted fractions were loaded onto a HiTrap Q anion exchange column (54816, EMD Millipore Corporation, Burlington, MA). The column was washed to baseline with IEX-A and Mff was eluted by IEX-B buffer (50 mM Tris-HCl pH 7.5, 1 M NaCl, 1 mM DTT) with a step gradient: step1 10% 5CV, linear 10-50% 30CV followed by linear 50-100% 5CV. Peak Mff fractions were concentrated by reloading onto the HiTrap IMAC column and eluted with 100% IMAC-B step wash. Mff fractions were pooled and further purified by size exclusion chromatography on Superdex200 with S200 buffer (20 mM HEPES, pH 7.4; 2 mM $MgCl_2$, 0.5 mM EGTA, 65 mM KCl, 1 mM DTT), spin concentrated with a 30,000 MWCO centrifugal concentrator (UFC903024, EMD Millipore Corporation, Burlington, MA), aliquots were frozen in liquid nitrogen, and stored at −80°C.

Mff-ΔCC was expressed and cleared as described above. Mff-ΔCC supernatant was loaded onto HisPur Ni-NTA resin (88221, Thermo Fisher Scientific, Rockford, IL) by gravity flow. The column was washed with 10 CV IMAC-A buffer and 30 CV ATP wash buffer (200 mM Tris-HCl, pH 7.5, 50 mM KCl, 20 mM $MgCl_2$, 5 mM ATP) followed by 10 CV IMAC-A buffer. To elute Mff-ΔCC, 0.16 mg/mL HRV3C protease was added for 16 h at 4°C. The Ni-NTA eluate was further purified by size exclusion chromatography on Superdex200 with S200 buffer, spin concentrated

(UFC901024, EMD Millipore Corporation, Burlington, MA), aliquots were frozen in liquid nitrogen, and stored at −80°C.

GFP-CC and GFP-L2P were expressed in Rosetta™2 BL21-(DE3) *Escherichia coli* in LB broth, induced by 1M IPTG at 16 °C for 16 h when OD reached to 1.0. Cell pellets were resuspended in lysis buffer and cleared as described above. 1% Triton was added to clarified supernatant and incubated for 30 mins. The supernatant was loaded onto a HiTrap IMAC column with a rate of 3 mL/min and washed to baseline with IMAC-A. Mff was eluted from the column by gradient step washes with IMAC-B buffer (50 mM Tris-HCl pH 7.5, 0.1 M NaCl, 500 mM imidazole): step1 10% IMAC-B for 5CV, step2 20% IMAC-B for 5CV, step3 100% for 5CV. Fractions from step3 were pooled and diluted 5-fold in GST buffer (50 mM HEPES pH 7.4, 500 mM NaCl, 1 mM EDTA, 1 mM DTT). Diluted fractions were loaded onto Glutathione Sepharose™ 4B resin (17-0756-05, GE Healthcare, Chicago, IL) by gravity flow followed by 5CV PBS wash. To elute protein, 0.32 mg/mL TEV protease was added to the column and incubated for 16 h at 4°C. The eluate was further purified by size exclusion chromatography on Superdex200 with S200 buffer, spin concentrated (UFC903024, EMD Millipore Corporation, Burlington, MA), aliquots were frozen in liquid nitrogen, and stored at −80°C.

Rabbit skeletal muscle actin was extracted from acetone powder as previously described [237], and further gel-filtered on Superdex 75 16/60 columns (GE Healthcare). Actin was stored in G buffer (2 mM Tris, pH 8.0, 0.5 mM DTT, 0.2 mM ATP, 0.1 mM $CaCl_2$, and 0.01% NaN_3) at 4°C.

Actin and Drp1 preparation for biochemical assays

For high-speed pelleting assay, actin filaments were polymerized from 30 µM monomers for 3 h at 23 °C by addition of a 10x stock of polymerization buffer (200 mM HEPES, pH 7.4, 650 mM KCl, 10 mM $MgCl_2$, 10 mM EGTA) to a final 1x concentration. For GTPase assay, actin monomers in G-buffer were incubated with AG1-X2 100–200 mesh anion exchange resin (Dowex; 1401241; Bio-Rad) at 4 °C for 5 min to remove ATP, followed by low-speed centrifugation. 20 µM actin filaments were polymerized as described before. To maintain ionic strength across all samples, an actin blank was prepared in parallel using G-buffer in place of actin monomers and used to dilute actin filaments as needed for each sample. Drp1 was diluted in MEHD buffer (20 mM HEPES, pH 7.4, 2 mM $MgCl_2$, 0.5 mM EGTA, 1 mM DTT) to adjust the ionic strength to the same as S200 buffer before biochemical assays.

Size exclusion Chromatography assays. Mff-ΔTM, Mff-L2P, Mff-ΔCC, GFP-CC, and GFP-L2P oligomeric distribution was determined by Superdex200 increase 10/300 GL SEC column in S200 buffer (20 mM HEPES, pH7.4, 65 mM KCl, 2 mM $MgCl_2$, 0.5 mM EGTA, 1 mM DTT). Protein at varying concentration was loaded onto the column in a total volume of 500 µL and gel-filtered with a flow rate of 0.7 mL/min.

High-speed pelleting assay.

Interactions between Drp1 and Mff (Mff-ΔTM, Mff-ΔCC, Mff-L2P) were tested in the S200 buffer plus 1 mM GTP, 1.3 µM Drp1 was incubated with varying concentrations of Mff (0-50 µM) for 10 min at 4 °C in a 200 µL volume. After incubation, samples were centrifuged at 80,000 rpm for 20 min at 4 °C in a TLA-100.1 rotor (Beckman). The supernatant was carefully removed. Pellets were washed three times with S200 buffer plus 1 mM GTP, and then resuspended in 100 µL of SDS-PAGE sample buffer and resolved by SDS-PAGE (LC6025; Invitrogen, Carlsbad, CA). To test the interaction between Mff and actin, 5 µM Mff-ΔTM was incubated with varying concentration of actin filaments (0-20 µM) for 1 h at 23 °C in a 200 µL volume. Samples were centrifuged and the pellets were resolved by SDS-PAGE. Gels were stained with Coomassie Brilliant Blue R-250 staining (1610400, BioRad, Hercules, CA), and band intensity was analyzed using ImageJ software.

GTPase assay

Drp1 (0.75 µM) was mixed with the indicated concentration of Mff or actin filaments. Sample were incubated at 37 °C for 5 min. At this point, GTP was added to a final concentration of 250 µM to start the reaction at 37 °C. Reactions were quenched at designated time points by mixing 15 µL of sample with 5 µL of 125 mM EDTA in a clear, flat-bottomed, 96-well plate (Greiner, Monroe, NC). Six time points were acquired for all conditions, high-speed reactions were monitored in a 12 min time range, while low-speed reactions were monitored in a 45 min time range. Released phosphate was determined by addition of 150 µL of malachite green solution as previously described [69] Absorbance at 650 nm was measured 15 min after malachite green solution incubation. GTP hydrolysis rates were determined by plotting phosphate concentration as a function of time.

Pyrene actin polymerization assay

Pyrene actin polymerization assay has been described previously [238]. Briefly, rabbit skeletal muscle actin (2 µM actin, 10% pyrene) was polymerized with varying concentrations of Mff-ΔTM in polymerization buffer (50 mM KCl, 1 mM $MgCl_2$, 1 mM EGTA, 10 mM HEPES pH 7.4, 1 mM DTT, 2 mM Tris-HCl, 0.2 mM ATP, 2 mM Tris-HCl, 0.2 mM ATP, 0.1 mM $CaCl_2$, and 0.01%

w/v NaN_3). Rabbit muscle actin and 200 nM INF2-FFC with varying concentrations of Mff-ΔTM were used to test the effects of Mff on formin-induced actin polymerization [239]. Pyrene fluorescence (365/410 nm) was monitored in a 96-well fluorescence plate reader (Infinite M1000; Tecan, Mannedorf, Switzerland) after 1min of inducing polymerization.

Protein Labeling

Mff-ΔTM and Mff-L2P N-term were labeled with 5-fold molar excess of 5/6-carboxyfluorescein succinimidyl ester (46410, Thermo scientific) in 20 mM HEPES pH 7.4 at 4 °C, 2 mM $MgCl_2$, 0.5 mM EGTA at 4 °C for 1 h. Reactions were quenched by 100-fold molar excess of Tris-HCl pH 7.4 at 4 °C. Drp1 N-term was labeled with 3.3-fold molar excess of Cy5 succinimidyl ester (1076-1, Click Chemistry Tools, Scottsdale, AZ) in 100 mM MES pH 6.1 at 4 °C, 2 mM $MgCl_2$, 0.5 mM EGTA for 10 min. Reactions were quenched by Tris-HCl as described above. Free dye was removed by gel filtration using Superdex200 increase 10/30 (GE Biosciences) in S200 buffer. For ΔTM and L2P, final protein concentration was determined by Bradford (BioRad) and fluorescein concentration using extinction coefficient 72,000 M^{-1} cm^{-1} at 494 nm. Calculated ratio of fluorescein-Mff-ΔTM is 0.49 and fluorescein-Mff-L2P is 0.44. For Drp1, Cy5 concentration was determined by extinction coefficient 255,000 M^{-1} cm^{-1}. Calculated ratio of Cy5-Drp1 is 0.75. Actin filaments (4 μM) were assembled from monomers for 3 h as described and then stabilized with either Tetramethylrhodamine (TRITC)-phalloidin (4 μM P1951; Sigma-Aldrich) or unlabeled 4 μM phalloidin (17466-45-4, Sigma-Aldrich) for 5 min.

Total internal reflection fluorescence microscopy imaging

Mff GMPPCP-Drp1 interaction experiment

To measure Mff and GMPPCP-Drp1 interaction, 1 μM Cy5-labeled Drp1 was incubated in S200 buffer plus 500 μM GMPPCP at room temperature (RT) overnight. Drp1 was manually added to the flow cell in a 10 μL volume while the current flow cell solution was removed with Whatman paper. Once Drp1 attached to the cell (15 min incubation), 2 μM fluorescein-labeled Mff (Mff-ΔTM and Mff-L2P) was flowed into the chamber. After 1 min incubation, Mff was washed by S200 buffer plus 500 μM GMPPCP. Two-color images were acquired at three time points: before, during Mff flow, and after buffer wash. ImageJ software was used to measure fluorescence intensity. Briefly, background-subtracted intensities of Drp1 and Mff on a punctum were measured at the time points mentioned above, the intensity ratio of Mff/Drp1 was calculated at each time point.

Mff-Drp1-mediated actin bundling experiment

TRITC-phalloidin-stabilized actin filaments (100 nM) were incubated with 200 nM Drp1 and varying concentration of unlabeled Mff overnight at RT. Samples were manually added to the flow cell in a 10 μL volume as mentioned above. Two-color images were acquired after 15 min sample incubation, the same exposure times and laser intensities were used for all conditions. Interestingly, due to the strong TRITC signal, actin filaments can be acquired by the 488 nm laser Under this condition, TRITC signal kept in a linear range without saturation.

To determine the number of actin filaments in a bundle, maximum intensity of 50 background-subtracted single actin filaments from actin alone group was measured by line scan. An average intensity of the filaments was used as the value of single actin filament. The number of actin filaments in a bundle was calculated by the ratio of the intensity of actin bundle to single actin filament, 50 actin bundles were measured.

To determine the intensity of actin-colocalized Drp1, actin was thresholded using an ImageJ plugin, Colocalization, with the following parameters: Ratio 30% (0–100%); Threshold channel 1: 50 (0–255); Threshold channel 2: 50 (0–255); Display value: 255 (100–255). Colocalized Drp1 puncta intensities were measured with ImageJ using line scans.

Mff binding to Drp1-actin bundles experiment

To measure the interaction between Mff and Drp1-pre-assembled actin bundles, 2.5 μM Cy5-labeled Drp1 was incubated with 100 nM unlabeled actin filaments overnight at RT. Drp1 and actin mixture was manually added to the flow cell as described before. The mixture was incubated in the chamber for 15 min to let actin attach to the cell. Fluorescein-labeled Mff was flowed into the chamber. After 1 min incubation, Mff was washed by S200 buffer. To test the effects of GTP on the interaction, 1 mM GTP was added to the Drp1 and actin mixture right before adding it into the chamber. Mff flow and buffer wash steps also included 1 mM GTP throughout the experiment. Two-color images were acquired at three time points: before, during Mff flow, and after buffer wash. ImageJ software was used to measure fluorescence intensity. Briefly, background-subtracted intensities of Drp1 and Mff on a given punctum were measured at the time points mentioned above, the intensity ratio of Mff/Drp1 was calculated at each time point.

Mff actin interaction experiment

To test the direct interaction between Mff and actin filaments, varying concentration of Mff were incubated with 100 nM TRITC-actin filaments overnight at RT. Samples were manually added to

the flow cell in a 10 µL volume as mentioned above. Two-color images were acquired after 15 min sample incubation, the same exposure times and laser intensities were used throughout all conditions tested.

Cell culture, transfection, and drug treatments

Human osteosarcoma U2OS cells (HTB96; American Type Culture Collection) were grown in DMEM (Invitrogen) supplemented with 10% calf serum (Atlanta Biologicals). All cells were cultivated at 37°C and in 5% CO_2 atmosphere.

For the generation of the Mff KO U2OS cell line, an appropriate guide sequence (5'- CAC CGT GAT AAT GCA AGT TCC GGA G-3') was cloned into LentiCRISPRv2 vector according to the protocol from http ://genome -engineering .org /gecko /. The resulting guide plasmid, along with helper plasmids psPAX2 and pMD2.G, were transfected into HEK293 cells using Lipofectamine LTX (Invitrogen). Supernatant containing lentivirus was collected 48 h post-transfection and filtered through a 0.45 µm filter. Fresh virus was used to infect U2OS cells. After 48 h, media containing virus was removed and replaced with fresh media containing 2 µg/ml puromycin. Cells clones were selected through puromycin resistance, single cell clones were expanded and tested for Mff depletion by Western blotting.

For transfections, cells were seeded at 5×10^5 cells per well in 3 cm culture dishes ~16 h before transfection. Plasmid transfections were performed in OPTI-MEM media (Invitrogen) with 2 µL Lipofectamine 2000 (Invitrogen) per plate for 6 h. For all experiments, the following amounts of DNA were transfected per plate: 25 ng for GFP-Mff WT and 50 ng for GFP-Mff-L2P. After ~6 h incubation, cells were trypsinized and replated onto fibronectin (Sigma-Aldrich, 1:100 in PBS)–coated glass coverslips (18 mm diameter, Electron Microscopy Sciences) at a density of $\sim 3.5 \times 10^5$ cells per dish.

Latrunculin A (428021; Calbiochem) treatment (**Figure S2-7B**) was performed before fixation of the cells. 2 µM LatA (from a 2 mM stock in DMSO) was dissolved in cell culture media and added to the cells for 15 min at 37°C. An equal volume of DMSO was used as control treatment.

Drp1 RNA interference

For siRNA transfections, Mff-KO cells were plated on 3 cm dishes, 1 x 10^5 cells were plated for control siRNA transfection and 2 x 10^5 cells were prepared for Drp1 siRNA as the knockdown affected cell growth. Sequence for scrambled control siRNA was: 5'-

CGTTAATCGCGTATAATACGCGTAT-3' and siRNA sequence for Drp1 silencing was 5'-GCCAGCTAGATATTAACAACAAGAA-3'. Transfections were carried out using 2 µL RNAi max (Invitrogen) and 63 pg siRNA per dish. siRNA transfections were repeated after 48 h, and cells were transfected with GFP-Mff constructs after 72 h, and finally analyzed 96 h posttransfection. Knockdown cells were plated onto fibronectin-coated coverslips, fixed and stained for Drp1 (**Figure S2-7A**).

Cell lysates and Western blotting

For generation of cell lysates (**Figure S2-5A**), cells were grown and transfected on 3 cm dishes as described before. On the following day, cells were washed three times with PBS, and lysed using 1xDB (125 mM Tris-HCl, pH 6.8, 1 mM EDTA, 10% glycerol, 0.4% SDS, 0.01% bromophenol blue, 500 mM NaCl, and 2 M urea). Cell lysates were collected from plates, boiled 5 min at 95°C, and sheared using a 27xG needle. Proteins were separated by standard SDS-PAGE and transferred to a PVDF membrane (polyvinylidine difluoride membrane; Millipore). The membrane was blocked with TBS-T (20 mM Tris-HCl, pH 7.6, 136 mM NaCl, and 0.1% Tween-20) containing 3% BSA (Research Organics) for 1 h, then incubated with the primary antibody solution at 4°C overnight. After washing with TBS-T, the membrane was incubated with IRDye-680RD goat-anti-mouse or IRDye-800CW goat-anti-rabbit secondary antibodies (#926-68070, #926-32211, LI-COR) for 1 h at room temperature. Membrane was washed with TBS-T and dried before exposure. Signals were detected using the Odyssey CLx imaging system (LI-COR). Primary antibodies applied were as follows: GFP (rabbit, self-made, 1:1000), GAPDH (mouse, Santa Cruz (G-9) sc-365062, 1:1000), Mff (rabbit, Proteintech 17090-1-AP, 1:1000).

Immunofluorescence staining

Cells were plated subconfluently onto fibronectin-coated coverslips and allowed to adhere overnight. The following day, cell culture media was removed, and cells were fixed in prewarmed 4% PFA/PBS for 20 min at RT, followed by three PBS washes and permeabilization with 0.1% TritonX-100 in PBS for 1 min. Coverslips were blocked with 10% calf serum for 30 min, followed by primary antibody incubation for 1 h. After three PBS washes, coverslips were incubated with respective secondary antibodies (Fluorescein anti-rabbit or -mouse, 1:300, FI-1000/FI-2000, Vector Laboratories and Texas-Red anti-rabbit or -mouse, 1:300, TI-1000/TI-2000, Vector Laboratories) for 45 min. Alexa Fluor 405-phalloidin (A30104, Invitrogen) was added with secondary antibodies. After three PBS washes, coverslips were mounted on glass slides using ProLong Gold Antifade mountant (P36930, Invitrogen). Primary antibodies were as follows: Mff

(Proteintech 17090-1-AP, rabbit, 1:200), Tom20 (Santa Cruz (F10): sc-17764, mouse, 1:50), Tom20 (Abcam ab78547, rabbit, 1:200), Drp1 (BD Transduction Laboratories 611112, mouse, 1:50), PMP70 (Abcam ab3421, rabbit, 1:100).

Confocal Microscopy

Imaging was performed at a Dragonfly 302 spinning disk confocal (Andor Technology, Inc.) on a Nikon Ti-E base and equipped with an iXon Ultra 888 EMCCD camera, and a Zyla 4.2 Mpixel sCMOS camera. Solid-state 405 smart diode 100-mW laser, solid-state 488 OPSL smart laser 50-mW laser, and solid-state 560 OPSL smart laser 50-mW laser were used (objective: 100× 1.4 NA CFI Plan Apo; Nikon). Images were acquired using Fusion software (Andor Technology, Inc.).

Mitochondrial/peroxisomal length analysis

Mff-KO cells with restored expression of either GFP-Mff WT or GFP-Mff-L2P were analyzed for their mitochondrial and peroxisomal morphology (**Figure 2-7**). Untransfected U2OS WT and Mff-KO cells served as controls for normal and abnormal phenotypes, respectively. Regions of interest were selected in the flat cell periphery with well resolvable, individual organelles. ROIs (400 μm^2 area) of mitochondria/peroxisomes were converted to 8-bit binary masks and analyzed using the 'analyze particles' plugin in FIJI to obtain the mean number of mitochondrial/peroxisomal fragments and the mean size of these organelles per ROI. Settings for analyzing particles were as follows: size ($pixel^2$): 0.05 – infinity, circularity 0.00-1.00 for mitochondria, and size ($pixel^2$): 0.02 – infinity, circularity 0.00-1.00 for peroxisomes, respectively. Data were plotted as bar graphs or box and whiskers plots.

Mff localization analysis

100x images of transfected cells were randomly taken and afterwards analyzed in a blinded manner. The localization of GFP-Mff WT or GFP-Mff-L2P was categorized into three groups: **uniform** distribution of the GFP signal on mitochondria, mainly uniform distribution with **few puncta** visible, or a clear **punctate** localization on mitochondria. The percentage of cells falling into these three classes were represented in stacked bar graphs with standard error of means from three independent experiments (**Figure S2-5B, C**).

Analysis of Mff/Drp1:mitochondrial area ratio

Regions of interest (ROIs) containing mitochondria in spread, peripheral cell areas (**Figure S2-6, S7B, C**) were thresholded using same contrast settings for Tom20 staining. Anti-Mff stainings were

first processed by background subtraction using FIJI (rolling ball radius 5 pixels), then further thresholded applying equal setting parameters. Mff or Drp1 with respective Tom20 stainings were analyzed using the FIJI 'Colocalization' plugin with the following parameters: ratio 30% (0-100%), threshold channel 1: 50 (0-255), threshold channel 2: 50 (0-255), display value (0-255): 255. Colocalized pixels were then converted to a binary mask and quantified using the 'analyze particles' tool with settings as follows: size (pixel^2) 0.01 – infinity, circularity 0.00-1.00.

Data Processing and Statistical Analyses.

Figures were processed and assembled with Photoshop CS4. Data analyses were carried out in ImageJ and Excel 2010. Statistical comparisons were performed with GraphPad Prism using unpaired t-test. A probability of error of 5% ($p \leq 0.05$; * in figure panels) was considered to indicate statistical significance. **, *** and **** indicated p-values $\leq$ 0.01, 0.001 and 0.0001, respectively.

Figures

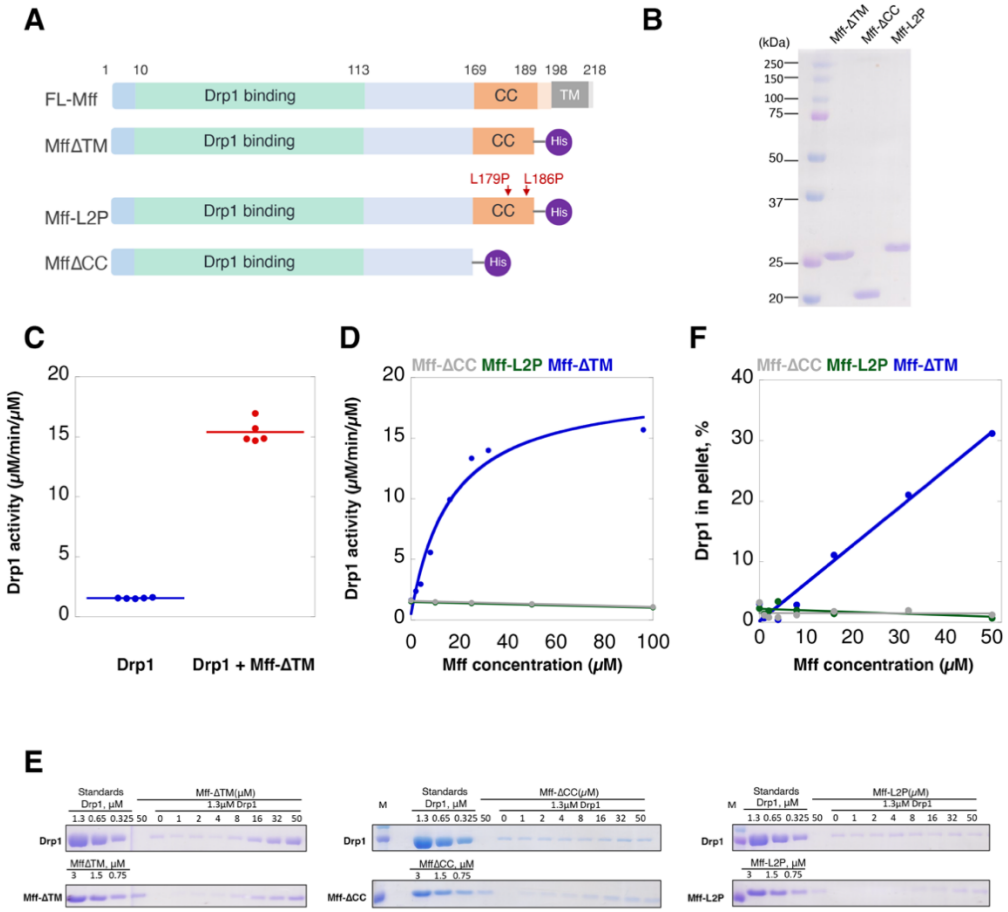

Figure 2-1: Mff stimulates Drp1 activity and oligomerization in a concentration dependent manner.

A) Bar diagrams of Mff constructs, based on the isoform with no optional splice inserts (isoform 4, UniProt ID Q9GZY8-4). 6xHis tag is purple ball.

B) Coomassie-stained SDS-PAGE of Mff constructs (2 μg loaded).

C) GTPase assay for Drp1 (0.75 μM) in the absence and presence of 100 μM Mff-ΔTM, data from five independent experiments. GTPase activities: 1.55 ± 0.05 and 15.53 ± 1.04 μM GTP hydrolyzed/min/μM Drp1 without and with Mff, respectively.

D) GTPase activity for Drp1 (0.75 μM) as a function of Mff concentration added.

E) High-speed pelleting assay of Drp1 (1.3 μM) in the presence GTP (1 mM) and of varying Mff concentration. Drp1 and Mff regions from the same SDS-PAGE gel are presented. Standards equivalent to the indicated concentrations of Drp1 or Mff in the assay on left of gels. Pellet fractions shown to the right.

F) Quantification of pelleting assay results from panel E.

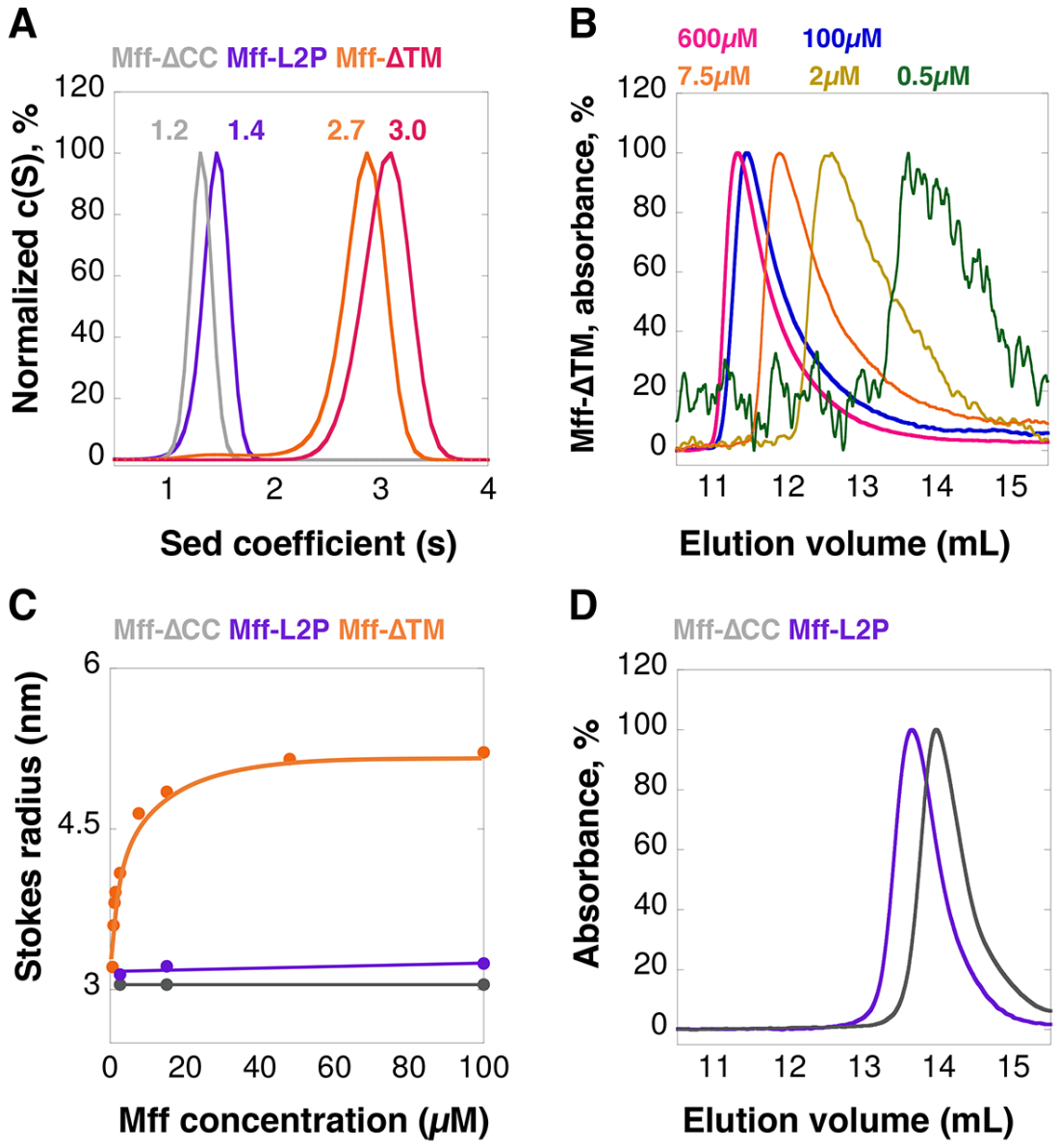

Figure 2-2: Mff undergoes reversible oligomerization, dependent on the coiled-coil region.

A) Velocity analytical ultracentrifugation of Mff-ΔTM at 100 μM (orange) or 250 μM (pink), and Mff-ΔCC (gray) or Mff-L2P (purple) at 100 μM. Y axis normalized to the peak c(S) for each sample, the maximum value of each curve is normalized as 100%, as for panel B-D. Peak sedimentation coefficients listed on graph.

B) SEC profiles for multiple concentrations of Mff-ΔTM, detected at 280 nm. Sample at 0.5 μM has low absorbance, thus gives a noisy trace. C) Graph of calculated Stokes radius (from SEC results) versus Mff concentration for Mff-ΔTM, Mff-ΔCC, and Mff-L2P. D) SEC for Mff-ΔCC and Mff-L2P at 100 μM.

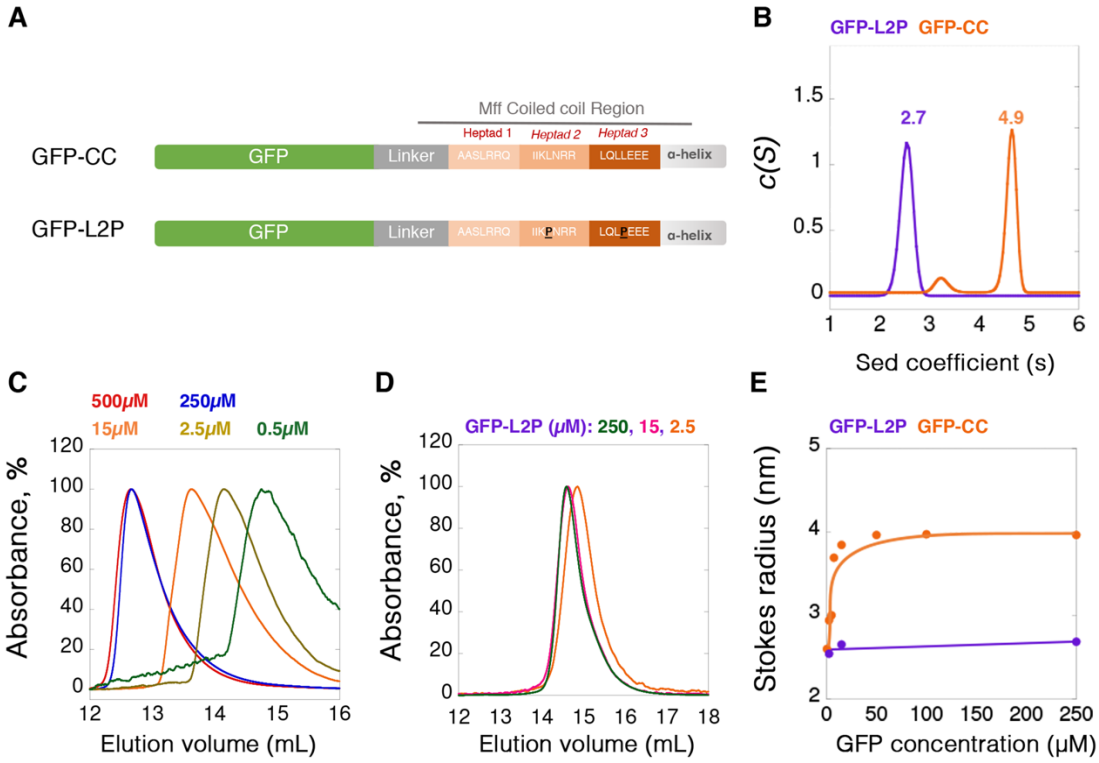

Figure 2-3: Oligomerization of Mff coiled-coil region.

A) Bar diagrams of two GFP-fusion constructs: top, the coiled-coil region of Mff (GFP-CC); and bottom, the L2P mutant of the same construct (GFP-L2P).

B) Velocity analytical ultracentrifugation of GFP-CC and GFP-L2P at 250 μM. Peak sedimentation coefficients noted on graph.

C) SEC profiles of GFP-CC at multiple concentrations, detected at 490 nm. Absorbances normalized to peak absorbance at each group, the maximum value of each curve is normalized as 100%, same for panel D.

D) SEC profiles of GFP-L2P at three concentrations. E) Graph of calculated Stokes radius (from SEC results) versus GFP concentration for GFP-CC and GFP-L2P.

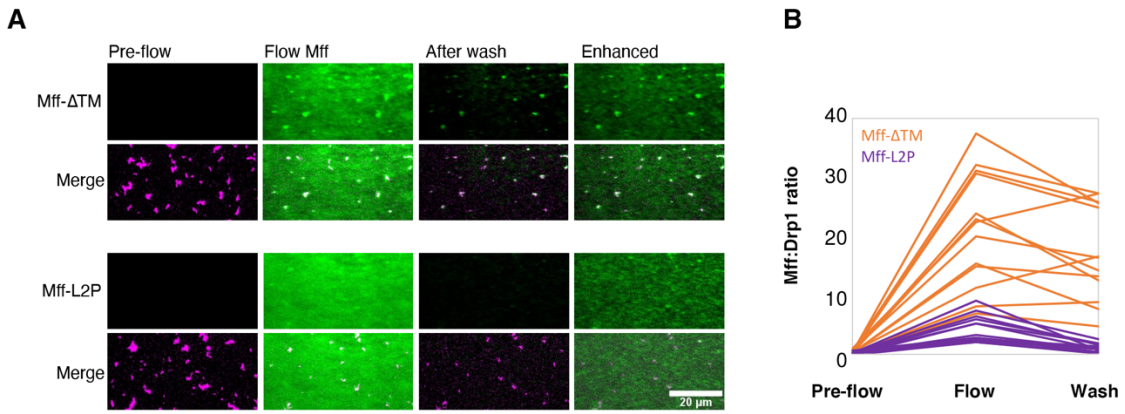

Figure 2-4: Mff oligomerization is necessary for Drp1 interaction and activation.

A) TIRF microscopy of Drp1/Mff interaction. Cy5-labeled Drp1 (purple, 1 µM) was incubated with 0.5 mM GMPPCP and then flowed into the TIRF chamber. "Pre-flow" represents Drp1 puncta prior to Mff addition. Fluorescein-labeled Mff (2 µM, green, either Mff-ΔTM or Mff-L2P) was then flowed in while imaging. "Flow Mff" represents an image taken after 30 sec of Mff addition. After 1 min, chamber was washed with buffer while imaging. "After wash" image is taken at 30 sec after buffer wash. "Enhanced" image is the After wash image with increased contrast to show background fluorescein channel signal. Example using Mff-ΔTM is top image set, and Mff-L2P is bottom set. For each set, the fluorescein-Mff signal alone is shown on top, and the merged fluorescein-Mff/Cy5-Drp1 signal on bottom. Bar, 20 µm.

B) Quantification of 14 individual puncta for fluorescein-Mff:Cy5-Drp1 ratio for both Mff-ΔTM and Mff-L2P.

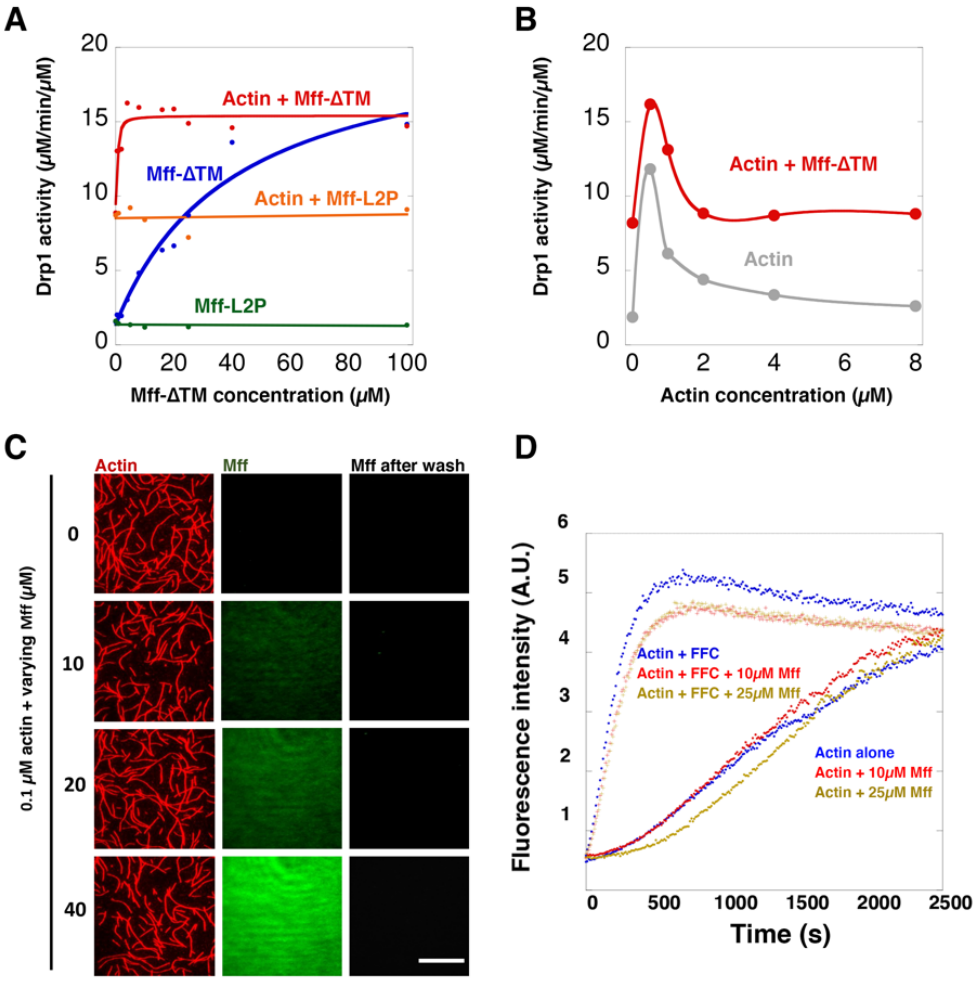

Figure 2-5: Synergistic effects of actin and Mff on Drp1 activity require Mff oligomerization.

A) GTPase activity of Drp1 (0.75 μM) as a function of Mff-ΔTM or Mff-L2P concentration added, in the absence or presence of 0.5 μM actin filaments.

B) GTPase activity of Drp1 (0.75 μM) as a function of actin filament concentration in the absence or presence of Mff-ΔTM (20 μM).

C) TIRF microscopy of actin filaments and Mff-ΔTM. Actin filaments (red) were polymerized at 4 μM, mixed with a 1.1 molar excess of TRITC-phalloidin. Fluorescein-labeled Mff-ΔTM of varying concentration was incubated with 0.1 μM TRITC-actin overnight and introduced into the TIRF chamber. Images of actin and Mff-ΔTM were taken after 15 min of actin/Mff addition. After another 1 min, chamber was washed with buffer while imaging. Bar, 20 μm.

D) Pyrene-actin polymerization assays of actin alone or in the presence of 200 nM INF2-FFC, a potent actin polymerization factor [239]. Also included was a varying concentration of Mff-ΔTM.

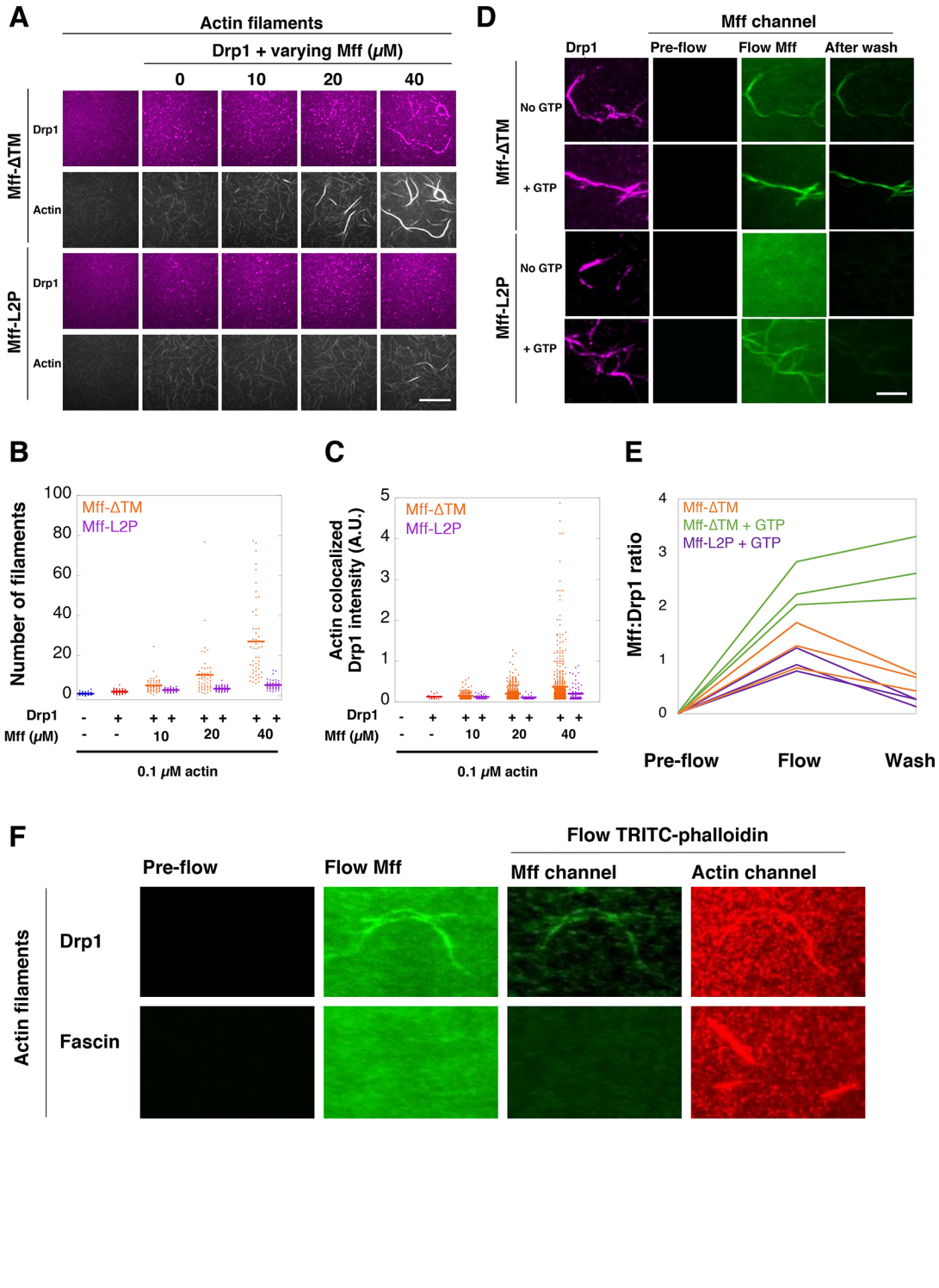
A
Actin filaments
Drp1 + varying Mff (μM)
0
10
20
40
Mff-ΔTM
Drp1
Actin
Mff-L2P
Drp1
Actin
D
Mff channel
Drp1
Pre-flow
Flow Mff
After wash
Mff-ΔTM
No GTP
+ GTP
Mff-L2P
No GTP
+ GTP
B
Number of filaments
100
80
60
40
20
0
Mff-ΔTM
Mff-L2P
Drp1 - + + + + +
Mff (μM) - - 10 20 40
0.1 μM actin
C
Actin colocalized Drp1 intensity (A.U.)
5
4
3
2
1
0
Mff-ΔTM
Mff-L2P
Drp1 - + + + + +
Mff (μM) - - 10 20 40
0.1 μM actin
E
Mff:Drp1 ratio
4
3
2
1
0
Mff-ΔTM
Mff-ΔTM + GTP
Mff-L2P + GTP
Pre-flow
Flow
Wash
F
Flow TRITC-phalloidin
Pre-flow
Flow Mff
Mff channel
Actin channel
Actin filaments
Drp1
Fascin

Figure 2-6: Mff interacts with Drp1-bound actin filaments.

A) TIRF assay with 0.1 μM actin filaments (TRITC-phalloidin labeled), 0.2 μM Cy5-labeled Drp1, and varying concentration of unlabeled Mff-ΔTM or Mff-L2P. No GTP present. Bar, 30 μm

B) Quantification of actin filament number in individual bundles.

C) Quantification of Cy5-Drp1 intensity in actin bundles.

D) TIRF assay of Mff interaction with Drp1-bundled actin filaments. Actin bundles were pre-formed with 0.1 μM actin (unlabeled, phalloidin-stabilized) and 2.5 μM Cy5-Drp1. Fluorescein-labeled Mff (1 μM, either Mff-ΔTM or Mff-L2P) was introduced to the chamber while imaging. After 1 min, the chamber was washed while imaging. Experiments ± 1mM GTP throughout the whole processes. Bar, 10 μm.

E) Quantification of fluorescein-Mff intensity on Cy5-Drp1-bundled actin filaments by taking the Mff:Drp1 ratio.

F) Comparison of fluorescein-Mff-ΔTM binding to Drp1-bundled or fascin-bundled actin filaments. Conducted in same manner as in panel D, except actin filaments were labeled with TRITC-phalloidin only during the wash step, to minimize bleed-through into the fluorescein channel. Bars, 10 μm.

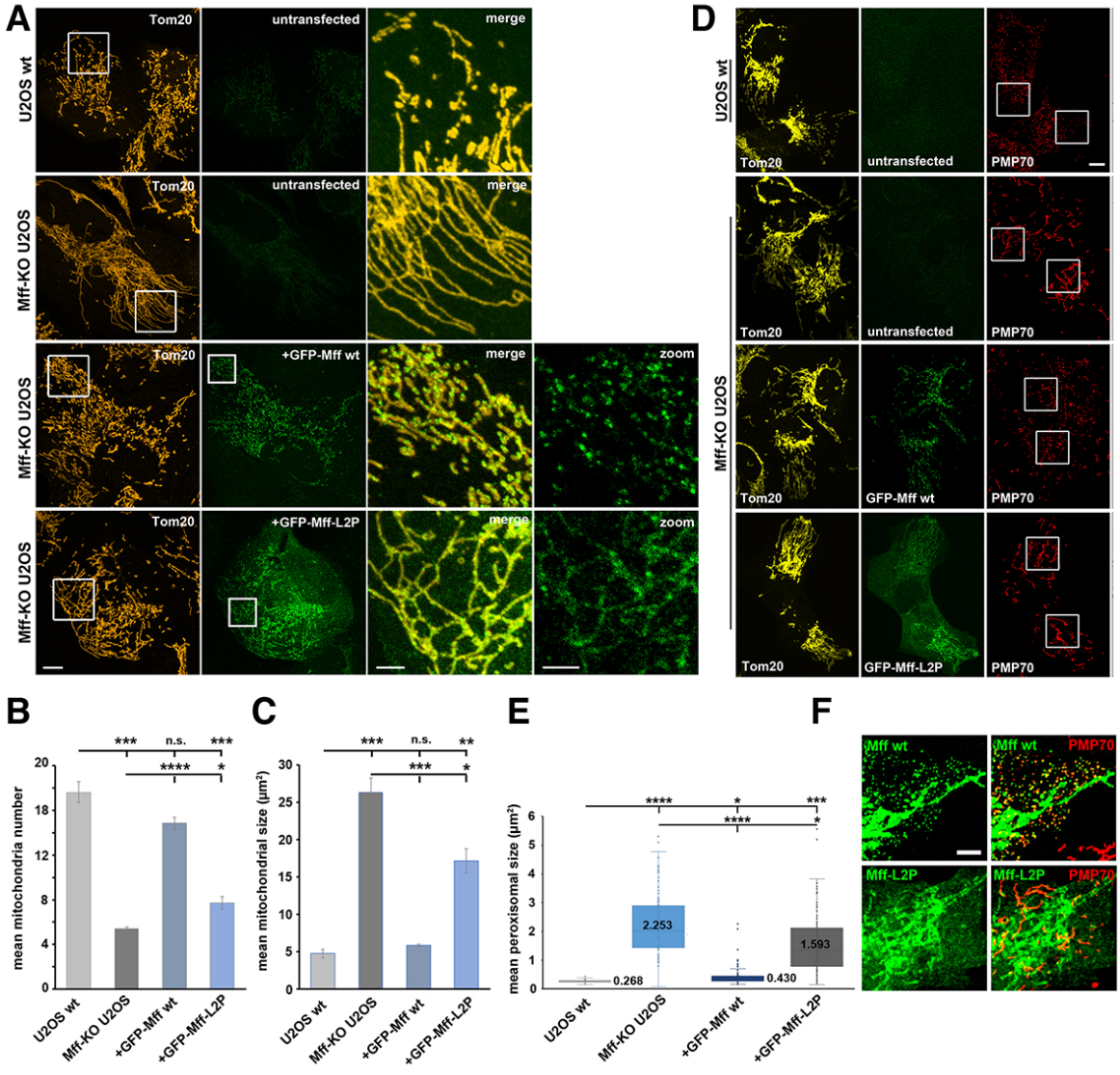
A
U2OS wt
Mff-KO U2OS
Mff-KO U2OS
Mff-KO U2OS
Tom20
untransfected
merge
+GFP-Mff wt
zoom
+GFP-Mff-L2P
D
PMP70
GFP-Mff wt
GFP-Mff-L2P
B
mean mitochondria number
C
mean mitochondrial size (µm²)
E
mean peroxisomal size (µm²)
0.268
2.253
0.430
1.593
F
Mff wt
Mff-L2P
U2OS wt
Mff-KO U2OS
+GFP-Mff wt
+GFP-Mff-L2P

Figure 2-7: Mff oligomerization is required for mitochondrial and peroxisomal division.

A) Mff-KO U2OS cells were transfected with either GFP-Mff-WT (25 ng plasmid) or GFP-Mff-L2P (50 ng) for 24 hrs, then fixed and stained with anti-Tom20 (red). GFP fluorescence is green. Controls are un-transfected WT and Mff-KO U2OS cells. Images at right are merges or GFP signal sof boxed regions.

B) Quantification of mean mitochondrial number for the indicated conditions, from regions of interest like those in panel A. Cells analyzed: 147, 148, 142, and 147 for U2OS WT, Mff-KO U2OS, and transfected GFP-Mff-WT or GFP-Mff-L2P, respectively. *, $p \leq 0.005$. ***, $p \leq 0.001$. ****, $p \leq 0.0001$. n.s. = not significant, $p > 0.05$.

C) Quantification of mean mitochondrial size for the indicated conditions, from regions of interest like those in panel A. Cells analyzed: 147, 148, 142, and 147 for U2OS WT, Mff-KO U2OS, and transfected GFP-Mff-WT or GFP-Mff-L2P, respectively. *, $p \leq 0.005$. ***, $p \leq 0.001$. ****, $p \leq 0.0001$. n.s. = not significant, $p > 0.05$.

D) Mff-KO U2OS cells were transfected with either GFP-Mff-WT or GFP-Mff-L2P as in panel A, then fixed and stained with anti-Tom20 (yellow) and anti-PMP70 (red, peroxisomes). GFP fluorescence is green. Images at right are inverted PMP70 staining of boxed regions.

E) Quantification of mean peroxisome area for the indicated conditions, from regions of interest of PMP70 micrographs like those in panel D. Cells analyzed: 119, 126, 108, and 108 for U2OS WT, Mff-KO U2OS, and the re-transfected GFP-Mff-WT or GFP-Mff-L2P, respectively. Numbers represent mean values. *, $p \leq 0.005$. ***, $p \leq 0.001$. ****, $p \leq 0.0001$.

F) Contrast-enhanced images of GFP-Mff distribution (either GFP-Mff-WT or GFP-Mff-L2P) from panel D. Scale bar, 10 μm (3 μm in insets) in panels A and D, 5 μm in panel F.

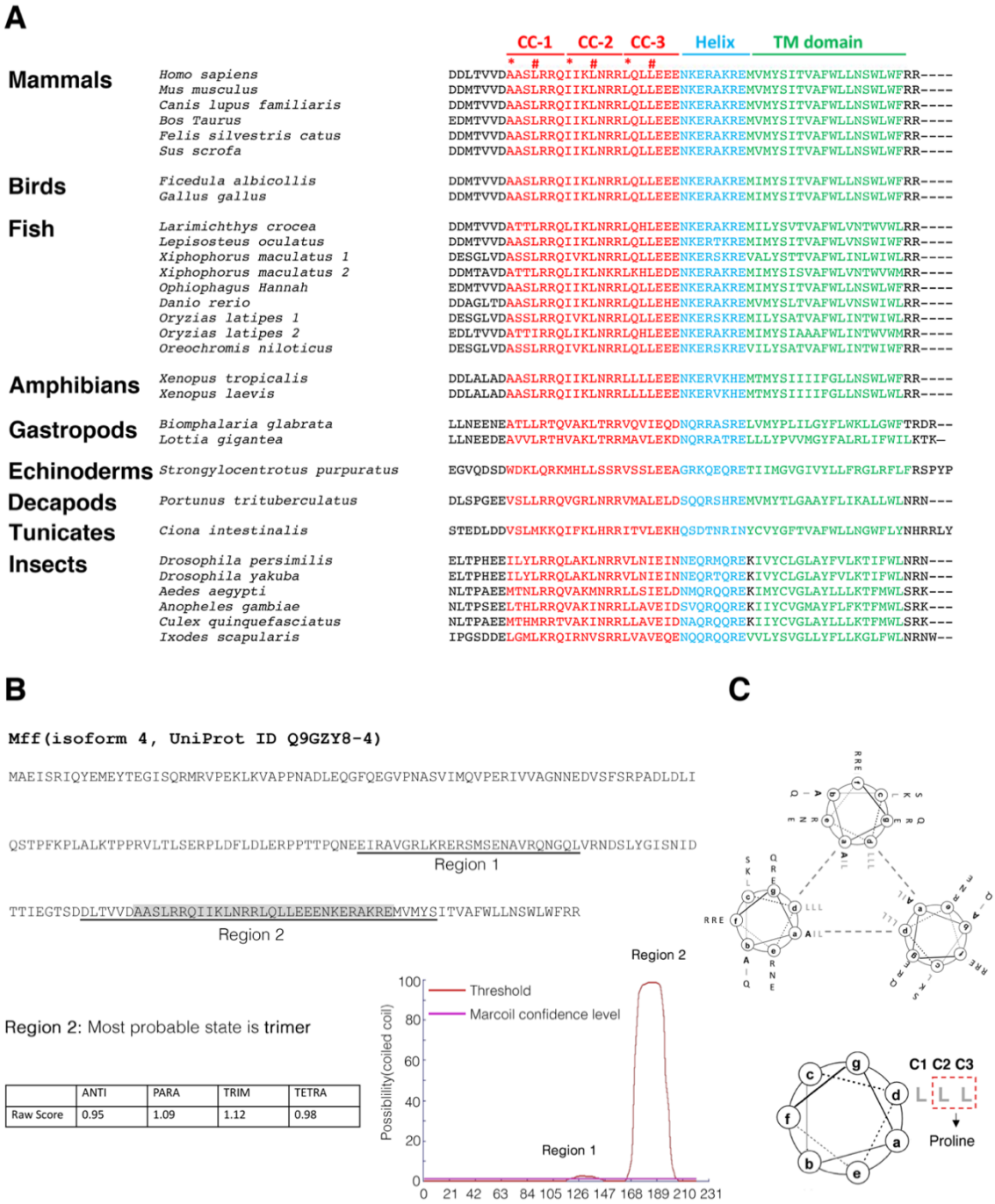
A
CC-1
CC-2
CC-3
Helix
TM domain
Mammals
Homo sapiens DDLTVVDAASLRRQIIKLNRRLQLLEEENKERAKREMVMYSITVAFWLLNSWLWFRR----
Mus musculus DDMTVVDAASLRRQIIKLNRRLQLLEEENKERAKREMVMYSITVAFWLLNSWLWFRR----
Canis lupus familiaris DDMTVVDAASLRRQIIKLNRRLQLLEEENKERAKREMVMYSITVAFWLLNSWLWFRR----
Bos Taurus EDMTVVDAASLRRQIIKLNRRLQLLEEENKERAKREMVMYSITVAFWLLNSWLWFRR----
Felis silvestris catus DDMTVVDAASLRRQIIKLNRRLQLLEEENKERAKREMVMYSITVAFWLLNSWLWFRR----
Sus scrofa DDMTVVDAASLRRQIIKLNRRLQLLEEENKERAKREMVMYSITVAFWLLNSWLWFRR----
Birds
Ficedula albicollis DDMTVVDAASLRRQIIKLNRRLQLLEEENKERAKREMIMYSITVAFWLLNSWLWFRR----
Gallus gallus DDMTVVDAASLRRQIIKLNRRLQLLEEENKERAKREMIMYSITVAFWLLNSWLWFRR----
Fish
Larimichthys crocea DDMTVVDATTLRRQLIKLNRRLQHLEEENKERAKREMILYSVTVAFWLVNTWVWLRR----
Lepisosteus oculatus DDMTVVDAASLRRQIIKLNRRLQLLEEENKERTKREMIMYSITVAFWLVNSWIWFRR----
Xiphophorus maculatus 1 DESGLVDASSLRRQIVKLNRRLQLLEEENKERSKREVALYSTTVAFWLINLWIWLRR----
Xiphophorus maculatus 2 DDMTAVDATTLRRQLIKLNKRLKHLEDENKERAKREMIMYSISVAFWLVNTWVWMRR----
Ophiophagus Hannah EDMTVVDAASLRRQIIKLNRRLQLLEEENKERAKREMIMYSITVAFWLLNSWLWFRR----
Danio rerio DDAGLTDAASLRRQIIKLNRRLQLLEHENKERAKREMVMYSLTVAFWLVNSWIWLRR----
Oryzias latipes 1 DESGLVDASSLRRQIVKLNRRLQLLEEENKERSKREMILYSATVAFWLINTWIWLRR----
Oryzias latipes 2 EDLTVVDATTIRRQLIKLNRRLQHLEEENKERAKREMIMYSIAAAFWLINTWVWMRR----
Oreochromis niloticus DESGLVDASSLRRQIVKLNRRLQLLEEENKERSKREVILYSATVAFWLINTWIWFRR----
Amphibians
Xenopus tropicalis DDLALADAASLRRQIIKLNRRLLLLEEENKERVKHEMTMYSIIIIFGLLNSWLWFRR----
Xenopus laevis DDLALADAASLRRQIIKLNRRLLLLEEENKERVKHEMTMYSIIIIFGLLNSWLWLRR----
Gastropods
Biomphalaria glabrata LLNEENEATLLRTQVAKLTRRVQVIEQDNQRRASRELVMYPLILGYFLWKLLGWFTRDR--
Lottia gigantea LLNEEDEAVVLRTHVAKLTRRMAVLEKDNQRRATRELLLYPVVMGYFALRLIFWILKTK—
Echinoderms
Strongylocentrotus purpuratus EGVQDSDWDKLQRKMHLLSSRVSSLEEAGRKQEQRETIIMGVGIVYLLFRGLRFLFRSPYP
Decapods
Portunus trituberculatus DLSPGEEVSLLRRQVGRLNRRVMALELDSQQRSHREMVMYTLGAAYFLIKALLWLNRN---
Tunicates
Ciona intestinalis STEDLDDVSLMKKQIFKLHRRITVLEKHQSDTNRINYCVYGFTVAFWLLNGWFLYNHRRLY
Insects
Drosophila persimilis ELTPHEEILYLRRQLAKLNRRVLNIEINNEQRMQREKIVYCLGLAYFVLKTIFWLNRN---
Drosophila yakuba ELTPHEEILYLRRQLAKLNRRVLNIEINNEQRTQREKIVYCLGLAYFVLKTIFWLNRN---
Aedes aegypti NLTPAEEMTNLRRQVAKMNRRLLSIELDNMQRQQREKIMYCVGLAYLLLKTFMWLSRK---
Anopheles gambiae NLTPSEELTHLRRQVAKINRRLLAVEIDSVQRQQREKIIYCVGMAYFLFKTFMWLSRK---
Culex quinquefasciatus NLTPAEEMTHMRRTVAKINRRLLAVEIDNAQRQQREKIIYCVGLAYLLLKTFMWLSRK---
Ixodes scapularis IPGSDDELGMLKRQIRNVSRRLVAVEQENQQRQQREVVLYSVGLLYFLLKGLFWLNRNW--
B
Mff(isoform 4, UniProt ID Q9GZY8-4)
MAEISRIQYEMEYTEGISQRMRVPEKLKVAPPNADLEQGFQEGVPNASVIMQVPERIVVAGNNEDVSFSRPADLDLI
QSTPFKPLALKTPPRVLTLSERPLDFLDLERPPTTPQNEEIRAVGRLKRERSMSENAVRQNGQLVRNDSLYGISNID
Region 1
TTIEGTSDDLTVVDAASLRRQIIKLNRRLQLLEEENKERAKREMVMYSITVAFWLLNSWLWFRR
Region 2
Region 2: Most probable state is trimer
ANTI PARA TRIM TETRA
Raw Score 0.95 1.09 1.12 0.98
Region 2
Threshold
Marcoil confidence level
Possibility(coiled coil)
Region 1
0 21 42 63 84 105 126 147 168 189 210 231
C
C1 C2 C3
Proline

Figure S2-1: The coiled-coil region of Mff.

A) Alignment of C-terminal region of Mff from a range of metazoans, showing the three heptad repeats of the coiled-coil (CC-1, 2 and 3), the helix region, the TM domain, and the short sequence in the inter-membrane space. A and D positions of the heptads shown with * and #, respectively. Sequence starts at amino acid[169] of human Mff isoform 0000.

B) Analysis of coiled-coil regions of Mff using LOGICOIL [229]. Sequences of full length Mff is on the top (isoform 4, UniProt ID Q9GZY8-4). Underline indicates two possible predicted coiled-coil regions, grey box highlights the conservative coiled-coil in panel A. Scores of four possible coiled coil structures are predicted, positive score suggests high possibility. ANTI - anti parallel dimer, PARA - parallel dimer, TRIM - trimer, and TETRA - tetramer.

C) Helical wheels for the Mff coiled-coil in a putative trimeric arrangement. To the bottom is illustrated the mutation of leucines in the D position of CC-2 and CC-3 to prolines to make the Mff-L2P construct [230].

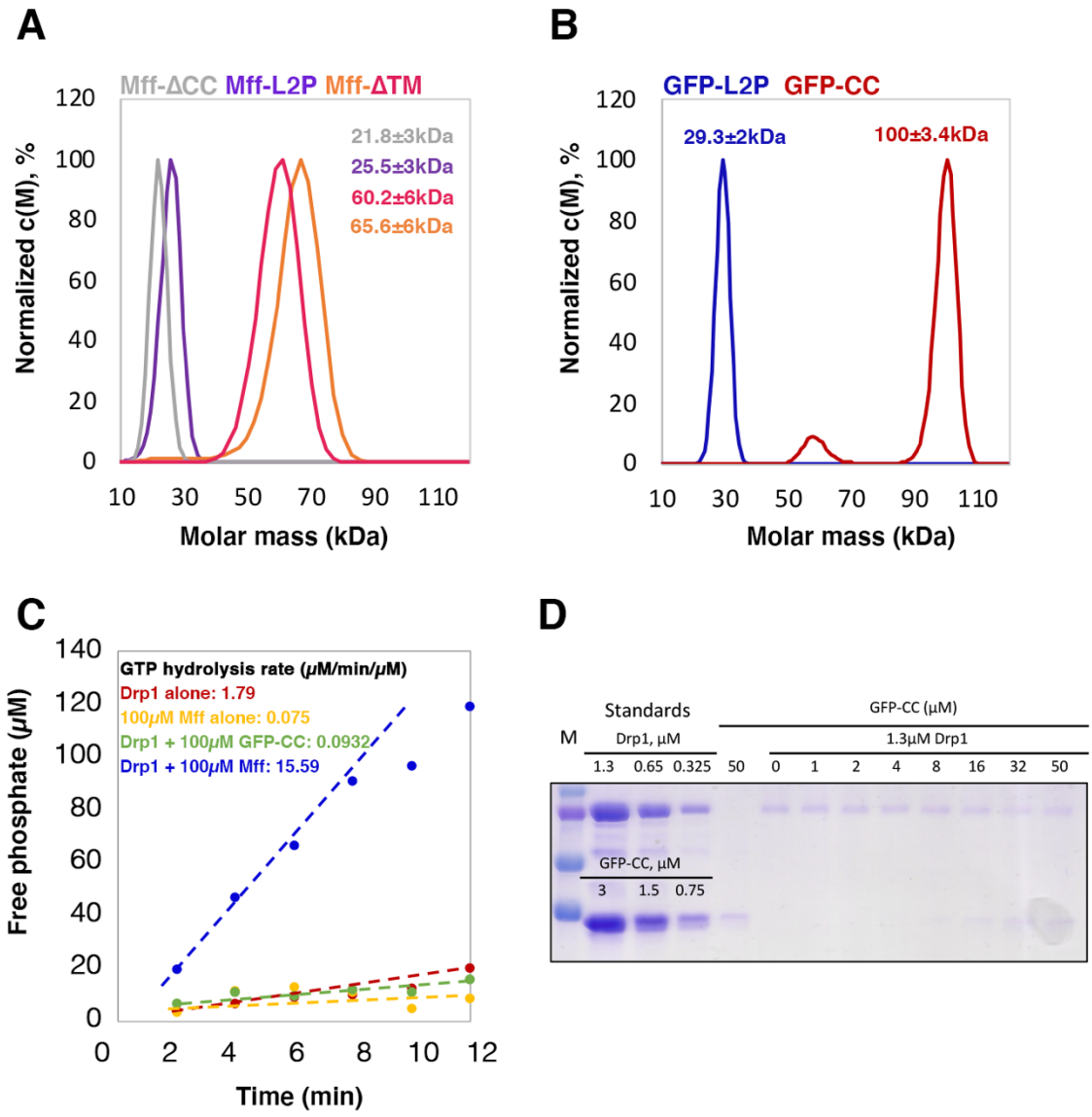
A
Mff-ΔCC Mff-L2P Mff-ΔTM
21.8±3kDa
25.5±3kDa
60.2±6kDa
65.6±6kDa
Normalized c(M), %
Molar mass (kDa)
B
GFP-L2P GFP-CC
29.3±2kDa
100±3.4kDa
Normalized c(M), %
Molar mass (kDa)
C
GTP hydrolysis rate (μM/min/μM)
Drp1 alone: 1.79
100μM Mff alone: 0.075
Drp1 + 100μM GFP-CC: 0.0932
Drp1 + 100μM Mff: 15.59
Free phosphate (μM)
Time (min)
D
Standards
GFP-CC (μM)
M
Drp1, μM
1.3μM Drp1
1.3 0.65 0.325 50 0 1 2 4 8 16 32 50
GFP-CC, μM
3 1.5 0.75

Figure S2-2: GFP-CC forms trimer and does not influence either Drp1 activity or its oligomerization.

A) Velocity analytical ultracentrifugation of Mff-ΔTM at 100 μM (orange) or 250 μM (pink), and Mff-ΔCC (gray) or Mff-L2P (purple) at 100 μM. Y axis normalized to the peak c(M) for each sample, the maximum value of each curve is normalized as 100%. Peak masses listed on graph.

B) Velocity analytical ultracentrifugation of 250 μM of GFP-CC (red) and GFP-L2P (blue). Peak molar mass prediction listed on graph.

C) Time course of GTP hydrolysis by Drp1 alone (red), Mff alone (yellow), Drp1 + 100 μM GFP-CC (green), and Drp1 + 100 μM Mff (blue).

D) High-speed pelleting assay of Drp1 (1.3 μM) in the presence GTP (1 mM) and of varying GFP-CC concentration. Drp1 and GFP-CC regions from the same SDS-PAGE gel are presented. Standards equivalent to the indicated concentrations of Drp1 or GFP-CC in the assay on left of gels. Pellet fractions shown to the right.

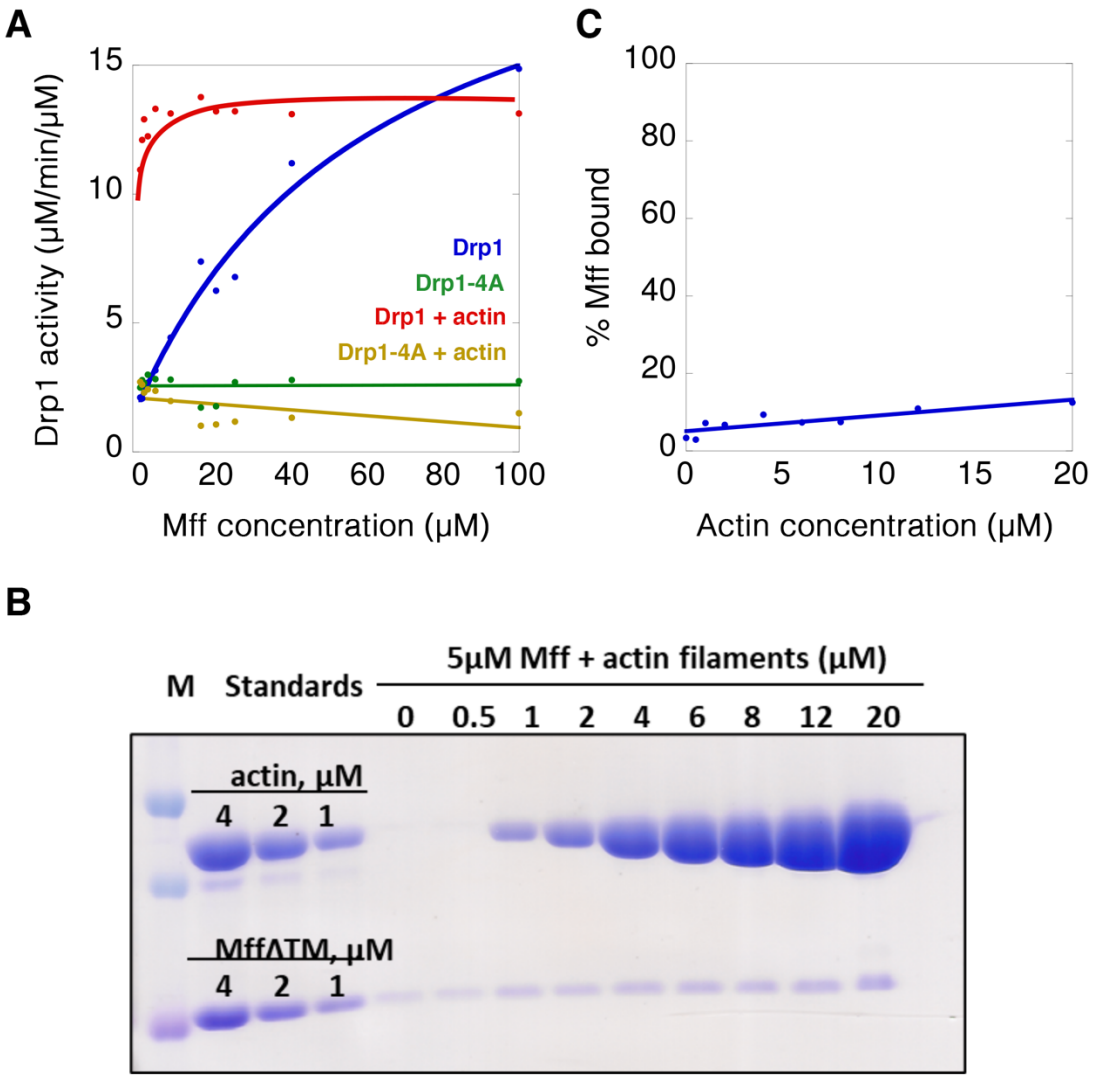

Figure S2-3: Mff-ΔTM does not directly interact directly with actin.

A) GTPase activity of wild-type and oligomerization-defective mutant Drp1 401-404 AAAA (0.75 μM) as a function of Mff-ΔTM added, in the absence or presence of 0.5 μM actin filaments.

B) High-speed pelleting assay of Mff-ΔTM (5 μM) in the presence of increasing concentrations of actin filaments. Standards equivalent to the indicated concentrations of Drp1 or Mff-ΔTM in the assay on the left. Pellet fractions shown to the right.

C) Quantification of high-speed pelleting assay from panel B.

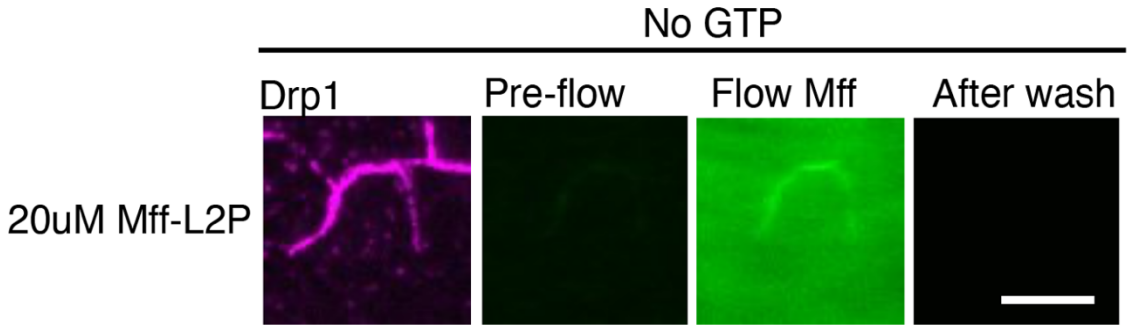

Figure S2-4: Binding of Mff-L2P to Drp1-bundled actin filaments at high concentration. TIRF assay conducted similarly to that in Figure 6D. Actin bundles were pre-formed with 0.1 μM actin (unlabeled, phalloidin-stabilized) and 2.5 μM Cy5-Drp1, then introduced into the TIRF chamber. Fluorescein-labeled Mff-L2P (20 μM) was introduced into the chamber in the absence of GTP while imaging. After 1 min, the chamber was washed while imaging. Bar, 10 μm.

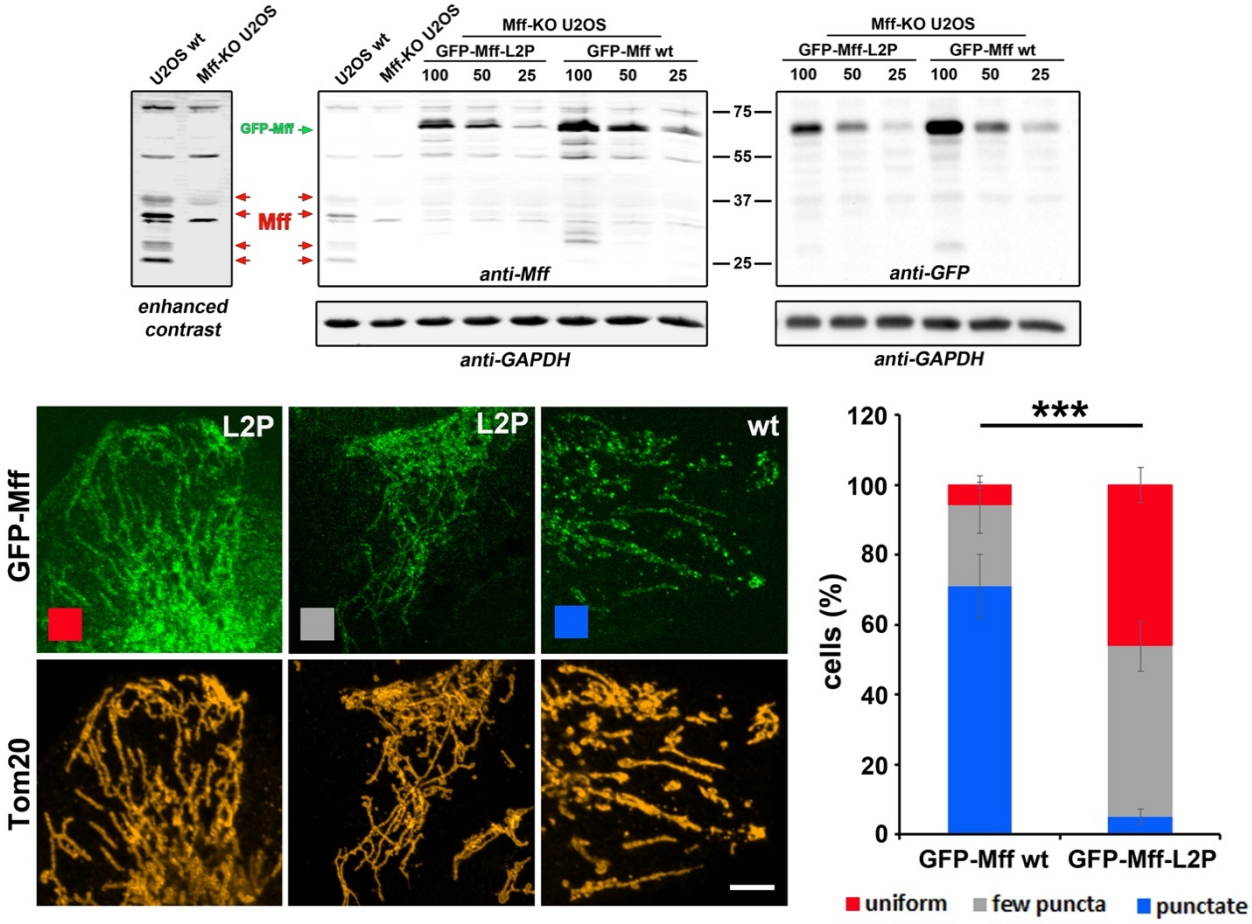
U2OS wt
Mff-KO U2OS
GFP-Mff
Mff
enhanced contrast
Mff-KO U2OS
GFP-Mff-L2P
GFP-Mff wt
100 50 25 100 50 25
75
55
37
25
anti-Mff
anti-GAPDH
anti-GFP
GFP-Mff
Tom20
L2P
L2P
wt
***
cells (%)
120
100
80
60
40
20
0
GFP-Mff wt
GFP-Mff-L2P
uniform
few puncta
punctate

Figure S2-5: Expression and localization of GFP-fusion Mff constructs in Mff-KO U2OS cells.

A) Western blots of cell extracts. Left and center blots are anti-Mff, with the left blot being an enhanced contrast version of a portion of the first two lanes of the center blot, showing that Mff KO results in disappearance of four bands (presumably corresponding to splice variants and/or post-translational modifications) but not of several background bands. Center blot shows change in anti-Mff signal for GFP-Mff with increasing amounts of plasmid transfected (in ng plasmid). Right blot shows anti-GFP of same transfected samples. Anti-GAPDH westerns are from the same blots.

B) Examples of categories used for punctate GFP-Mff quantification in cells in panel C. Bar, 5 μm.

C) Quantification of punctate nature of GFP-Mff mitochondrial localization, on Mff-KO U2OS cells transfected with either GFP-Mff-WT (25 ng plasmid) or GFP-Mff-L2P (50 ng plasmid), then fixed and stained for outer mitochondrial membrane with anti-Tom20. Data from 3 independent experiments, with 142 and 163 cells analyzed for GFP-Mff-WT and GFP-Mff-L2P, respectively. ***, p value < 0.001.

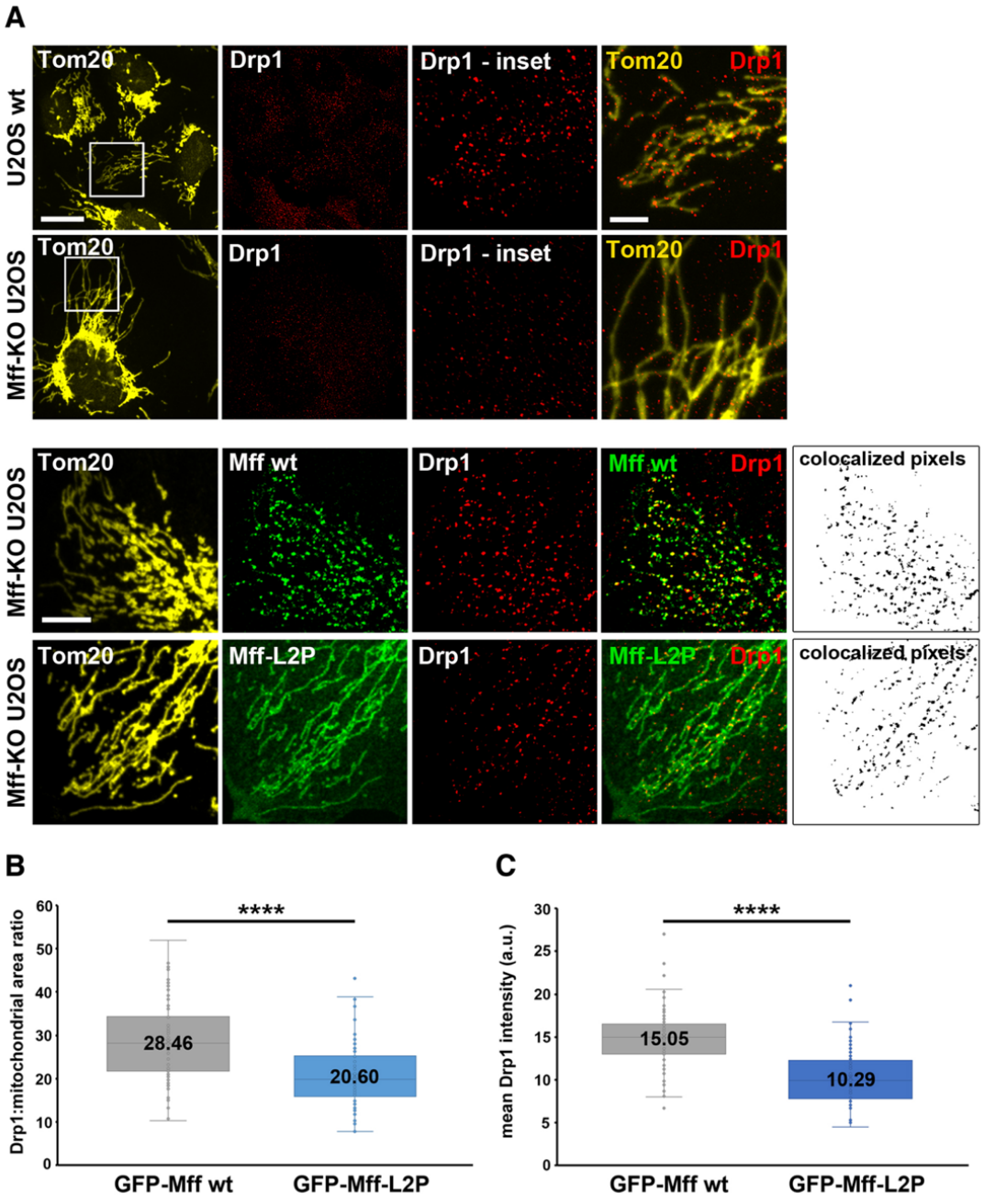
A
U2OS wt
Mff-KO U2OS
Tom20
Drp1
Drp1 - inset
Tom20 Drp1
Mff wt
Mff wt Drp1
colocalized pixels
Mff-L2P
Mff-L2P Drp1
B
Drp1:mitochondrial area ratio
****
28.46
20.60
GFP-Mff wt
GFP-Mff-L2P
C
mean Drp1 intensity (a.u.)
15.05
10.29

Figure S2-6: Distribution of Drp1 in Mff-KO U2OS cells expressing GFP-Mff constructs.

A) Images of endogenous Drp1 distribution upon GFP-Mff expression in Mff-KO U2OS cells. Cells were transfected with either GFP-Mff-WT (25 ng plasmid) or GFP-Mff-L2P (50 ng plasmid), then fixed and stained with anti-Tom20 and anti-Drp1. Controls are untransfected WT and Mff-KO U2OS cells. Right-most image shows Drp1-stained pixels that co-localize with Tom20. Bars, 20 μm in overviews and 5 μm in insets.

B) Quantification of area of mitochondrial Drp1 puncta as a function of mitochondria area from micrographs such as in panel A. ****, $p < 0.0001$. Numbers represent mean values.

C) Quantification of mean Drp1 intensity per puncta, from micrographs such as in panel A. ****, $p < 0.0001$. 83 and 82 cells analyzed for Mff-WT and Mff-L2P, respectively.

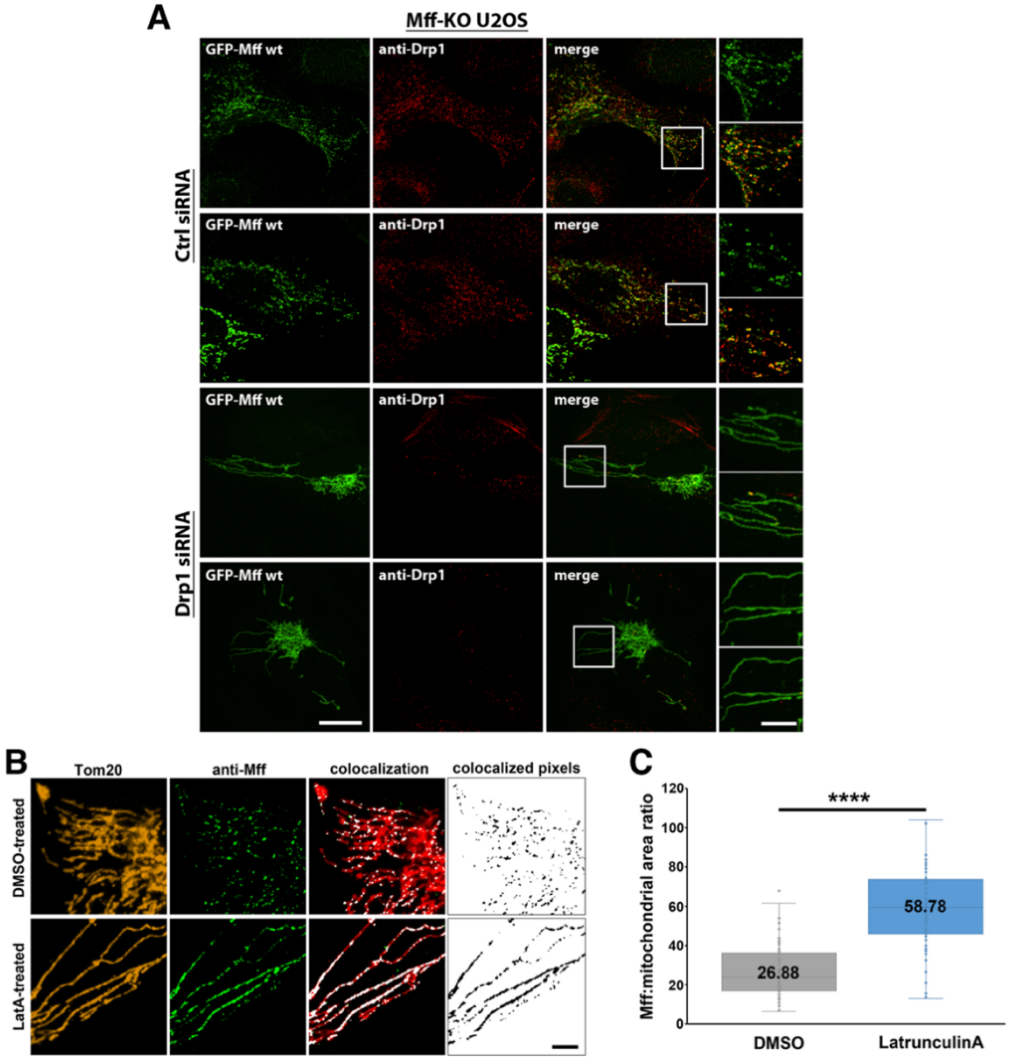

Figure S2-7: Effects of Drp1 and actin on cellular Mff puncta.

A) Mff-KO U2OS cells were subjected to either control knock-down (top) or Drp1 knock-down (bottom) for 72 hrs, then transfected with GFP-Mff-WT (25 ng plasmid) for 24 hrs. Cells were fixed and stained with anti-Drp1. Two examples from control KD and Drp1 KD shown. Note long mitochondria and low anti-Drp1 staining in Drp1 KD cells, indicative of siRNA efficacity.

B) Examples of WT U2OS cells treated with either DMSO (top) or 2 μM LatA (bottom) for 15 min before fixation and staining with anti-Tom20 and anti-Mff. Right-most images show the patterns of Mff staining on mitochondria.

C) Quantification of mitochondrial area covered by Mff, as judged by the ratios of the mitochondrial Mff staining versus total mitochondrial staining from micrographs as in panel B. ****, $p < 0.0001$. 85 and 89 cells analyzed for DMSO and LatA, respectively.

Table S2-1: Hydrodynamic parameters of Mff and GFP by vAUC.

	Mff				GFP	
	250 μM	100 μM			250μM	
	Mff-ΔTM	Mff-ΔTM	Mff-ΔCC	Mff-L2P	GFP-CC	GFP-L2P
S value	3.03 ± 0.22	2.72 ± 0.171	1.21 ± 0.104	1.44 ± 0.136	4.89 ± 0.106	2.67 ± 0.134
Molecular Mass (kDa)	59.6 ± 6.4	65.6 ± 5.8	21.8 ± 2.7	25.5 ± 0.35	100.3 ± 3.4	29.3 ± 2
Frictional ratio	1.7133	2.036175	2.19496	2.044859	1.58723	1.279531
rmsd	0.005875	0.01225	0.021506	0.006419	0.007212	0.008566

*S value is defined as mean ± standard deviations.

Chapter III:

Long-chain fatty acyl-coenzyme A activates the mitochondrial fission factors MiD49 and MiD51 by inducing their oligomerization

Chapter III

Long-chain fatty acyl-coenzyme A activates the mitochondrial fission factors MiD49 and MiD51 by inducing their oligomerization

Ao Liu[1,3], Frieda Kage[1,3], Asan F. Abdulkareem[1,4], Mac Pholo Aguirre Huamani[1,4], Gracie Sapp[2], Halil Aydin[2] & Henry N. Higgs[1]

[1]Department of Biochemistry and Cell Biology, Geisel School of Medicine at Dartmouth College, Hanover NH 03755, USA

[2]Department of Biochemistry, University of Colorado Boulder, Boulder CO 80309, USA

[3]These authors contributed equally to this work

[4]Current address: Department of Molecular and Systems Biology, Geisel School of Medicine at Dartmouth College, Hanover NH 03755, USA

The text and data here are adapted or reproduced in full from the manuscript under review in ***Nature Cell Biology***

(DOI: https://doi.org/10.1101/2023.07.31.551267)

This work was supported by NIH R35 GM122545 and R01 DK088826 to HNH, NIH P20 GM113132 to the Dartmouth BioMT, and by the Deutsche Forschungsgemeinschaft (DFG) fellowship KA5106/1-1 (418076373) to FK.

3.1 Abstract

Mitochondrial fission occurs in many cellular processes, but the regulation of fission is poorly understood. We show that long-chain acyl coenzyme A (LCACA) activates two related mitochondrial fission proteins, MiD49 and MiD51, by inducing their oligomerization, activating their ability to stimulate DRP1 GTPase activity. The 1:1 stoichiometry of LCACA:MiD in the oligomer suggests interaction in the previously identified nucleotide-binding pocket, and a point mutation in this pocket reduces LCACA binding and LCACA-induced oligomerization for MiD51. In cells, this LCACA binding mutant does not assemble into puncta on mitochondria or rescue MiD49/51 knock-down effects on mitochondrial length and DRP1 recruitment. Furthermore, cellular treatment with the fatty acid analogue 2-bromopalmitate, which causes increased acyl-CoA, promotes mitochondrial fission in an MiD49/51-dependent manner. These results suggest that LCACA is an endogenous ligand for MiDs, inducing mitochondrial fission and providing a potential mechanism for fatty acid-induced mitochondrial fragmentation. Finally, MiD49 or MiD51 oligomers synergize with MFF, but not with actin filaments, in DRP1 activation, suggesting distinct pathways for DRP1 activation.

3.2 Introduction

Mitochondrial fission is a key cellular process, with defects in fission being linked to multiple human diseases[54]. The reasons for which mitochondria undergo fission vary considerably, including for distribution to daughter cells during cell division, distribution to remote areas of polarized cells, and in response to changing metabolic conditions[38,68]. In addition, mitochondrial fission is an important step in mitophagy of damaged mitochondrial segments, and defects in fission result in decreased overall mitochondrial health[240]. Finally, mitochondrial fission proteins participate in the production of mitochondrially-derived vesicles[46], an additional mechanism for removal of dysfunctional mitochondrial components.

A key protein in mitochondrial fission is the membrane-remodeling GTPase DRP1, which is recruited from the cytoplasm to the outer mitochondrial membrane (OMM), where it oligomerizes into a ring structure around the mitochondrion[68]. Oligomerization activates DRP1's GTPase activity by bringing the GTPase domains in close proximity[70,98,101]. GTP hydrolysis by the DRP1 oligomer results in constriction of the oligomer, driving the fission process.

Given the variety of cellular situations requiring mitochondrial fission, it is likely that there are multiple mechanisms for regulating the process. One potential step for differential control of mitochondrial fission is in DRP1 recruitment to the OMM. In mammals, three DRP1 receptors have been identified: mitochondrial fission factor (MFF), and two related proteins: mitochondrial dynamics proteins of 49 and 51 kDa (MiD49 and MiD51, also called MIEF2 and MIEF1 respectively)[68]. All three proteins are widely expressed in mammalian cells. However, it is unclear to what extent these receptors function together versus independently. Knock-down or knock-out of MFF alone causes dramatic mitochondrial elongation in many metazoan cell types tested[113,115,116,123,231] with one exception[122], suggesting that it might play a role in many forms of mitochondrial fission. Knock-down or knock-out of MiD49 and MiD51 also causes mitochondrial elongation, although the effect is more variable between studies and there are differing reports of the redundancy between MiD49 and 51[116,120–123].

These findings suggest that MiD49 and MiD51 might play roles in a sub-set of mitochondrial fission events. Three other properties of MiD49/51 suggest that they act in a context-specific manner. First, while depletion of MiD49/51 results in mitochondrial elongation, over-expression of either protein has the same effect [51,116,120,121]. Over-expressed MiD49/51 also causes extensive

DRP1 recruitment to mitochondria [51,116,120,121], suggesting that unregulated MiD-mediated DRP1 recruitment is detrimental to its controlled assembly during fission. Second, MiD49/51 expressed at low levels appear punctate on mitochondria, suggesting oligomerization [51,123,195]. In contrast, the purified cytoplasmic regions of either MiD49 or MiD51 behave as monomers or dimers[124,125], suggesting that this oligomerization is regulated.

A third property of both MiD49 and MiD51 is that their purified cytoplasmic regions do not stimulate DRP1 GTPase activity biochemically[125,126], in contrast to MFF[96,109,241]. These findings suggest that the MiD proteins themselves require activation in order to activate DRP1. The structures of both proteins reveal large putative ligand-binding cavities (**Figure 3-1A**). MiD51 is capable of binding purine nucleotide diphosphate, with ADP being preferred to GDP[124,125], while MiD49 displays no affinity for these ligands[124]. The effect of ADP on MiD51's ability to activate DRP1 is modest, with an approximate 2-fold stimulation of DRP1 GTPase activity over DRP1 alone [124]. These results suggest that MiD49 and MiD51 might bind alternate ligands to stimulate their DRP1-activating ability in cells.

We have previously shown that actin filaments can bind and activate DRP1[69,91], and that inhibition of actin polymerization or of the actin polymerization factor INF2 decreases mitochondrial DRP1 recruitment and inhibits mitochondrial fission in cells[60,91,171]. Actin activates DRP1 GTPase activity in a characteristic 'bi-phasic' manner, in which low concentrations stimulate while higher concentrations do not[69,241]. This bi-phasic behavior is likely due to the fact that DRP1 activation requires inter-molecular binding between GTPase domains[70,98,101], with low actin concentrations facilitating this juxtaposition while higher actin concentrations cause DRP1 to bind more sparsely along the filament, minimizing interaction. In addition to its ability to increase DRP1 activity in a stand-alone manner, actin can synergize with MFF in DRP1 activation, decreasing the concentration of MFF needed for DRP1 stimulation[241]. It is not clear what effect MiD49 or MiD51 would have on actin- or MFF-mediated DRP1 activation.

While mitochondrial fission is often associated with mitochondrial dysfunction and mitophagy, fission has also been correlated with increased mitochondrial fatty acid oxidation in several contexts, including brown adipocytes, hepatocytes, and pancreatic beta cells[36,38]. An obligatory step in mitochondrial long-chain fatty acid import is coupling of fatty acid to coenzyme A to make long-chain acyl-coenzyme A (LCACA). In this paper, we show that both MiD49 and MiD51 bind LCACA, which induces MiD oligomerization. LCACA-oligomerized MiD49 or MiD51 activates

DRP1 GTPase activity ~10-fold, and this activation is synergistic with MFF-mediated DRP1 activation but not with actin-mediated activation. An MiD51 mutant defective in LCACA binding does not assemble into punctate structures on mitochondria, recruit DRP1 to mitochondria, or rescue the mitochondrial elongation phenotype caused by MiD49/51 knock-down. Overall, our work suggests that MiD49 and MiD51 might respond to LCACA for DRP1 recruitment *en route* to mitochondrial fission.

3.3 Results

3.3.1 Long-chain acyl-CoA induces MiD49 oligomerization

Both MiD49 and MiD51 contain putative nucleotide-binding pockets structurally similar to that of cyclic GMP-AMP synthase (cGAS) (**Figure 3-1A**). While MiD51 can bind ADP or GDP in this pocket, MiD49 displays no apparent binding to these purine nucleotides[124]. Interestingly, the purine rings of ADP and GDP adopt distinct orientations in the binding pocket of MiD51 (**Figure 3-1B**).

The absence of a strong effect of ADP or GDP on MiD51's ability to stimulate DRP1[124,125], coupled with the absence of a known ligand for MiD49, prompted us to screen for other possible ligands. We postulated that a ligand for MiD49 might induce oligomerization, because of the punctate appearance of MiD49 in cells. Using blue-native gel electrophoresis (BNGE) on a murine MiD49 cytoplasmic region construct (amino acids 125-454, **Figure S3-1A, B**), we screened several purine-containing compounds for the ability to cause a shift in MiD49 mobility, indicative of higher oligomeric species. Of these compounds, only palmitoyl-coenzyme A (palmitoyl-CoA) causes such a mobility shift (**Figure 3-1C**). Neither the fatty acid moiety alone nor CoA alone causes a similar shift (**Figure 3-1D, E**). Long-chain acyl-CoAs (LCACA) including stearoyl (18 carbons), oleoyl (18 carbons, 1 double bond), palmitoyl (16 carbons), myristoyl (14 carbon) and lauroyl-CoA (12 carbon) cause a shift in MiD49 mobility (**Figure 3-1D**). In contrast, octanoyl-CoA (8 carbon) does not cause an MiD49 mobility shift, nor do two short-chain acyl-CoAs found in the cytoplasm, acetyl-CoA and malonoyl-CoA (**Figure 3-1D**). We also tested lysophosphatidic acid (LPA), as well as geranylgeranyl-pyrophosphate (GG-PP), neither of which display an ability to shift MiD49 mobility (**Figure 3-1D**).

To examine the oligomerization effect further, we used size exclusion chromatography (SEC). MiD49 cytoplasmic region alone (100 μM) elutes near the position of ovalbumin (~ 45 kDa), suggestive of a monomer (**Figure S3-1C**). Palmitoyl-CoA concentrations from 10 to 100 μM cause a fraction of the protein to shift to a peak near the void volume, indicative of higher-order oligomers (**Figure 3-1F, Figure S3-1C**). By velocity analytical ultracentrifugation, this void fraction sediments as a broad peak centered at 82 S (**Figure 3-1G**), with a calculated mass of 4815 kDa (**Figure S3-1D**), which would suggest oligomers averaging 126 subunits. In contrast, the late-eluting fraction sediments at 2.9 S (**Figure 3-1G**), with an apparent mass of 36.4kDa (**Figure S3-1D**), which is close to the calculated monomer mass (38.7 kDa). Negative-stain transmission

electron microscopy (EM) reveals that the void fraction contains a heterogeneous array of oblate particles, whereas the late-eluting fraction contains a more uniform spread of small particles (**Figure 3-1H**). Analysis of a limited number of particles from the void fraction reveals long and short particle axes of 66.7±12.7 and 39.7±13.5 nm, respectively (**Figure S3-2A-C**), for a mean axial ratio of 0.61±0.20. For comparison, the majority of palmitoyl-CoA micelles are more spherical, with an axial ratio of 0.85±0.15 and a mean diameter of 9.5±1.8 nm (17 particles measured, **Figure S3-2D**).

The negative-stain EM also allows determination of the critical micelle concentration (cmc) for palmitoyl-CoA. From quantification of micelle number over a range of palmitoyl-CoA concentrations, we calculate a cmc of 47 μM in our buffer conditions (**Figure S3-2E**), similar to published values at similar ionic strength[242]. The fact that palmitoyl-CoA concentrations below this value cause a shift in MiD49 to by size-exclusion chromatography (**Figure 3-1F**) suggests that MiD49 is not binding to palmitoyl-CoA micelles to affect this shift. In the ensuing experiments, we refer to the void peak as MiD49 oligomers, and the late-eluting peak as MiD49 monomers.

One question regards the stoichiometry of palmitoyl-CoA:MiD49 in the oligomer fraction. To quantify palmitoyl-CoA, we conducted reversed phase HPLC analysis. Palmitoyl-CoA elutes at 14.7 mL in this solvent system (**Figure S3-3A**), and the peak area (from 260 nm absorbance) is proportional to the quantity of palmitoyl-CoA loaded in the range of 0.5 – 2 nmole (**Figure S3-3B,C**). In an oligomer fraction containing 5.3 μM MiD49, the measured palmitoyl-CoA concentration is 5.5 μM (**Figure S3-3D**).

As a second technique to determine palmitoyl-CoA concentration in MiD49 oligomer fractions, we used a phosphate assay (coenzyme A contains three phosphates). From these assays, the palmitoyl-CoA:MiD49 ratios from three oligomerization reactions range from 0.8 to 1.11 (**Figure S3-3E,F**). These results suggest that palmitoyl-CoA binds in a 1:1 complex with MiD49 in oligomers.

We also used the HPLC analysis method to test acyl chain preference of MiD49 further, by incubating MiD49 with equal concentrations of six acyl-CoAs (stearoyl, oleoyl, palmitoyl, myristoyl, lauroyl, and octanoyl), and then analyzing the acyl-CoA composition of the isolated MiD49 oligomer fraction. The three longer-chain acyl-CoAs (stearoyl, oleoyl, palmitoyl) are abundant in this fraction, while there is minimal myristoyl-CoA or lauroyl-CoA and no detectable octanoyl-CoA (**Figure S3-4**). This result suggests that, even though myristoyl-CoA or lauroyl-

CoA can induce MiD49 oligomerization (**Figure 3-1D**), they are out-competed by longer chain acyl-CoAs.

3.3.2 MiD49 oligomers stimulate DRP1 GTPase activity

The preceding results suggest that LCACA binds MiD49 in a 1:1 complex, and promotes MiD49 oligomerization. We next tested the effect of MiD49 oligomers on DRP1 GTPase activity. Similar to past results[124,125], MiD49 monomers do not stimulate DRP1 GTPase activity (**Figure 3-2A**). In contrast, MiD49 oligomers display an approximate 10-fold stimulation (**Figure 3-2A**). We then analyzed the concentration dependence of DRP1 activation by MiD49 oligomers. Intriguingly, MiD49 oligomers have a bi-phasic effect on DRP1 GTPase activity, with stimulatory effects up to 1 μM and then decreasing activation at higher concentrations (**Figure 3-2B**). This effect is similar for MiD49 oligomers isolated from a range of initial MiD49:palmitoyl-CoA ratios in the oligomerization reaction (**Figure 3-2B**).

The bi-phasic effect of MiD49 oligomer concentration on DRP1 GTPase activity is reminiscent of that shown by actin filaments[69] (**Figure 3-2C, Figure S3-5A**). We postulate that, in both cases, low concentrations of the oligomeric molecule (MiD49 or actin filaments) induce the juxtaposition of DRP1 G domains, which stimulates GTPase activity[70,98,101]. Beyond a certain concentration of oligomeric molecule, however, DRP1 binding becomes sparser and G domains are separated (**Figure 3-2D**). If this situation is true, increasing the DRP1 concentration should shift the optimally stimulating MiD49 oligomer concentration to a higher value. Indeed, the concentration of MiD49 oligomer needed to reach peak activation increases with increasing DRP1 concentration (**Figure 3-2E**).

We have previously shown that actin filaments synergize with MFF in stimulating DRP1, with actin filaments decreasing the concentration of MFF needed for optimal stimulation[69,241]. We tested the possibility that MiD49 oligomers might act in a similar manner to actin. Indeed, an MiD49 concentration that causes sub-optimal DRP1 activation alone (250 nM) allows further DRP1 activation by low concentrations of MFF (EC_{50} 1 μM, **Figure 3-2F, Figure S3-5B**), as opposed to the situation for MFF alone, in which 100 μM MFF is required for full DRP1 activation (**Figure S3-5C**). In contrast, MiD49 monomer reduces the effectiveness of MFF in DRP1 activation (**Figure 3-2F, Figure S3-5B,C**). We tested whether MiD49 oligomers, like MFF, had the ability to synergize with actin filaments. However, varying concentrations of actin filaments do not

change the effect of MiD49 monomers or oligomers on DRP1 activity (**Figure 3-2G**). In addition, MiD49 monomers inhibit the effect of actin filaments on DRP1 GTPase activity (**Figure 3-2G**), with an IC_{50} below 500 nM (**Figure 3-2H**).

These results suggest that LCACA-induced oligomerization converts MiD49 into a DRP1-activating protein. MiD49 oligomers are synergistic with MFF for DRP1 activation, in a similar manner to the synergism between actin filaments and MFF. In contrast, MiD49 and actin filaments do not synergize. In fact, MiD49 monomers eliminate the activating effect of actin filaments on DRP1 activity, suggesting that the two are competitive for DRP1 binding.

3.3.3 MiD51 displays acyl-CoA induced oligomerization

We next tested the ability of LCACA to induce oligomerization of the cytoplasmic region of MiD51 (**Figure S3-1A,B**). Similar to MiD49, MiD51 migration on BNGE is slower in the presence of acyl-CoA of 12 carbons or longer, but not with octanoyl-CoA , acetyl-CoA, malonyl-CoA, CoA alone, palmitic acid, lyso-PA (**Figure 3-3A**), or a series of purine nucleotides (**Figure S3-6A**). By size-exclusion chromatography, palmitoyl-CoA causes a shift in MiD51 to an apparent oligomer, with the size depending on the palmitoyl-CoA:MiD51 ratio in the oligomerization reaction. Lower palmitoyl-CoA concentrations cause migration in the void volume (**Figure S3-6B**) and higher concentrations result in an oligomer that is resolved in the column (**Figure 3-3B**). By velocity analytical ultracentrifugation, this resolved oligomer sediments at 51 S (**Figure 3-3C**), and has an apparent mass of 2450 kDa (**Figure S3-6C)**, suggesting oligomers averaging 68 subunits. In contrast, the MiD51 peak in the absence of palmitoyl-CoA elutes similarly to the ovalbumin marker by size-exclusion chromatography (**Figure 3-3B**) and sediments at 2.9 S (**Figure 3-3C**) with a calculated mass of 38.3 kDa (**Figure S3-6C**), suggestive of a monomer. By negative stain electron microscopy, the oligomer displays a range of particle sizes, generally smaller than those for MiD49 oligomers (**Figure 3-3D, Figure S3-2**). We assessed palmitoyl-CoA:MiD51 ratio across the oligomer peak, and found an approximate 1:1 correspondence (**Figure 3-3E**). These results suggest that the increase in MiD51 size is due to LCACA-induced oligomerization of MiD51.

MiD51 has been previously shown to bind ADP[124,125]. We find that ADP does not induce MiD51 oligomerization (**Figure S3-6D**). ADP does decrease palmitoyl-CoA induced MiD51 oligomerization at higher concentrations, whereas CoA or acetyl-CoA have less effect (**Figure S3-**

6D). This result suggests that ADP and palmitoyl-CoA compete for MiD51 binding. Even at 0.5 mM ADP, however, significant MiD51 still oligomerizes.

We took advantage of a previously used assay to examine MiD51 binding specificity in more detail. In this assay[124], MiD51 is mixed with fluorescent MANT-ADP, and the change in MANT-ADP fluorescence is monitored, with binding correlating with higher fluorescence intensity. Similar to the past study, MiD51 binds MANT-ADP with an apparent K_d of 0.65 μM, while MiD49 displays no detectable MANT-ADP binding (**Figure S3-6E**). We then assessed MiD51 binding to potential ligands using a competition assay in which increasing competitor ligand is mixed with fixed concentrations of MANT-ADP and MiD51. Palmitoyl-CoA causes a concentration-dependent decrease in MANT-ADP fluorescence back to the level of MANT-ADP alone, with an EC_{50} of 2 μM (**Figure 3-3F**), suggesting competition for the same binding site on MiD51. Using this assay, we screened several molecules at fixed concentration (20 μM) for competition with MANT-ADP. LCACAs (stearoyl, oleoyl, palmitoyl, myristoyl) compete efficiently, whereas lauroyl-CoA, octanoyl-CoA, malonoyl-CoA, acetyl-CoA, CoA alone, palmitoyl-carnitine, and lyso-phosphatidic acid display no competition (**Figure 3-3G**). Interestingly, ADP is a poor competitor for MANT-ADP (**Figure 3-3F**), suggesting that the hydrophobic MANT group contributes significantly to the affinity of MiD51 for MANT-ADP in a similar manner to the fatty acid tail of acyl-CoA.

As with MiD49, oligomerized MiD51 activates DRP1 GTPase activity, whereas monomeric MiD51 does not (**Figure S3-6F**). Also similar to MiD49, MiD51 oligomers activate DRP1 in a bi-phasic manner, with an optimal concentration at 1 μM (**Figure 3-3H**). The optimal concentration increases if DRP1 concentration is increased (**Figure 3-3I**), supporting the model of increased DRP1 density on MiD51 oligomers to allow GTPase domain interaction (**Figure 3-2D**). In addition, MiD51 oligomers synergize with MFF for DRP1 activation, with the EC_{50} of MFF being 2 μM in the presence of MiD51 oligomers, which is over 10-fold lower than for MFF alone (**Figure 3-3J, Figure S3-6G**). In contrast, the same concentration of MiD51 monomers reduces MFF-mediated DRP1 activation (**Figure 3-3J, Figure S3-6G**). Similar to MiD49, MiD51 displays no ability to synergize with actin filaments in DRP1 activation (**Figure S3-6H**), and MiD51 monomers are potent inhibitors of actin-stimulated DRP1 GTPase activity (**Figure 3-3K**).

These results suggest that, similar to MiD49, MiD51 binding to LCACA induces oligomerization, and these oligomers are capable of DRP1 activation. While MiD51 is capable of binding ADP, LCACAs are preferred ligands, presumably constituting the physiological ligands in cells. MiD51

oligomers synergize with MFF in DRP1 activation, while MiD51 monomers inhibit both MFF- and actin-mediated DRP1 activation.

3.3.4 Mutation of R342 in MiD51 reduces LCACA-induced oligomerization

We sought to design an MiD51 mutant deficient in LCACA binding, using published structural information as a guide [124,125]. We made mutations to two residues protruding from either side of MiD51's pocket, Y185A and R342A. The R342 side chain is in close proximity to the alpha phosphate of both ADP and GDP, whereas Y185 is in the vicinity of the purine ring (**Figure 3-4A**). The cytoplasmic regions of both MiD51-R342A and MiD51-Y185A express and purify in bacteria similar to WT MiD51 (**Figure S3-1B**), eluting from SEC as apparent monomers (**Figure 3-4B**). MiD51-R342A displays an apparent inability to bind MANT-ADP, whereas MiD51-Y185A displays binding similar to WT (K_d WT 0.27 μM, K_d Y185A 0.9 μM, **Figure 3-4C**). By BNGE, MiD51-R342A displays a reduced ability to oligomerize in response to palmitoyl-CoA (**Figure 3-4D**), quantified by loss of the MiD51 monomer band with increasing palmitoyl-CoA (**Figure 3-4E**). Similarly, a lower amount of oligomer peak is recovered from SEC for the R342A mutant upon incubation with palmitoyl-CoA (**Figure 3-4F**). Interestingly, the MiD51-R342A oligomer maintains the ability to activate DRP1 GTPase activity (**Figure 3-4G**) suggesting that, although MiD51-R342A has reduced affinity for LCACA, it maintains DRP1 binding and activation once oligomerized.

3.3.5 Acyl-CoA binding mutants display reduced oligomerization and mitochondrial phenotypes in cells

At low expression levels, MiD proteins display a punctate appearance[51,120], suggestive of oligomerization. At higher expression, MiD distribution is uniform and causes mitochondrial elongation by its ability to sequester DRP1 [51,116,120]. We found similar effects with GFP-fusions of MiD49 and MiD51 (**Figure 3-5A, Figure S3-7A**). Live-cell imaging suggests that, for both MiD49 and MiD51, the puncta appear stable on the mitochondria, despite considerable fluctuation of the mitochondria themselves.

Identification of an MiD51 mutant defective in LCACA binding provided an opportunity to test the importance of LCACA binding to MiD function in cells. We expressed GFP-fusions of WT, Y185A or R342A MiD51 in HeLa cells and evaluated their ability to form puncta at low expression

level, as well as their effect on mitochondria at high expression level. Low level expression of either MiD51-WT or MiD51-Y185A results in punctate GFP accumulation on mitochondria, in contrast to the even distribution of MiD51-R342A (**Figure 3-5A,B**). The expression levels of these constructs are similar, and lower than endogenous MiD51 levels (**Figure 3-5C**). We quantified MiD51 puncta by examining the average size of each MiD51 particle and the % of mitochondrial area covered by MiD51 staining (examples in **Figure S3-7B**), with lower numbers denoting puncta. Both average particle size and % mitochondrial area are significantly lower for MiD51-WT and MiD51-Y185A than for MiD51-R342A (**Figure 3-5D,E**). At higher expression, MiD51-WT and MiD51-Y185A are evenly distributed along mitochondria and cause mitochondrial elongation, while MiD51-R342A causes a collapsed mitochondrial phenotype, which could be due to dominant negative effects of this mutant on the endogenous MiD51 and/or MiD49 proteins (**Figure S3-7C,D**).

We next tested whether MiD51-WT, MiD51-Y185A or MiD51-R342A could rescue phenotypes caused by siRNA-mediated double knock-down (KD) of MiD49 and MiD51. MiD49/51 KD in HeLa cells results in significant mitochondrial elongation (**Figure 3-6A**). Expression of MiD51-WT or MiD-Y185A results in substantial rescue of the mitochondrial elongation phenotype, while expression of MiD51-R342A does not (**Figure 3-6A,B**). In addition, MiD51-R342A appears diffuse on mitochondria in the MiD49/51 KD cells (**Figure 3-6A**), similar to its distribution in WT HeLa cells (**Figure 3-5A).**

Knock-down of MiD49/51 also results in a decrease in the punctate appearance of DRP1 on mitochondria (**Figure 3-6C)**, similar to results from other studies[120,122,123]. We quantified these effects either by % mitochondrial area covered by DRP1 (**Figure 3-6D)** or the size of DRP1 puncta (**Figure 3-6E)**. Re-expression of MiD51-WT or MiD51-Y185A results in a recovery of DRP1 puncta to larger sizes and mitochondrial coverage than in control cells (**Figure 3-6C-E)**, suggesting enhanced DRP1 oligomerization. In contrast, expression of MiD51-R342A does not cause recovery of DRP1 puncta size or overall mitochondrial area covered by DRP1 (**Figure 3-6C-E)**. The combination of these results suggest that LCACA binding is required for MiD51-mediated DRP1 recruitment and mitochondrial fission.

3.3.6 Increased cellular LCACA causes increased MiD-dependent mitochondrial fission

To test the involvement of LCACA in MiD-mediated mitochondrial fission, we treated cells with 2-bromopalmitate (2-BP), a palmitate analogue that gets converted to 2-bromopalmitoyl-CoA that is slow in subsequent processing [243,244] . We treated HeLa cells for 1-hr with either 150 μM 2-BP

or methyl-palmitate (MP) as a negative control [244], and evaluated the mitochondrial phenotype. In HeLa WT cells, a 1-hr treatment with 2-BP causes a 2.8-fold decrease in mitochondrial area after 1 h (**Figure 3-7A-C**), as well as an increase in mitochondrial DRP1 accumulation (**Figure S3-8**) when compared to control (MP-treated) cells. DRP1 KD causes mitochondrial area to increase 3.4-fold in control cells, and eliminates the 2-BP mediated decrease, suggesting that the change in mitochondrial length is due to increased fission (**Figure 3-7A-D**). Similarly, MiD49/51 KD causes mitochondrial area to increase 2-fold in control cells, and eliminates the 2-BP-induced mitochondrial shortening (**Figure 3-7A-D**). These results suggest that 2-BP mediated mitochondrial fission occurs through increased acyl-CoA levels, activating MiD49/51.

3.4 Discussion

We report that long chain fatty acyl CoAs (LCACAs) are ligands for the mitochondrial DRP1 receptors MiD49 and MiD51, triggering oligomerization which in turn enables activation of the DRP1 GTPase. LCACA-oligomerized MiD can synergize with MFF in activating DRP1, but is not synergistic with actin. A mutant compromising LCACA binding reduces cellular MiD51 oligomerization and its ability to enhance mitochondrial fission. Cellular treatment with 2-bromopalmitic acid, which increases acyl-CoA levels, stimulates mitochondrial fission in an MiD-dependent manner.

The identification of LCACAs as MiD ligands answers an outstanding question concerning these proteins. Both MiD49 and MiD51 contain large interior pockets similar to that of cGAS, but no ligand had been identified for MiD49, whereas the ligands identified for MiD51 (ADP or GDP) do not result in a dramatic change in its ability to activate DRP1[124,125]. We find that the affinity of MiD51 for palmitoyl-CoA is significantly higher than for ADP, suggesting that LCACAs likely out-compete ADP for MiD51 binding in cells. The demonstration that LCACAs bind with 1:1 stoichiometry to MiDs and cause a substantial increase in DRP1 activation suggests that these are physiological ligands. In addition, the fact that palmitoyl-CoA concentrations below its critical micelle concentration (measured here to be 47 μM) can induce MiD oligomerization suggests that MiDs are not simply aggregating around micelles. Furthermore, LCACAs are preferred over other possible ligands such as lyso-phosphatidic acid, acetyl-CoA, malonyl-CoA, or a variety of nucleotides.

The activation mechanism induced by LCACA is intriguing. In this study and previous studies[124,125], the cytoplasmic regions of MiD49 or MiD51 cannot activate DRP1, and even display an inhibitory effect on GTPase activity. We show that LCACA-induced MiD oligomers activate DRP1. This activation is presumably induced by bringing GTPase domains in close proximity, which is a common activation mechanism for dynamin proteins in general[70,98,101]. The fact that MiDs display bi-phasic concentration effects on DRP1 activation, with activation reaching a peak and then declining at higher MiD oligomer concentrations, further suggests activation through inducing GTPase domain proximity.

DRP1 recruitment to and activation by oligomeric ‘receptors’ occurs in two other contexts: with MFF, which requires oligomerization through its coiled-coil[241]; and with actin filaments[69,241]. A

recent paper revealed the structure of 'cofilaments' assembled by DRP1 and MiD49 in the presence of GTP or non-hydrolyzable GTP analogues[245]. In this structure, monomeric MiD49 is bound around a core of DRP1, and GTP hydrolysis causes MiD49 release. It is unclear how the assembly of MiD49 oligomers might alter this interaction.

Another intriguing aspect of MiD effects on DRP1 is the ability of oligomerized MiD49 or MiD51 to synergize with MFF in DRP1 activation. MFF alone is a poor DRP1 activator, requiring high concentrations to stimulate DRP1 activity. Addition of a low concentration of MiD49 or MiD51 oligomers reduces the concentration of MFF required for DRP1 activation. We have observed a similar effect for actin filaments[241].

These results raise a model whereby either activation of MiD proteins (by increased LCACA) or polymerization of specific actin-based structures (through the polymerization factors INF2 or Spire1C[171,174]) might serve as initiating signals for DRP1 recruitment, with MFF working downstream. A previous study suggests that MFF preferentially binds DRP1 oligomers[222], supporting the model. This model might also suggest that MiDs and actin operate in distinct mitochondrial fission events, which is further supported by the lack of synergy between oligomerized MiDs and actin, as well as the potent inhibition of actin-mediated DRP1 activation by monomeric MiDs. While the possibility of actin and MiDs operating in distinct pathways has not been tested directly, a recent publication reveals two mechanistically distinct pathways to DRP1-dependent mitochondrial fission[29], one which is actin-dependent and one which is actin-independent. Interestingly, deletion of MiD49 and MiD51 partially reduces both types of fission in this study, suggesting that additional factors might be at play.

Another question pertains to the pools of LCACA that stimulate MiD activity in cells. LCACAs are involved in both anabolic (phospholipid and triacylglycerol synthesis) and catabolic (beta-oxidation) processes, in addition to being required for protein myristoylation and palmitoylation. In principle, processes involving LCACA on the mitochondrial surface, such as fatty acid import into mitochondria for beta-oxidation, would be the most likely candidates for MiD regulation. For fatty acid import, long chain fatty acids are first coupled to CoA in the cytoplasm, then converted to acyl-carnitine by carnitine O-palmitoyltransferase 1 (CPT1) on the outer mitochondrial membrane[246].

A recently published paper has established a correlation between increased mitochondrial fission and increased fatty acid oxidation, with the fission-activated step being CPT1[38]. A possible mechanism for fission-mediated CPT1 activation is through increased membrane curvature, facilitating intra-molecular interactions[247,248]. The results presented here, in combination with this recent publication, lead to a model whereby increased cytoplasmic fatty acid leads to increased fatty acyl-CoA, activating MiD proteins to trigger mitochondrial fission. Fission leads to CPT1 activation, increased fatty acid import and beta-oxidation (**Figure 3-8**), which could be used for ATP production (hepatocytes, pancreatic beta-cells, and oxphos-dependent B lymphoma cells [38]) or for heat generation (brown adipocytes [36]). Interestingly, a recent publication suggests that CPT1 might have a reciprocal effect, enhancing mitochondrial fission through succinylation-mediated stabilization of MFF[249].

MiD proteins are only found in metazoans, so it is unclear whether LCACA influences mitochondrial fission in non-metazoans. Interestingly, knocking out cytoplasmic acyl-CoA binding protein in *Schizosaccharomyces pombe* causes DRP1-dependent mitochondrial fission [250], implying that increasing levels of free acyl-CoA induces mitochondrial fission. The proteins mediating this effect remain to be elucidated.

The regulation of MiD49/51 adds to a growing list of LCACA regulatory functions. LCACAs are allosteric inhibitors of acetyl-CoA carboxylase (ACC), with this inhibition simultaneously decreasing fatty acid synthesis and relieving inhibition of CPT1 [244]. Interestingly, the basis for this inhibition might be in regulating ACC's oligomeric state[251]. Recently, LCACAs have also been shown to act as allosteric activators AMP-dependent kinase beta1, further inhibiting ACC [244]. All of these effects lead to more efficient mitochondrial fatty oxidation, and could act in a concerted fashion toward these goals.

3.5 Materials and Methods

Plasmids/siRNA. For bacterial expression, MiD49Δ1-124 (mouse amino acids 125-454, UniProt ID Q5NCS9) was inserted into a modified pGEX-KT vector by BamH1 and EcoR1 sites, in which a GST-thrombin site-6xHis-TEV tag is in front of multiple cloning site (MCS). MiD51Δ1-133 (human amino acids 134-463, UniProt ID Q9NQG6) was inserted into another modified pGEX-KT vector by BamH1 and EcoR1 sites, where a GST-thrombin site-6xHis-HRV3C-6xHis sequence is in front of MCS. Quick Change mutagenesis was performed to make MiD49 or MiD51 mutants. Full-length of human DRP1 isoform 3 (NP_055681.2, UniProt ID O00429-4) and truncated human MFF isoform 4 (UniProt ID Q9GZY8-4) (MFF-ΔTM) have been described previously [69,122]. For cellular assays, full length MiD49/51 and corresponding mutants were inserted into a modified GFP-N1 vector, in which the MCS is followed by HRV3C-GFP-2xStrep-tag. Mito-plum plasmid was obtained from Addgene (#55988). The following oligonucleotides used for siRNA-mediated protein silencing were synthesized by Integrated DNA Technologies: MiD49 (3'UTR Exon 4): 5'-AUUCUGACUUUGAAGCCUGUUAAGA-3'; MiD51 (3'UTR Exon 6): 5′-GAAGAGCUGUGAUAGCAUGUUUCAA-3'; DRP1 (CDS Exon 8): 5'-GCCAGCTAGATATTAACAACAAG AA-3′; silencer negative control (IDT) was 5′-CGUUAAUCGCGUAUAAUACGCGUAU-3′.

Protein Expression, Purification.

MiD49 and MiD51 was expressed in One Shot BL21 Star (DE3) *Escherichia coli* (C6010-03; Life Technologies, Carlsbad, CA) in LB broth, induced by isopropyl-β-D-thiogalactoside (IPTG) at 16 °C for 16 h when OD600 reached 1.5. Cell pellets were resuspended in MiD lysis buffer (25 mM 4-(2-hydroxyethyl)-1-piperazineethanesulfonic acid [Hepes], pH 7.4, 500 mM NaCl, 1 mM dithiothreitol [DTT], 2 μg/ml leupeptin, 10 μg/ml aprotinin, 2 μg/ml pepstatin A, 2 mM benzamidine, 1 μg/ml calpain inhibitor I [ALLN], and 1 μg/ml calpeptin) and lysed using a high-pressure homogenizer (M-110L Microfluidizer Processor; Microfluidics, Newton, MA). The lysate was cleared by centrifugation at 40,000 rpm (type 45 Ti rotor; Beckman, Brea, CA) for 1 hour at 4°C and then was loaded onto Pierce™ Glutathione Agarose (16101; Thermofisher) by gravity flow. The column was washed with 20 column volumes (CV) of lysis buffer without protease inhibitors. To elute MiD49/51, 1 unit/μL thrombin (T4648, Sigma-Aldrich) or 0.01 mg/ml HRV3C protease in lysis buffer without protease inhibitors was added for 16 hours at 4°C. The protein eluate was captured by HiTrap IMAC column (17-5248-01, GE Healthcare, Chicago, IL) and eluted by IMAC-B buffer (50 mM Tris-HCl pH 7.5, 0.1 M NaCl, 500 mM imidazole). The His-trap protein

eluate was further purified by size exclusion chromatography on Superdex200 (GE Biosciences, Piscataway, NJ) with S200 buffer (20 mM Hepes, pH 7.4, 65 mM KCl, 2 mM $MgCl_2$, 1 mM DTT, 0.5 mM ethylene glycol tetraacetic acid [EGTA]), spin concentrated (UFC903024, EMD Millipore Corporation, Burlington, MA), frozen in liquid nitrogen, and stored at −80 °C.

DRP1 was expressed and purified as previously described with modifications[69]. Briefly, DRP1 construct was expressed in One Shot BL21 Star (DE3) *Escherichia coli* in LB broth, induced by isopropyl-β-D-thiogalactoside (IPTG) at 16 °C for 16 hours when OD600 reached to 1.5. Cell pellets were resuspended in lysis buffer (100 mM Tris-Cl, pH 8.0, 500 mM NaCl, 1 mM dithiothreitol [DTT], 1 mM Ethylenediaminetetraacetic acid [EDTA], 2 µg/ml leupeptin, 10 µg/ml aprotinin, 2 µg/ml pepstatin A, 2 mM benzamidine, 1 µg/ml ALLN, and 1 µg/ml calpeptin) and lysed using a high-pressure homogenizer. The lysate was cleared by centrifugation at 40,000 rpm in Ti-45 rotor for 1 hour at 4°C. Avidin (20 µg/ml; PI-21128; Thermo Fisher Scientific, Waltham, MA) was added to the supernatant, and then was loaded onto Strep-Tactin Superflow resin (2-1206-025; IBA, Göttingen, Germany) by gravity flow. The column was washed with 20 column volumes (CV) of lysis buffer without protease inhibitors. To elute DRP1, 0.01 mg/ml HRV3C protease in lysis buffer without protease inhibitors was added for 16 hours at 4°C. The Strep-Tactin Superflow eluate was further purified by size exclusion chromatography on Superdex200 with DRP1-S200 buffer (20 mM HEPES pH 7.5, 150 mM KCl, 2 mM $MgCl_2$, 1 mM DTT, 0.5 mM EGTA), spin concentrated, frozen in liquid nitrogen, and stored at −80 °C.

MFF-ΔTM was expressed in Rosetta^{TM}2 BL21-(DE3) *Escherichia coli* (71400; EMD Millipore Corporation, Burlington, MA) in LB broth, induced by 1M IPTG at 30 °C for 4 h when OD600 reached to 1.5. Cell pellets were resuspended in lysis buffer (50 mM Tris-HCl, pH 7.5, 500 mM NaCl, 20 mM imidazole, pH 7.5, 1 mM DTT, 1 mM EDTA, 2 µg/ml leupeptin, 10 µg/ml aprotinin, 2 µg/ml pepstatin A, 2 mM benzamidine, 1 µg/ml ALLN, and 1 µg/ml calpeptin) and lysed using M-110 microfluidizer processor. The lysate was cleared by centrifugation at 40, 000 rpm in Ti45 for 40 minutes at 4°C, the supernatant was saved. Affinity capture was performed using FPLC and a HiTrap IMAC column (17-5248-01, GE Healthcare, Chicago, IL) equilibrated with IMAC-A buffer (50 mM Tris-HCl pH 7.5, 0.1 M NaCl, 20 mM imidazole). Cleared lysate was loaded onto the column with a rate of 3 mL/min and washed to baseline with IMAC-A. MFF was eluted from the column with gradient step washes by IMAC-B buffer (50 mM Tris-HCl pH 7.5, 0.1 M NaCl, 500 mM imidazole): step1 10% IMAC-B for 5CV, step2 20% IMAC-B for 5CV, step3 100% for 5CV. Fractions from step3 were pooled and diluted 10-fold in ion exchange (IEX)-A buffer (50

mM Tris-HCl pH 7.5, 1 mM DTT). Diluted fractions were loaded onto a HiTrap Q anion exchange column (54816, EMD Millipore Corporation, Burlington, MA). The column was washed to baseline with IEX-A and MFF was eluted by IEX-B buffer (50 mM Tris-HCl pH 7.5, 1 M NaCl, 1 mM DTT) with a step gradient: step1 10% 5CV, linear 10-50% 30CV followed by linear 50-100% 5CV. Peak MFF fractions were concentrated by reloading onto the HiTrap IMAC column and eluted with 100% IMAC-B step wash. MFF fractions were pooled and further purified by size exclusion chromatography on Superdex200 with S200 buffer (20 mM HEPES, pH 7.4; 2 mM $MgCl_2$, 0.5 mM EGTA, 65 mM KCl, 1 mM DTT), spin concentrated (UFC903024, EMD Millipore Corporation, Burlington, MA), aliquots were frozen in liquid nitrogen, and stored at −80 °C.

Rabbit skeletal muscle actin was extracted from acetone powder as previously described [237], and further gel-filtered on Superdex 75 16/60 columns (GE Healthcare). Actin was stored in G buffer (2 mM Tris, pH 8.0, 0.5 mM DTT, 0.2 mM ATP, 0.1 mM $CaCl_2$, and 0.01% NaN_3) at 4°C.

Actin preparation for biochemical assays

For high-speed pelleting assay, actin filaments were polymerized from 20 µM monomers for 3 h at 23 °C by addition of a 10x stock of polymerization buffer (200 mM HEPES, pH 7.4, 650 mM KCl, 10 mM $MgCl_2$, 10 mM EGTA) to a final 1x concentration. For GTPase assay, actin monomers in G-buffer were incubated with AG1-X2 100–200 mesh anion exchange resin (Dowex; 1401241; Bio-Rad) at 4 °C for 5 min to remove ATP, followed by low-speed centrifugation. 20 µM actin filaments were polymerized as described before. To maintain ionic strength across all samples, an actin blank was prepared in parallel using G-buffer in place of actin monomers and used to dilute actin filaments as needed for each sample. DRP1 was diluted in MEHD buffer (20 mM HEPES, pH 7.4, 2 mM $MgCl_2$, 0.5 mM EGTA, 1 mM DTT) to adjust the ionic strength to the same as S200 buffer before biochemical assays.

Size exclusion Chromatography assays.

MiD49Δ1-124 and MiD51Δ1-133 oligomeric distribution was determined by Superose 6 increase 10/300 GL SEC column (GE Biosciences) in S200 buffer (20 mM HEPES, pH7.4, 65 mM KCl, 2 mM $MgCl_2$, 0.5 mM EGTA, 1 mM DTT). Protein at varying concentration was loaded onto the column in a total volume of 500 µL and gel-filtered with a flow rate of 0.4 mL/min.

Purine-containing ligand screening and Blue-Native PAGE

Purine-containing ligands were incubated with MiD49 or MiD51 at 37 °C for 1 hour before BN-PAGE analysis. Ligands include: NADP+ (Sigma-Aldrich, 077K7000), NAD+ (Sigma-Aldrich, N1636), NADH (Sigma-Aldrich, 10107735001), c-di-AMP (Sigma-Aldrich, A3262), 2'3'-GAMP (Sigma-Aldrich, 1229), AMP (Sigma-Aldrich, 01930), ADP(Sigma-Aldrich, 01897), ATP (Sigma-Aldrich, A2383), GMP (Sigma-Aldrich, G8377), GDP (Sigma-Aldrich, G7127), GTP (Sigma-Aldrich, G8877), cAMP (Sigma-Aldrich, 1231), dNTP (New England Biolabs, N0447S), hypoxanthine (Sigma-Aldrich, H9377), stearoyl-CoA (Sigma-Aldrich, S0802), oleoyl-CoA (Sigma-Aldrich, O1012), palmitoyl-CoA (Sigma-Aldrich, P9716), myristoyl-CoA (Sigma-Aldrich, M4414), lauoryl-CoA (Sigma-Aldrich, L2659), octanoyl-CoA (Sigma-Aldrich, O6877), malonoyl-CoA (Sigma-Aldrich, 4263), acetyl-CoA (Sigma-Aldrich, A2056), coenzyme A (Sigma-Aldrich, C4282), lyso-PA (Avanti Polar Lipids, 857127P25MG), geranylgeranyl pyrophosphate (Sigma-Aldrich, G6025), palmitic acid (Sigma-Aldrich, P0500), palmityl-carnitine (Sigma-Aldrich, P1645). If not stated in the legend, concentrations were 500 μM ligand, 100 μM MiD49, and 50 μM MiD51.

MiD49 or MiD51 was incubated with ligand for 1hr at 37 °C for 1 hr in S200 buffer, then mixed with the Native PAGE Sample buffer (Thermo Fisher Scientific, catalog BN2003). The samples were separated on a NativePAGE Novex 3%–12% Bis-Tris protein gel system (Thermo Fisher Scientific, catalog BN1003BOX) according to the manufacturer's instructions. In brief, the electrophoresis was performed with 1× NativePAGE Running Buffer (Thermo Fisher Scientific, BN2001) and blue cathode buffer (containing 0.002% G-250). BN PAGE gel was destained in distilled water overnight, and band intensity was analyzed using ImageJ software.

GTPase assay

DRP1 (0.75 μM) was mixed with indicated concentrations of MiD49, 51, MFF and/or actin filaments in S200 buffer. Sample were incubated at 37 °C for 5 min. At this point, GTP was added to a final concentration of 500 μM to start the reaction at 37 °C. Reactions were quenched at designated time points by mixing 15 μL sample with 5 μL of 125 mM EDTA in a clear, flat-bottomed, 96-well plate (Greiner, Monroe, NC). Six time points were acquired for all conditions, either in a 12 min time range, or in a 45 min time range depending on reaction speed. Released phosphate was determined by addition of 150 μL of malachite green solution as previously described [69] Absorbance at 650 nm was measured 15 min after malachite green solution incubation. GTP hydrolysis rates were determined by plotting phosphate concentration as a function of time in the linear phase of the reaction.

Velocity Analytical Ultracentrifugation

Analytical ultracentrifugation was conducted using a Beckman Proteomelab XL-A and an AN-60 rotor. For sedimentation velocity analytical ultracentrifugation, MiD49/51 (5μM) in S200 buffer (65 mM KCl, 1 mM MgCl2, 0.5 mM EGTA, 1 mM DTT, 20 mM HEPES, pH 7.4) was centrifuged at either 5,000 (for oligomer) or 35,000 (for monomer) rpm with monitoring at 280 nm. Data analyzed by Sedfit to determine sedimentation coefficient, frictional ratio, and apparent mass. Sedimentation coefficient reported is that of the major peak (at least 80% of the total analyzed mass) at OD_{280}.

MANT-ADP assay

MANT-ADP assay was performed as previously described with modifications[124]. Fluorescence measurements of MANT-ADP (Sigma-Aldrich, 19511) were performed using a 96-well fluorescence plate reader (Infinite M1000; Tecan, Mannedorf, Switzerland) at room temperature in S200 buffer (65 mM KCl, 1 mM MgCl2, 0.5 mM EGTA, 1 mM DTT, 20 mM HEPES, pH 7.4). Samples were excited at 355 nm, and fluorescence emission was monitored at 448 nm. For titrations, MANT-nucleotide was held constant at 300 nM and the protein concentration was varied as indicated, measurements were conducted after 30 minutes incubation at room temperature.

High-speed pelleting assay

Interactions between DRP1, actin and MiD49 were tested in the S200 buffer; 1.3 μM DRP1, 1 μM actin, and 4 μM MFF were mixed as described and were incubated for 1 hr at room temperature in a 100 μl volume. After incubation, samples were centrifuged at 80,000 rpm for 20 min at 4°C in a TLA-100.1 rotor (Beckman). The supernatant was carefully removed. Pellets were washed three times with S200 buffer and then resuspended in 100 μl of SDS–PAGE sample buffer and resolved by SDS–PAGE (LC6025; Invitrogen, Carlsbad, CA). Gels were stained with Coomassie Brilliant Blue R-250 staining (1610400, Bio-Rad, Hercules, CA), and band intensity was analyzed using ImageJ software.

HPLC analysis of long-chain Acyl-CoA esters.

HPLC analysis was performed as previously described with modifications[252]. A Betasil C18 column (150 x 4.6 mm) from Thermo (0711365H; Thermo Fisher Scientific, Waltham, MA) was used. The two mobile-phase solvents were 25 mM KH_2PO_4, pH 5.3 (pump A) and acetonitrile (pump B). Column was equilibrated in 95% pump A/5% pump B at 2 mL/min. A discontinuous

gradient for elution of long-chain acyl-CoA esters was divided into four steps. Step 1: 95%/5% to 70%/30% over 5 min. Step 2: 70%/30% to 60%/40% over 2.5 min. Step 3: 60%/40% to 54%/46% over 4.5 min. Step 4: 54%/46% to 38%/62% over 2.5 min, then held for an additional 2.5 min at 38%/62% before re-equilibration by a 5 min reversed-flow gradient. The volume of the sample injected was 200 µL. The acyl-CoA esters were detected at. 260 nm. Quantitation was based on peak areas.

Phosphate Assay

Fractions from Superose 6 size exclusion chromatography were assayed for phosphate content as follows. The fraction (0.4 mL) was mixed with 0.1 mL of 70% perchloric acid (Sigma-Aldrich 244252) in a 13x100 mm glass tube, and heated to 190˚C for 20 min. After cooling, the following were added: 0.6 mL water, 0.25 mL molybdate solution (1.25% ammonium molybdate in 2.5 N sulfuric acid), and 0.06 mL Fiske-Subbarow reducer (Sigma-Aldrich 46345, 16% solution in water). Sample heated to 90˚C for 20 min. After cooling, absorbance at 820 nm recorded. Phosphate content determined against standard curve of sodium phosphate, and converted to coenzyme A content by dividing by 3. This assay provides linear detection of inorganic phosphate from 1.5-40 nmole, and displays near-100% detection of known amounts of palmitoyl-CoA.

Negative-stain transmission electron microscopy

Negative-stain TEM grids of purified MiD49 and MiD51 were prepared following an established protocol[253]. Briefly, 4ul of the sample at a concentration range of 0.1 – 0.4 mg/ml was applied to a glow-discharged 400 mesh copper grid coated with a continuous thin carbon film (prepared in house), blotted with filter paper, and then stained with freshly prepared 0.75% (w/v) uranyl formate. Grids were visualized at room temperature using a Tecnai T12 Spirit (FEI) equipped with an AMT 2k x 2k side-mounted CCD camera and operated at a voltage of 100 kV. Images were recorded at a nominal magnification range of 120,000-150,000x at the sample level with a calibrated pixel size range of 5.28-4.22 Å per pixel. Particle dimensions were measured by cropping 150x150 nm boxes from the original fields, and then determining the length of the longest and shortest axis for each particle manually. For critical micelle concentration calculation of palmitoyl-CoA from negative stain micrographs, we used a linear regression technique similar to that used to calculate the critical polymerization concentration for actin[254]. The numbers of particles per 800x800 nm field were counted for 3-5 fields over a range of palmitoyl-CoA concentrations. A fit of the data points between 125 and 1000 mM palmitoyl-CoA results an X-intercept at 47 mM palmitoyl-CoA, after

subtracting the background particle number in the absence of palmitoyl-CoA (8.2 particles/field, presumably debris).

Cell culture and transfections

Human cervical cancer HeLa cells were purchased from ATCC (CCL-2) and grown in DMEM (Corning; 10-013-CV) supplemented with 10% fetal bovine serum (F4135; Sigma). Cells were cultivated at 37°C with 5% CO_2. For plasmid transfections, cells were seeded at 4×10^5 cells per 35 mm well 24 h before transfection. Transfections were performed in OPTI-MEM medium (Life Technologies; 31985062) with 2 µl of Lipofectamine 2000 (Invitrogen; 11668) per well for 6 h, followed by trypsinization and replating onto coverslips or glass-bottomed dishes (MatTek Corporation; P35G-1.5-14-C) at a cell density of ~2×10^5 cells per well. For MiD51 plasmid transfections carried out in wildtype HeLa cells 50 ng of each plasmid were transfected, respectively. For live-cell time-lapse acquisition, 100 ng of mito-plum were co-transfected with 50 ng of the respective MiD49 or 51 constructs.

For siRNA transfections, 1×10^5 cells for control knockdown and 1.5 x 10^5 cells for MiD49/51 or DRP1 knockdown were plated on 6-well plates, and 2 µl RNAi max (Invitrogen; 13778) and 63 pmol of each siRNA was used per well. Since MiD51 constructs were not sequence-modified for RNAi-resistance, 150 ng of the respective GFP-tagged MiD51 plasmids were used in MiD49/51 siRNA-treated cells. For these rescue experiments, siRNA-treated cells were transfected with 150 ng of respective MiD51 plasmids and 2 µl Lipofectamine 2000 ~48 h after siRNAs have been transfected. Overall, cells were fixed and analyzed 72 h post siRNA-transfection.

Western blotting and antibodies

For preparation of whole-cell extracts, confluent cell layers in 35 mm dishes were washed 3× with phosphate-buffered saline (PBS), lysed using ~350 µl of 1×DB (50 mM Tris-HCl, pH 6.8, 2 mM EDTA, 20%glycerol, 0.8% SDS, 0.02% bromophenol blue, 1000 mM NaCl, 4 M urea), and boiled for 5 min at 95°C, and genomic DNA was sheared using a 27×G needle. Proteins were separated by standard SDS-PAGE and transferred to a PVDF (polyvinylidine difluoride) membrane (Millipore). The membrane was blocked with TBS-T (20 mM Tris-HCl, pH 7.6, 136 mM NaCl, and 0.1% Tween-20) containing 3% bovine serum albumin for 1 h and then incubated with the primary antibody solution at 4°C overnight. Primary antibodies used were as follows: MiD51 (rabbit; 20164-1-AP; Proteintech; 1:1000), GFP (rabbit, self-made,1:1000), DRP1 (mouse; 611112; BD Transduction Laboratories; 1:1000), GAPDH (G-9, mouse; Santa Cruz Biotechnology; 1:500), actin (mouse; mab1501R; Millipore; 1:1000), tubulin (DM1-α, mouse; T9026; Sigma; 1:10,000).

After being washed with TBS-T, the membrane was incubated with horseradish peroxidase (HRP)-conjugated secondary antibodies (goat anti mouse #1721011; Bio-Rad or goat anti rabbit #1706515; BioRad) for 1 h at room temperature. Chemiluminescence signals were detected upon incubation with ECL Prime Western Blotting Detection Reagent (45-002-40; Cytiva Amersham) and recorded with an ECL Chemocam imager (SYNGENE G:BOX Chemi XRQ). For LI-COR Western blots, membranes were incubated with either IRDye 680 goat anti-mouse (926-68070; LI-COR), IRDye 800CW goat anti-rabbit (926-32211; LI-COR), or IRDye 680 donkey anti-chicken (926-68075) secondary antibodies for 1 h at room temperature. Signals were detected using the LI-COR Odyssey CLx imaging system.

Immunofluorescence staining

For immunolabeling of proteins of interest, cells were seeded subconfluently on fibronectin (F1141; Sigma)-coated (1:100 in PBS) coverslips (72222-01; Electron Microscopy Sciences) in 35 mm dishes and allowed to spread overnight. On the following day, cells were fixed in pre-warmed 4% paraformaldehyde (PFA; 15170; Electron Microscopy Sciences) in PBS for 20 min followed by three PBS washes. Then, cells were permeabilized with 0.1% Triton X-100 in PBS for 1 min and washed 3x with PBS. Before antibody staining, cells were blocked with 10% calf serum in PBS for ∼30 min. Primary antibodies were diluted in 1% calf serum in PBS and incubated for 1 h. Mitochondria were visualized using a primary antibody against the OMM protein Tom20 (rabbit; ab78547; Abcam; 1:200). DRP1 was stained using DRP1 primary antibody (mouse; 611112; BD Transduction Laboratories; 1:50). Coverslips were washed several times in PBS and incubated with secondary antibody solution for 45 min. Either anti-rabbit Texas Red (TI-1000; Vector Laboratories; 1:300), anti-mouse Texas Red (TI-2000; Vector Laboratories; 1:300) or anti-rabbit Alexa Fluor 405 (A31556; Invitrogen; 1:300) were used as secondary antibodies. Coverslips were washed in PBS and fixed on glass slides using ProLong Gold antifade mounting media (P36930; Invitrogen).

2-bromopalmitate treatment

A 100 mM stock of 2-bromopalmitic acid (2-BP, Sigma-Aldrich 248422) or methyl-palmitate (MP, Sigma-Aldrich P5177) was made in DMSO, and diluted to 150 μM in DMEM+10% fetal bovine serum that had been pre-equilibrated overnight to 37˚C/5% CO_2 immediately prior to use. HeLa cells (80-90% confluent) were treated for 1 hr with this 150 μM 2-BP stock or MP as control. Cells were then fixed and stained as indicated above.

Confocal microscopy

Imaging was performed on a Dragonfly 302 spinning-disk confocal (Andor Technology) on a Nikon Ti-E base and equipped with an iXon Ultra 888 EMCCD camera, and a Zyla 4.2 Mpixel sCMOS camera, and a Tokai Hit stage-top incubator was used. A solid-state 405 smart diode 100-mW laser, solid-state 488 OPSL smart laser 50-mW laser, solid-state 560 OPSL smart laser 50-mW laser, and a solid-state 637 OPSL smart laser 140-mW laser were used (objective: 100 × 1.4 NA CFI Plan Apo; Nikon). Images were acquired using Fusion software (Andor Technology). Live-cell imaging was performed in DMEM (21063-029; Life Technologies) with 25 mM D-glucose, 4 mM D-glutamine, and 25 mM HEPES, supplemented with 10% FBS (F4135; Sigma) on glass-bottomed dishes (MatTek Corporation; P35G-1.5-14-C).

Analysis of MiD51 localization patterns on mitochondria

HeLa WT cells were transfected with 50 ng of either GFP-tagged MiD51 WT or various MiD51 mutants harboring a single amino acid exchange within their putative acyl-CoA binding pocket. After ~6 h of transfection, cells were plated on fibronectin-coated coverslips, fixed and stained for Tom20 on the following day. GFP-fusion expression level was assessed by the detectability of GFP signal upon short (<100 msec, <50% laser power) or long (500 msec, 100% laser power) exposure, binning cells into high expression and low expression categories, respectively. Cells were classified in a blinded manner. For low expression, classification was for GFP pattern on mitochondria (punctate or non-punctate). For high expression, classification was for mitochondrial morphology (elongated, collapsed). Respective fractions of cells [%] were plotted in a stacked bar graph. Results combine three independently performed replicates of this experiment.

To assess the different localization patterns of MiD51 constructs in a more quantitative manner, the % coverage of the mitochondrial surface by GFP signal, as well as the average size of the GFP signal on the mitochondrion, were determined using ImageJ. 20 μm^2-sized ROIs with representative MiD51 localization were auto-thresholded for the Tom20 staining and converted to binary masks. GFP signals were first processed by background subtraction using ImageJ (math → subtract → value: 500), then converted to a binary mask. Binary images were analyzed using the "analyze particles" tool with settings as follows: size (pixel2) 0.05–infinity, circularity 0.00–1.00. MiD51: Mito area ratios [%] as well as MiD51 average sizes [μm^2] were plotted as box-and-whiskers plots using Microsoft Excel. Data corresponds to three independent experiments.

Mitochondrial area quantification

Cells were silenced for both MiD49 and MiD51 and compared to cells treated with a scrambled siRNA. 48 h after siRNA transfections, cells were transfected with 150 ng of GFP-tagged MiD51

construct. Transfected cells were re-plated onto fibronectin-coated coverslips, fixed and stained for Tom20 on the following day. To avoid adverse effects of high MiD51 expression on mitochondria morphology, only cells with low expression levels were used for mitochondrial area analysis (requiring 500 msec exposure with 100% power of the 488 nm laser for GFP detection). For mitochondrial area quantifications, a 20 μm^2-sized ROI of resolvable mitochondria (Tom20 signal) was selected, auto-thresholded, converted to a binary mask and analyzed using the "analyze particles" plug-in in ImageJ to obtain the number of mitochondrial fragments and the area of each fragment per ROI. The data shown as mean mitochondrial area in μm^2 was plotted in a bar graph combining the results of four biological replicates.

HeLa cells, treated with siRNAs for either DRP1, MiD49/51 or containing a scrambled sequence, were plated on fibronectin-coated coverslips, and treated with growth medium containing either 150 µM 2-BP or MP for 1 h. Afterwards, cells were washed, fixed, stained and subjected to mitochondrial area measurements essentially as described above.

Quantification of mitochondrially-associated DRP1 puncta

HeLa cells knocked down for MiD49/51 with or without re-expression of MiD51 constructs were analyzed for DRP1 recruitment to mitochondria as well as DRP1 puncta size. Cells were fixed and stained for endogenous DRP1 in combination with Tom20. 20 μm^2-sized ROIs containing resolvable mitochondria in spread cell areas were thresholded using the same contrast settings for the Tom20 staining. DRP1 stainings were first processed by background subtraction using ImageJ (math → subtract → value: 1500), then converted to an 8-bit image. To determine DRP1 recruitment to mitochondria, DRP1 fluorescence signals overlapping with corresponding Tom20 staining were measured using the ImageJ "Colocalization" plug-in with the following parameters: ratio 40% (0–100%), threshold channel 1: 50 (0–255), threshold channel 2: 50 (0–255), display value (0–255): 255. Colocalized pixels were then converted to a binary mask and analyzed using the "analyze particles" tool with settings as follows: size (pixel2) 0.05–infinity, circularity 0.00–1.00. DRP1: Mito area ratios [%] were plotted as box-and-whiskers plots using Microsoft Excel. Furthermore, average DRP1 puncta size [μm^2] was determined from these binary masks using the "analyze particles" plug-in. Three independent experiments were performed.

Data processing and statistical analyses

For biochemical assays, numerical data were processed and assembled with Kaleidagraph (Synergy Software) and Photoshop CS4 (Adobe). Data analyses were carried out in ImageJ and Excel 2010 (Microsoft). Statistical comparisons were performed with GraphPad Prism 6.01 (Dotmatics) using unpaired t test. A probability of error of 5% ($p \leq 0.05$; * in figure panels) was considered to indicate statistical significance; **, ***, **** indicated p values ≤ 0.01, 0.001, and 0.0001, respectively.

For imaging data, brightness and contrast levels were adjusted using ImageJ software. Figures were further processed and assembled with Photoshop CS4. Data analyses were carried out in ImageJ and Microsoft Excel. All statistical analyses and p-value determinations were done using GraphPad Prism 6.01. Data sets were either compared using an unpaired Student's t-test or a One-way Anova multiple comparisons (Dunnett's) test, as indicated in respective figures. A probability of error of 5% ($p \leq 0.05$; * in figure panels) was considered to indicate statistical significance. **, ***, and **** indicate p values ≤ 0.01, ≤0.001, and ≤0.0001, respectively.

Figures

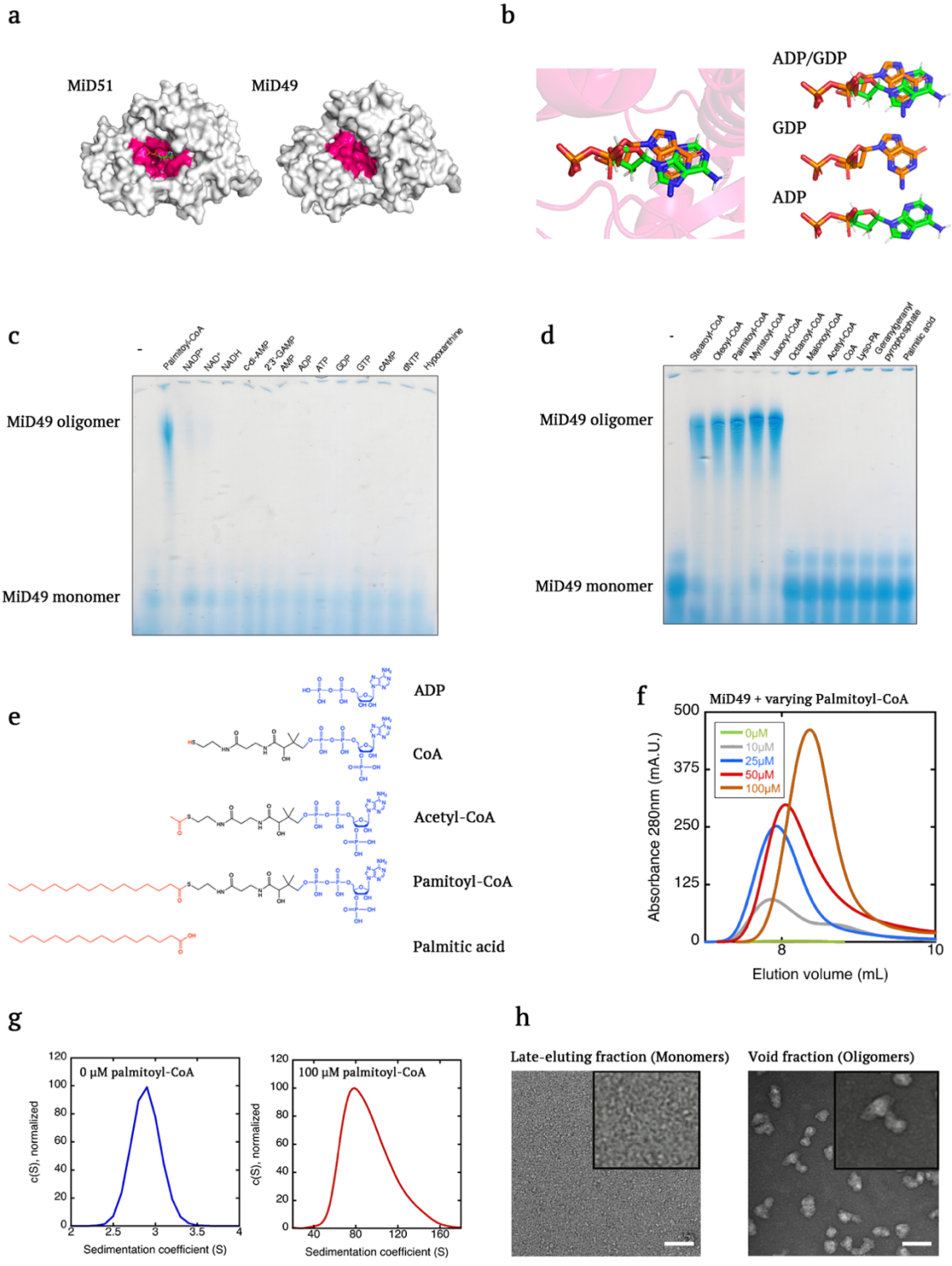
a
MiD51
MiD49
b
ADP/GDP
GDP
ADP
c
-
Palmitoyl-CoA
NADP+
NAD+
NADH
c-di-AMP
2'3'-cGAMP
AMP
ADP
ATP
GDP
GTP
cNMP
dNTP
Hypoxanthine
MiD49 oligomer
MiD49 monomer
d
-
Stearoyl-CoA
Oleoyl-CoA
Palmitoyl-CoA
Myristoyl-CoA
Lauroyl-CoA
Octanoyl-CoA
Malonyl-CoA
Acetyl-CoA
CoA
Lyso-PA
Geranylgeranyl pyrophosphate
Palmitic acid
MiD49 oligomer
MiD49 monomer
e
ADP
CoA
Acetyl-CoA
Pamitoyl-CoA
Palmitic acid
f
MiD49 + varying Palmitoyl-CoA
0μM
10μM
25μM
50μM
100μM
Absorbance 280nm (mA.U.)
Elution volume (mL)
g
0 μM palmitoyl-CoA
100 μM palmitoyl-CoA
c(S), normalized
Sedimentation coefficient (S)
h
Late-eluting fraction (Monomers)
Void fraction (Oligomers)

Figure 3-1: Long-chain acyl CoA induces MiD49 oligomerization.

A) Surface model of human MiD51 with bound ADP (PDB 4NXW, left) and murine MiD49 without bound ligand (PDB 4WOY, right). Residues lining the binding pocket in pink.

B) Configurations of ADP and GDP bound to human MiD51, from PDB 4NXW and 4NXX.

C) Blue-native gel electrophoresis of MiD49 cytoplasmic region (100 μM) mixed with 500 μM of the indicated purine-containing compounds.

D) Blue-native gel electrophoresis of MiD49 cytoplasmic region (100 μM) mixed with 500 μM of the indicated molecule.

E) Bond-line formulas comparing ADP, CoA, acetyl-CoA, palmitoyl-CoA and palmitate.

F) Size exclusion chromatography of MiD49 (100 μM) incubated with the indicated concentrations of palmitoyl-CoA. Peak shown is near the void volume of the Superose 6 column, indicative of a high molecular weight species. Full chromatogram in Figure S3-1c.

G) Velocity analytical ultracentrifugation of peak fractions from Superose 6 size exclusion chromatography of MiD49 cytoplasmic region (100 μM) incubated without or with palmitoyl-CoA (100 μM). Sedimentation coefficients shown (2.9 and 82 S for 0 and 100 μM palmitoyl-CoA, respectively). C(S) normalized to the maximum peak value. Figure S3-1d shows molecular mass conversion.

H) Negative stain electron microscopy of the void fraction from the 50 μM palmitoyl-CoA condition or the late-eluting fraction from the 0 μM palmitoyl-CoA condition from panel F. Scale bar, 150 nm.

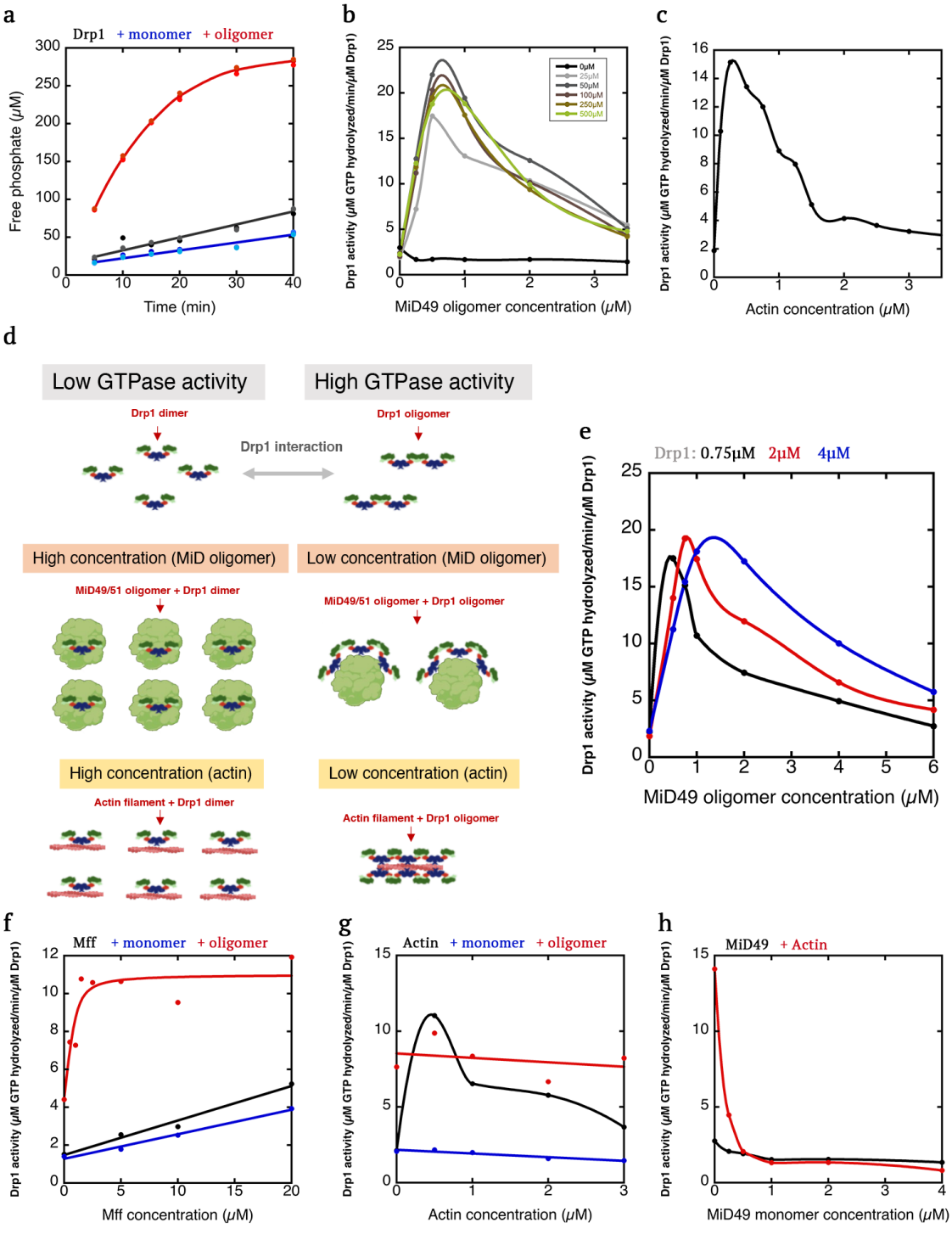
a
Drp1 + monomer + oligomer
Free phosphate (μM)
Time (min)
b
Drp1 activity (μM GTP hydrolyzed/min/μM Drp1)
0μM
25μM
50μM
100μM
250μM
500μM
MiD49 oligomer concentration (μM)
c
Drp1 activity (μM GTP hydrolyzed/min/μM Drp1)
Actin concentration (μM)
d
Low GTPase activity
High GTPase activity
Drp1 dimer
Drp1 oligomer
Drp1 interaction
High concentration (MiD oligomer)
Low concentration (MiD oligomer)
MiD49/51 oligomer + Drp1 dimer
MiD49/51 oligomer + Drp1 oligomer
High concentration (actin)
Low concentration (actin)
Actin filament + Drp1 dimer
Actin filament + Drp1 oligomer
e
Drp1: 0.75μM 2μM 4μM
Drp1 activity (μM GTP hydrolyzed/min/μM Drp1)
MiD49 oligomer concentration (μM)
f
Mff + monomer + oligomer
Drp1 activity (μM GTP hydrolyzed/min/μM Drp1)
Mff concentration (μM)
g
Actin + monomer + oligomer
Drp1 activity (μM GTP hydrolyzed/min/μM Drp1)
Actin concentration (μM)
h
MiD49 + Actin
Drp1 activity (μM GTP hydrolyzed/min/μM Drp1)
MiD49 monomer concentration (μM)

Figure 3-2: LCACA-induced MiD49 oligomers activate Drp1 in a synergistic manner with Mff.

A) Drp1 GTPase assays (0.75 μM Drp1) alone (black points) or in the presence of 0.5 μM MiD49 oligomers (red) or monomers (blue). MiD49 oligomers from the 50 μM palmitoyl-CoA condition described in panel B.

B) Effect of varying concentrations of MiD49 oligomers (assembled from mixtures of 100 μM MiD49 and varying concentrations of palmitoyl-CoA (given in μM)) on Drp1 GTPase activity (0.75 μM Drp1). Concentration effect of MiD49 monomers also shown.

C) Effect of varying concentrations of actin filaments on Drp1 GTPase activity (0.75 μM Drp1).

D) Schematic diagram of effect of MiD49 oligomers or actin filaments on Drp1 activity. At low concentration, MiD49 oligomers or actin filaments cause close juxtaposition of bound Drp1, allowing interaction between G domains and higher GTPase activity. At high concentration, Drp1 molecules are no longer juxtaposed, so that increased GTPase activity does not occur.

E) Effect of varying concentrations of MiD49 oligomers (assembled from mixtures of 100 μM MiD49 and 50 μM palmitoyl-CoA) on Drp1 GTPase activity at 0.75, 2 and 4 μM Drp1.

F) Effect of varying concentrations of Mff on Drp1 GTPase activity (0.75 μM Drp1) in the absence or presence of 250 nM MiD49 oligomers (red) or monomers (blue). Full curve to 100 μM Mff shown in Extended Data 5c.

G) Effect of varying concentrations of actin filaments on Drp1 GTPase activity (0.75 μM Drp1) in the absence (black) or presence of 100 nM MiD49 oligomers (red) or monomers (blue).

H) Effect of varying concentrations of MiD49 monomers on Drp1 GTPase activity (0.75 μM Drp1) in the absence (black) or presence (red) of 500 nM actin filaments.

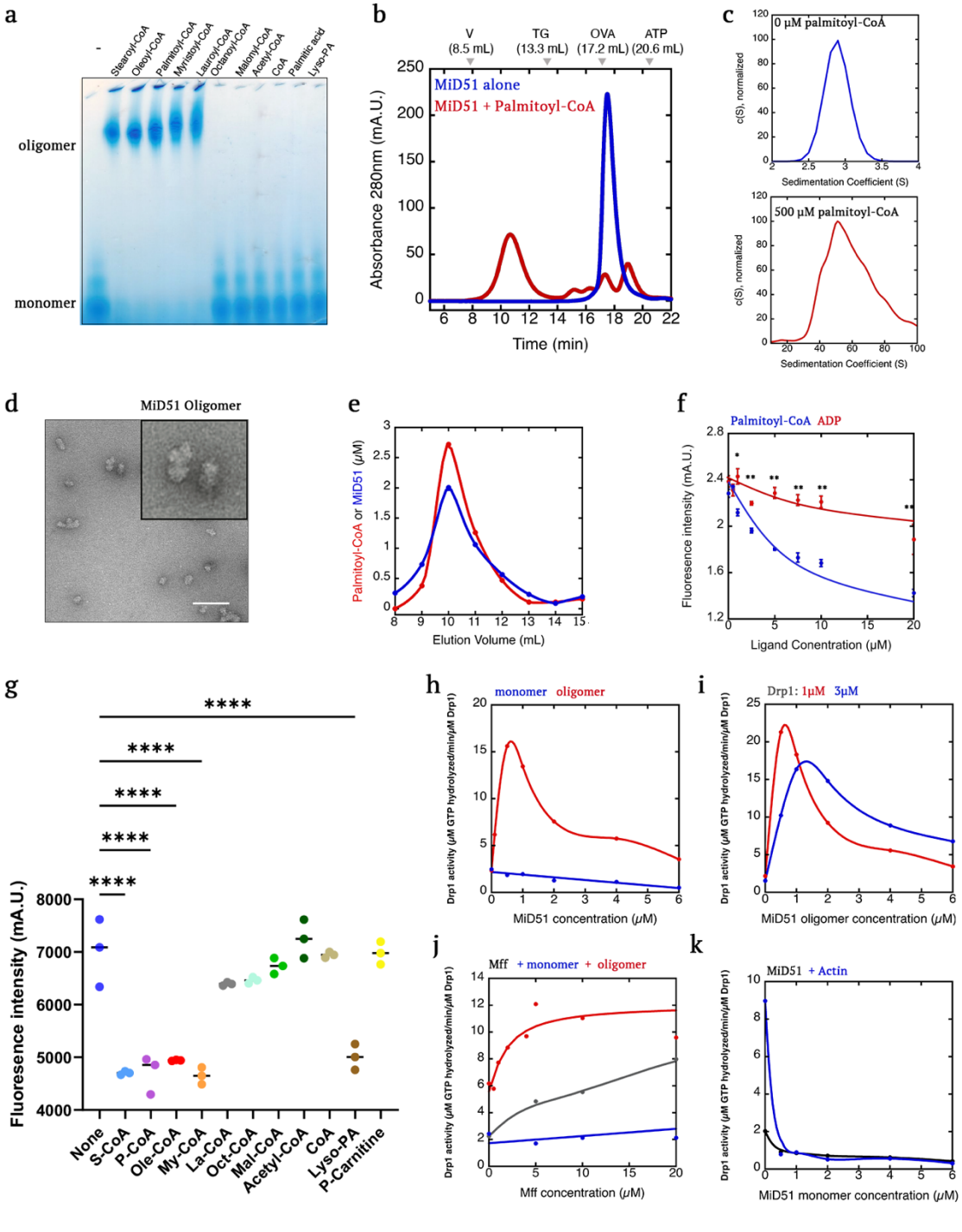
a
-
Stearoyl-CoA
Oleoyl-CoA
Palmitoyl-CoA
Myristoyl-CoA
Lauroyl-CoA
Octanoyl-CoA
Malonyl-CoA
Acetyl-CoA
CoA
Palmitic acid
Lyso-PA
oligomer
monomer
b
V (8.5 mL)
TG (13.3 mL)
OVA (17.2 mL)
ATP (20.6 mL)
MiD51 alone
MiD51 + Palmitoyl-CoA
Absorbance 280nm (mA.U.)
Time (min)
c
0 μM palmitoyl-CoA
500 μM palmitoyl-CoA
c(S), normalized
Sedimentation Coefficient (S)
d
MiD51 Oligomer
e
Palmitoyl-CoA or MiD51 (μM)
Elution Volume (mL)
f
Palmitoyl-CoA ADP
Fluoresence intensity (mA.U.)
Ligand Conentration (μM)
g
****
Fluoresence intensity (mA.U.)
None
S-CoA
P-CoA
Ole-CoA
My-CoA
La-CoA
Oct-CoA
Mal-CoA
Acetyl-CoA
CoA
Lyso-PA
P-Carnitine
h
monomer oligomer
Drp1 activity (μM GTP hydrolyzed/min/μM Drp1)
MiD51 concentration (μM)
i
Drp1: 1μM 3μM
MiD51 oligomer concentration (μM)
j
Mff + monomer + oligomer
Mff concentration (μM)
k
MiD51 + Actin
MiD51 monomer concentration (μM)

Figure 3-3: MiD51 oligomerizes in the presence of long-chain acyl-CoA.

A) Blue-native gel electrophoresis of MiD51 cytoplasmic region (50 μM) alone or in the presence of 500 μM of the indicated molecules.

B) Size-exclusion chromatography (Superose 6) of MiD51 (50 μM) alone or in the presence of 500 μM palmitoyl-CoA.

C) Velocity analytical ultracentrifugation of the MiD51 oligomer peak from panel B (left) and the un-treated MiD51 monomer (right). MiD51 polypeptide concentration 5 μM in both cases. Calculated mass distribution shown in Figure S3-6c.

D) Negative-stained electron micrograph of a representative particle from the MiD51 oligomer peak from panel B. More examples in Figure S3-2.

E) Quantification of palmitoyl-CoA (phosphate assay) and MiD51 (Bradford assay) concentrations across the oligomer peak from panel b.

F) MANT-ADP competition assay in which 300 nM MANT-ADP and 1 μM MiD51 are mixed with varying concentrations of palmitoyl-CoA (blue) or ADP (red) and the fluorescence intensity monitored.

G) MANT-ADP competition assays in which 300 nM MANT-ADP and 1 μM MiD51 are mixed with 20 μM of the indicated molecule and the fluorescence intensity monitored. S-, P-, O-, M-, L-, Oct- and Mal- indicate stearoyl, palmitoyl, oleoyl, myristoyl, lauroyl-, octanoyl-, and malonyl-, respectively.

H) Effect of varying concentrations of MiD51 oligomers on Drp1 GTPase activity (0.75 μM Drp1). Concentration effect of MiD51 monomers also shown.

I) Similar experiment to that in Panel B, using two concentrations of Drp1, 1 μM and 3 μM.

J) Effect of varying concentrations of Mff on Drp1 GTPase activity (0.75 μM Drp1) in the absence (gray) or presence of 100 nM MiD51 oligomers (red) or monomers (blue).

K) Effect of varying concentrations of MiD51 monomers on Drp1 GTPase activity (0.75 μM Drp1) in the absence (black) or presence (blue) of 500 nM actin filaments. *, **, *** and **** denotes p value of ≤ 0.05, ≤ 0.01, ≤ 0.001 respectively, by ANOVA (Dunnett's multiple comparisons) test. p value > 0.05 is not indicated in the figure.

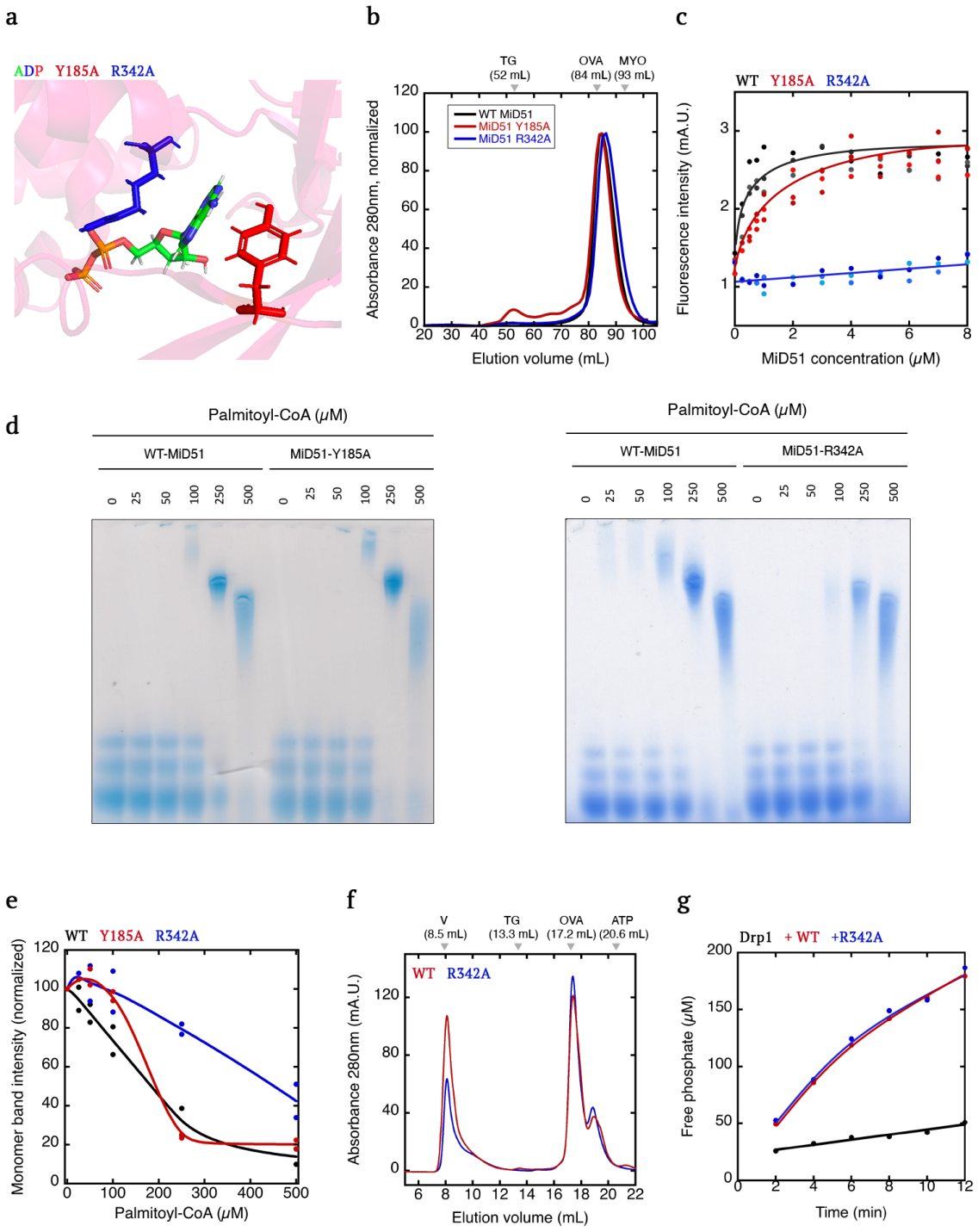
a
ADP Y185A R342A
b
TG (52 mL)
OVA (84 mL)
MYO (93 mL)
WT MiD51
MiD51 Y185A
MiD51 R342A
Absorbance 280nm, normalized
Elution volume (mL)
c
WT Y185A R342A
Fluorescence intensity (mA.U.)
MiD51 concentration (μM)
d
Palmitoyl-CoA (μM)
WT-MiD51
MiD51-Y185A
0 25 50 100 250 500
Palmitoyl-CoA (μM)
WT-MiD51
MiD51-R342A
0 25 50 100 250 500
e
WT Y185A R342A
Monomer band intensity (normalized)
Palmitoyl-CoA (μM)
f
V (8.5 mL)
TG (13.3 mL)
OVA (17.2 mL)
ATP (20.6 mL)
WT R342A
Absorbance 280nm (mA.U.)
Elution volume (mL)
g
Drp1 + WT +R342A
Free phosphate (μM)
Time (min)

Figure 3-4: Mutation of R342 in MiD51 reduces LCACA-induced oligomerization.

A) Model of human MiD51 with bound ADP (PDB 4NXW), showing the positions of R342 and Y185.

B) Superdex 200 size exclusion chromatograms from the bacterial preparations of MiD51-WT, MiD51-R342A and MiD51-Y185A. Marker positions shown for: TG, thyroglobulin (660 kDa); OVA, ovalbumin (43 kDa); myoglobulin (17 kDa).

C) MANT-ADP binding assay in which 300 nM MANT-ADP is mixed with the indicated concentrations of MiD51-WT, MiD51-R342A or MiD51-Y185A, and the fluorescence change monitored.

D) Blue-native gel electrophoresis of MiD51-WT, MiD51-R342A or MiD51-Y185A (50 μM) mixed with varying concentrations of palmitoyl-CoA.

E) Graph of density of the MiD51 monomer band as a function of palmitoyl-CoA concentration, from the blue-native gels such as in panel B (two independent gels for each construct).

F) Superose 6 size exclusion chromatography of 50 μM MiD51-WT or MiD51-R342A mixed with 250 μM palmitoyl-CoA. Oligomer and monomer peaks indicated.

G) Drp1 GTPase assays containing Drp1 alone (0.75 μM, black points) or in the presence of 2 μM MiD51-WT (red) or MiD51-R342A (blue).

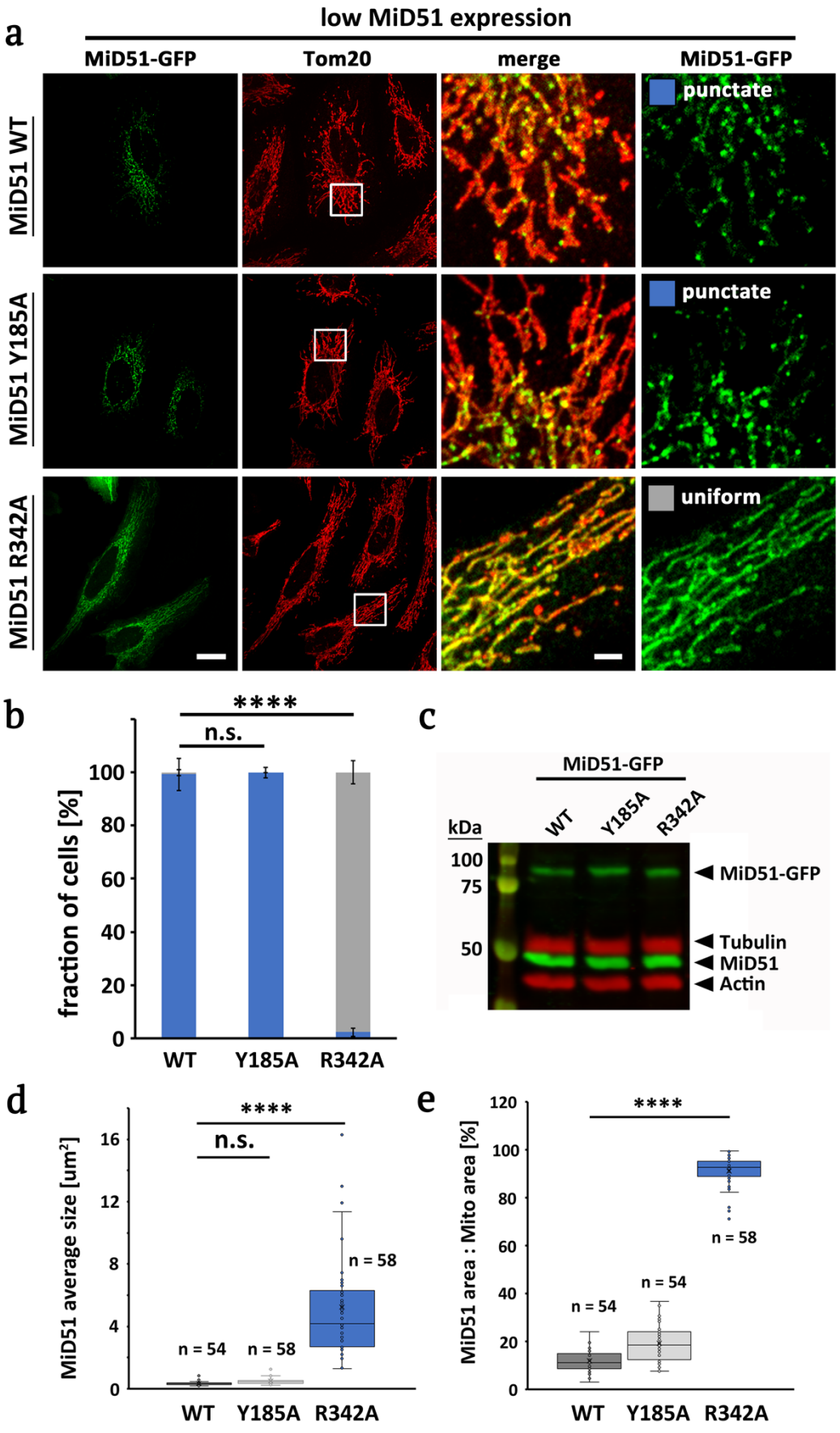
a
low MiD51 expression
MiD51-GFP
Tom20
merge
MiD51-GFP
MiD51 WT
MiD51 Y185A
MiD51 R342A
punctate
punctate
uniform
b
****
n.s.
fraction of cells [%]
100
80
60
40
20
0
WT
Y185A
R342A
c
MiD51-GFP
kDa
WT
Y185A
R342A
100
75
50
MiD51-GFP
Tubulin
MiD51
Actin
d
****
n.s.
MiD51 average size [um²]
16
12
8
4
0
n = 54
n = 58
n = 58
WT
Y185A
R342A
e
****
MiD51 area : Mito area [%]
120
100
80
60
40
20
0
n = 54
n = 54
n = 58
WT
Y185A
R342A

Figure 3-5: Effect of LCACA binding mutant on ability of MiD51 to form puncta in cells.

A) GFP fusion constructs of MiD51-WT, MiD51-Y185A or MiD51-R342A were transiently transfected into HeLa cells, then cells were fixed and stained for mitochondria (Tom20). Low-expressing cells shown here (requiring 500 msec exposure at 100% laser power for GFP). Boxed regions denote insets shown in merges to the right of full images. Scale bars, 20 mm in full images and 3 mm in insets.

B) Bar graph illustrating % cells displaying punctate (blue) or uniform (gray) mitochondrial GFP pattern for low-expressing cells. Representative examples of respective phenotypes are shown on the right. Scale bar is 10 mm. N = 276, 266, and 281 cells analyzed for MiD51 WT, Y185A, R342A, respectively. **** denotes p value of ≤ 0.0001 by ANOVA (Dunnett's multiple comparisons) test. n.s. = not significant (p value > 0.05).

C) Western blot showing expression levels of GFP-fusion constructs, versus endogenous MiD51 using anti-MiD51 (green). Actin and tubulin levels in red.

D) Box and whiskers plot of average MiD51 puncta size for MiD51-WT, MiD51-Y185A and MiD51-R342A. Number of cells analyzed per condition denoted by n. **** indicates a p value of ≤ 0.0001 and n.s. (not significant) corresponds to p > 0.05 by ANOVA (Dunnett's multiple comparisons) test.

E) Box and whiskers plot of % mitochondrial area covered by MiD51 staining, for MiD51-WT, MiD51-Y185A and MiD51-R342A. Number of cells analyzed per condition denoted by n. **** indicates a p-value of ≤ 0.0001 by ANOVA (Dunnett's multiple comparisons) test.

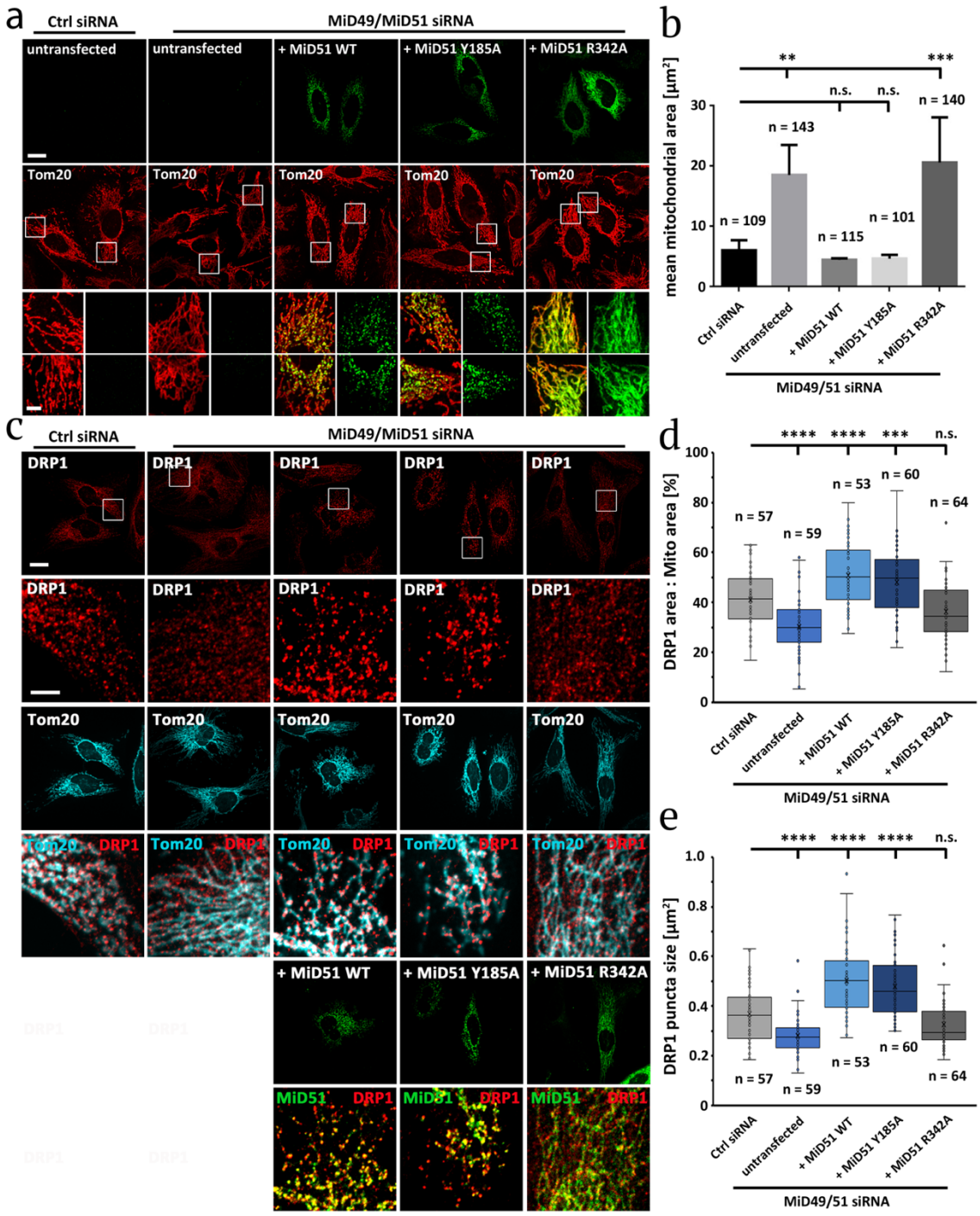
a
Ctrl siRNA
MiD49/MiD51 siRNA
untransfected
untransfected
+ MiD51 WT
+ MiD51 Y185A
+ MiD51 R342A
Tom20
b
mean mitochondrial area [µm²]
**
***
n.s.
n.s.
n = 109
n = 143
n = 115
n = 101
n = 140
Ctrl siRNA
untransfected
+ MiD51 WT
+ MiD51 Y185A
+ MiD51 R342A
MiD49/51 siRNA
c
DRP1
Tom20
MiD51
d
DRP1 area : Mito area [%]
****
****
***
n.s.
n = 57
n = 59
n = 53
n = 60
n = 64
e
DRP1 puncta size [µm²]
****
****
****
n.s.
n = 57
n = 59
n = 53
n = 60
n = 64

Figure 3-6: Effect of LCACA binding defect on ability of MiD51 re-expression to rescue mitochondrial elongation caused by MiD49/51 suppression.

A) C-terminal GFP fusion constructs of MiD51-WT, MiD51-Y185A or MiD51-R342A were transiently transfected into HeLa cells that had been previously treated with siRNAs against MiD49 and MiD51. Cells were then fixed and stained for mitochondria (Tom20). Cells displaying low GFP levels were imaged. Boxed regions denote insets shown in zoom to the right of full images. Zoom images either display MiD51-GFP signal alone or as corresponding merge image with Tom20. Scale bars, 20 mm in overview images and 5 mm in inset images.

B) Graph of mean mitochondrial area, determined as described in Methods, under the indicated conditions. N represents the number of cells analyzed per respective condition. ** and *** indicate p values ≤ 0.01 and ≤ 0.001 by ANOVA (Dunnett's multiple comparisons) test. n.s. = not significant (p value > 0.05). Statistical test was performed on the average values of four independent experiments.

C) Drp1 distribution on mitochondria in control versus MiD49/51 siRNA-treated HeLa cells either without or with re-expression of the indicated MiD51-GFP construct. Cells fixed and stained for Drp1 and Tom20. Scale bars, 20 mm in overview images and 5 mm in zoom images.

D) Quantification of % mitochondrial area covered by Drp1 for the indicated conditions. **** and *** indicate p values ≤ 0.0001 and ≤ 0.001 by ANOVA (Dunnett's multiple comparisons) test. n.s. = not significant (p value > 0.05). N represents the number of cells analyzed per condition. **e,** Quantification of Drp1 puncta size for the indicated conditions. **** indicate a p value of ≤ 0.0001 by ANOVA (Dunnett's multiple comparisons) test. n.s. = not significant (p value > 0.05). N represents the number of cells analyzed per condition.

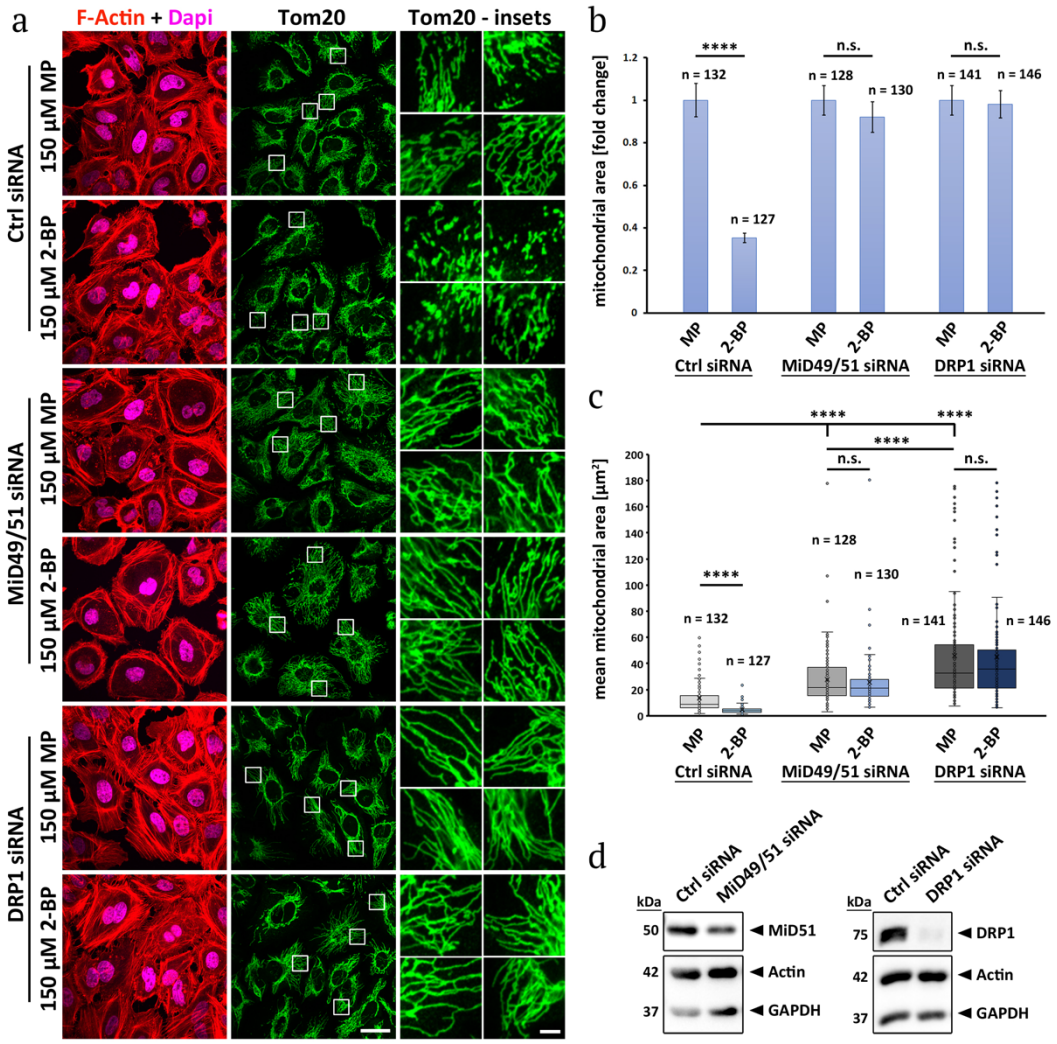
a
F-Actin + Dapi
Tom20
Tom20 - insets
Ctrl siRNA
MiD49/51 siRNA
DRP1 siRNA
150 µM MP
150 µM 2-BP
b
mitochondrial area [fold change]
****
n.s.
n = 132
n = 127
n = 128
n = 130
n = 141
n = 146
MP
2-BP
Ctrl siRNA
MiD49/51 siRNA
DRP1 siRNA
c
mean mitochondrial area [µm²]
d
kDa
Ctrl siRNA
MiD49/51 siRNA
DRP1 siRNA
50
42
37
75
MiD51
DRP1
Actin
GAPDH

Figure 3-7: 2-bromopalmitate induced mitochondrial fission is MiD-dependent.

A) Fixed-cell fluorescence micrographs of HeLa cells transfected with the indicated siRNAs, treated for 1-hr with either 2-BP or MP and stained for actin (TRITC-phalloidin, red) with Dapi (magenta) and mitochondria (Tom20, green).

B) Quantification of relative mitochondrial lengths between the MP and 2-BP treatments. Data normalized to the MP treatment. Corresponding non-normalized data are in Panel C. **** indicates p value ≤ 0.0001 by unpaired Student's t-test. n.s. = not significant (p value > 0.05). N represents the number of cells analyzed per condition.

C) Quantification of mean mitochondrial area between the MP and 2-BP treatments. Corresponding normalized data are in Panel B. **** indicates p value ≤ 0.0001 by unpaired Student's t-test. n.s. = not significant (p value > 0.05). N represents the number of cells analyzed per condition. Mean values are as follows: Ctrl siRNA/MP = 13.46; Ctrl siRNA/2-BP = 4.75; MiD49/51 siRNA/MP = 27.64; MiD49/51 siRNA/2-BP = 25.44; DRP1 siRNA/MP = 45.88; DRP1 siRNA/2-BP = 44.97.

D) Western blot of HeLa cells knocked down for either MiD49/MiD51 or DRP1, confirming the efficiency of the used siRNAs. Actin and GAPDH serve as loading controls.

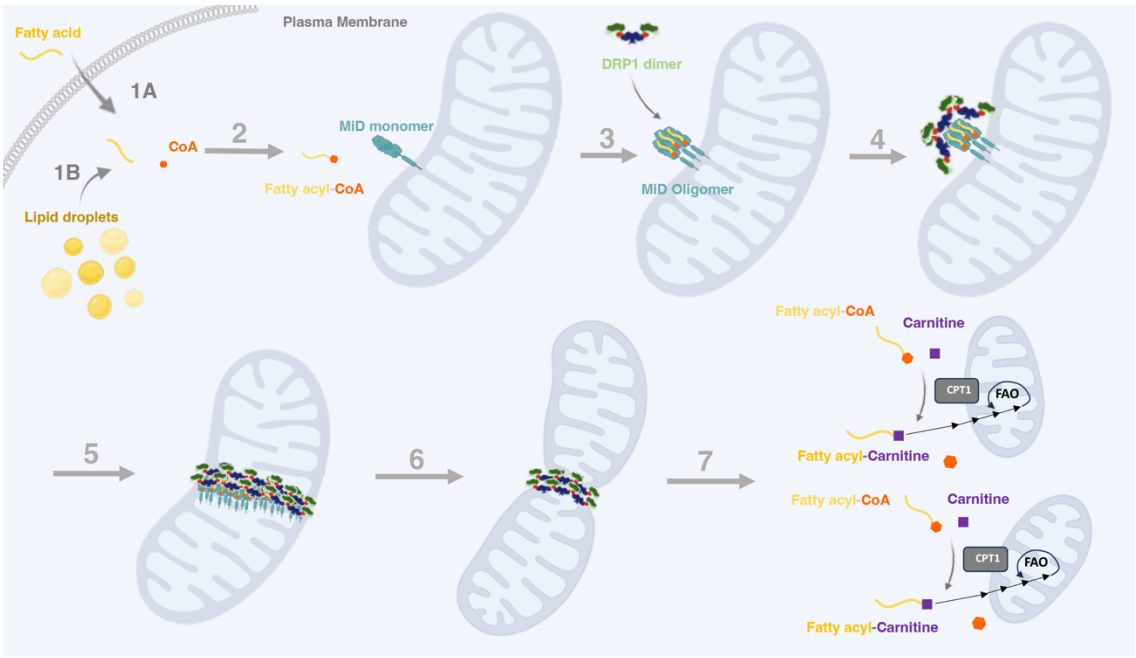

Figure 3-8: Model for MiD function in activation of fatty acid oxidation.

This model is developed from results in this paper and from (Ngo *et* al, 2023). Step 1. Long-chain fatty acid enters cytoplasm from the extracellular milieu (1A) or from intracellular lipid droplets (1B). Step 2. Fatty acid is coupled to CoA through fatty acyl-CoA synthetase. Step 3. Fatty acyl-CoA binds to MiD49 and/or MiD51 monomers on the outer mitochondrial membrane (OMM), inducing their oligomerization. Step 4. Oligomerized MiD initiates assembly of active DRP1 oligomers on the OMM. Step 5. DRP1 oligomerization continues on the OMM to create a ring around the mitochondrion. Step 6. DRP1-mediated constriction of the OMM leads to mitochondrial fission. Step 7. Mitochondrial fission causes increased carnitine-palmitoyl transferase 1 (CPT1) activity, increasing fatty acid import into the mitochondrial matrix and subsequent fatty acid oxidation (FAO).

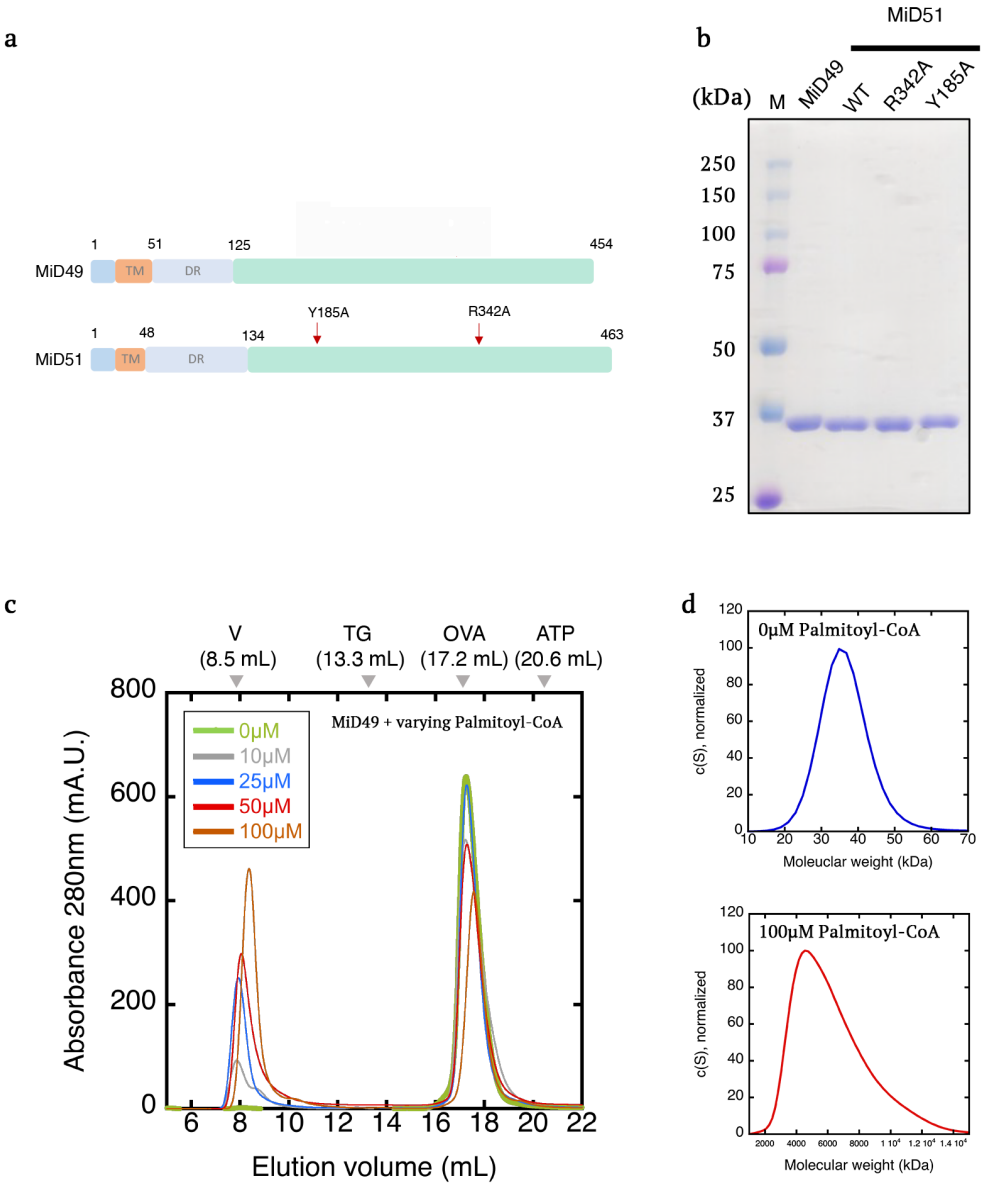
a
MiD49
1
51
125
454
TM
DR
MiD51
1
48
134
463
Y185A
R342A
b
MiD51
(kDa)
M
MiD49
WT
R342A
Y185A
250
150
100
75
50
37
25
c
V
(8.5 mL)
TG
(13.3 mL)
OVA
(17.2 mL)
ATP
(20.6 mL)
MiD49 + varying Palmitoyl-CoA
0μM
10μM
25μM
50μM
100μM
Absorbance 280nm (mA.U.)
Elution volume (mL)
d
0μM Palmitoyl-CoA
c(S), normalized
Moleuclar weight (kDa)
100μM Palmitoyl-CoA
c(S), normalized
Molecular weight (kDa)

Figure S3-1: Proteins used in this study, and effect of palmitoyl-CoA on MiD49 oligomerization.

A) Bar diagrams of MiD49 and MiD51, showing the regions used in our biochemical studies: 125-454 for murine MiD49 (38.7 kDa), and 134-463 for human MiD51 (38.3 kDa). TM = transmembrane sequence, DR = disordered region. Green region = segment used for biochemical studies here, and for crystallization studies by others.

B) Coomassie-stained SDS-PAGE of proteins used in this study. 2 μg protein loaded. Mass markers in kDa shown.

C) Superose 6 size exclusion chromatography of MiD49 cytoplasmic region (100 μM) mixed with varying concentrations of palmitoyl-CoA.

D) Velocity analytical ultracentrifugation of peak fractions from Superose 6 size exclusion chromatography of MiD49 cytoplasmic region (100 μM) incubated without or with palmitoyl-CoA (100 μM). Molecular masses calculated by these vAUC data: 36.4 kDa (without palmitoyl-CoA), and 4815 kDa (with palmitoyl-CoA).

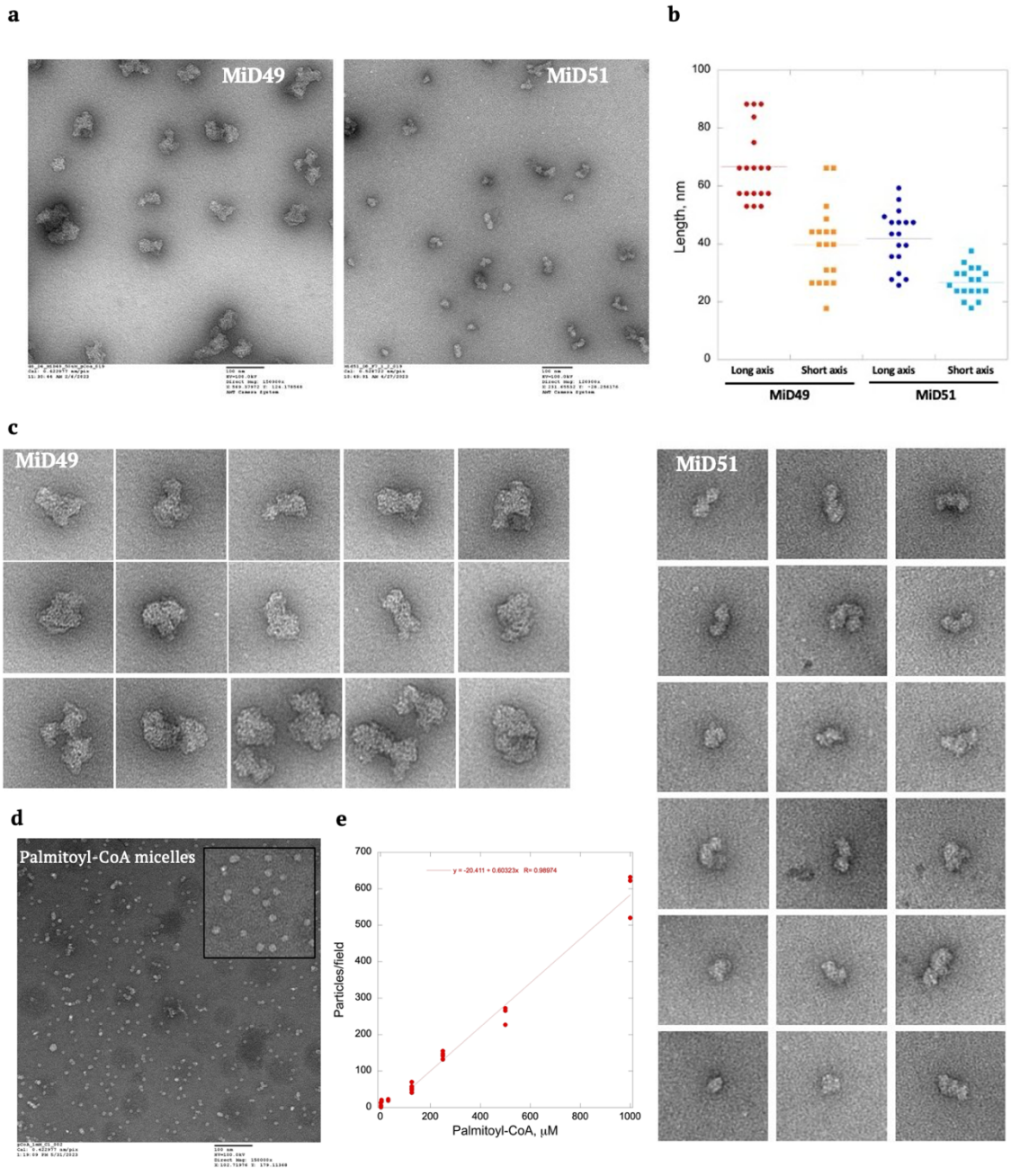
a
MiD49
MiD51
b
Length, nm
100
80
60
40
20
0
Long axis
Short axis
Long axis
Short axis
MiD49
MiD51
c
MiD49
MiD51
d
Palmitoyl-CoA micelles
e
y = -20.411 + 0.60323x R= 0.98974
Particles/field
700
600
500
400
300
200
100
0
0
200
400
600
800
1000
Palmitoyl-CoA, μM

Figure S3-2: Negative stain EM of MiD49 and MiD51 oligomers.

Peak oligomer fractions from Superose 6 chromatography after mixing MiD49 (100 μM) or MiD51 (50 μM) with palmitoyl-CoA (50 or 500 μM, respectively).

A) Full-field examples for MiD49 and MiD51.

B) Montage of MiD49 (left) or MiD51 (right) oligomer particles. Each image represents a 150 x 150 nm box.

C) Graph of long axis and short axis lengths for 18 particles of MiD49 or MiD51 oligomers.

D) Palmitoyl-CoA alone (1 mM) in same buffer as MiDs (10 mM Hepes pH 7.4, 65 mM KCl, 1 mM MgCl2, 1 mM EGTA, 1 mM DTT). Inset represents zoom of a 150 x 150 nm region. **e,** Graph of particles/field (800 x 800 nm field) versus palmitoyl-CoA concentration. 3-5 fields quantified for each concentration. X intercept for linear fit (after accounting for background particles, 8.2/field) represents critical micelle concentration (47 μM).

a

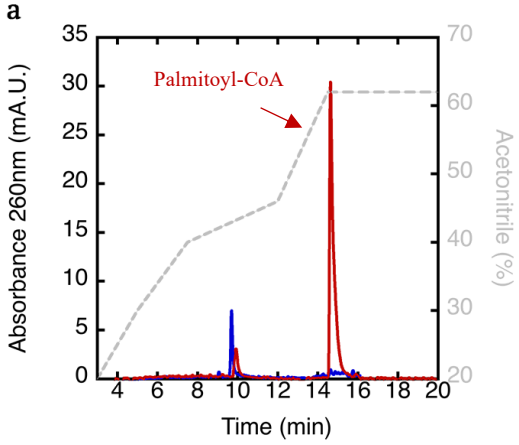

b

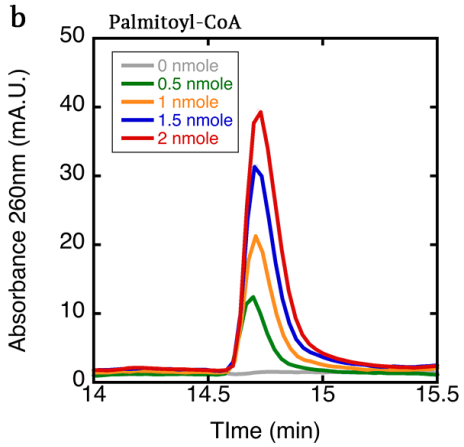

c

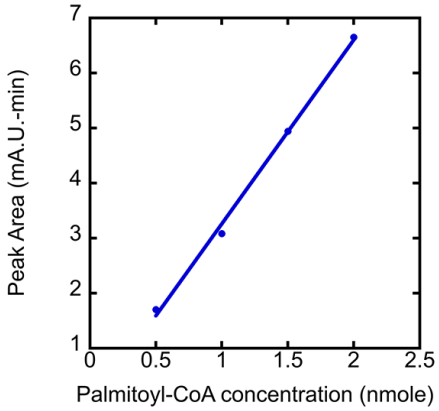

d

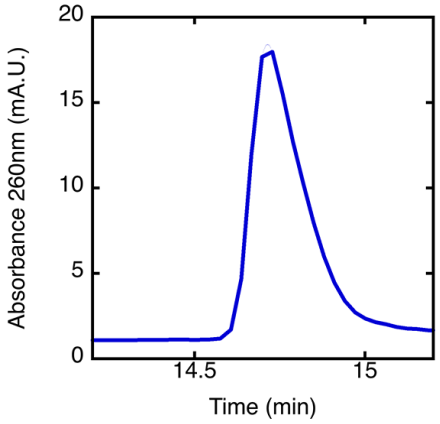

e

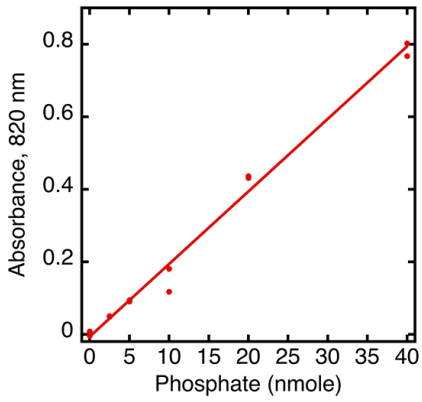

f

Condition	MiD49 µM	Phosphate nmole	Palmitoyl-CoA µM	Ratio Palmitoyl-CoA : MiD49
50	4.78	4.58	3.82	0.8
100	8.77	11.74	9.78	1.11
100	2.34	2.83	2.36	1.01

Figure S3-3: Palmitoyl-CoA quantification in MiD49 oligomer fraction.

A) Reversed-phase HPLC profile of 1.5 nmole palmitoyl-CoA (red) or solvent alone (blue). Position of palmitoyl-CoA elution shown with arrow. Dashed gray line represents acetonitrile concentration.

B) Palmitoyl-CoA peaks from four quantities of loaded palmitoyl-CoA (0, 0.5, 1, 1.5 and 2 nmole).

C) Peak area as a function of palmitoyl-CoA loaded.

D) Palmitoyl-CoA HPLC peak obtained when 200 mL of MiD49 oligomer fraction (Superose 6 oligomer fraction after incubating 100 μM MiD49 with 500 μM palmitoyl-CoA). Peak area, 3.42 A.U.-min, corresponding to 1.1 nmole Palmitoyl-CoA, or 5.5 μM. MiD49 concentration in this fraction (by Bradford assay), 5.3 μM.

E) Standard curve of phosphate using the Fiske-Subbarow assay.

F) Palmitoyl-CoA concentrations calculated from Fiske-Subbarow assay in which 400 μL oligomer fraction from Superose 6 was assayed. "Condition" refers to the μM amount of palmitoyl-CoA that was incubated with 100 μM MiD49 (37˚C, 1 hr) prior to separation of oligomers from monomers by Superose 6. MiD49 concentration determined by Bradford assay

a

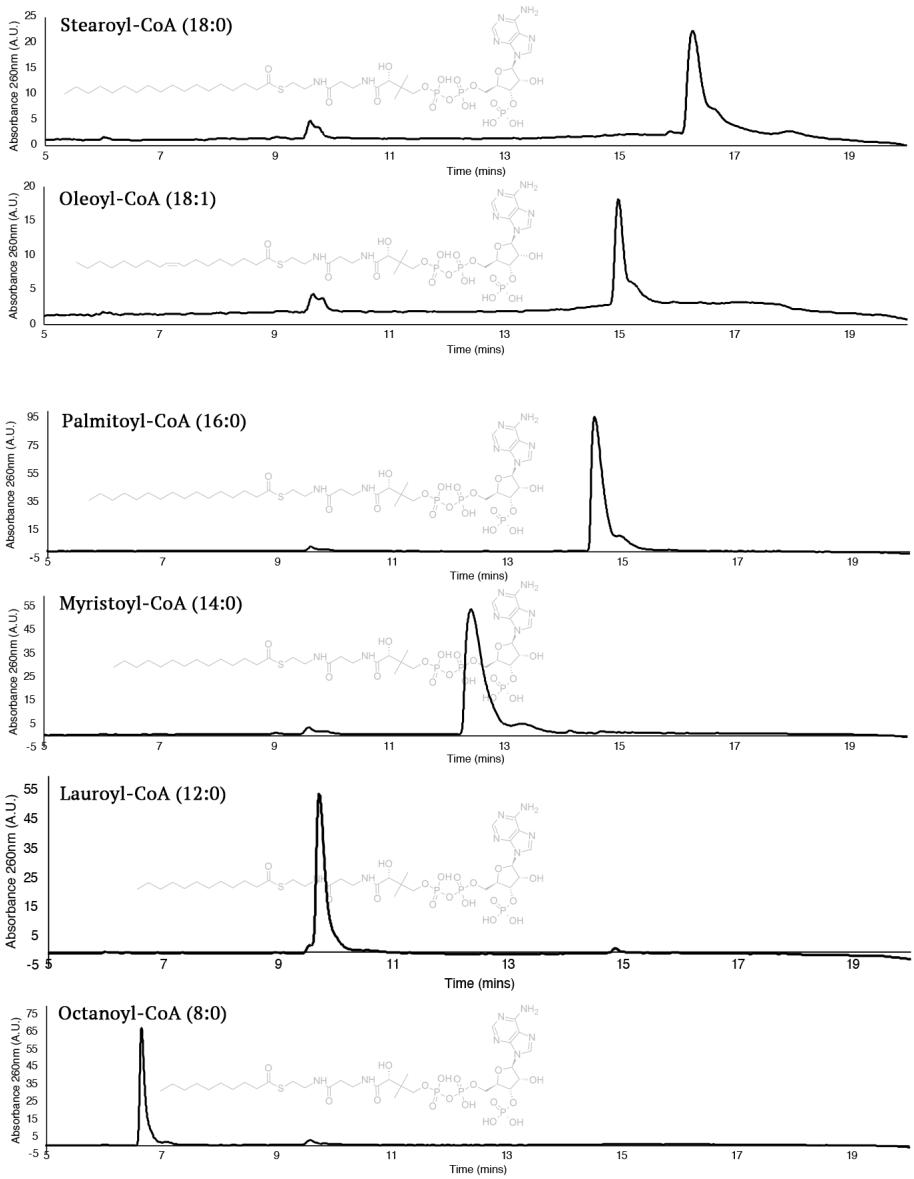
Stearoyl-CoA (18:0)
Oleoyl-CoA (18:1)
Palmitoyl-CoA (16:0)
Myristoyl-CoA (14:0)
Lauroyl-CoA (12:0)
Octanoyl-CoA (8:0)
Absorbance 260nm (A.U.)
Time (mins)

b

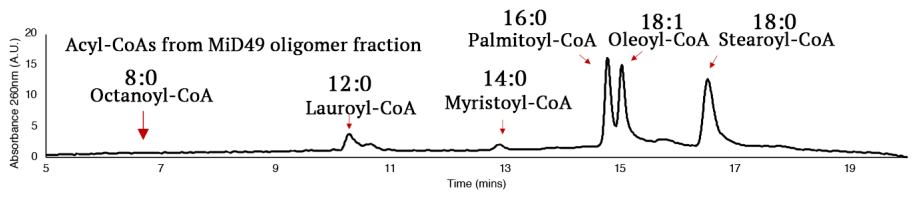
Acyl-CoAs from MiD49 oligomer fraction
8:0
Octanoyl-CoA
12:0
Lauroyl-CoA
14:0
Myristoyl-CoA
16:0
Palmitoyl-CoA
18:1
Oleoyl-CoA
18:0
Stearoyl-CoA
Absorbance 260nm (A.U.)
Time (mins)

Figure S3-4: HPLC analysis of acyl-CoAs bound to MiD49 oligomer.

A) Individual HPLC traces of each of the acyl-CoAs (4 nmole loaded).

B) HPLC trace of the MiD49 oligomer fraction from the following experiment. MiD49 cytoplasmic construct (100 μM) was mixed simultaneously with 83.3 μM of six acyl-CoAs (stearoyl, oleoyl, palmitoyl, myristoyl, lauroyl, octanoyl) for 1 hr at 37˚C, then MiD49 oligomer isolated by Superose 6 chromatography. Acyl-CoA distribution was then analyzed in the oligomer fraction by reversed-phase HPLC.

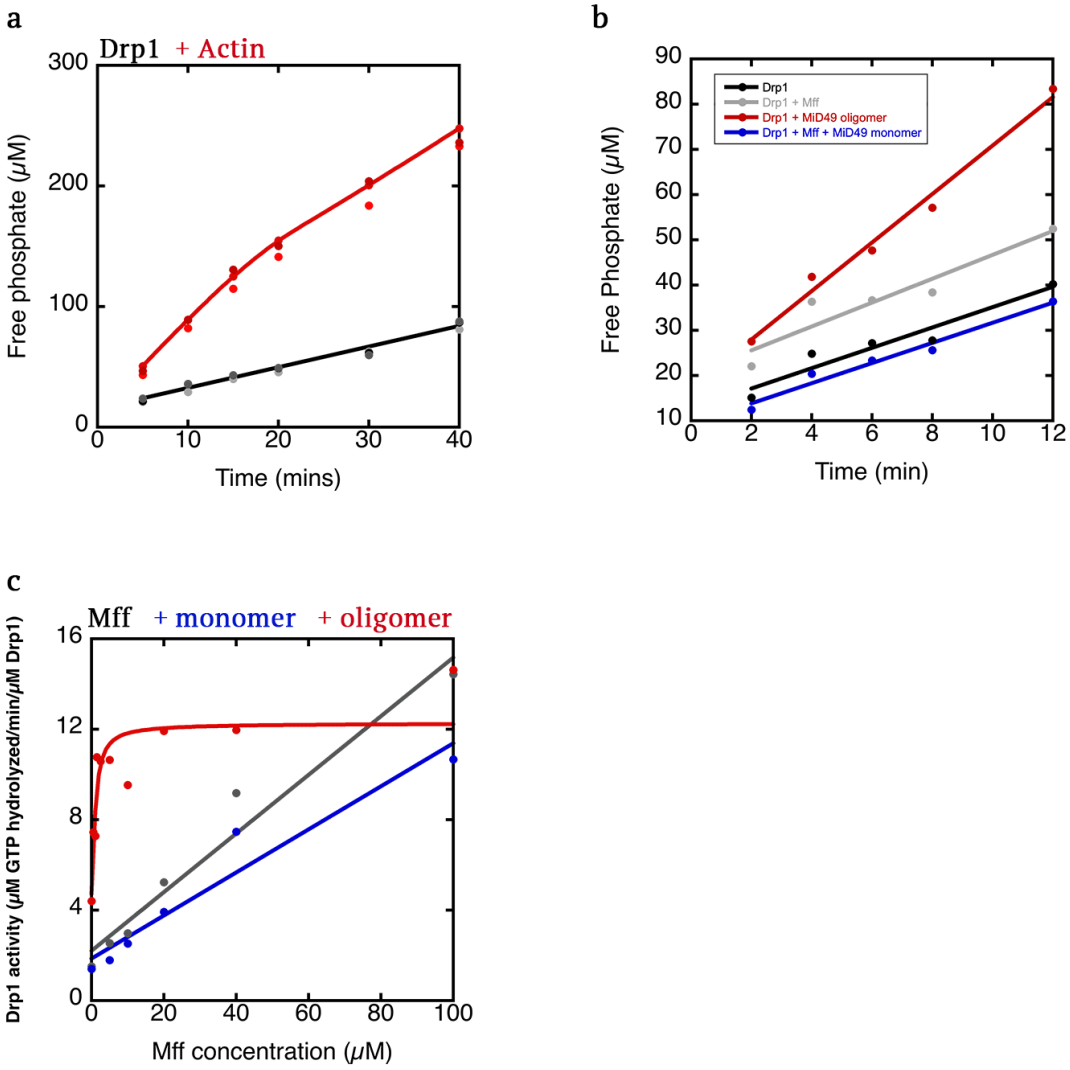

Figure S3-5: Effect of MiD49 and actin filaments on Drp1 activity

A) Drp1 GTPase assays (0.75 μM Drp1) alone (black points) or in the presence of 0.5 μM actin filaments (red).

B) Drp1 GTPase assays (0.75 μM Drp1) alone (black points) or in the presence of 10 μM MFF alone (gray) or with 250 nM MiD49 oligomers (red) or monomers (blue) added.

C) Effect of varying concentrations of MFF on Drp1 GTPase activity (0.75 μM Drp1) in the absence or presence of 250 nM MiD49 oligomers (red) or monomers (blue). Full curve to 100 μM MFF. Zoom to 20 μM MFF shown in Figure 3-3f.

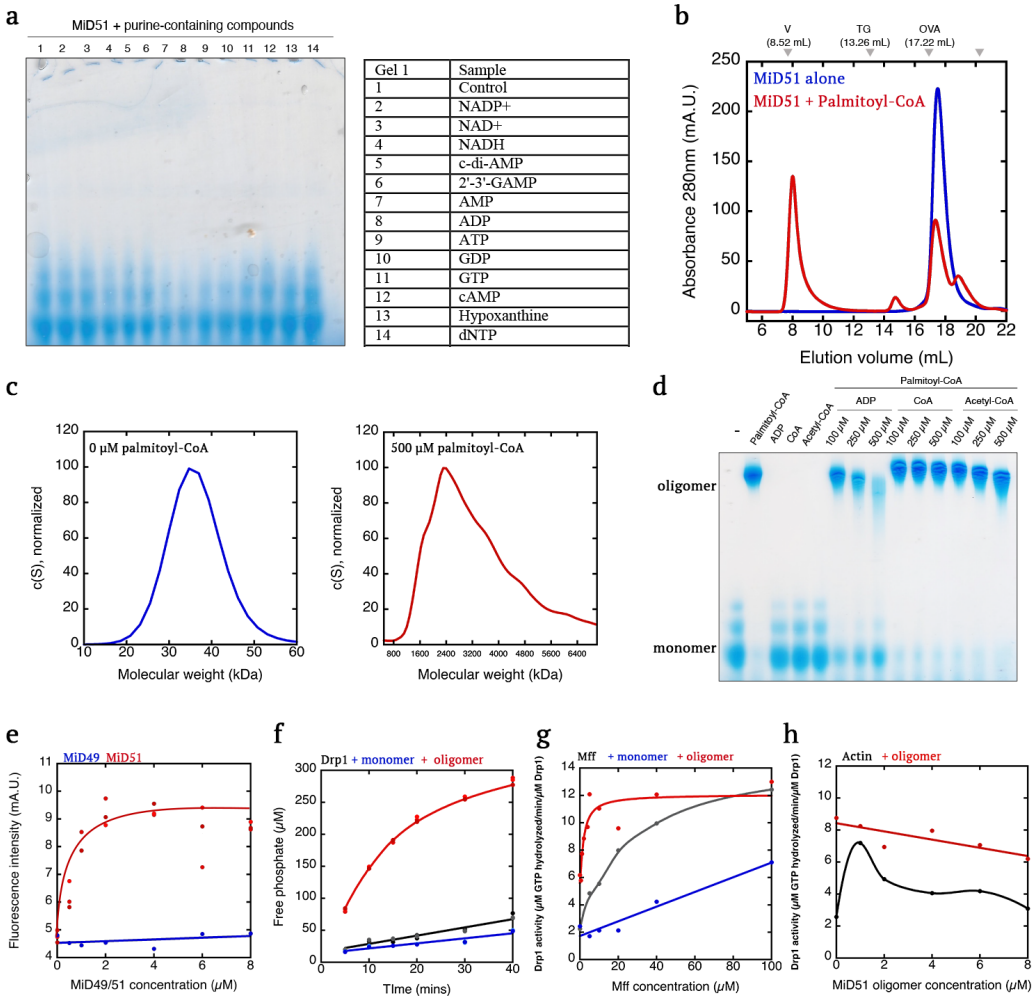

Gel 1	Sample
1	Control
2	NADP+
3	NAD+
4	NADH
5	c-di-AMP
6	2'-3'-GAMP
7	AMP
8	ADP
9	ATP
10	GDP
11	GTP
12	cAMP
13	Hypoxanthine
14	dNTP

Figure S3-6: Effects of LCACA on MiD51 biochemical properties

A) Blue-native gel electrophoresis of MiD51 cytoplasmic region (50 μM) mixed with 500 μM of the indicated molecule.

B) Size-exclusion chromatography (Superose 6) of MiD51 (50 μM) alone (blue) or in the presence of 100 μM palmitoyl-CoA (red).

C) Velocity analytical ultracentrifugation of the MiD51 oligomer peak Figure 3-4b (left) and the monomer MiD5 peak (right), showing calculated molecular masses.

D) Blue-native gel electrophoresis of MiD51 (50 μM) with 500 μM of the indicated molecules, or with 500 μM palmitoyl-CoA + the indicated concentrations of ADP, CoA or acetyl-CoA.

E) MANT-ADP binding assay in which 300 nM MANT-ADP is mixed with the indicated concentrations of MiD51 or MiD49 and the fluorescence intensity monitored.

F) Drp1 GTPase assays containing Drp1 alone (0.75 μM, black points) or in the presence of 0.5 μM MiD51 oligomers (red) or monomers (blue) added.

G) Effect of varying concentrations of MFF on Drp1 GTPase activity (0.75 μM Drp1) in the absence or presence of 250 nM MiD51 oligomers (red) or monomers (blue). Full curve to 100 μM Mff. Zoom to 20 μM Mff shown in Figure 3-5d.

H) Effect of varying concentrations of actin filaments on Drp1 GTPase activity (0.75 μM Drp1) in the absence (black) or presence of MiD51 oligomers (blue).

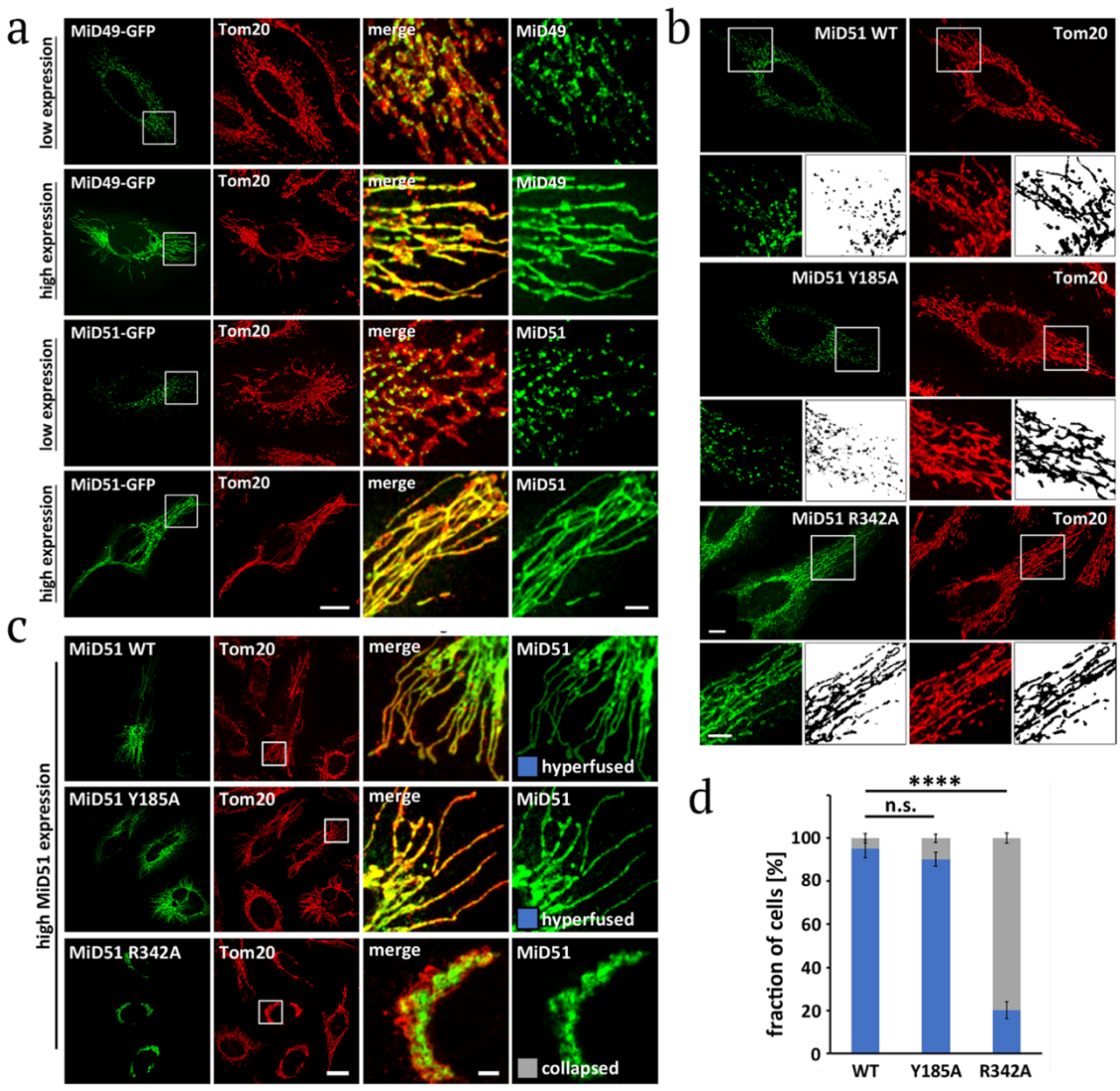
a
low expression
high expression
low expression
high expression
MiD49-GFP
MiD49-GFP
MiD51-GFP
MiD51-GFP
Tom20
merge
MiD49
MiD51
b
MiD51 WT
MiD51 Y185A
MiD51 R342A
Tom20
c
high MiD51 expression
MiD51 WT
MiD51 Y185A
MiD51 R342A
hyperfused
hyperfused
collapsed
d
****
n.s.
fraction of cells [%]
100
80
60
40
20
0
WT
Y185A
R342A

Figure S3-7: Expression of MiD49 and MiD51 GFP fusion constructs in HeLa cells.

A) C-terminal GFP fusion constructs of MiD49 or MiD51 were transiently transfected into HeLa cells, then cells were fixed and stained for mitochondria (Tom20). At low expression levels (requiring 500 msec exposure at 100% laser power), the GFP fusions did not alter mitochondrial length, and displayed a punctate appearance on mitochondria. At high expression (100 msec exposure, 50% laser power), the GFP pattern on mitochondria was uniform and mitochondria were hyperfused. Scale bars: 20 mm (whole cell) and 3 mm (insets).

B) Examples of image processing for quantification of GFP-MiD51 puncta size, and % mitochondrial area covered by GFP-MiD51. Boxed regions are shown in higher magnification below overview images. Binary masks of the respective inset images are shown on the right. These binary masks are representative of the images that were used for analyses in E and F. Scale bars are 10 mm in full images and 3 mm in insets.

C) C-terminal GFP fusion constructs of the indicated MiD51 constructs were transiently transfected into HeLa cells, then cells were fixed and stained for mitochondria (Tom20). Cells were selected for high expression under the criteria described above. Images at right represent indicated boxed regions. Examples for WT and Y185 constructs represent hyper-fused phenotype quantified in panel D, while example for R342A mutant represents collapsed phenotype. Scale bars, 20 mm in full images and 3 mm in insets.

D) Graph quantifying % cells displaying hyperfused (blue) or collapsed (gray) mitochondria. Representative examples of each pattern are shown below. Scale bar is 10 mm. N = 122, 82, and 85 cells were analyzed for MiD51 WT, Y185A, R342A, respectively. *** denotes p value of ≤ 0.001 by ANOVA (Dunnett's multiple comparisons) test. n.s. = not significant (p value > 0.05).

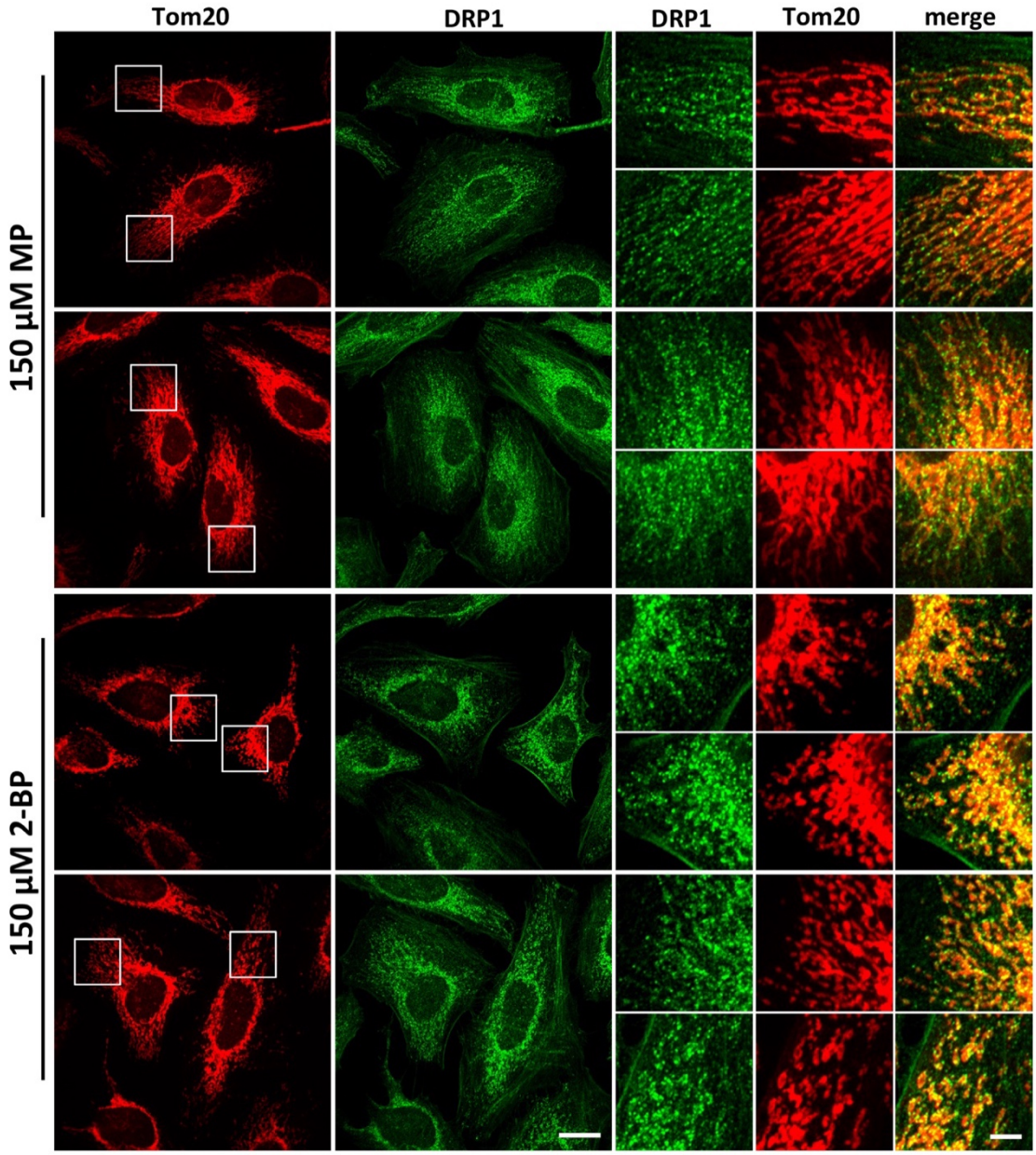

Figure S3-8: Effect of 2-bromopalmitate on DRP1 mitochondrial puncta.

HeLa cells were treated with either methyl-palmitate (MP) or 2-bromopalmitate (2BP) for 1-hr, then fixed and stained for mitochondria (Tom20, red) and DRP1 (green). Images at right represent zooms of indicated boxes at left. Two representative examples for either treatment are shown.

Chapter IV:

Effects of phosphorylation on Drp1 activation by its receptors, actin, and cardiolipin

Chapter IV

Effects of phosphorylation on Drp1 activation by its receptors, actin, and cardiolipin

Ao Liu[1,2], Anna L. Hatch[2,3] & Henry N. Higgs[1]

[1]Department of Biochemistry and Cell Biology, Geisel School of Medicine at Dartmouth College, Hanover NH 03755, USA

[2]These authors contributed equally to this work

[3]Current address: 7800 Fairborn Court, Derwood MD 20855

The text and data here are adapted or reproduced in full from the manuscript under review at ***Molecular Biology Cell***

(DOI: https://doi.org/10.1101/2023.08.20.554022)

This work was supported by NIH R01 GM069818 and R35 GM112545 to HNH, and NIH P20 GM113132 to the BioMT COBRE.

4.1 Abstract

Drp1 is a dynamin family GTPase that is required for mitochondrial and peroxisomal division, in which it oligomerizes into a ring and constricts the underlying membrane in a GTP hydrolysis-dependent manner. Oligomerization increases Drp1 GTPase activity through interactions between neighboring GTPase domains. In cells, Drp1 is regulated by several factors including Drp1 receptors, actin filaments, cardiolipin, and phosphorylation at two sites: S579 and S600. Phosphorylation of S579 is widely regarded as activating, while S600 phosphorylation is commonly considered inhibiting. However, the direct effects of phosphorylation on Drp1 GTPase activity have not been investigated in detail. In this study, we compare the effects of S579 and S600 phosphorylation on purified Drp1, using phospho-mimetic mutants and in vitro phosphorylation. The oligomerization state of both phospho-mimetic mutants is shifted toward smaller oligomers. Both phospho-mimetic mutations maintain basal GTPase activity, but eliminate GTPase stimulation by actin and decrease GTPase stimulation by cardiolipin, Mff, and MiD49. Phosphorylation of S579 by Erk2 produces similar effects. When mixed with wild-type Drp1, both S579D and S600D phospho-mimetic mutants reduce the actin-stimulated GTPase activity of Drp1-WT. Conversely, a Drp1 mutant that lacks GTPase activity, the K38A mutant, stimulates Drp1-WT GTPase activity under both basal and actin-stimulated conditions, similar to previous results for dynamin-1. These results suggest that the effect of S579 phosphorylation is not to activate Drp1 directly, and likely requires additional factors for stimulation of mitochondrial fission in cells. In addition, our results suggest that nearest neighbor interactions within the Drp1 oligomer affect catalytic activity.

4.2 Introduction

The dynamin family GTPase Drp1 is an important mediator of membrane fission for at least two organelles, mitochondria and peroxisomes [68]. When not mediating membrane fission, Drp1 is a cytoplasmic protein. To induce membrane fission, Drp1 is recruited to the target membrane by receptor proteins, where it oligomerizes into a ring structure around the membrane. Oligomerization increases Drp1 GTPase activity by bringing the N-terminal GTPase domains into close proximity [70,98,101]. GTP hydrolysis results in constriction of the Drp1 ring and membrane constriction.

Drp1 receptors can directly activate Drp1. One Drp1 receptor, Mff, is on both mitochondrial and peroxisomal membranes. Mff itself is a trimer, and its binding causes increased Drp1 GTPase activity *in vitro* [109,241]. A second set of Drp1 receptors, MiD49 and MiD51, are only found on mitochondria. In their inactive state, MiD proteins are monomeric and do not activate Drp1. Binding to fatty acyl-coenzyme A stimulates MiD oligomerization, which in turn stimulates Drp1 GTPase activity [255].

Other regulatory molecules for Drp1 include actin filaments and phospholipids. Biochemically, actin filaments stimulate Drp1 GTPase activity ~4-fold through direct binding [69,91]. In cells, actin polymerization through an endoplasmic reticulum-bound formin protein, INF2, increases Drp1 oligomerization and mitochondrial recruitment [71,91,171]. The mitochondrial lipid cardiolipin (CL) can affect a >20-fold stimulation of GTPase activity biochemically [227], while CL-derived phosphatidic acid suppresses Drp1 activation [186].

Drp1 is also subject to a number of post-translational modifications [89,256], with phosphorylation in particular being correlated with changes in Drp1-mediated mitochondrial fission. Two well-studied phosphorylation sites occur within a 21 amino acid segment of the Variable Domain of Drp1[89] (**Figure 4-1A),** which forms an unstructured loop at one end of the elongated Drp1 structure[70] (**Figure 4-1B**). Depending on the splice variant and species studied [85,86], the positions of these sites differ (**Figure 4-1C**), with the most common names in the literature being S616 and S637, but which will be referred to here mostly as S579 and S600, as explained in the Results section.

Phosphorylation of S579 has been observed for multiple kinases, including by CDK1, CDK5, ERK2, CaMKII, ROCK, PKC, and PINK [85,105,145–150,153], with phosphorylation being correlated with

increased mitochondrial fission. Phosphorylation of S600 by protein kinase A (PKA), CaMK1a, ROCK1, AMPK and protein kinase D has been reported [104,106,155–158]. In most cases, S600 phosphorylation has been correlated with decreased mitochondrial fission[104,106,157,159]. However, some studies show evidence for a positive effect of S600 phosphorylation on cellular Drp1 activity [155,156,158,257], while another study reports no effect [166]. Finally, one report suggests that S600 phosphorylation promotes S579 phosphorylation, and that the doubly phosphorylated S579/S600 protein correlates with increased mitochondrial fission [162]. Many of the above-cited publications utilize phospho-mimetic mutants to induce similar mitochondrial changes to phosphorylation-induced changes, suggesting that phospho-mimetics can elicit similar effects.

It is unclear whether phosphorylation at either site directly alters Drp1 activity. For S579 phosphorylation, no biochemical data addressing Drp1 activity are available. For S600 phosphorylation, the biochemical data are conflicting. In one study, a phospho-mimetic mutant of Drp1 maintains oligomerization and GTP hydrolysis activity [106]. In another study, *in vitro* phosphorylation of GST-Drp1 by PKA inhibits GTPase activity [104]. Recent structural work suggests that S600 phosphorylation inhibits MiD49 binding[97], although other cellular co-IP experiments suggest that the S600D phospho-mimetic binds better to MiD49 and MiD51 than does the non-phosphorylatable S600A mutant [116]. Other studies show that the region of Drp1 containing both phosphorylation sites (the Variable Domain) inhibits binding to Mff [109,110], although neither S579D nor S600D phospho-mimetics alter this effect [110].

In this study, we assess the biochemical effects of Drp1 phosphorylation on oligomerization and GTPase activity of Drp1 alone, and in the presence of several activators (actin, cardiolipin, Mff, MiD49). For these studies, we use both phospho-mimetic S-to-D mutations and *in vitro* phosphorylation on the S579 site. Surprisingly, we find that both types of phosphorylation inhibit the abilities of these activators to stimulate Drp1 activity.

4.3 Results

4.3.1 Phospho-mimetic mutants are less oligomerized in the nucleotide-free state

We constructed two phospho-mimetic Drp1 mutants corresponding to S616D and S637D in isoform 1. We refer to these mutants, however, as S579D and S600D respectively, because we use isoform 3 of Drp1 (**Figure 4-1C**). In HeLa, HL60 and PC12 cells, isoform 3 is the most abundant isoform present, making up over 40% of total Drp1 protein [85].

The S579 site, generally thought to activate Drp1, is located within the Variable Domain; while the S600 site, generally thought to inhibit Drp1, marks the boundary between the Variable Domain and the stalk (**Figure 4-1A**). The region encompassing both sites is poorly resolved in the existing structural models of nucleotide-free Drp1[70] (**Figure 4-1B**) or other models [97].

By size exclusion chromatography at high Drp1 concentration (30 μM), both phospho-mutants are slightly shifted to smaller sizes compared to Drp1-WT (**Figure 4-2A**). For more detailed analysis of Drp1 hydrodynamic properties, we used velocity analytical ultracentrifugation (vAUC). Previously, we reported that purified Drp1-WT exists in several oligomeric states [69], similar to the results of other studies[70,227]. We compared the Drp1-S579D and Drp1-S600D to Drp1-WT by vAUC at three concentrations: 8, 4, and 1.5 μM (**Figure 4-2B**). As with Drp1-WT, both mutants display a 7 S species that is similar to the sedimentation pattern of a oligomerization-deficient mutant [69,70], suggesting that this is the dimeric species. In addition, several species of higher S values, corresponding to larger oligomers, are present for Drp1-WT. At all concentrations tested, both Drp1 S579D and S600D shift towards smaller oligomers when compared with WT, with the S600D mutant displaying a greater shift.

We also tested the ability of Drp1 to form larger oligomers in the presence of the non-hydrolysable GTP analogue GMP-PCP using a high-speed sedimentation assay[69]. At three Drp1 concentrations (0.5, 1.0, and 2.0 μM), GMP-PCP causes similar degrees of Drp1 sedimentation for all constructs, suggesting that GTP-mediated oligomerization is not affected by these mutations (**Figure 4-2 C,D**).

These data suggest that both the S579D and S600D mutants display less ability to oligomerize in the nucleotide-free state than WT Drp1, but that non-hydrolyzable GTP induces all three proteins to oligomerize.

4.3.2 Phospho-mimetic mutants for both S579 and S600 reduce Drp1 responses to activators

We next examined the GTPase activities of the two phospho-mimetic mutants. Both mutants display similar GTPase activity to Drp1-WT (1.57±0.09, 1.51±0.02, and 1.33±0.14 μM/min/μM for WT, S579D, and S600D, respectively). Previously, we reported that actin filaments have a bi-phasic effect on Drp1 GTPase activity, where low actin filament concentrations are stimulatory but higher concentrations bring the activity back to the Drp1-alone values [69]. We tested whether the phospho-mimetic mutants responded to actin in a similar manner. Surprisingly, actin does not activate Drp1 S579D or Drp1 S600D at any concentration tested (**Figure 4-3A**).

Previously, we reported that Drp1 binds actin filaments with a K_d^{app} in the range of 1-2 μM [69,91]. We compared actin binding for Drp1-WT, Drp1-S579D and Drp1-S600D by co-sedimentation assay at two ionic strengths: 65 mM and 140 mM NaCl. Drp1-WT and Drp1-S579D display similar K_d for actin at 65 mM NaCl (K_d^{app} 1.7 and 2.5 μM for WT and S579D, respectively), while Drp1-S600D displays significantly lower actin affinity (K_d^{app} 7.1 μM). We previously reported that Drp1-WT binding to actin filaments saturates at approximately 50% Drp1 bound [69]. Both mutants display lower % bound at saturating actin (48%, 27%, 18% bound for WT, S579D, and S600D respectively) (**Figure 4-3B**; **Figure S4-1A, B**). At 140 mM NaCl, Drp1 S579D has a similar affinity for actin filaments as WT (1.1 and 1.2 μM for S579D and wild-type respectively) and a comparable % bound (10.9% and 8.3% for S579D and WT respectively), while Drp1 S600 has lower affinity and % bound than the other constructs (4.3 μM and 6.1% bound) (**Figure 4-3C; Figure S4-1C-E**). These results show that the phospho-site mutants have altered actin-binding properties, with Drp1 S600D displaying less actin interaction under all conditions.

We also asked whether GTPase stimulation by another Drp1 activator, cardiolipin (CL) [227], was affected by the S579D or S600D mutations. Interestingly, unilamellar vesicles containing 25 mole% cardiolipin are less stimulatory to Drp1-S579D and Drp1-S600D than they are for Drp1-WT (**Figure 4-3D**).

We have previously shown that the cytoplasmic region of the Drp1 receptor Mff activates Drp1, and that actin filaments synergize with Mff by reducing the Mff concentration needed for maximal Drp1 activation [241]. Both phospho-mimetic mutants display slightly decreased activation by Mff alone (**Figure 4-3E**). Interestingly, actin filaments still synergize with Mff for Drp1-S579D

stimulation, albeit with a lower maximal activation (**Figure 4-3F**). In contrast, the Drp1-S600D mutant displays greatly reduced synergy between actin and Mff (**Figure 4-3F**).

Two other Drp1 receptors, MiD49 and MiD51, do not activate Drp1 GTPase activity when they themselves are not activated. Upon binding their activating ligand, acyl-CoA, MiD proteins oligomerize, resulting in Drp1 GTPase activation in a bi-phasic manner, similar to actin [255]. Here, we find that both Drp1 phospho-mimetic mutants are also activated by acyl-CoA-bound MiD49 in a bi-phasic manner. However, the degree of activation is lower, with Drp1-S600D being most affected (**Figure 4-3G**). Similar to Drp1-WT, neither phospho-mimetic mutant is stimulated by MiD49 monomer (**Figure 4-3G**).

As with actin filaments, oligomerized MiD49 synergizes with Mff by reducing the Mff concentration required for maximal Drp1 activation. Drp1-S579D displays maximal activity in the presence of low concentrations of Mff and oligomerized MiD49, albeit at a lower maximum than Drp1-WT (**Figure 4-3H**). Similarly, despite its decreased ability to stimulate Drp1-S600D, oligomerized MiD49 is able to reduce the concentration of Mff required for Drp1-S600D stimulation.

These results show that phospho-mimetics of both the 'activating' (S579D) and 'inhibitory' (S600D) sites on Drp1 result in a reduction of Drp1 activation by a variety of activators. This reduction is most dramatic for actin filaments.

4.3.3 Drp1 phosphorylated on S579 displays similar properties to the S579D phospho-mimetic

The results for Drp1-S579D were surprising, considering that this site has been found to be associated with increased mitochondrial fission in cells. We sought to test these results further by directly phosphorylating Drp1 on S579 using recombinant ERK2, one of the kinases shown to mediate this phosphorylation [146,147] Incubation with ERK2 for 4-hr results in a slight decrease in mobility on SDS-PAGE, suggestive of phosphorylation (**Figure 4-4A**). Western blotting using an antibody against phospho-S579 shows saturation of this signal on a similar time scale (**Figure 4-4B**). Gel filtration chromatography of 4-hr phosphorylated Drp1 results in a similar elution profile to mock-phosphorylated sample (**Figure 4-4C,** 30 μM Drp1 loaded). Analysis by tryptic digest and mass spectrometry reveals that phospho-S579 accounts for 94.5% of the phosphorylated

peptides identified, with other detectable phosphorylation sites being S526 (5.2%), S136 (0.3%), S570 (0.02%), and T394 (0.01%). No phosphorylated peptides were detected for mock-phosphorylated Drp1. These results suggest that our ERK2-treated Drp1 is efficiently phosphorylated on S579, with minor phosphorylation on other residues.

Similar to its phospho-mimetic analogue, S579-phosphorylated Drp1 (P-S579-Drp1) is not stimulated by actin filaments (**Figure 4-4D**). In actin binding assays, P-S579-Drp1 displays a ~2-fold decrease in maximal actin binding relative to Drp1-mock, while maintaining a similar affinity (**Figure 4-4E, Figure S4-2**), similar to the S579D mutant. Cardiolipin-containing vesicles only weakly stimulate P-S579-Drp1 (**Figure 4-4F**), which is a comparatively greater effect than that of the phospho-mimetic. Similar to Drp1-S579D, P-S579-Drp1 is stimulated by Mff or by MiD49 oligomers to a lesser extent than Drp1-WT (**Figure 4-4G,H**). Interestingly, the synergy of Mff with actin filaments is strongly reduced for Drp1-S579D (**Figure 4-4I**) while the synergy between Mff and MiD49 oligomers is maintained (**Figure 4-4J**).

A recent publication reports that phosphorylation at the S600 position can stimulate S579 phosphorylation in some cases, and this doubly phosphorylated Drp1 leads to increased mitochondrial fragmentation [162]. We therefore tested whether doubly phosphorylated Drp1 displays different properties to either singly phosphorylated protein. For these experiments, we phosphorylated Drp1-S600D on S579 using Erk2, resulting in a similar gel shift as Drp1-phosphoS579 (**Figure 4-5A**). Similarly to the Erk2-phosphorylated Drp1-WT, Drp1-phosphoS579/S600D is not activated by actin filaments or cardiolipin (**Figure 4-5B,C**), and displays reduced activation by Mff (**Figure 4-5D**). Interestingly, Drp1-phosphoS579/S600D displays no activation by MiD49 oligomers (**Figure 4-5E**), and no synergistic effect of actin or MiD49 oligomers on Mff activation (**Figure 4-5F, G**).

The Drp1 protein used thus far (isoform 3) contains none of the three possible alternately spliced inserts. While isoform 3 predominates in some cell types, it is a minor isoform in others, and the other splice variants also make up an appreciable percentage of total Drp1 in most cells and tissues [85]. We asked whether the isoform containing all three splice inserts (isoform 6) reacts similarly to isoform 3 in response to Erk2 phosphorylation. Treatment of isoform 6 with Erk2 results in decreased mobility on SDS-PAGE (**Figure 4-6A**), suggesting successful phosphorylation on S629 (equivalent to S579 in isoform 3). Similar to isoform 3, P-S629-Drp1(i6) is not activated by actin filaments (**Figure 4-6B**). In addition, Mff and MiD49 stimulate P-S629-Drp1(i6) to a lesser extent

than non-phosphorylated Drp1 (**Figure 4-6 C,D**). These results suggest that the presence of the three splice inserts do not alter Drp1's response to phosphorylation on the canonical 'activating' site.

These results show that Drp1-phosS579 possesses similar properties to the phospho-mimetic S579D mutant in its reduced stimulation by all tested activators. In fact, Drp1-phosS579 displays less stimulation by cardiolipin than Drp1-S579D, and displays no synergy between actin and Mff.

4.3.4 Drp1-S579D does not stimulate actin-mediated activation of Drp1-WT

The ability of the S579D to bind actin without stimulation of its GTPase activities allowed us to test the effects of Drp1-S579D on actin-mediated activation of Drp1-WT GTPase activity. Our reasoning was as follows: if GTPase activation is a consequence of interaction between two neighboring GTPase domains, heteromeric assemblies between phosphorylated and non-phosphorylated Drp1 might have effects on GTPase activation. We used GFP-tagged Drp1 as the WT version of Drp1, to distinguish between WT and mutant proteins in co-sedimentation assays. In previous studies, we found that GFP-Drp1 also bound actin filaments[69].

First, we varied percentages of Drp1-S579D and GFP-Drp1-WT, while maintaining a constant total Drp1 concentration, to assess effects on both actin binding and actin-stimulated GTPase activity by the WT construct. In these experiments, we used concentrations of total Drp1 (1.3 μM) and actin (1 μM) that result in sub-saturating Drp1 on actin. There is a linear increase in the % GFP-Drp1 bound as the ratio of GFP-Drp1-WT:Drp1-S579D increases (**Figure 4-7A,B**), suggesting no effects of Drp1-S579D on Drp1-WT binding to filaments. Interestingly, there is a non-linear increase in actin-stimulated GTPase activity when GFP-Drp1-WT is titrated into Drp1-S579D, whereby no increase in GTPase activity is observed until 40% GFP-Drp1-WT is present (**Figure 4-7C**). A similar non-linear effect of Drp1-S579D occurs when un-tagged Drp1-WT is used (**Figure 4-7D**), indicating that the GFP-tag is not the source of the effect. This non-linear effect of Drp1-S579D on actin-activated Drp1-WT GTPase activity suggests that the S579D mutant slightly inhibits Drp1-WT activation when heteromerically bound to actin.

We tested an additional mutant, Drp1-K38A, for effects on Drp1-WT activity under activating conditions. This mutant is widely used as a dominant-negative in cellular experiments. An equivalent mutant in dynamin 1 is also a dominant-negative in cells, and causes increased

oligomerization of the wild-type protein [258]. As expected, Drp1-K38A displays no GTP hydrolysis in the absence or presence of actin filaments (**Figure 4-8A**), while still binding actin filaments with similar properties to Drp1-WT (**Figure 4-8B,C**).

The absence of all GTPase activity for Drp1-K38A allowed us to test its effect on the specific activity of Drp1-WT directly, when the two are bound to actin filaments. Interestingly, Drp1-K38A has a significant stimulatory effect on actin-activated GTPase activity for Drp1-WT in these assays. The maximum effect occurs at 30-40% Drp1-K38A, where Drp1-WT specific activity is over 3-fold higher than for 100% Drp1-WT (**Figure 4-8D**). We also compared GTPase activity of varying ratios of WT and K38A mutants with no actin present. In this case, K38A has an even more dramatic effect, with an 80:20 ratio of K38A:WT having 10-fold higher specific activity than 100% Drp1 (**Figure 4-8E**). A similar effect has previously been observed for dynamin-1 [258].

To verify that the stimulatory effect of Drp1-K38A on Drp1-WT is due to hetero-oligomerization, we utilized the Drp1 dimer mutant (Drp1-DM) in place of Drp1-WT. Drp1-DM has similar basal GTPase activity to Drp1-WT [70], but remains dimeric at all concentrations tested and does not form a sedimentable species in the presence of GMP-PCP [69]. As the percentage of Drp1-DM increases relative to Drp1-K38A, there is a linear increase in GTPase activity and no increase in specific activity (**Figure 4-8F**). We conclude that the stimulatory effect of Drp1-K38A on Drp1-WT GTPase activity is due to hetero-oligomerization effects.

These results suggest that Drp1-S579D reduces the activity of Drp1-WT when both are bound to actin filaments. In contrast, the GTPase activity of Drp1-WT is increased by the proximity of the catalytically inactive Drp1-K38A, either when bound to actin filaments or free in solution.

4.4 Discussion

In this study, we have tested the effects of two phospho-mimetic mutants on Drp1 activity. The S579D mutant is widely thought to be stimulatory to Drp1 activity in cells [85,105,145–150,153], while the S600D mutant has been shown to be inhibitory in most cellular studies [104,106,157,159], but stimulatory in others [155,156,158,257]. Both phospho-mimetic mutants display decreased oligomerization in a GTP-free state, but oligomerize in the presence of GTP. Both phospho-mimetic mutants display low GTPase stimulation by actin filaments, and reduced stimulation by cardiolipin or the Drp1 receptors Mff and MiD49. Drp1 phosphorylated *in vitro* on S579 displays similar attributes, with its cardiolipin-stimulated GTPase activity being even less than for its corresponding phospho-mimetic. When mixed with Drp1-WT on actin filamentsDrp1-S579D decreases the actin-stimulated activity of Drp1-WT.

The most striking aspect of these results is that phosphorylation at the S579 site, which has been associated with increased Drp1 activity in cellular studies, causes a decrease in activator-stimulated GTP hydrolysis, a fundamental read-out of biochemical Drp1 activity, GTP hydrolysis. One possible reason for this apparent contradiction is that the Drp1 isoforms used here: isoform 3 which contains none of the alternately spliced exons and isoform 6 which contains all three exons (**Figure 4-1**), do not display activation by S579 phosphorylation while other isoforms do. In the most comprehensive assessment to-date of Drp1 isoform abundance at the protein level [85], most cell and tissue types contain a mix of isoforms, with isoform 3 being the most abundant in some (but not all) cell lines. Nonetheless, other isoforms represent a significant proportion of total Drp1. The abundance of isoform 6 is unclear, but in commonly used cell lines such as HeLa is was not detected compared with four other isoforms [85]. Considering that two alternatively spliced exons lie near the S579 site, additional studies are needed to test isoform-specific effects of phosphorylation.

Another possibility is that the positive effect of S579 phosphorylation depends on additional factors. For instance, S579 phosphorylation might result in recruitment of a factor that is stimulatory to Drp1 oligomerization, GTPase activity, or ability to constrict membranes. It is unclear what such a factor might be, but one possibility is a member of the nucleotide diphosphate kinase (NDPK) family that can catalyze GTP synthesis from GDP and ATP. Cytosolic NDPK family members NME1 and NME2 have been shown to increase activity of dynamin1 and dynamin2, while mitochondrial NME4 increases activity of the mitochondrial inner membrane dynamin Opa1 under conditions of low GTP [259]. Physical interaction between these NDPKs and their respective dynamin

proteins might raise the local concentration of GTP, increasing GTPase activity. There is evidence that another NDPK, NME3, enriches on peroxisomes and mitochondria, and might work with Drp1 in a similar manner [260,261].

Our results also provide information as to Drp1's interaction with actin filaments. Both phospho-mimetic mutations, as well as S579 *in vitro* phosphorylation, eliminate actin-activated GTPase activity. This effect suggests that the Variable Domain is involved in the actin interaction. Interestingly, actin still seems to synergize with Mff for activation of the phospho-mimetics, suggesting that the important feature for this synergy is actin binding, not the activation that actin alone causes for Drp1.

It should be noted that, while the phospho-mimetic S579D mutant largely displays similar properties to S579-phosphorylated Drp1, the effects of phosphorylation are generally more pronounced. In particular, activation by cardiolipin-containing vesicles, as well as the synergy between actin and Mff, is practically eliminated for Drp1-phosphoS579, whereas it is partially inhibited for Drp1-S579D.

Finally, the inhibitory effect of Drp1-S579D on WT Drp1 GTPase activity is likely due to the decreased oligomerization of the mutant, which decreases the interactions between G domains necessary for GTPase activation. In contrast, the K38A mutation might activate WT Drp1 by stabilization of the oligomeric state. A similar effect of the equivalent mutation in dynamin-1, K44A, was described many years ago [258]. These results emphasize the effect of oligomerization on Drp1 activity, with mechanisms that increase oligomerization being likely to increase GTPase activity.

4.5 Materials and Methods

Plasmids. For bacterial expression, full-length of human DRP1 isoform 3 (NP_055681.2, UniProt ID O00429-4), truncated human MFF isoform 4 (UniProt ID Q9GZY8-4) (MFF-ΔTM), and MiD49Δ1-124 (mouse amino acids 125-454, UniProt ID Q5NCS9) have been described previously [69,122,255]. Quick Change mutagenesis was performed to make Drp1 mutants K38A, S579D, S600D, and Drp1 dimer mutant (Drp1-DM) [69,70].

Protein Expression, Purification.

DRP1 and its mutants were expressed and purified as previously described with modifications[69]. Briefly, DRP1 construct was expressed in One Shot BL21 Star (DE3) *Escherichia coli* in LB broth, induced by isopropyl-β-D-thiogalactoside (IPTG) at 16 °C for 16 hours when OD600 reached to 1.5. Cell pellets were resuspended in lysis buffer (100 mM Tris-Cl, pH 8.0, 500 mM NaCl, 1 mM dithiothreitol [DTT], 1 mM Ethylenediaminetetraacetic acid [EDTA], 2 µg/ml leupeptin, 10 µg/ml aprotinin, 2 µg/ml pepstatin A, 2 mM benzamidine, 1 µg/ml ALLN, and 1 µg/ml calpeptin) and lysed using a high-pressure homogenizer. The lysate was cleared by centrifugation at 40,000 rpm in Ti-45 rotor for 1 hour at 4°C. Avidin (20 µg/ml; PI-21128; Thermo Fisher Scientific, Waltham, MA) was added to the supernatant, and then was loaded onto Strep-Tactin Superflow resin (2-1206-025; IBA, Göttingen, Germany) by gravity flow. The column was washed with 20 column volumes (CV) of lysis buffer without protease inhibitors. To elute DRP1, 0.01 mg/ml HRV3C protease in lysis buffer without protease inhibitors was added for 16 hours at 4°C. The Strep-Tactin Superflow eluate was further purified by size exclusion chromatography on Superdex200 with DRP1-S200 buffer (20 mM HEPES pH 7.5, 150 mM KCl, 2 mM $MgCl_2$, 1 mM DTT, 0.5 mM EGTA), spin concentrated, frozen in liquid nitrogen, and stored at −80 °C.

MFF-ΔTM was expressed in Rosetta^{TM}2 BL21-(DE3) *Escherichia coli* (71400; EMD Millipore Corporation, Burlington, MA) in LB broth, induced by 1M IPTG at 30 °C for 4 h when OD600 reached to 1.5. Cell pellets were resuspended in lysis buffer (50 mM Tris-HCl, pH 7.5, 500 mM NaCl, 20 mM imidazole, pH 7.5, 1 mM DTT, 1 mM EDTA, 2 µg/ml leupeptin, 10 µg/ml aprotinin, 2 µg/ml pepstatin A, 2 mM benzamidine, 1 µg/ml ALLN, and 1 µg/ml calpeptin) and lysed using M-110 microfluidizer processor. The lysate was cleared by centrifugation at 40, 000 rpm in Ti45 for 40 minutes at 4°C, the supernatant was saved. Affinity capture was performed using FPLC and a HiTrap IMAC column (17-5248-01, GE Healthcare, Chicago, IL) equilibrated with IMAC-A buffer (50 mM Tris-HCl pH 7.5, 0.1 M NaCl, 20 mM imidazole). Cleared lysate was loaded onto the column with a rate of 3 mL/min and washed to baseline with IMAC-A. MFF was eluted from

the column with gradient step washes by IMAC-B buffer (50 mM Tris-HCl pH 7.5, 0.1 M NaCl, 500 mM imidazole): step1 10% IMAC-B for 5CV, step2 20% IMAC-B for 5CV, step3 100% for 5CV. Fractions from step3 were pooled and diluted 10-fold in ion exchange (IEX)-A buffer (50 mM Tris-HCl pH 7.5, 1 mM DTT). Diluted fractions were loaded onto a HiTrap Q anion exchange column (54816, EMD Millipore Corporation, Burlington, MA). The column was washed to baseline with IEX-A and MFF was eluted by IEX-B buffer (50 mM Tris-HCl pH 7.5, 1 M NaCl, 1 mM DTT) with a step gradient: step1 10% 5CV, linear 10-50% 30CV followed by linear 50-100% 5CV. Peak MFF fractions were concentrated by reloading onto the HiTrap IMAC column and eluted with 100% IMAC-B step wash. MFF fractions were pooled and further purified by size exclusion chromatography on Superdex200 with S200 buffer (20 mM HEPES, pH 7.4; 2 mM $MgCl_2$, 0.5 mM EGTA, 65 mM KCl, 1 mM DTT), spin concentrated (UFC903024, EMD Millipore Corporation, Burlington, MA), aliquots were frozen in liquid nitrogen, and stored at −80 °C.

MiD49 was expressed in One Shot BL21 Star (DE3) *Escherichia coli* (C6010-03; Life Technologies, Carlsbad, CA) in LB broth, induced by isopropyl-β-D-thiogalactoside (IPTG) at 16 °C for 16 h when OD600 reached 1.5. Cell pellets were resuspended in MiD lysis buffer (25 mM 4-(2-hydroxyethyl)-1-piperazineethanesulfonic acid [Hepes], pH 7.4, 500 mM NaCl, 1 mM dithiothreitol [DTT], 2 µg/ml leupeptin, 10 µg/ml aprotinin, 2 µg/ml pepstatin A, 2 mM benzamidine, 1 µg/ml calpain inhibitor I [ALLN], and 1 µg/ml calpeptin) and lysed using a high-pressure homogenizer (M-110L Microfluidizer Processor; Microfluidics, Newton, MA). The lysate was cleared by centrifugation at 40,000 rpm (type 45 Ti rotor; Beckman, Brea, CA) for 1 hour at 4°C and then was loaded onto Pierce™ Glutathione Agarose (16101; Thermofisher) by gravity flow. The column was washed with 20 column volumes (CV) of lysis buffer without protease inhibitors. To elute MiD49/51, 1 unit/µL thrombin (T4648, Sigma-Aldrich) or 0.01 mg/ml HRV3C protease in lysis buffer without protease inhibitors was added for 16 hours at 4°C. The protein eluate was captured by HiTrap IMAC column (17-5248-01, GE Healthcare, Chicago, IL) and eluted by IMAC-B buffer (50 mM Tris-HCl pH 7.5, 0.1 M NaCl, 500 mM imidazole). The His-trap protein eluate was further purified by size exclusion chromatography on Superdex200 (GE Biosciences, Piscataway, NJ) with S200 buffer (20 mM Hepes, pH 7.4, 65 mM KCl, 2 mM $MgCl_2$, 1 mM DTT, 0.5 mM ethylene glycol tetraacetic acid [EGTA]), spin concentrated (UFC903024, EMD Millipore Corporation, Burlington, MA), frozen in liquid nitrogen, and stored at −80 °C.

Rabbit skeletal muscle actin was extracted from acetone powder as previously described [237], and further gel-filtered on Superdex 75 16/60 columns (GE Healthcare). Actin was stored in G buffer (2 mM Tris, pH 8.0, 0.5 mM DTT, 0.2 mM ATP, 0.1 mM $CaCl_2$, and 0.01% NaN_3) at 4°C.

***In vitro* phosphorylation of Drp1 by ERK2**

For *in vitro* phosphorylation assay, 30μM purified Drp1 or Drp1-S600D was incubated with 100 nM ERK2 kinase (Thermo Fisher PV3313) at 30 °C for 4hrs. Reaction was conducted in 25mM Hepes, pH 7.4, 150 mM KCl, 10 mM $MgCl_2$, 2 mM DTT, 1 mM ethylene glycol tetraacetic acid [EGTA]), 1% Thesit. Phosphorylated Drp1 was further purified by size exclusion chromatography on Superdex200 with S200 buffer (20 mM HEPES, pH 7.4; 2 mM $MgCl_2$, 0.5 mM EGTA, 65 mM KCl, 1 mM DTT), spin concentrated (UFC903024, EMD Millipore Corporation, Burlington, MA), aliquots were frozen in liquid nitrogen, and stored at −80 °C.

Phospho-Drp1 analysis by mass spectroscopy

In vitro phosphorylated Drp1 were diluted in SDS-PAGE sample buffer and resolved by SDS-PAGE. Gels were stained with Coomassie blue staining. Bands were excised from the gel (2 μg Drp1) and analyzed for phosphorylated peptides by the Taplin mass spectrometry facility (Harvard Medical School).

Actin preparation for biochemical assays

For high-speed pelleting assay, actin filaments were polymerized from 20 μM monomers for 3 h at 23 °C by addition of a 10x stock of polymerization buffer (200 mM HEPES, pH 7.4, 650 mM KCl, 10 mM $MgCl_2$, 10 mM EGTA) to a final 1x concentration. For GTPase assay, actin monomers in G-buffer were incubated with AG1-X2 100–200 mesh anion exchange resin (Dowex; 1401241; Bio-Rad) at 4 °C for 5 min to remove ATP, followed by low-speed centrifugation. 20 μM actin filaments were polymerized as described before. To maintain ionic strength across all samples, an actin blank was prepared in parallel using G-buffer in place of actin monomers and used to dilute actin filaments as needed for each sample. DRP1 was diluted in MEHD buffer (20 mM HEPES, pH 7.4, 2 mM $MgCl_2$, 0.5 mM EGTA, 1 mM DTT) to adjust the ionic strength to the same as S200 buffer before biochemical assays.

Size exclusion Chromatography assays

Drp1 and Dpr1-phosS579 oligomeric distribution was determined by Superose 6 increase 10/300 GL SEC column (GE Biosciences) in S200 buffer (20 mM HEPES, pH7.4, 65 mM KCl, 2 mM

$MgCl_2$, 0.5 mM EGTA, 1 mM DTT). Protein at varying concentration was loaded onto the column in a total volume of 500 µL and gel-filtered with a flow rate of 0.4 mL/min.

MiD49 oligomer preparation

For in making MiD49 oligomer, 100µM purified MiD49Δ1-124 were incubated with 500µM Palmitoyl-CoA (Sigma-Aldrich, P9716) at 37 ℃ for 1hrs. Reaction was conducted in with S200 buffer (20 mM HEPES, pH 7.4; 2 mM $MgCl_2$, 0.5 mM EGTA, 65 mM KCl, 1 mM DTT). MiD49Δ1-124 mixture was further purified by size exclusion chromatography on Superdex200 with S200 buffer.

Liposome preparation

All lipids were purchased from Avanti Polar Lipids (Alabaster, AL). Liposomes were prepared by extrusion through polycarbonate membranes of 250nm pore diameter. 0% Cardiolipin liposome contained 65% DOPC (850375P, Avanti Polar lipid) and 35% DOPE (850725, Avanti Polar lipid). 25% Cardiolipin liposome contained 40% DOPC, 35% DOPE, and 25% cardiolipin (840012C, Avanti Polar lipid).

GTPase assay

DRP1 (0.75 µM) was mixed with indicated concentrations of MiD49, MFF and/or actin filaments in S200 buffer. Sample were incubated at 37 °C for 5 min. At this point, GTP was added to a final concentration of 500 µM to start the reaction at 37 °C. Reactions were quenched at designated time points by mixing 15 µL sample with 5 µL of 125 mM EDTA in a clear, flat-bottomed, 96-well plate (Greiner, Monroe, NC). Six time points were acquired for all conditions, either in a 12 min time range, or in a 45 min time range depending on reaction speed. Released phosphate was determined by addition of 150 µL of malachite green solution as previously described [69] Absorbance at 650 nm was measured 15 min after malachite green solution incubation. GTP hydrolysis rates were determined by plotting phosphate concentration as a function of time in the linear phase of the reaction.

Velocity Analytical Ultracentrifugation

Analytical ultracentrifugation was conducted using a Beckman Proteomelab XL-A and an AN-60 rotor. For sedimentation velocity analytical ultracentrifugation, Drp1 and its mutants in S200 buffer (65/150 mM KCl, 1 mM MgCl2, 0.5 mM EGTA, 1 mM DTT, 20 mM HEPES, pH 7.4) was centrifuged at either 5,000 (for oligomer) or 35,000 (for monomer) rpm with monitoring at 280 nm.

Data analyzed by Sedfit to determine sedimentation coefficient, frictional ratio, and apparent mass. Sedimentation coefficient reported is that of the major peak (at least 80% of the total analyzed mass) at OD_{280}.

High-speed pelleting assay

Interactions between DRP1 and actin were tested in the S200 buffer; DRP1 and actin were mixed as described and were incubated for 1 hr at room temperature in a 100 µl volume. After incubation, samples were centrifuged at 80,000 rpm for 20 min at 4°C in a TLA-100.1 rotor (Beckman). The supernatant was carefully removed. Pellets were washed three times with S200 buffer and then resuspended in 100 µl of SDS–PAGE sample buffer and resolved by SDS–PAGE (LC6025; Invitrogen, Carlsbad, CA). Gels were stained with Coomassie Brilliant Blue R-250 staining (1610400, Bio-Rad, Hercules, CA), and band intensity was analyzed using ImageJ software.

Figures

A

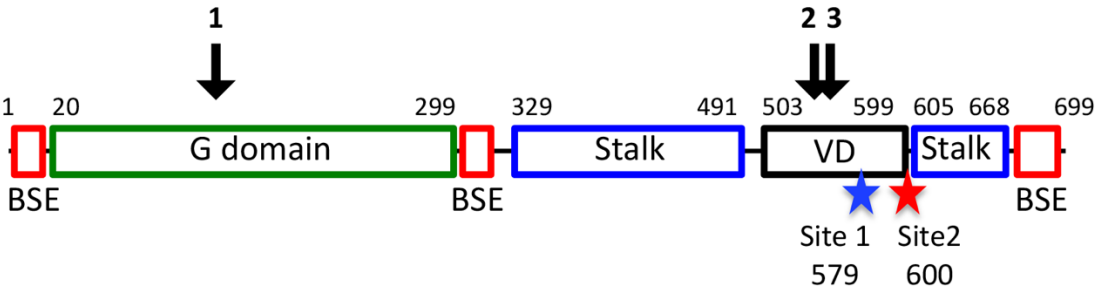

B

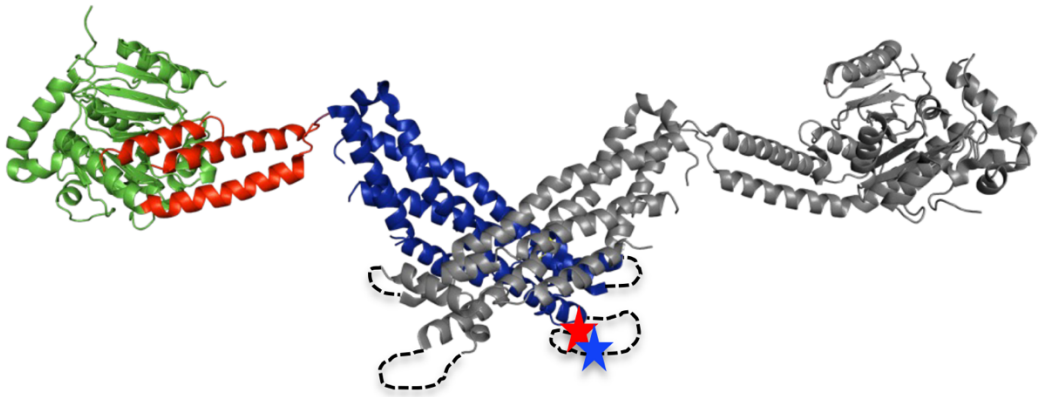

C

Isoform name*	Binary nomenclature**	UniProtKB	Protein length (amino acids)	Phosphorylation site 1	Phosphorylation site 2
isoform 1	0 1 1	o0042-1	736	616	637
isoform 2	0 0 1	o00429-3	710	590	611
isoform 3	0 0 0	o00429-4	699	579	600
isoform 4	0 1 0	o00429-2	725	605	626
isoform 5	0 x 0	o00429-5	710	590	611
isoform 6	1 1 1	o00429-6	749	629	650
isoform 7	x 1 1	o00429-7	533	413	434
isoform 8	1 1 0	o00429-8	738	618	639
isoform 9	1 0 0	o00429-9	712	592	613

Figure 4-1: Drp1 phosphorylation sites.

A) Domain organization of Drp1 isoform 3 (also called Drp1-000): GTPase domain (green), Bundle Signaling Element (BSE, red), stalk (blue), Variable Domain (VD, black, also called the B-insert in some publications). Blue and red stars indicate phosphorylation sites S579 (site 1) and S600 (site 2), respectively. Black arrows indicate locations of the three alternatively spliced inserts.

B) Structural model of Drp1 dimer (PDB 4BEJ) showing positions of phosphorylation sites S579 (blue star) and S600 (red star) on one subunit (color coded similar to panel A). Dashed loops for Variable Domain denote that this was not resolved in PDB 4BEJ.

C) Table listing positions of the phosphorylation sites corresponding to S579 (Site 1) and S600 (Site 2) in this paper for the nine Drp1 isoforms listed in UniProt, following isoform designation given by [86] and binary nomenclature used by [85]. Binary nomenclature based on presence (1) or absence (0) of the three alternatively spliced inserts, with 'x' denoting a variation of the indicated site (described in [86]).

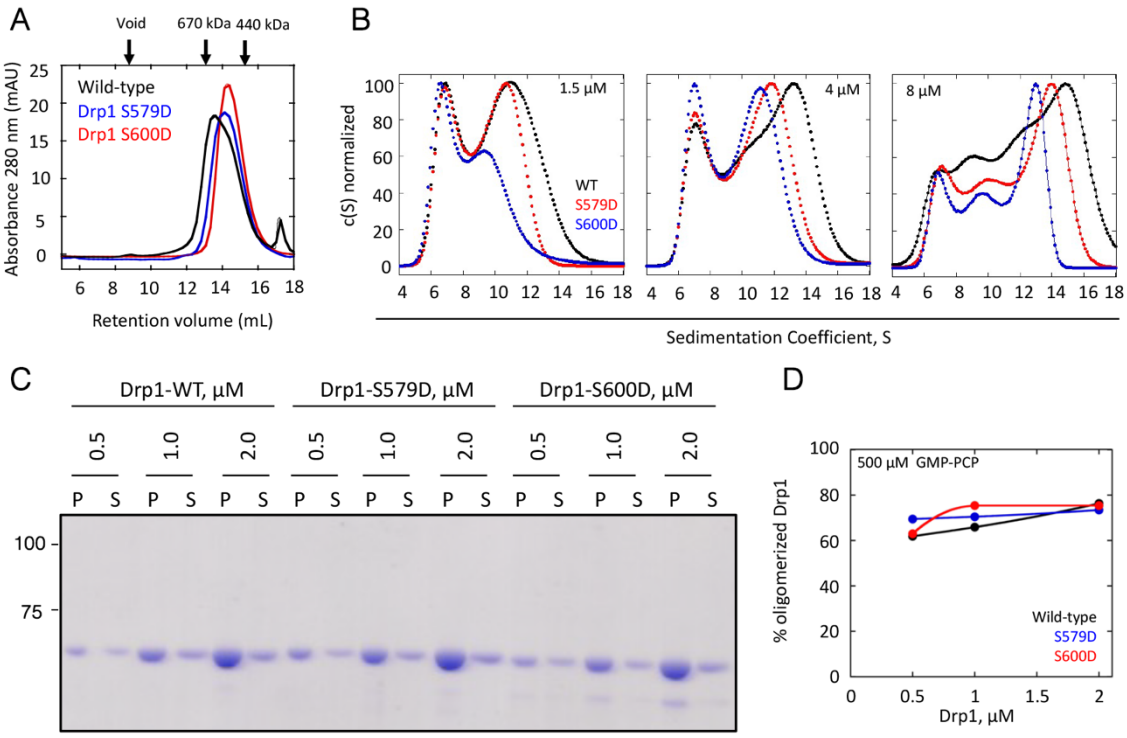

Figure 4-2: Oligomeric properties of Drp1 phospho-mimetic mutants.

A) Superose 6 gel filtration profiles of 30 µM of Drp1-WT, Drp1-S579D, and Drp1-S600D. At top are peak elution positions for two standards (thyroglobulin (670 kDa) and ferritin (440 kDa)) as well as the void volume position.

B) Velocity analytical ultracentrifugation of Drp1-WT, Drp1-S579D, and Drp1-S600D (black, red and blue respectively) at three concentrations: 8, 4 and 1.5 µM.

C) Coomassie-stained gel showing sedimentation assays graphed in panel C. Mass markers (in kDa) shown at left. P = pellet, S = supernatant.

D) Quantification of % oligomerized Drp1 from sedimentation assays of Drp1-WT, Drp1-S579D, and Drp1-S600D in the presence of the non-hydrolysable GTP analogue GMP-PCP (500 µM) at 0.5, 1.0, and 2.0 µM Drp1

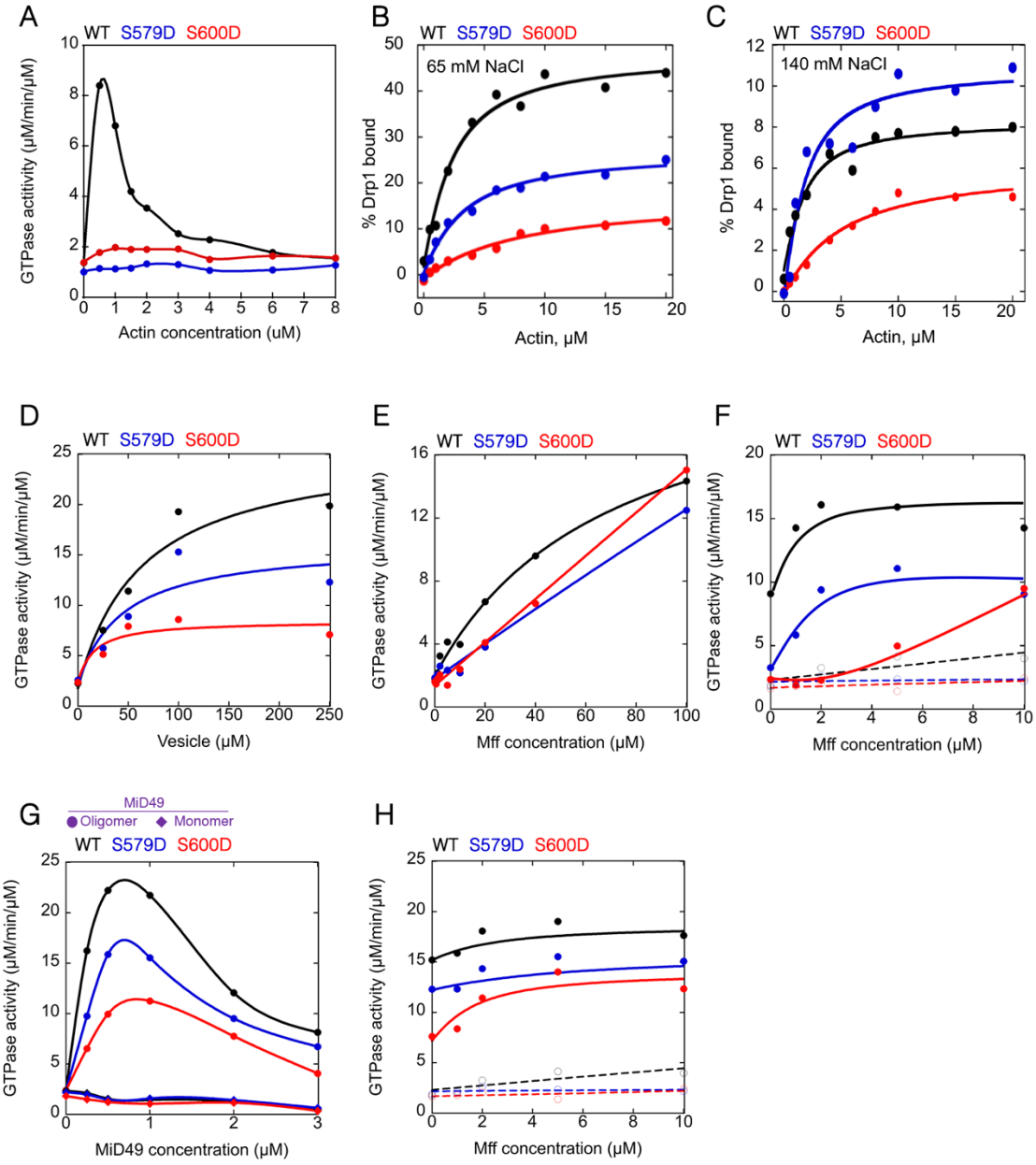
A
WT S579D S600D
GTPase actitivity (μM/min/μM)
Actin concentration (uM)
B
WT S579D S600D
65 mM NaCl
% Drp1 bound
Actin, μM
C
WT S579D S600D
140 mM NaCl
% Drp1 bound
Actin, μM
D
WT S579D S600D
GTPase activity (μM/min/μM)
Vesicle (μM)
E
WT S579D S600D
GTPase activity (μM/min/μM)
Mff concentration (μM)
F
WT S579D S600D
GTPase activity (μM/min/μM)
Mff concentration (μM)
G
MiD49
Oligomer Monomer
WT S579D S600D
GTPase activity (μM/min/μM)
MiD49 concentration (μM)
H
WT S579D S600D
GTPase activity (μM/min/μM)
Mff concentration (μM)

Figure 4-3: Effects of Drp1 phospho-mimetic mutants on actin binding and GTPase stimulation by actin, Mff, and MiD49.

Wild-type, Drp1 S579D, Drp1 S600D shown in black, blue, and red respectively for all panels. All GTPase assays contain 0.75 μM Drp1.

A) GTPase assays containing 0.75 μM Drp1 that was pre-incubated with the indicated concentration of actin filaments for 5 min before GTP addition. Activity expressed as μM phosphate released per minute per μM Drp1.

B) Graphs of % Drp1 bound versus actin concentration, from co-sedimentation assays at 65 mM, respectively (1.3 μM Drp1 in all cases). Raw data in Supplemental Figure 4-1.

C) Graphs of % Drp1 bound versus actin concentration, from co-sedimentation assays at 150 mM, respectively (1.3 μM Drp1 in all cases). Raw data in Supplemental Figure 4-1.

D) GTPase assays containing Drp1 that was pre-incubated with the indicated concentration of cardiolipin-containing vesicles (40% DOPC, 35% DOPE, 25% CL) for 5 min before GTP addition.

E) Comparison of Drp1-WT with Drp1-S579D and Drp1-S600D GTPase activities in the presence of the indicated concentration of Mff for 5 min before GTP addition.

F) Comparison of Drp1-WT with Drp1-S579D and Drp1-S600D GTPase activities in the presence of 0.5 μM actin filaments and the indicated concentration of Mff for 5 min before GTP addition. Values for Mff alone are indicated by open circles and dashed lines, while values for Mff/actin are indicated by closed circles and solid lines.

G) Comparison of Drp1-WT with Drp1-S579D and Drp1-S600D GTPase activities in the presence of the indicated concentration of MiD49 monomer (diamonds) or MiD49 oligomer (circles) for 5 min before GTP addition.

H) Comparison of Drp1-WT with Drp1-S579D and Drp1-S600D GTPase activities in the presence of 0.25 μM MiD49 oligomer and the indicated concentration of Mff for 5 min before GTP addition. Values for Mff alone are indicated by open circles and dashed lines, while values for Mff/MiD49 are indicated by closed circles and solid lines.

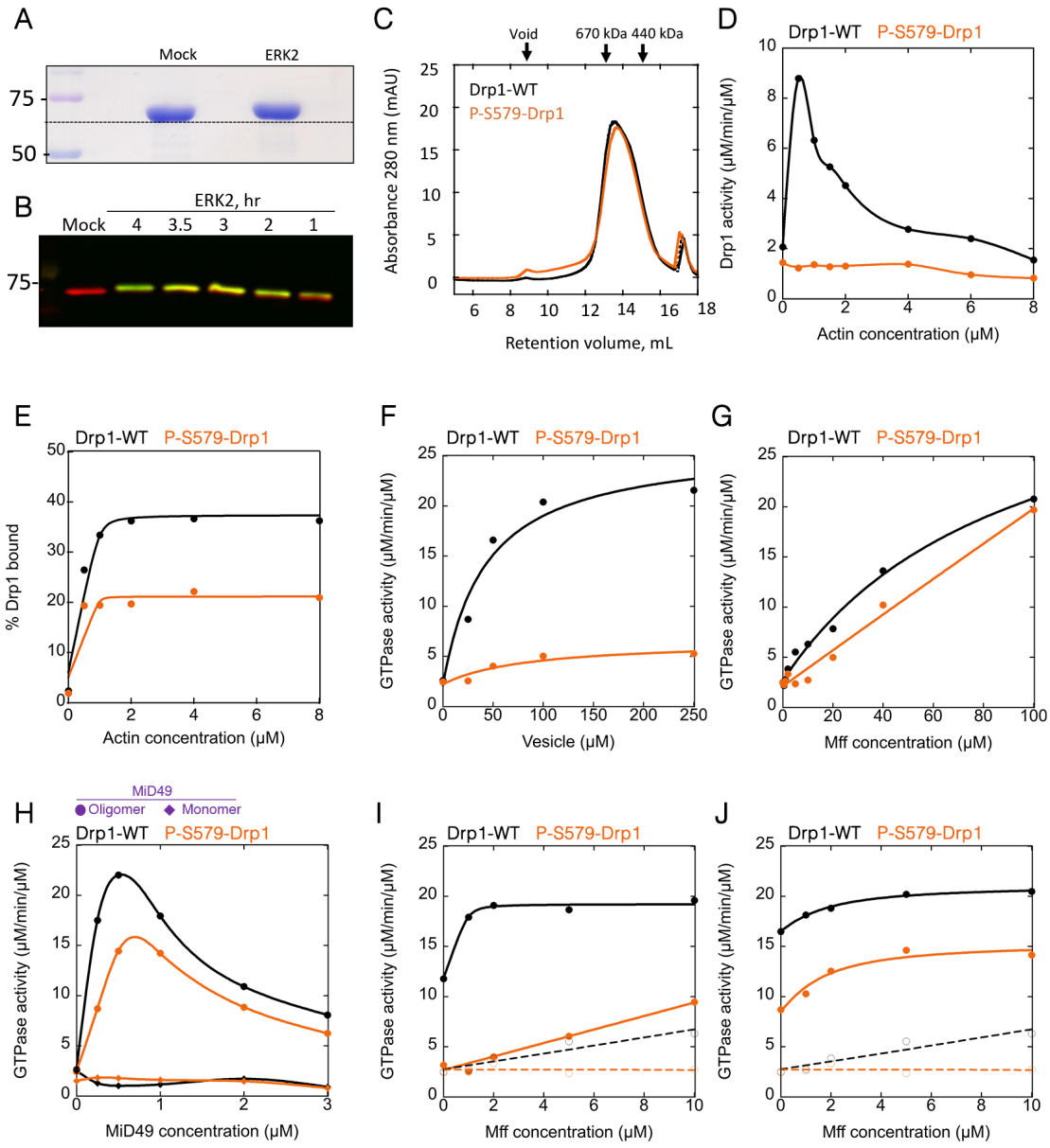
A
Mock
ERK2
75
50
B
ERK2, hr
Mock 4 3.5 3 2 1
75
C
Void
670 kDa 440 kDa
Drp1-WT
P-S579-Drp1
Absorbance 280 nm (mAU)
Retention volume, mL
D
Drp1-WT P-S579-Drp1
Drp1 activity (μM/min/μM)
Actin concentration (μM)
E
Drp1-WT P-S579-Drp1
% Drp1 bound
Actin concentration (μM)
F
Drp1-WT P-S579-Drp1
GTPase activity (μM/min/μM)
Vesicle (μM)
G
Drp1-WT P-S579-Drp1
GTPase activity (μM/min/μM)
Mff concentration (μM)
H
MiD49
Oligomer Monomer
Drp1-WT P-S579-Drp1
GTPase activity (μM/min/μM)
MiD49 concentration (μM)
I
Drp1-WT P-S579-Drp1
GTPase activity (μM/min/μM)
Mff concentration (μM)
J
Drp1-WT P-S579-Drp1
GTPase activity (μM/min/μM)
Mff concentration (μM)

Figure 4-4: Effects of Phospho-S579-Drp1 on actin binding and GTPase stimulation by actin, Mff, and MiD49

In all graphs, Drp1-WT and P-S579-Drp1 in black and orange, respectively. All GTPase assays contain 0.75 μM Drp1.

A) Coomassie-stained SDS-PAGE of Drp1 from either mock phosphorylation or ERK2 phosphorylation reactions (4 hr). 2 μg Drp1 on gel. Positions of size standards (in kDa) on left.

B) Western blot showing anti-Drp1 (red) and anti-phospho-S579-Drp1 (green) at varying times after ERK2 treatment.

C) Superose 6 gel filtration profiles of WT and P-S579-Drp1. At top are peak elution positions for two standards (thyroglobulin (670 kDa) and ferritin (440 kDa)) as well as the void volume position.

D) GTPase assays containing Drp1 that was pre-incubated with the indicated concentration of actin filaments for 5 min before GTP addition. Activity expressed as μM phosphate released per minute per μM Drp1.

E) Graph of % Drp1 bound versus actin concentration, from co-sedimentation assays at 65 mM NaCl. Raw data in Supplemental Figure S4-2.

F) GTPase assays containing Drp1 that was pre-incubated with the indicated concentration of cardiolipin-containing vesicles (mM total lipid, vesicles contain 40% DOPC, 35% DOPE, 25% CL) for 5 min before GTP addition.

G) Comparison of WT and P-S579-Drp1 GTPase activities in the presence of the indicated concentration of Mff for 5 min before GTP addition.

H) Comparison of WT and P-S579-Drp1 GTPase activities in the presence of the indicated concentration of MiD49 monomer (diamond) or MiD49 oligomer (circle) for 5 min before GTP addition.

I) Comparison of WT and P-S579-Drp1 GTPase activities in the presence of 0.5 μM actin filaments and the indicated concentration of Mff for 5 min before GTP addition. Values for Mff alone are indicated by open circles and dashed lines, while values for Mff/actin are indicated by closed circles and solid lines.

J) Comparison of WT and P-S579-Drp1 GTPase activities in the presence of 0.25 μM MiD49 oligomer and the indicated concentration of Mff for 5 min before GTP addition. Values for Mff alone are indicated by open circles and dashed lines, while values for Mff/MiD49 are indicated by closed circles and solid lines.

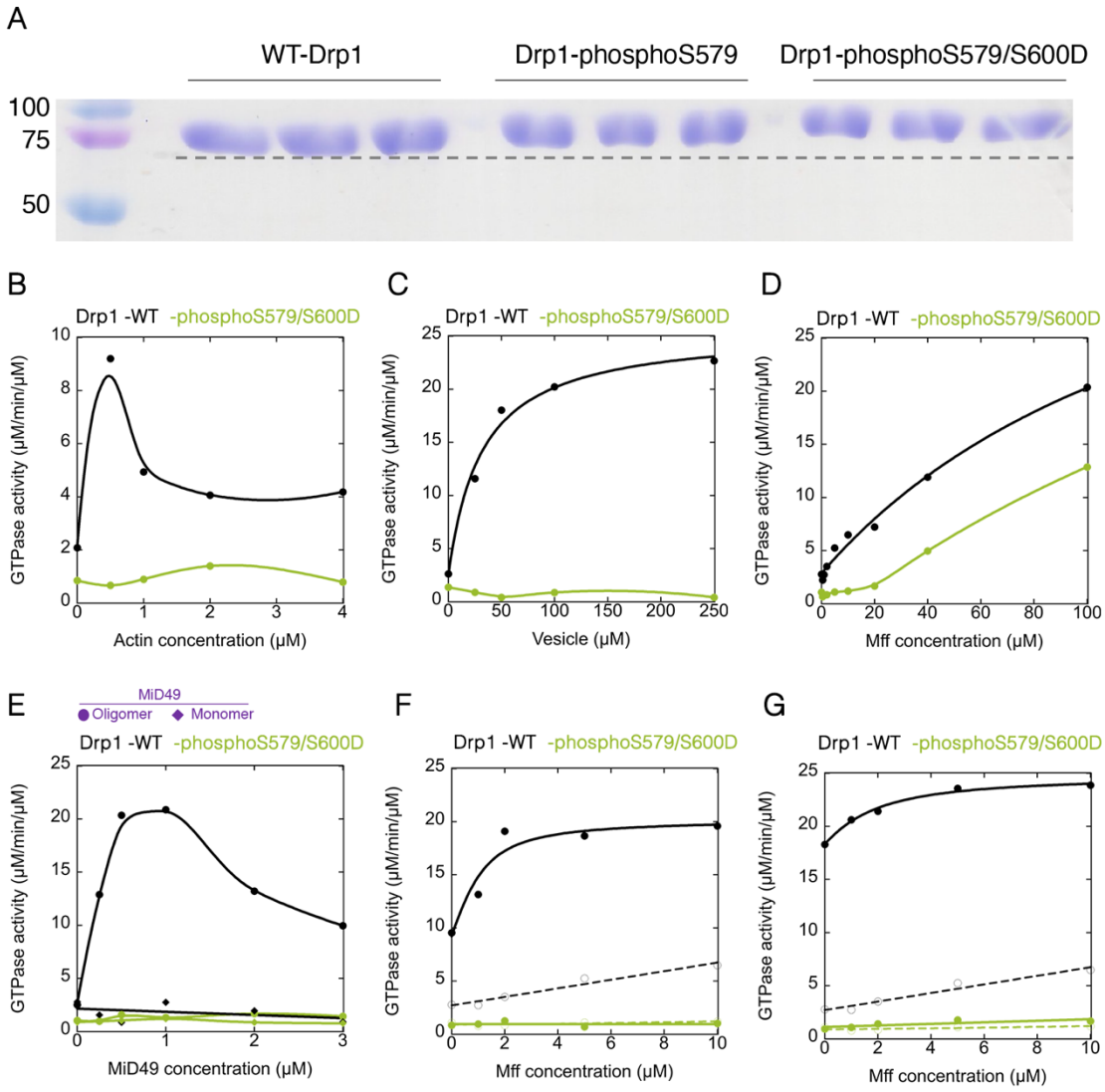
A
WT-Drp1
Drp1-phosphoS579
Drp1-phosphoS579/S600D
100
75
50
B
Drp1 -WT -phosphoS579/S600D
GTPase activity (μM/min/μM)
Actin concentration (μM)
C
Drp1 -WT -phosphoS579/S600D
GTPase activity (μM/min/μM)
Vesicle (μM)
D
Drp1 -WT -phosphoS579/S600D
GTPase activity (μM/min/μM)
Mff concentration (μM)
E
MiD49
Oligomer
Monomer
Drp1 -WT -phosphoS579/S600D
GTPase activity (μM/min/μM)
MiD49 concentration (μM)
F
Drp1 -WT -phosphoS579/S600D
GTPase activity (μM/min/μM)
Mff concentration (μM)
G
Drp1 -WT -phosphoS579/S600D
GTPase activity (μM/min/μM)
Mff concentration (μM)

Figure 4-5: Effects of Drp1-phosphoS579/S600D on GTPase stimulation.

In all graphs, Drp1-WT and Drp1-phosphoS579/S600D in black and green, respectively. All GTPase assays contain 0.75 μM Drp1.

A) Coomassie-stained SDS-PAGE of Drp1 from either Drp1- mock phosphorylation, Drp1-ERK2 phosphorylation, or Drp1-S600D- ERK2 phosphorylation reactions (4 hr). 2 μg Drp1 on gel. Positions of size standards (in kDa) on left.

B) GTPase assays containing Drp1 that was pre-incubated with the indicated concentration of actin filaments for 5 min before GTP addition. Activity expressed as μM phosphate released per minute per μM Drp1.

C) GTPase assays containing Drp1 that was pre-incubated with the indicated concentration of cardiolipin-containing vesicles (40% DOPC, 35% DOPE, 25% CL) for 5 min before GTP addition.

D) Comparison of Drp1-WT and Drp1-phosphoS579/S600D GTPase activities in the presence of the indicated concentration of Mff for 5 min before GTP addition.

E) Comparison of Drp1-WT and Drp1-phosphoS579/S600D activities in the presence of the indicated concentration of MiD49 monomer (diamond) or MiD49 oligomer (circle) for 5 min before GTP addition.

F) Comparison of Drp1-WT and Drp1-phosphoS579/S600D GTPase activities in the presence of 0.5 μM actin filaments and the indicated concentration of Mff for 5 min before GTP addition. Values for Mff alone are indicated by open circles and dashed lines, while values for Mff/actin are indicated by closed circles and solid lines.

G) Comparison of Drp1-WT and Drp1-phosphoS579/S600D activities in the presence of 0.25 μM MiD49 oligomer and the indicated concentration of Mff for 5 min before GTP addition. Values for Mff alone are indicated by open circles and dashed lines, while values for Mff/MiD49 are indicated by closed circles and solid lines.

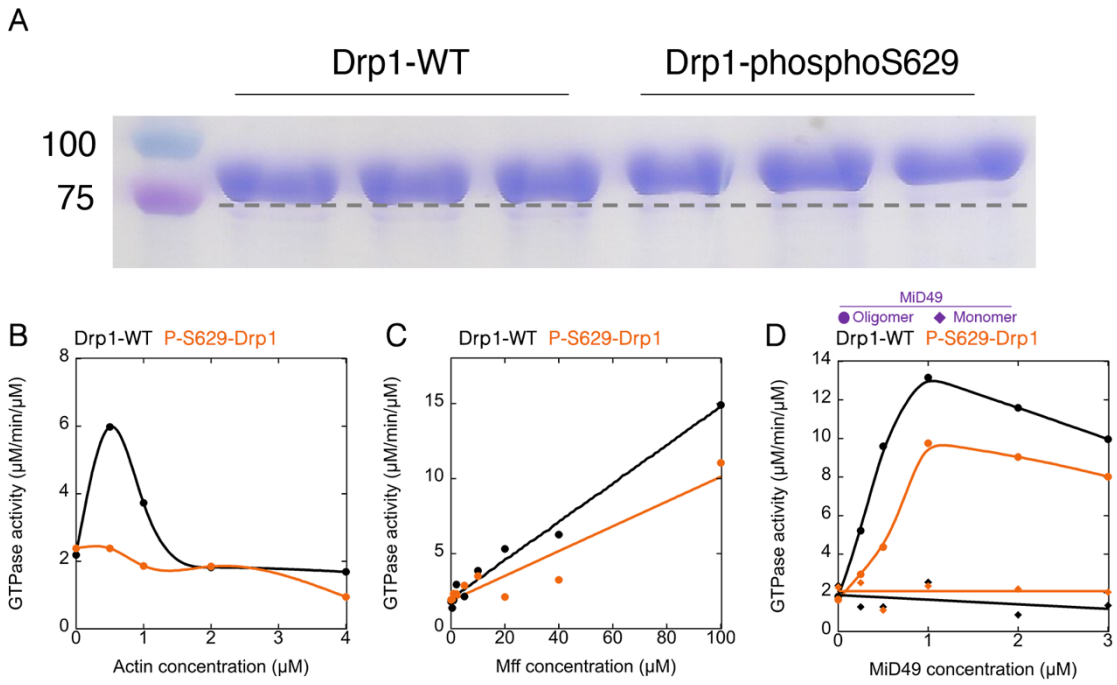

Figure 4-6: Effects of Erk2 phosphorylation on GTPase activity of Drp1 isoform 6.

In all graphs, Drp1-WT and Drp1-phosphoS629 in black and orange, respectively. All GTPase assays contain 0.75 μM Drp1.

A) Coomassie-stained SDS-PAGE of Drp1 isoform 6 from either Drp1- mock phosphorylation or Drp1- ERK2 phosphorylation (4 hr). 2 μg Drp1 on gel. Positions of size standards (in kDa) on left.

B) GTPase assays containing Drp1 that was pre-incubated with the indicated concentration of actin filaments for 5 min before GTP addition. Activity expressed as μM phosphate released per minute per μM Drp1.

C) Comparison of Drp1-WT and P-S629-Drp1 GTPase activities in the presence of the indicated concentration of Mff for 5 min before GTP addition.

D) Comparison of Drp1-WT and P-S629-Drp1 activities in the presence of the indicated concentration of MiD49 monomer (diamonds) or MiD49 oligomer (circles) for 5 min before GTP addition.

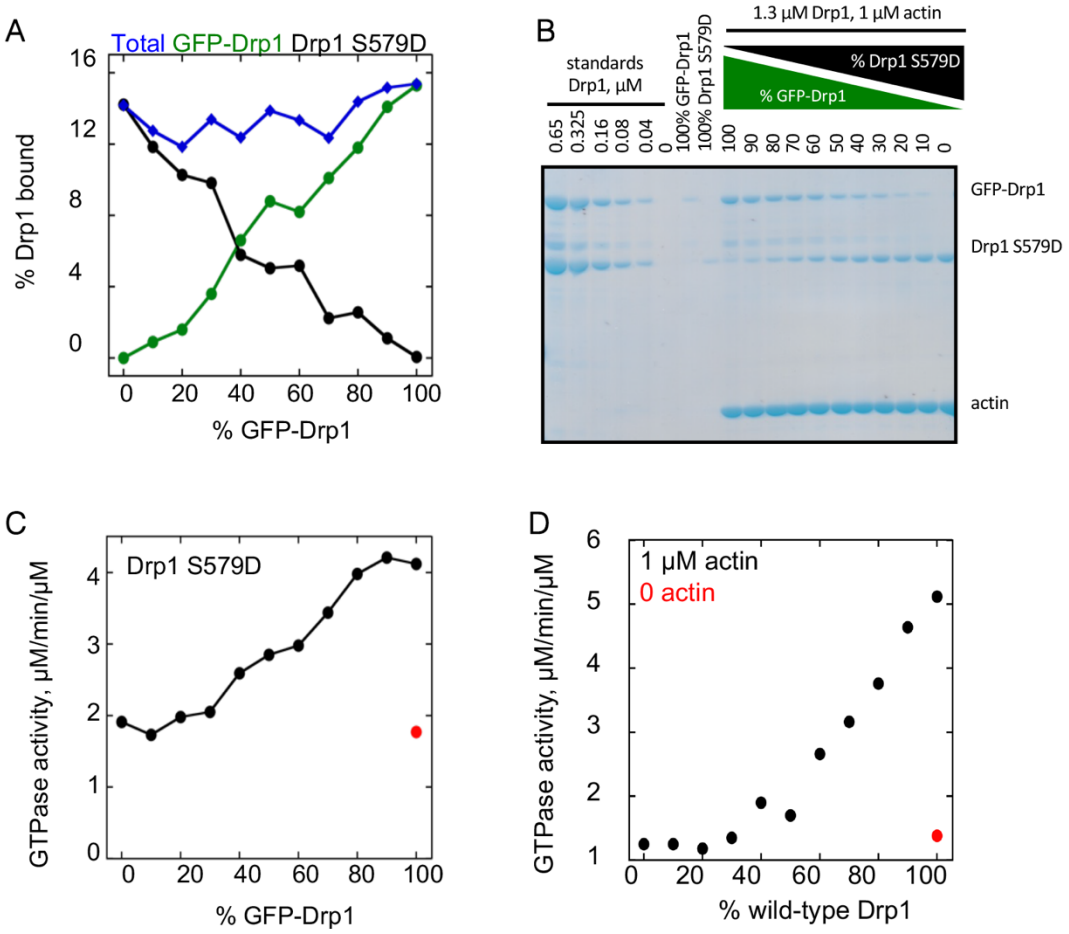

Figure 4-7: Drp1 phospho-mimetic mutants reduce the ability of actin filaments to activate wild-type Drp1.

In all panels, the actin filament concentration is constant at 1 µM, and the total Drp1 concentration (combination of GFP-Drp1 and phospho-mimetic mutant Drp1 without GFP) is constant at 1.3 µM.

A) Graph of Drp1 binding to actin filaments with varying ratios of GFP-Drp1-WT:Drp1-S579D.

B) Corresponding Coomassie gels for binding assays quantified in panel A.

C) GTPase activity of Drp1 at varying ratios of GFP-Drp1-WT:Drp1-S579D in the presence of actin filaments. Red point represents GTPase activity of GFP-Drp1-WT in the absence of actin filaments.

D) GTPase activity of Drp1 (without the GFP tag) at varying ratios of Drp1-WT:Drp1-S579D in the presence of actin filaments. Red point represents GTPase activity of Drp1-WT in the absence of actin filaments.

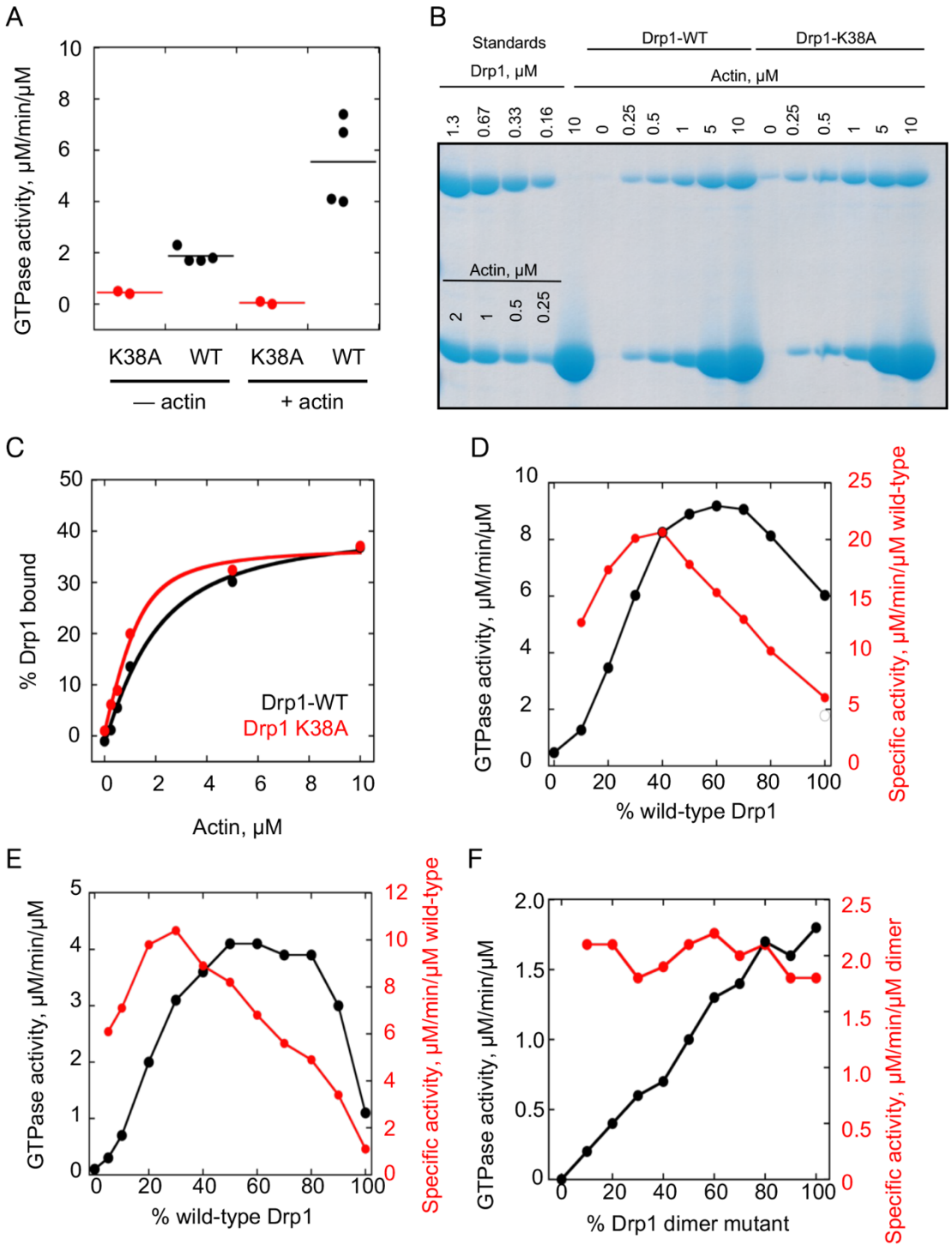

Figure 4-8: Drp1-K38A mutant stimulates the GTPase activity of Drp1-WT.

A) GTPase activity of Drp1-WT or Drp1-K38A (1.3 μM) in the presence or absence of actin filaments (1 μM).

B) Coomassie-stained SDS-PAGE of Drp1/actin co-sedimentation at 65 mM NaCl, with 1.3 μM Drp1-WT or Drp1-K38A and varying actin. Standards of known μM amounts of Drp1-WT and actin on left, pellets from sedimentation assays on right.

C) Graph of % Drp1 in the pellet for Drp1-WT and Drp1-K38A as a function of actin concentration.

D) GTPase activity of Drp1 at varying ratios of Drp1-WT:Drp1-K38A (1.3 μM total Drp1) in the presence of actin filaments (1 μM). Black line denotes total Drp1 specific activity (factoring both WT and K38A mutant) while red line denotes specific activity of Drp1-WT.

E) GTPase activity of Drp1 at varying ratios of Drp1-WT:Drp1-K38A (1.3 μM total Drp1) in the absence of actin filaments. Black line and red lines as described in panel D.

F) GTPase activity of Drp1 at varying ratios of Drp1-DM:Drp1-K38A (1.3 μM total Drp1) in the presence of actin filaments (1 μM). Black line denotes total Drp1 specific activity (factoring both Drp1-DM and K38A mutant) while red line denotes specific activity of Drp1-DM. DM, dimer mutant.

Supplemental Figures

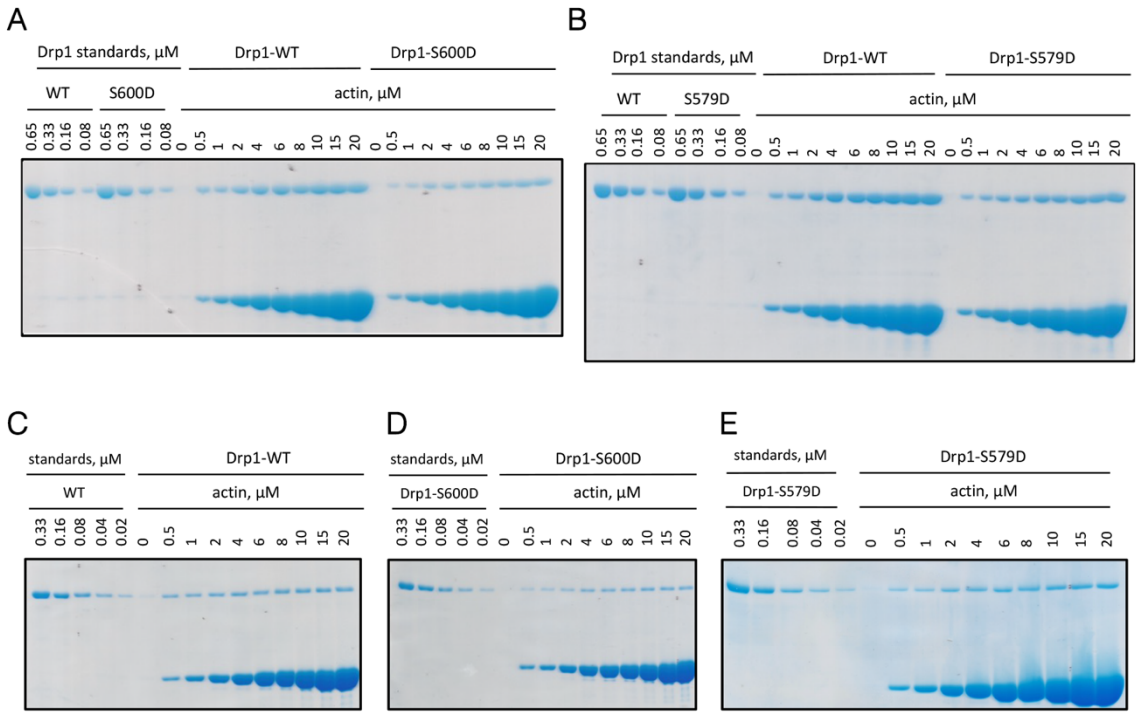

Figure S4-1: Drp1/actin co-sedimentation assays for phospho-mimetic mutants.

A) Coomassie-stained SDS-PAGE of Drp1/actin co-sedimentation assay at 65 mM NaCl similar to graph in Figure 3A. Standards of known µM amounts of Drp1 on left, pellets from sedimentation assays on right. A) Comparison of Drp1-WT with Drp1-S600D.

B) Comparison of Drp1-WT with Drp1-S579D.

C) Coomassie-stained SDS-PAGE of Drp1/actin co-sedimentation assay at 140 mM NaCl similar to graph shown in Figure 4-3B. Standards of known µM amounts of Drp1 on left, pellets on right. C) Drp1-WT. D) Drp1-S600D. E) Drp1-S579D. 1.3 µM Drp1 used in all assays.

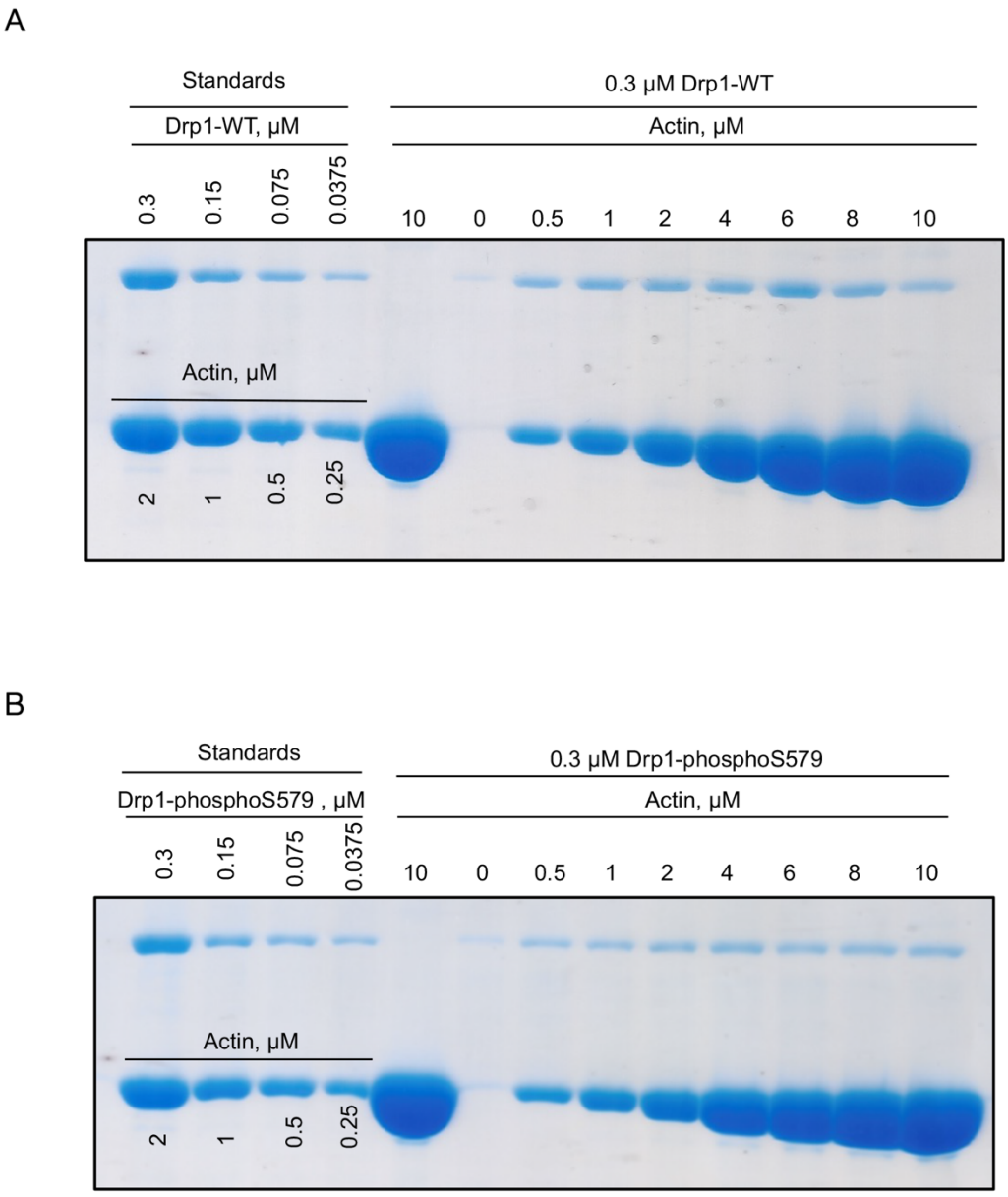

Figure S4-2: Drp1/actin co-sedimentation assays for ERK2-phosphorylated Drp1.
Coomassie-stained SDS-PAGE of Drp1/actin co-sedimentation assay at 65 mM NaCl similar to graph in Figure 4-4E. Standards of known μM amounts of Drp1 on left, pellets from sedimentation assays on right.

A) Coomassie-stained SDS-PAGE of Drp1/actin co-sedimentation of Drp1-WT.

B) Coomassie-stained SDS-PAGE of Drp1/actin co-sedimentation of Drp1-phosphoS579.

Chapter V: Overall Model and Future Directions

My study here investigates the mechanism for mitochondrial division and proposes a new model. This model is derived from my own findings as well as from previous research (**Figure 5-1**). Some aspects of the model are speculative. We divide Drp1 assembly into two stages, "nucleation" and "elongation", akin to actin polymerization. The nucleation step can be triggered by three known signals: increased cytoplasmic calcium, increased fatty acyl-CoA, or disruption of mitochondrial membrane integrity. Increased cytosolic calcium activates the ER-bound formin INF2, leading to actin polymerization at ER-mitochondrial contact sites. A rise in fatty acyl-CoA levels causes MiD49/MiD51 oligomerization on the OMM. Mitochondrial membrane disruption causes exposure of cardiolipin on the OMM. Any of these three events (actin polymerization, MiD49/51 oligomerization, or cardiolipin exposure) can recruit Drp1 from the cytosol and initiate Drp1 oligomerization ('nucleation'). These Drp1 oligomers then transfer to Mff, which mediates 'elongation' of the Drp1 oligomers into a productive ring around the OMM.

There are other levels of regulation as well, such as Drp1 and Mff phosphorylation. Mff phosphorylation serves as another regulator for triggering mitochondrial division, with AMPK playing a role in this pathway. However, a comprehensive understanding of this process requires further biochemical and cell studies. As for Drp1 phosphorylation, it is unclear what the specific effect of the two phosphorylation events (S579 and S600) is on Drp1. S579 phosphorylation is commonly thought of as stimulatory to division, but its biochemical effect on purified Drp1 is to decrease GTPase activity, suggesting the involvement of other regulators in the cellular context. S579 phosphorylation is reported to be inhibitory in many cellular contexts, and our biochemical results also show inhibition of GTPase activity. However, several cellular studies report S600-mediated stimulation of mitochondrial division, suggesting that there is more to learn here.

There are multiple future directions for this project. Although it is difficult to list them all here, and careful readers would come up with interesting ideas of their own, here are some of the future directions I believe would contribute greatly for understanding mitochondrial division.

- Understanding the mechanism of how Mff triggers the activation of Drp1

Although we've demonstrated the vital role of Mff oligomerization in Drp1 activation, the precise mechanism by which Mff initiates this activation remains unclear. The challenge lies in the disordered structure of the cytosolic Mff domain. Through the use of supported lipid bilayers and

fluorescence microscopy, I observed that His-Mff can self-assemble into puncta of a specific size on the lipid membrane, indicating a stable oligomer structure. These oligomers, in turn, effectively recruit Drp1 (**Figurer 5-2**). Resolving the structure of Mff or the Drp1-Mff complex would yield valuable insights. Another avenue worth exploring is understanding the cellular signals that prompts Mff accumulation at the mitochondrial division site. Published work suggests that adenosine monophosphate (AMP)–activated protein kinase (AMPK), a sensor of cellular energy levels, activates Mff through phosphorylation. Investigating the signaling pathway involved in this activation could provide further clarity.

- Understanding specific roles for MiD49 and MiD51.

While MiD49 and MiD51 exhibit remarkably similar structures, unraveling their distinct roles remains a fascinating challenge. Clearly, their nucleotide binding sites are somewhat different, since MiD51 can bind ADP and GDP whereas MiD49 does not display measurable affinity. So, it is possible that these proteins respond to sub-sets of fatty acyl-CoA ligands in a cellular context. One approach to explore these potential differences is to generate MiD49-null and MiD51-null cells and observe how they respond to various physiological conditions. Additionally, investigating whether MiD49 and MiD51 form heterogeneous oligomers biochemically could shed light on the functions of each receptor. Furthermore, though we have established that MiD49/51 can form large oligomers to activate Drp1 activity, the specific oligomeric state required for this activation is still unknown. Examining the oligomer structure of MiD49/51 might provide valuable insights in this regard.

- Exploring possible regulators for phosphorylated Drp1

The biochemical investigations presented here reveal that phosphorylation at either S579 or S600 sites alone is insufficient to trigger Drp1 activity and diminishes the synergistic effects with other regulators. These findings imply the involvement of additional regulators in the regulation processes. Yet, uncovering these regulators poses a long-term challenge, given the contradictory effects of phosphorylation observed in different cell lines. Nevertheless, the complexity of this question does not diminish its significance and intrigue.

Figures

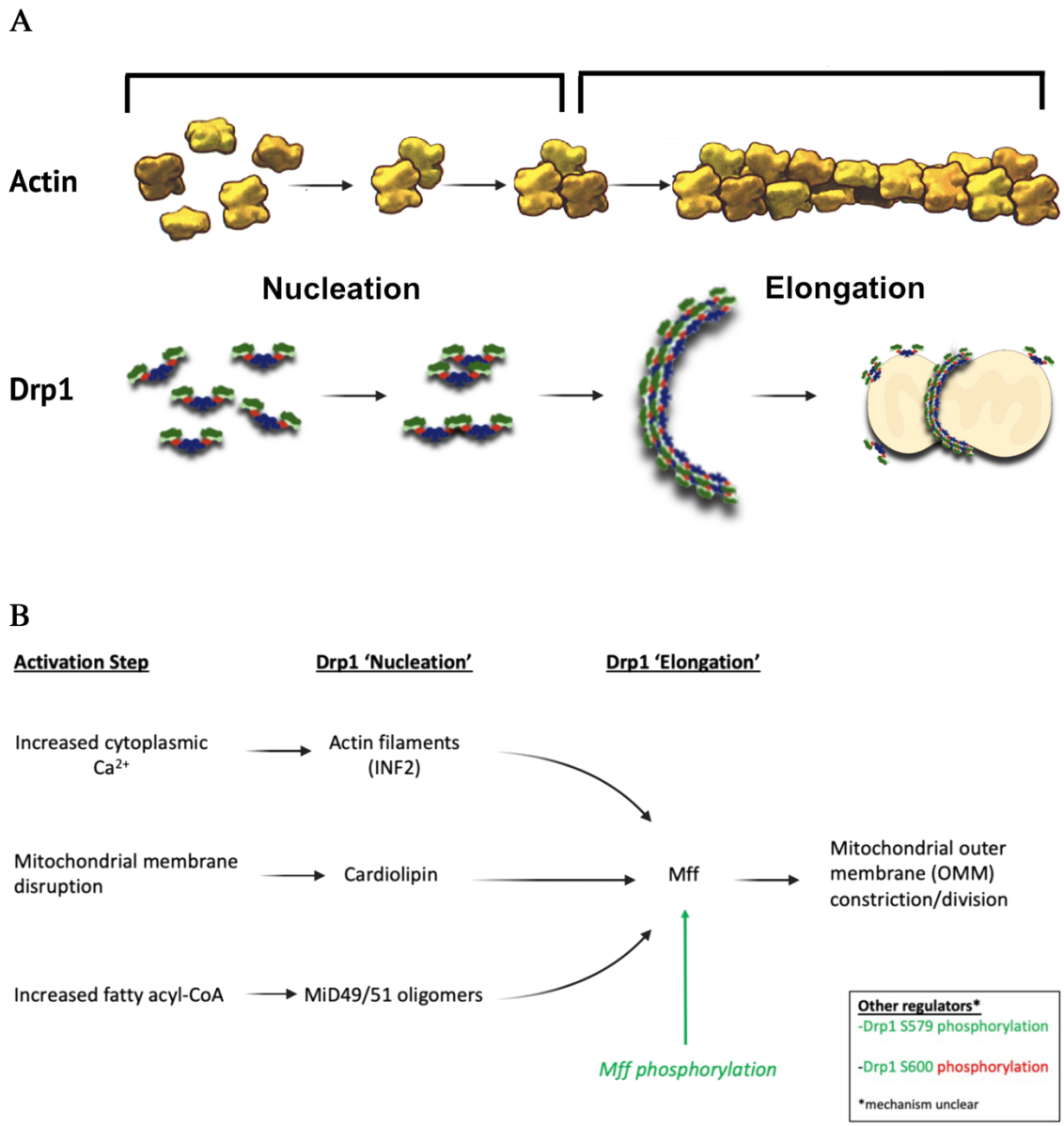

Figure 5-1: Overall Model for mitochondrial division in this study.

A) Model showing nucleation and elongation of Drp1, relating this to actin nucleation and elongation, figure is adapted from Molecular Biology of the Cell (Edition 5).

B) Pathway of Drp1 nucleation through three distinct stimuli, followed by elongation through Mff. Other regulatory mechanisms (phosphorylation of Mff and Drp1) are also shown.

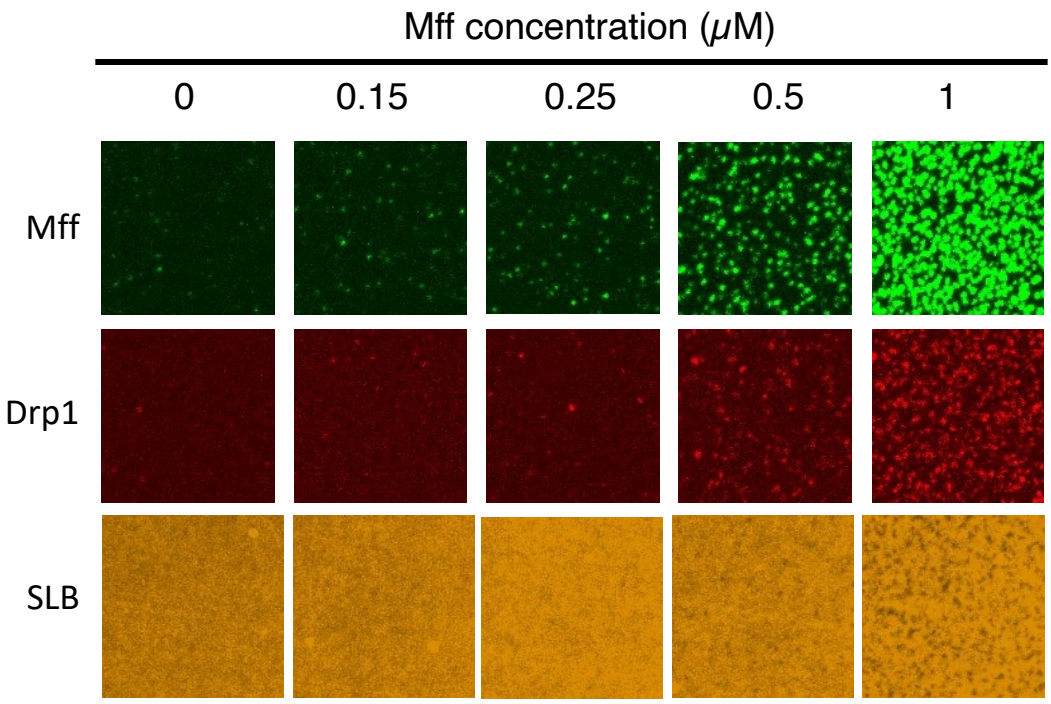

Figure 5-2: Mff forms stable puncta on the supported lipid bilayer.

Cysteine-Strep-MffΔTM-His is labeled by Fluorescein-5-Maleimide, Drp1 is labeled by Cy5-succinamide. Supported lipid bilayer (SLB) liposome is consist of Rho-DOPC:DOPC:CL:Ni-NTA; 0.5:94:5:0.5 mol%. Varying concentration of Mff is incubated with SLB for 40 mins, then wash twice with PBS buffer. After wash, 1μM Drp1 is flowed and incubate for an additional 10 mins. Then PBS wash again to remove extra Drp1 and capture images.

Chapter VI:

Literature cited

1. Vafai, S. B. & Mootha, V. K. Mitochondrial disorders as windows into an ancient organelle. *Nat. 2012 4917424* **491**, 374–383 (2012).

2. Picard, M. & Shirihai, O. S. Mitochondrial signal transduction. *Cell Metabolism* vol. 34 1620–1653 (2022).

3. Gray, M. W. Mosaic nature of the mitochondrial proteome: Implications for the origin and evolution of mitochondria. *Proc. Natl. Acad. Sci. U. S. A.* **112**, 10133–10138 (2015).

4. Karnkowska, A. *et al.* A eukaryote without a mitochondrial organelle. *Curr. Biol.* **26**, 1274–1284 (2016).

5. Wiesner, R. J., Rüegg, J. C. & Morano, I. Counting target molecules by exponential polymerase chain reaction: Copy number of mitochondrial DNA in rat tissues. *Biochem. Biophys. Res. Commun.* **183**, (1992).

6. Wang, X. *et al.* Mitochondrial flashes regulate ATP homeostasis in the heart. *Elife* **6**, (2017).

7. Roger, A. J., Muñoz-Gómez, S. A. & Kamikawa, R. The Origin and Diversification of Mitochondria. *Current Biology* vol. 27 R1177–R1192 (2017).

8. Sagan, L. On the origin of mitosing cells. *J. Theor. Biol.* **14**, (1967).

9. Yang, D., Oyaizu, Y., Oyaizu, H., Olsen, G. J. & Woese, C. R. Mitochondrial origins. *Proc. Natl. Acad. Sci. U. S. A.* **82**, 4443–4447 (1985).

10. Wang, Z. & Wu, M. An integrated phylogenomic approach toward pinpointing the origin of mitochondria. *Sci. Rep.* **5**, (2015).

11. Taanman, J. W. The mitochondrial genome: Structure, transcription, translation and replication. *Biochimica et Biophysica Acta - Bioenergetics* vol. 1410 103–123 (1999).

12. Knoll, N. *et al.* Mitochondrial DNA variants in obesity. *PLoS One* **9**, (2014).

13. Miyazono, Y. *et al.* Uncoupled mitochondria quickly shorten along their long axis to form indented spheroids, instead of rings, in a fission-independent manner. *Sci. Rep.* **8**, 1–14 (2018).

14. Kage, F., Vicente-Manzanares, M., McEwan, B. C., Kettenbach, A. N. & Higgs, H. N. Myosin II proteins are required for organization of calcium-induced actin networks upstream of mitochondrial division. *Mol. Biol. Cell* **33**, (2022).

15. Collins, T. J., Berridge, M. J., Lipp, P. & Bootman, M. D. Mitochondria are morphologically and functionally heterogeneous within cells. *EMBO J.* **21**, 1616–1627 (2002).

16. Rausser, S. *et al.* Version R2: Mitochondrial phenotypes in purified human immune cell subtypes and cell mixtures. *Elife* **10**, (2021).

17. Fung, T. S., Chakrabarti, R. & Higgs, H. N. The multiple links between actin and mitochondria. *Nature Reviews Molecular Cell Biology* vol. 24 651–667 (2023).

18. Wai, T. & Langer, T. Mitochondrial Dynamics and Metabolic Regulation. *Trends in Endocrinology and Metabolism* vol. 27 105–117 (2016).

19. Yapa, N. M. B., Lisnyak, V., Reljic, B. & Ryan, M. T. Mitochondrial dynamics in health and disease. *FEBS Letters* vol. 595 1184–1204 (2021).

20. Bogenhagen, D. & Clayton, D. A. The number of mitochondrial deoxyribonucleic acid genomes in mouse L and human HeLa cells. Quantitative isolation of mitochondrial deoxyribonucleic acid. *J. Biol. Chem.* **249**, 7991–7995 (1974).

21. Satoh, M. & Kuroiwa, T. Organization of multiple nucleoids and DNA molecules in mitochondria of a human cell. *Exp. Cell Res.* **196**, 137–140 (1991).

22. Mishra, P. & Chan, D. C. Mitochondrial dynamics and inheritance during cell division, development and disease. *Nat. Rev. Mol. Cell Biol.* **15**, 634–646 (2014).

23. Cason, S. E. & Holzbaur, E. L. F. Selective motor activation in organelle transport along axons. *Nature Reviews Molecular Cell Biology* vol. 23 699–714 (2022).

24. Sheng, Z. H. & Cai, Q. Mitochondrial transport in neurons: Impact on synaptic homeostasis and neurodegeneration. *Nature Reviews Neuroscience* vol. 13 77–93 (2012).

25. Li, Z., Okamoto, K. I., Hayashi, Y. & Sheng, M. The importance of dendritic mitochondria in the morphogenesis and plasticity of spines and synapses. *Cell* **119**, 873–887 (2004).

26. Verstreken, P. *et al.* Synaptic mitochondria are critical for mobilization of reserve pool vesicles at Drosophila neuromuscular junctions. *Neuron* **47**, 365–378 (2005).

27. Youle, R. J. & Van Der Bliek, A. M. Mitochondrial fission, fusion, and stress. *Science* (2012) doi:10.1126/science.1219855.

28. Twig, G. *et al.* Fission and selective fusion govern mitochondrial segregation and elimination by autophagy. *EMBO J.* **27**, 433–446 (2008).

29. Kleele, T. *et al.* Distinct fission signatures predict mitochondrial degradation or biogenesis. *Nature* **593**, 435–439 (2021).

30. Suen, D. F., Norris, K. L. & Youle, R. J. Mitochondrial dynamics and apoptosis. *Genes and Development* vol. 22 1577–1590 (2008).

31. Li, P. *et al.* Cytochrome c and dATP-dependent formation of Apaf-1/caspase-9 complex initiates an apoptotic protease cascade. *Cell* **91**, 479–489 (1997).

32. Adams, J. M. & Cory, S. Life-or-death decisions by the Bcl-2 protein family. *Trends in Biochemical Sciences* vol. 26 61–66 (2001).

33. Frank, S. *et al.* The Role of Dynamin-Related Protein 1, a Mediator of Mitochondrial Fission, in Apoptosis. *Dev. Cell* **1**, 515–525 (2001).

34. Lee, Y. J., Jeong, S. Y., Karbowski, M., Smith, C. L. & Youle, R. J. Roles of the mammalian mitochondrial fission and fusion mediators Fis1, Drp1, Opa1 in apoptosis. *Mol. Biol. Cell* **15**, 5001–5011 (2004).

35. Gomes, L. C., Benedetto, G. Di & Scorrano, L. During autophagy mitochondria elongate, are spared from degradation and sustain cell viability. *Nat. Cell Biol.* **13**, 589–598 (2011).

36. Liesa, M. & Shirihai, O. S. Mitochondrial dynamics in the regulation of nutrient utilization and energy expenditure. *Cell Metabolism* vol. 17 491–506 (2013).

37. Namgaladze, D. & Brüne, B. Fatty acid oxidation is dispensable for human macrophage IL-4-induced polarization. *Biochim. Biophys. Acta - Mol. Cell Biol. Lipids* **1841**, 1329–1335 (2014).

38. Ngo, J. *et al.* Mitochondrial morphology controls fatty acid utilization by changing CPT1 sensitivity to malonyl-CoA. *EMBO J.* e111901 (2023) doi:10.15252/embj.2022111901.

39. Yu, T., Sheu, S. S., Robotham, J. L. & Yoon, Y. Mitochondrial fission mediates high glucose-induced cell death through elevated production of reactive oxygen species. *Cardiovasc. Res.* **79**, 341–351 (2008).

40. Rovira-Llopis, S. *et al.* Mitochondrial dynamics in type 2 diabetes: Pathophysiological implications. *Redox Biology* vol. 11 637–645 (2017).

41. Soubannier, V. *et al.* A vesicular transport pathway shuttles cargo from mitochondria to lysosomes. *Curr. Biol.* **22**, 135–141 (2012).

42. Schuler, M. H. *et al.* Mitochondrial-derived compartments facilitate cellular adaptation to amino acid stress. *Mol. Cell* **81**, 3786-3802.e13 (2021).

43. Neuspiel, M. *et al.* Cargo-Selected Transport from the Mitochondria to Peroxisomes Is Mediated by Vesicular Carriers. *Curr. Biol.* **18**, 102–108 (2008).

44. Soubannier, V., Rippstein, P., Kaufman, B. A., Shoubridge, E. A. & McBride, H. M. Reconstitution of Mitochondria Derived Vesicle Formation Demonstrates Selective Enrichment of Oxidized Cargo. *PLoS One* **7**, (2012).

45. Sugiura, A., McLelland, G., Fon, E. A. & McBride, H. M. A new pathway for mitochondrial quality control: mitochondrial-derived vesicles. *EMBO J.* **33**, 2142–2156 (2014).

46. König, T. *et al.* MIROs and DRP1 drive mitochondrial-derived vesicle biogenesis and promote quality control. *Nat. Cell Biol.* **23**, 1271–1286 (2021).

47. Hughes, A. L., Hughes, C. E., Henderson, K. A., Yazvenko, N. & Gottschling, D. E. Selective sorting and destruction of mitochondrial membrane proteins in aged yeast. *Elife* **5**, (2016).

48. Chan, D. C. Fusion and fission: Interlinked processes critical for mitochondrial health. *Annu. Rev. Genet.* **46**, 265–287 (2012).

49. Labbé, K., Murley, A. & Nunnari, J. Determinants and functions of mitochondrial behavior. *Annual Review of Cell and Developmental Biology* vol. 30 357–391 (2014).

50. Liu, X., Weaver, D., Shirihai, O. & Hajnóczky, G. Mitochondrial kiss-and-run: Interplay between mitochondrial motility and fusion-fission dynamics. *EMBO J.* **28**, 3074–3089 (2009).

51. Palmer, C. S. *et al.* Adaptor proteins MiD49 and MiD51 can act independently of Mff and Fis1 in Drp1 recruitment and are specific for mitochondrial fission. *J. Biol. Chem.* **288**, 27584–27593 (2013).

52. Chen, H. *et al.* Mitochondrial fusion is required for mtdna stability in skeletal muscle and tolerance of mtDNA mutations. *Cell* **141**, 280–289 (2010).

53. Frohman, M. A. Role of mitochondrial lipids in guiding fission and fusion. *Journal of Molecular Medicine* vol. 93 263–269 (2015).

54. Chan, D. C. Mitochondrial Dynamics and Its Involvement in Disease. *Annu. Rev. Pathol. Mech. Dis.* **15**, 235–259 (2020).

55. Rambold, A. S., Kostelecky, B., Elia, N. & Lippincott-Schwartz, J. Tubular network formation protects mitochondria from autophagosomal degradation during nutrient starvation. *Proc. Natl. Acad. Sci. U. S. A.* **108**, 10190–10195 (2011).

56. Song, M., Franco, A., Fleischer, J. A., Zhang, L. & Dorn, G. W. Abrogating Mitochondrial Dynamics in Mouse Hearts Accelerates Mitochondrial Senescence. *Cell Metab.* **26**, 872-883.e5 (2017).

57. Mishra, P. & Chan, D. C. Metabolic regulation of mitochondrial dynamics. *J. Cell Biol.* (2016) doi:10.1083/jcb.201511036.

58. Shamseldin, H. E. *et al.* Genomic analysis of mitochondrial diseases in a consanguineous population reveals novel candidate disease genes. *J. Med. Genet.* **49**, 234–241 (2012).

59. Adebayo, M., Singh, S., Singh, A. P. & Dasgupta, S. Mitochondrial fusion and fission: The fine-tune balance for cellular homeostasis. *FASEB Journal* vol. 35 (2021).

60. Chakrabarti, R. *et al.* INF2-mediated actin polymerization at the ER stimulates mitochondrial calcium uptake, inner membrane constriction, and division. *J. Cell Biol.* **217**, 251–268 (2018).

61. Duvezin-Caubet, S. *et al.* Proteolytic processing of OPA1 links mitochondrial dysfunction to alterations in mitochondrial morphology. *J. Biol. Chem.* **281**, 37972–37979 (2006).

62. Fu, D. & Lippincott-Schwartz, J. Monitoring the Effects of Pharmacological Reagents on Mitochondrial Morphology. *Curr. Protoc. Cell Biol.* **79**, (2018).

63. Kwon, D., Park, E., Sesaki, H. & Kang, S. J. Carbonyl cyanide 3-chlorophenylhydrazone (CCCP) suppresses STING-mediated DNA sensing pathway through inducing mitochondrial fission. *Biochem. Biophys. Res. Commun.* **493**, 737–743 (2017).

64. De Vos, K. J., Allan, V. J., Grierson, A. J. & Sheetz, M. P. Mitochondrial function and actin regulate dynamin-related protein 1-dependent mitochondrial fission. *Curr. Biol.* **15**, 678–683 (2005).

65. Liu, X. & Hajnóczky, G. Altered fusion dynamics underlie unique morphological changes in mitochondria during hypoxia-reoxygenation stress. *Cell Death Differ.* **18**, 1561–1572 (2011).

66. Fung, T. S., Ji, W. K., Higgs, H. N. & Chakrabarti, R. Two distinct actin filament populations have effects on mitochondria, with differences in stimuli and assembly factors. *J. Cell Sci.* **132**, (2019).

67. Chakrabarti, R. *et al.* Mitochondrial dysfunction triggers actin polymerization necessary for rapid glycolytic activation. *J. Cell Biol.* **221**, (2022).

68. Kraus, F., Roy, K., Pucadyil, T. J. & Ryan, M. T. Function and regulation of the divisome for mitochondrial fission. *Nature* vol. 590 57–66 (2021).

69. Hatch, A. L., Ji, W. K., Merrill, R. A., Strack, S. & Higgs, H. N. Actin flaments as dynamic reservoirs for Drp1 recruitment. *Mol. Biol. Cell* **27**, 3109–3121 (2016).

70. Fröhlich, C. *et al.* Structural insights into oligomerization and mitochondrial remodelling of dynamin 1-like protein. *EMBO J.* **32**, 1280–1292 (2013).

71. Ji, W. K. *et al.* Receptor-mediated Drp1 oligomerization on endoplasmic reticulum. *J. Cell Biol.* **216**, 4123–4139 (2017).

72. Koch, A. *et al.* Dynamin-like protein 1 is involved in peroxisomal fission. *J. Biol. Chem.* **278**, 8597–8605 (2003).

73. Smirnova, E., Shurland, D. L., Ryazantsev, S. N. & Van Der Bliek, A. M. A human dynamin-related protein controls the distribution of mitochondria. *J. Cell Biol.* **143**, 351–358 (1998).

74. Smirnova, E., Griparic, L., Shurland, D. L. & Van der Bliek, A. M. Dynamin-related protein Drp1 is required for mitochondrial division in mammalian cells. *Mol. Biol. Cell* **12**, 2245–2256 (2001).

75. Wakabayashi, J. *et al.* The dynamin-related GTPase Drp1 is required for embryonic and brain development in mice. *J. Cell Biol.* **186**, 805–816 (2009).

76. Ishihara, N. *et al.* Mitochondrial fission factor Drp1 is essential for embryonic development and synapse formation in mice. *Nat. Cell Biol.* **11**, 958–966 (2009).

77. Hu, J. *et al.* Plant peroxisomes: Biogenesis and function. *Plant Cell* vol. 24 2279–2303 (2012).

78. Bleazard, W. *et al.* The dynamin-related GTPase Dnm1 regulates mitochondrial fission in yeast. *Nat. Cell Biol.* **1**, 298–304 (1999).

79. Voleman, L. & Dolezăl, P. Mitochondrial dynamics in parasitic protists. *PLoS Pathogens* vol. 15 (2019).

80. Gammie, A. E., Kurihara, L. J., Vallee, R. B. & Rose, M. D. DNM1, a dynamin-related gene, participates in endosomal trafficking in yeast. *J. Cell Biol.* **130**, 553–566 (1995).

81. Labrousse, A. M., Zappaterra, M. D., Rube, D. A. & Van der Bliek, A. M. C. elegans dynamin-related protein DRP-1 controls severing of the mitochondrial outer membrane. *Mol. Cell* **4**, 815–826 (1999).

82. Sesaki, H. & Jensen, R. E. Division versus fusion: Dnm1p and Fzo1p antagonistically regulate mitochondrial shape. *J. Cell Biol.* **147**, 699–706 (1999).

83. Mears, J. A. *et al.* Conformational changes in Dnm1 support a contractile mechanism for mitochondrial fission. *Nat. Struct. Mol. Biol.* (2011) doi:10.1038/nsmb.1949.

84. Wenger, J. *et al.* Functional mapping of human dynamin-1-like GTPase domain based on

x-ray structure analyses. *PLoS One* **8**, (2013).

85. Strack, S., Wilson, T. J. & Cribbs, J. T. Cyclin-dependent kinases regulate splice-specific targeting of dynamin-related protein 1 to microtubules. *J. Cell Biol.* **201**, 1037–1051 (2013).

86. Rosdah, A. A. *et al. New perspectives on the role of Drp1 isoforms in regulating mitochondrial pathophysiology*. *Pharmacology and Therapeutics* vol. 213 107594 (Pergamon, 2020).

87. Macdonald, P. J. *et al.* A dimeric equilibrium intermediate nucleates Drp1 reassembly on mitochondrial membranes for fission. *Mol. Biol. Cell* (2014) doi:10.1091/mbc.E14-02-0728.

88. Onoue, K. *et al.* Fis1 acts as a mitochondrial recruitment factor for TBC1D15 that is involved in regulation of mitochondrial morphology. *J. Cell Sci.* **126**, 176–185 (2013).

89. Wilson, T. J., Slupe, A. M. & Strack, S. Cell signaling and mitochondrial dynamics: Implications for neuronal function and neurodegenerative disease. *Neurobiology of Disease* vol. 51 13–26 (2013).

90. Itoh, K. *et al.* A brain-enriched drp1 isoform associates with lysosomes, late endosomes, and the plasma membrane. *J. Biol. Chem.* **293**, 11809–11822 (2018).

91. Ji, W. K., Hatch, A. L., Merrill, R. A., Strack, S. & Higgs, H. N. Actin filaments target the oligomeric maturation of the dynamin GTPase Drp1 to mitochondrial fission sites. *Elife* **4**, e11553 (2015).

92. Kwapiszewska, K. *et al.* Determination of oligomerization state of Drp1 protein in living cells at nanomolar concentrations. *Sci. Rep.* **9**, (2019).

93. Yoon, Y., Pitts, K. R. & McNiven, M. A. Mammalian dynamin-like protein DLP1 tubulates membranes. *Mol. Biol. Cell* **12**, 2894–2905 (2001).

94. Basu, K. *et al.* Molecular mechanism of DRP1 assembly studied in vitro by cryo-electron microscopy. *PLoS One* **12**, (2017).

95. Naylor, K. *et al.* Mdv1 interacts with assembled Dnm1 to promote mitochondrial division. *J. Biol. Chem.* **281**, 2177–2183 (2006).

96. Kamerkar, S. C., Kraus, F., Sharpe, A. J., Pucadyil, T. J. & Ryan, M. T. Dynamin-related protein 1 has membrane constricting and severing abilities sufficient for mitochondrial and peroxisomal fission. *Nat. Commun.* **9**, 1–15 (2018).

97. Kalia, R. *et al.* Structural basis of mitochondrial receptor binding and constriction by DRP1. *Nature* **558**, 401–405 (2018).

98. Bui, H. T. & Shaw, J. M. Dynamin assembly strategies and adaptor proteins in mitochondrial fission. *Curr. Biol.* **23**, 891–899 (2013).

99. Bustillo-Zabalbeitia, I. *et al.* Specific interaction with cardiolipin triggers functional activation of dynamin-related protein 1. *PLoS One* **9**, e102738 (2014).

100. Ingerman, E. *et al.* Dnm1 forms spirals that are structurally tailored to fit mitochondria. *J. Cell Biol.* **170**, 1021–1027 (2005).

101. Koirala, S. *et al.* Interchangeable adaptors regulate mitochondrial dynamin assembly for membrane scission. *Proc. Natl. Acad. Sci.* **110**, 1342–1351 (2013).

102. Francy, C. A., Alvarez, F. J. D., Zhou, L., Ramachandran, R. & Mears, J. A. The mechanoenzymatic core of dynamin-related protein 1 comprises the minimal machinery required for membrane constriction. *J. Biol. Chem.* (2015) doi:10.1074/jbc.M114.610881.

103. Lu, B. *et al.* Steric interference from intrinsically disordered regions controls dynamin-related protein 1 self-assembly during mitochondrial fission. *Sci. Rep.* **8**, 10879 (2018).

104. Chang, C. R. & Blackstone, C. Cyclic AMP-dependent protein kinase phosphorylation of Drp1 regulates its GTPase activity and mitochondrial morphology. *J. Biol. Chem.* **282**,

21583–21587 (2007).

105. Taguchi, N., Ishihara, N., Jofuku, A., Oka, T. & Mihara, K. Mitotic phosphorylation of dynamin-related GTPase Drp1 participates in mitochondrial fission. *J. Biol. Chem.* **282**, 11521–11529 (2007).

106. Cribbs, J. T. & Strack, S. Reversible phosphorylation of Drp1 by cyclic AMP-dependent protein kinase and calcineurin regulates mitochondrial fission and cell death. *EMBO Rep.* **8**, 939–944 (2007).

107. Harder, Z., Zunino, R. & McBride, H. Sumo1 Conjugates Mitochondrial Substrates and Participates in Mitochondrial Fission. *Curr. Biol.* **14**, 340–345 (2004).

108. Figueroa-Romero, C. *et al.* SUMOylation of the mitochondrial fission protein Drp1 occurs at multiple nonconsensus sites within the B domain and is linked to its activity cycle. *FASEB J.* (2009) doi:10.1096/fj.09-136630.

109. Clinton, R. W., Francy, C. A., Ramachandran, R., Qi, X. & Mears, J. A. Dynamin-related protein 1 oligomerization in solution impairs functional interactions with membrane-anchored mitochondrial fission factor. *J. Biol. Chem.* **291**, 478–492 (2016).

110. Liu, R. & Chan, D. C. The mitochondrial fssion receptor Mff selectively recruits oligomerized Drp1. *Mol. Biol. Cell* **26**, 4466–4477 (2015).

111. Hill, B. *et al.* The variable domain from the mitochondrial fission mechanoenzyme Drp1 promotes liquid-liquid phase separation. *Biophys. J.* **121**, 40a (2022).

112. Mahajan, M. *et al.* NMR identification of a conserved Drp1 cardiolipin-binding motif essential for stress-induced mitochondrial fission. *Proc. Natl. Acad. Sci. U. S. A.* **118**, (2021).

113. Gandre-Babbe, S. & van der Bliek, A. M. The Novel Tail-anchored Membrane Protein Mff Controls Mitochondrial and Peroxisomal Fission in Mammalian Cells. *Mol. Biol. Cell* **19**, 2402–2412 (2008).

114. Echeverri, C. J. & Perrimon, N. High-throughput RNAi screening in cultured cells: A user's guide. *Nature Reviews Genetics* vol. 7 373–384 (2006).

115. Otera, H. *et al.* Mff is an essential factor for mitochondrial recruitment of Drp1 during mitochondrial fission in mammalian cells. *J. Cell Biol.* **191**, 1141–1158 (2010).

116. Losón, O. C., Song, Z., Chen, H. & Chan, D. C. Fis1, Mff, MiD49, and MiD51 mediate Drp1 recruitment in mitochondrial fission. *Mol. Biol. Cell* **24**, 659–667 (2013).

117. Toyama, E. Q. *et al.* Metabolism: AMP-activated protein kinase mediates mitochondrial fission in response to energy stress. *Science (80-.).* **351**, 275–281 (2016).

118. Otera, H. & Mihara, K. Discovery of the membrane receptor for mitochondrial fission GTPase Drp1. *Small GTPases* **2**, 167–172 (2011).

119. Strack, S. & Cribbs, J. T. Allosteric modulation of Drp1 mechanoenzyme assembly and mitochondrial fission by the variable domain. *J. Biol. Chem.* **287**, 10990–11001 (2012).

120. Palmer, C. S. *et al.* MiD49 and MiD51, new components of the mitochondrial fission machinery. *EMBO Rep.* **12**, 565–573 (2011).

121. Zhao, J. *et al.* Human MIEF1 recruits Drp1 to mitochondrial outer membranes and promotes mitochondrial fusion rather than fission. *EMBO J.* **30**, 2762–2778 (2011).

122. Osellame, L. D. *et al.* Cooperative and independent roles of the Drp1 adaptors Mff, MiD49 and MiD51 in mitochondrial fission. *J. Cell Sci.* **129**, 2170–2181 (2016).

123. Otera, H., Miyata, N., Kuge, O. & Mihara, K. Drp1-dependent mitochondrial fission via MiD49/51 is essential for apoptotic cristae remodeling. *J. Cell Biol.* **212**, 531–544 (2016).

124. Losón, O. C. *et al.* The mitochondrial fission receptor MiD51 requires ADP as a cofactor. *Structure* **22**, 367–377 (2014).

125. Richter, V. *et al.* Structural and functional analysis of mid51, a dynamin receptor required for mitochondrial fission. *J. Cell Biol.* (2014) doi:10.1083/jcb.201311014.

126. Losõn, O. C. *et al.* Crystal structure and functional analysis of MiD49, a receptor for the mitochondrial fission protein Drp1. *Protein Sci.* (2015) doi:10.1002/pro.2629.

127. Walczak, J., Partyka, M., Duszyński, J. & Szczepanowska, J. Implications of mitochondrial network organization in mitochondrial stress signalling in NARP cybrid and Rho0 cells. *Sci. Rep.* **7**, 1–14 (2017).

128. Otsuga, D. *et al.* The dynamin-related GTPase, Dnm1p, controls mitochondrial morphology in yeast. *J. Cell Biol.* **143**, 333–349 (1998).

129. Mozdy, A. D., McCaffery, J. M. & Shaw, J. M. Dnm1p GTPase-mediated mitochondrial fission is a multi-step process requiring the novel integral membrane component Fis1p. *J. Cell Biol.* **151**, 367–379 (2000).

130. Zhang, Y., Chan, N. C., Ngo, H. B., Gristick, H. & Chan, D. C. Crystal structure of mitochondrial fission complex reveals scaffolding function for Mitochondrial division 1 (Mdv1) coiled coil. *J. Biol. Chem.* **287**, 9855–9861 (2012).

131. Griffin, E. E., Graumann, J. & Chan, D. C. The WD40 protein Caf4p is a component of the mitochondrial fission machinery and recruits Dnm1p to mitochondria. *J. Cell Biol.* **170**, 237–248 (2005).

132. Guo, Q., Koirala, S., Perkins, E. M., McCaffery, J. M. & Shaw, J. M. The Mitochondrial Fission Adaptors Caf4 and Mdv1 Are Not Functionally Equivalent. *PLoS One* **7**, e53523 (2012).

133. Tieu, Q. & Nunnari, J. Mdv1p is a WD repeat protein that interacts with the dynamin-related GTPase, Dnm1p, to trigger mitochondrial division. *J. Cell Biol.* **151**, 353–365 (2000).

134. Alirol, E. *et al.* The mitochondrial fission protein hFis1 requires the endoplasmic

reticulum gateway to induce apoptosis. *Mol. Biol. Cell* **17**, 4593–4605 (2006).

135. James, D. I., Parone, P. A., Mattenberger, Y. & Martinou, J. C. hFis1, a novel component of the mammalian mitochondrial fission machinery. *J. Biol. Chem.* **278**, 36373–36379 (2003).

136. Iwasawa, R., Mahul-Mellier, A. L., Datler, C., Pazarentzos, E. & Grimm, S. Fis1 and Bap31 bridge the mitochondria-ER interface to establish a platform for apoptosis induction. *EMBO J.* **30**, 556–568 (2011).

137. Yamano, K., Fogel, A. I., Wang, C., van der Bliek, A. M. & Youle, R. J. Mitochondrial Rab GAPs govern autophagosome biogenesis during mitophagy. *Elife* **3**, (2014).

138. Barsoum, M. J. *et al.* Nitric oxide-induced mitochondrial fission is regulated by dynamin-related GTPases in neurons. *EMBO J.* **25**, 3900–3911 (2006).

139. Koch, A., Yoon, Y., Bonekamp, N. A., McNiven, M. A. & Schrader, M. A role for Fis1 in both mitochondrial and peroxisomal fission in mammalian cells. *Mol. Biol. Cell* **16**, (2005).

140. Ihenacho, U. K., Meacham, K. A., Harwig, M. C., Widlansky, M. E. & Hill, R. B. Mitochondrial Fission Protein 1: Emerging Roles in Organellar Form and Function in Health and Disease. *Frontiers in Endocrinology* vol. 12 (2021).

141. Wong, Y. C., Ysselstein, D. & Krainc, D. Mitochondria-lysosome contacts regulate mitochondrial fission via RAB7 GTP hydrolysis. *Nature* **554**, 382–386 (2018).

142. Yu, R., Jin, S., Lendahl, U., Nistér, M. & Zhao, J. Human Fis1 regulates mitochondrial dynamics through inhibition of the fusion machinery. *EMBO J.* **38**, (2019).

143. Xian, H., Yang, Q., Xiao, L., Shen, H. M. & Liou, Y. C. STX17 dynamically regulated by Fis1 induces mitophagy via hierarchical macroautophagic mechanism. *Nat. Commun.* **10**, (2019).

144. Zhou, L. *et al.* C-Abl-mediated Drp1 phosphorylation promotes oxidative stress-induced mitochondrial fragmentation and neuronal cell death. *Cell Death Dis.* **8**, (2017).

145. Yu, T., Jhun, B. S. & Yoon, Y. High-glucose stimulation increases reactive oxygen species production through the calcium and mitogen-activated protein kinase-mediated activation of mitochondrial fission. *Antioxidants Redox Signal.* **14**, 425–437 (2011).

146. Kashatus, J. A. *et al.* Erk2 phosphorylation of Drp1 promotes mitochondrial fission and MAPK-driven tumor growth. *Mol. Cell* **57**, 537–551 (2015).

147. Serasinghe, M. N. *et al.* Mitochondrial division is requisite to RAS-induced transformation and targeted by oncogenic MAPK pathway inhibitors. *Mol. Cell* (2015) doi:10.1016/j.molcel.2015.01.003.

148. Qi, X., Disatnik, M.-H., Shen, N., Sobel, R. A. & Mochly-Rosen, D. Aberrant mitochondrial fission in neurons induced by protein kinase C under oxidative stress conditions in vivo. *Mol. Biol. Cell* (2011) doi:10.1091/mbc.e10-06-0551.

149. Brand, C. S., Tan, V. P., Brown, J. H. & Miyamoto, S. RhoA regulates Drp1 mediated mitochondrial fission through ROCK to protect cardiomyocytes. *Cell. Signal.* (2018) doi:10.1016/j.cellsig.2018.06.012.

150. Xu, S. *et al.* CaMKII induces permeability transition through Drp1 phosphorylation during chronic β-AR stimulation. in *Nature Communications* vol. 7 1–13 (Nature Publishing Group, 2016).

151. Tresse, E. *et al.* IFN-β rescues neurodegeneration by regulating mitochondrial fission via STAT5, PGAM5, and Drp1. *EMBO J.* **40**, (2021).

152. Guo, M. Y. *et al.* The role of Cdk5-mediated Drp1 phosphorylation in Aβ 1-42 induced mitochondrial fission and neuronal apoptosis. *J. Cell. Biochem.* **119**, 4815–4825 (2018).

153. Han, H. *et al.* PINK 1 phosphorylates Drp1 S616 to regulate mitophagy-independent mitochondrial dynamics. *EMBO Rep.* **21**, e48686 (2020).

154. Ma, R. *et al.* DUSP6 SUMOylation protects cells from oxidative damage via direct regulation of Drp1 dephosphorylation. *Sci. Adv.* **6**, (2020).

155. Wang, W. *et al.* Mitochondrial fission triggered by hyperglycemia is mediated by ROCK1 activation in podocytes and endothelial cells. *Cell Metab.* (2012) doi:10.1016/j.cmet.2012.01.009.

156. Han, X. J. *et al.* CaM kinase Iα-induced phosphorylation of Drp1 regulates mitochondrial morphology. *J. Cell Biol.* **182**, 573–585 (2008).

157. Wikstrom, J. D. *et al.* AMPK regulates ER morphology and function in stressed pancreatic β-cells via phosphorylation of DRP1. *Mol. Endocrinol.* **27**, 1706–1723 (2013).

158. Jhun, B. S. *et al.* Protein kinase D activation induces mitochondrial fragmentation and dysfunction in cardiomyocytes. *J. Physiol.* **596**, 827–855 (2018).

159. Cereghetti, G. M. *et al.* Dephosphorylation by calcineurin regulates translocation of Drp1 to mitochondria. *Proc. Natl. Acad. Sci.* (2008) doi:10.1073/pnas.0808249105.

160. Pennanen, C. *et al.* Mitochondrial fission is required for cardiomyocyte hypertrophy mediated by a Ca2+-calcineurin signaling pathway. *J. Cell Sci.* **127**, 2659–2671 (2014).

161. Yu, B. *et al.* Mitochondrial phosphatase PGAM5 modulates cellular senescence by regulating mitochondrial dynamics. *Nat. Commun.* **11**, (2020).

162. Valera-Alberni, M. *et al.* Crosstalk between Drp1 phosphorylation sites during mitochondrial remodeling and their impact on metabolic adaptation. *Cell Rep.* **36**, (2021).

163. Lee, D. shin & Kim, J. E. PDI-mediated S-nitrosylation of DRP1 facilitates DRP1-S616 phosphorylation and mitochondrial fission in CA1 neurons. *Cell Death Dis.* **9**, (2018).

164. Cha, Y. *et al.* SIRT2 regulates mitochondrial dynamics and reprogramming via MEK1-ERK-DRP1 and AKT1-DRP1 axes. *Cell Rep.* **37**, (2021).

165. Hu, J. *et al.* ROCK1 activation-mediated mitochondrial translocation of Drp1 and cofilin are required for arnidiol-induced mitochondrial fission and apoptosis. *J. Exp. Clin. Cancer Res.* **39**, (2020).

166. Yu, R. *et al.* The phosphorylation status of Ser-637 in dynamin-related protein 1 (Drp1) does not determine Drp1 recruitment to mitochondria. *J. Biol. Chem.* **294**, 17262–17277 (2019).

167. Chakrabarti, R., Lee, M. & Higgs, H. N. Multiple roles for actin in secretory and endocytic pathways. *Current Biology* vol. 31 (2021).

168. Elkin, S. R., Lakoduk, A. M. & Schmid, S. L. Endocytic pathways and endosomal trafficking: a primer. *Wiener Medizinische Wochenschrift* vol. 166 196–204 (2016).

169. Gardel, M. L., Schneider, I. C., Aratyn-Schaus, Y. & Waterman, C. M. Mechanical integration of actin and adhesion dynamics in cell migration. *Annual Review of Cell and Developmental Biology* vol. 26 315–333 (2010).

170. Zhang, R. *et al.* Dynamin regulates the dynamics and mechanical strength of the actin cytoskeleton as a multifilament actin-bundling protein. *Nat. Cell Biol.* **22**, 674–688 (2020).

171. Korobova, F., Ramabhadran, V. & Higgs, H. N. An actin-dependent step in mitochondrial fission mediated by the ER-associated formin INF2. *Science (80-.).* **339**, 464–467 (2013).

172. Shao, X., Li, Q., Mogilner, A., Bershadsky, A. D. & Shivashankar, G. V. Mechanical stimulation induces formin-dependent assembly of a perinuclear actin rim. *Proc. Natl. Acad. Sci. U. S. A.* **112**, E2595–E2601 (2015).

173. Wales, P. *et al.* Calcium-mediated actin reset (CaAR) mediates acute cell adaptations. *Elife* **5**, (2016).

174. Manor, U. *et al.* A mitochondria-anchored isoform of the actin-nucleating spire protein

regulates mitochondrial division. *Elife* **4**, (2015).

175. Ardail, D. *et al.* Mitochondrial contact sites. Lipid composition and dynamics. *J. Biol. Chem.* **265**, 18797–18802 (1990).

176. Schlattner, U., Tokarska-Schlattner, M. & Wallimann, T. Mitochondrial creatine kinase in human health and disease. *Biochimica et Biophysica Acta - Molecular Basis of Disease* vol. 1762 164–180 (2006).

177. Tatsuta, T., Scharwey, M. & Langer, T. Mitochondrial lipid trafficking. *Trends in Cell Biology* vol. 24 44–52 (2014).

178. Cosentino, K. & García-Sáez, A. J. Bax and Bak Pores: Are We Closing the Circle? *Trends in Cell Biology* vol. 27 266–275 (2017).

179. Horvath, S. E. & Daum, G. Lipids of mitochondria. *Progress in Lipid Research* (2013) doi:10.1016/j.plipres.2013.07.002.

180. Van Meer, G., Voelker, D. R. & Feigenson, G. W. Membrane lipids: Where they are and how they behave. *Nature Reviews Molecular Cell Biology* vol. 9 112–124 (2008).

181. Kameoka, S., Adachi, Y., Okamoto, K., Iijima, M. & Sesaki, H. Phosphatidic Acid and Cardiolipin Coordinate Mitochondrial Dynamics. *Trends in Cell Biology* vol. 28 67–76 (2018).

182. Beltrán-Heredia, E. *et al.* Membrane curvature induces cardiolipin sorting. *Commun. Biol.* **2**, (2019).

183. Elmer-Dixon, M. M., Hoody, J., Steele, H. B. B., Becht, D. C. & Bowler, B. E. Cardiolipin Preferentially Partitions to the Inner Leaflet of Mixed Lipid Large Unilamellar Vesicles. *J. Phys. Chem. B* **123**, 9111–9122 (2019).

184. Konar, S. & Allolio, C. Mitochondrial membranes: model lipid compositions, curvature elastic properties and the puzzle of cardiolipin. *Biophys. J.* **121**, 173a (2022).

185. Lackner, L. L., Horner, J. S. & Nunnari, J. Mechanistic analysis of a dynamin effector. *Science (80-.).* **325**, 874–877 (2009).

186. Adachi, Y. *et al.* Coincident Phosphatidic Acid Interaction Restrains Drp1 in Mitochondrial Division. *Mol. Cell* **63**, 1034–1043 (2016).

187. Rowland, A. A. & Voeltz, G. K. Endoplasmic reticulum-mitochondria contacts: Function of the junction. *Nature Reviews Molecular Cell Biology* vol. 13 607–615 (2012).

188. Cho, B. *et al.* Constriction of the mitochondrial inner compartment is a priming event for mitochondrial division. *Nat. Commun.* **8**, 15754 (2017).

189. Lewis, S. C., Uchiyama, L. F. & Nunnari, J. ER-mitochondria contacts couple mtDNA synthesis with Mitochondrial division in human cells. *Science (80-.).* **353**, (2016).

190. Deus, C. M., Yambire, K. F., Oliveira, P. J. & Raimundo, N. Mitochondria–Lysosome Crosstalk: From Physiology to Neurodegeneration. *Trends in Molecular Medicine* vol. 26 71–88 (2020).

191. Donaldson, J. G. & Jackson, C. L. ARF family G proteins and their regulators: Roles in membrane transport, development and disease. *Nature Reviews Molecular Cell Biology* vol. 12 362–375 (2011).

192. Godi, A. *et al.* ARF mediates recruitment of Ptdlns-4-OH kinase-β and stimulates synthesis of Ptdlns(4,5)P2 on the Golgi complex. *Nat. Cell Biol.* **1**, 280–287 (1999).

193. Waugh, M. G. The Great Escape: How phosphatidylinositol 4-kinases and PI4P promote vesicle exit from the Golgi (and drive cancer). *Biochemical Journal* vol. 476 2321–2346 (2019).

194. Nagashima, S. *et al.* Golgi-derived PI(4)P-containing vesicles drive late steps of mitochondrial division. *Science (80-.).* **367**, 1366–1371 (2020).

195. Elgass, K. D., Smith, E. A., LeGros, M. A., Larabell, C. A. & Ryan, M. T. Analysis of ER-mitochondria contacts using correlative fluorescence microscopy and soft X-ray tomography of mammalian cells. *J. Cell Sci.* (2015) doi:10.1242/jcs.169136.

196. Zerihun, M., Sukumaran, S. & Qvit, N. The Drp1-Mediated Mitochondrial Fission Protein Interactome as an Emerging Core Player in Mitochondrial Dynamics and Cardiovascular Disease Therapy. *International Journal of Molecular Sciences* vol. 24 (2023).

197. Yu, R. *et al.* The Molecular Assembly State of Drp1 Controls its Association With the Mitochondrial Recruitment Receptors Mff and MIEF1/2. *Front. Cell Dev. Biol.* **9**, (2021).

198. Yu, R. *et al.* MIEF1/2 orchestrate mitochondrial dynamics through direct engagement with both the fission and fusion machineries. *BMC Biol.* **19**, (2021).

199. Lee, J. E., Westrate, L. M., Wu, H., Page, C. & Voeltz, G. K. Multiple dynamin family members collaborate to drive mitochondrial division. *Nature* **540**, 139–143 (2016).

200. Frolov, V. A., Escalada, A., Akimov, S. A. & Shnyrova, A. V. Geometry of membrane fission. *Chem. Phys. Lipids* **185**, 129–140 (2015).

201. Friedman, J. R. & Nunnari, J. Mitochondrial form and function. *Nature* vol. 505 335–343 (2014).

202. Yang, C. & Svitkina, T. M. Ultrastructure and dynamics of the actin−myosin II cytoskeleton during mitochondrial fission. *Nat. Cell Biol.* **21**, (2019).

203. Korobova, F., Gauvin, T. J. & Higgs, H. N. A role for myosin II in mammalian mitochondrial fission. *Curr. Biol.* **24**, 409–414 (2014).

204. Connor, O. M., Matta, S. K. & Friedman, J. R. Completion of mitochondrial division requires the intermembrane space protein Mdi1/Atg44. *J. Cell Biol.* **222**, (2023).

205. Westermann, B. Mitochondrial double membrane fission: A mystery solved? *J. Cell Biol.* **222**, (2023).

206. Chakrabarti, R. & Higgs, H. N. Revolutionary view of two ways to split a mitochondrion. *Nature* vol. 593 346–347 (2021).

207. Francy, C. A., Clinton, R. W., Fröhlich, C., Murphy, C. & Mears, J. A. Cryo-EM Studies of Drp1 Reveal Cardiolipin Interactions that Activate the Helical Oligomer. *Sci. Rep.* **7**, 1–12 (2017).

208. Roy, K. & Pucadyil, T. J. Metal-Binding Propensity in the Mitochondrial Dynamin-Related Protein 1. *J. Membr. Biol.* **255**, 143–150 (2022).

209. Eisner, V., Picard, M. & Hajnóczky, G. Mitochondrial dynamics in adaptive and maladaptive cellular stress responses. *Nature Cell Biology* vol. 20 755–765 (2018).

210. Ramachandran, R. Mitochondrial dynamics: The dynamin superfamily and execution by collusion. *Seminars in Cell and Developmental Biology* vol. 76 201–212 (2018).

211. Kraus, F. & Ryan, M. T. The constriction and scission machineries involved in mitochondrial fission. *J. Cell Sci.* **130**, 2953–2960 (2017).

212. Galloway, C. A. & Yoon, Y. Mitochondrial morphology in metabolic diseases. *Antioxidants Redox Signal.* **19**, 415–430 (2013).

213. Nunnari, J. & Suomalainen, A. Mitochondria: In sickness and in health. *Cell* **148**, 1145–1159 (2012).

214. Serasinghe, M. N. & Chipuk, J. E. Mitochondrial fission in human diseases. in *Handbook of Experimental Pharmacology* 159–188 (2017). doi:10.1007/164_2016_38.

215. Waterham, H. R. *et al.* A Lethal Defect of Mitochondrial and Peroxisomal Fission. *N. Engl. J. Med.* **356**, 1736–1741 (2007).

216. Longo, F. *et al.* Impaired turnover of hyperfused mitochondria in severe axonal neuropathy due to a novel DRP1 mutation. *Hum. Mol. Genet.* **29**, 177–188 (2020).

217. Fahrner, J. A., Liu, R., Perry, M. S., Klein, J. & Chan, D. C. A novel de novo dominant negative mutation in DNM1L impairs mitochondrial fission and presents as childhood epileptic encephalopathy. *Am. J. Med. Genet. Part A* **170**, 2002–2011 (2016).

218. Hoppins, S., Lackner, L. & Nunnari, J. The machines that divide and fuse mitochondria. *Annual Review of Biochemistry* vol. 76 751–780 (2007).

219. Koirala, S. *et al.* Molecular architecture of a dynamin adaptor: Implications for assembly of mitochondrial fission complexes. *J. Cell Biol.* **191**, 1127–1139 (2010).

220. Koch, J. *et al.* Disturbed mitochondrial and peroxisomal dynamics due to loss of MFF causes Leigh-like encephalopathy, optic atrophy and peripheral neuropathy. *J. Med. Genet.* **53**, 270–278 (2016).

221. Nasca, A. *et al.* Clinical and biochemical features in a patient with mitochondrial fission factor gene alteration. *Front. Genet.* **9**, 625 (2018).

222. Liu, R. & Chan, D. C. The mitochondrial fission receptor Mff selectively recruits oligomerized Drp1. *Mol. Biol. Cell* **26**, 4466–4477 (2015).

223. Braschi, E., Zunino, R. & McBride, H. M. MAPL is a new mitochondrial SUMO E3 ligase that regulates mitochondrial fission. *EMBO Rep.* **10**, 748–754 (2009).

224. Nakamura, N., Kimura, Y., Tokuda, M., Honda, S. & Hirose, S. MARCH-V is a novel mitofusin 2- and Drp1-binding protein able to change mitochondrial morphology. *EMBO Rep.* **7**, 1019–1022 (2006).

225. Gawlowski, T. *et al.* Modulation of dynamin-related protein 1 (DRP1) function by increased O-linked-β-N-acetylglucosamine modification (O-GlcNAc) in cardiac myocytes. *J. Biol. Chem.* **287**, 30024–30034 (2012).

226. Cho, D.-H. *et al.* S-Nitrosylation of Drp1 Mediates β-Amyloid-Related Mitochondrial Fission and Neuronal Injury. *Science (80-.).* **324**, 102–105 (2009).

227. Macdonald, P. J. *et al.* A dimeric equilibrium intermediate nucleates Drp1 reassembly on mitochondrial membranes for fission. *Mol. Biol. Cell* (2014) doi:10.1091/mbc.e14-02-0728.

228. Friedman, J. R. *et al.* ER tubules mark sites of mitochondrial division. *Science (80-.).* **334**, 358–362 (2011).

229. Vincent, T. L., Green, P. J. & Woolfson, D. N. LOGICOIL - Multi-state prediction of coiled-coil oligomeric state. *Bioinformatics* **29**, 69–76 (2013).

230. Chang, D. K., Cheng, S. F., Trivedi, V. D. & Lin, K. L. Proline affects oligomerization of a coiled coil by inducing a kink in a long helix. *J. Struct. Biol.* **128**, 270–279 (1999).

231. Shen, Q. *et al.* Mutations in Fis1 disrupt orderly disposal of defective mitochondria. *Mol. Biol. Cell* **25**, 145–59 (2014).

232. Passmore, J. B. *et al.* Mitochondrial fission factor (MFF) is a critical regulator of peroxisome maturation. *Biochim. Biophys. Acta - Mol. Cell Res.* **1867**, 118709 (2020).

233. Hatch, A. L., Gurel, P. S. & Higgs, H. N. Novel roles for actin in mitochondrial fission. *Journal of Cell Science* vol. 127 4549–4560 (2014).

234. Lee, K. S. *et al.* Altered ER-mitochondria contact impacts mitochondria calcium homeostasis and contributes to neurodegeneration in vivo in disease models. *Proc. Natl. Acad. Sci. U. S. A.* **115**, E8844–E8853 (2018).

235. Gurel, P. S. *et al.* INF2-mediated severing through actin filament encirclement and disruption. *Curr. Biol.* **24**, 156–164 (2014).

236. Zacharias, D. A., Violin, J. D., Newton, A. C. & Tsien, R. Y. Partitioning of lipid-modified monomeric GFPs into membrane microdomains of live cells. *Science (80-.).* **296**, 913–916 (2002).

237. Spudich, J. A. & Watt, S. The regulation of rabbit skeletal muscle contraction. I. Biochemical studies of the interaction of the tropomyosin-troponin complex with actin and the proteolytic fragments of myosin. *J. Biol. Chem.* **246**, 4866–4871 (1971).

238. Gurel, P. S. *et al.* Assembly and turnover of short actin filaments by the formin INF2 and profilin. *J. Biol. Chem.* **290**, 22494–22506 (2015).

239. Chhabra, E. S. & Higgs, H. N. INF2 is a WASP homology 2 motif-containing formin that severs actin filaments and accelerates both polymerization and depolymerization. *J. Biol. Chem.* **281**, 26754–26767 (2006).

240. Pickles, S., Vigié, P. & Youle, R. J. Mitophagy and Quality Control Mechanisms in Mitochondrial Maintenance. *Current Biology* vol. 28 R170–R185 (2018).

241. Liu, A., Kage, F. & Higgs, H. N. Mff oligomerization is required for Drp1 activation and synergy with actin filaments during mitochondrial division. *Mol. Biol. Cell* **32**, (2021).

242. Constantinides, P. P. & Steim, J. M. Physical properties of fatty acyl-CoA. Critical micelle concentrations and micellar size and shape. *J. Biol. Chem.* **260**, 7573–7580 (1985).

243. Davda, D. *et al.* Profiling targets of the irreversible palmitoylation inhibitor 2-bromopalmitate. *ACS Chem. Biol.* **8**, 1912–1917 (2013).

244. Pinkosky, S. L. *et al.* Long-chain fatty acyl-CoA esters regulate metabolism via allosteric control of AMPK β1 isoforms. *Nat. Metab.* **2**, 873–881 (2020).

245. Kalia, R. *et al.* Structural basis of mitochondrial receptor binding and constriction by DRP1. *Nat. 2018 5587710* **558**, 401–405 (2018).

246. Houten, S. M., Violante, S., Ventura, F. V. & Wanders, R. J. A. The Biochemistry and Physiology of Mitochondrial Fatty Acid β-Oxidation and Its Genetic Disorders. *Annual Review of Physiology* vol. 78 23–44 (2016).

247. Frigini, E. N., Barrera, E. E., Pantano, S. & Porasso, R. D. Role of membrane curvature on

the activation/deactivation of Carnitine Palmitoyltransferase 1A: A coarse grain molecular dynamic study. *Biochim. Biophys. Acta - Biomembr.* **1862**, 183094 (2020).

248. Rao, J. N., Warren, G. Z. L., Estolt-Povedano, S., Zammit, V. A. & Ulmer, T. S. An environment-dependent structural switch underlies the regulation of carnitine palmitoyltransferase 1A. *J. Biol. Chem.* **286**, 42545–42554 (2011).

249. Zhu, Y. *et al.* Carnitine palmitoyltransferase 1A promotes mitochondrial fission by enhancing MFF succinylation in ovarian cancer. *Commun. Biol.* **6**, 1–14 (2023).

250. He, J. *et al.* The acyl-CoA-binding protein Acb1 regulates mitochondria, lipid droplets, and cell proliferation. *FEBS Lett.* **596**, 1795–1808 (2022).

251. Hunkeler, M. *et al.* Structural basis for regulation of human acetyl-CoA carboxylase. *Nature* **558**, 470–474 (2018).

252. Woldegiorgis, G., Spennetta, T., Corkey, B. E., Williamson, J. R. & Shrago, E. Extraction of tissue long-chain acyl-CoA esters and measurement by reverse-phase high-performance liquid chromatography. *Anal. Biochem.* **150**, 8–12 (1985).

253. Booth, D. S., Avila-Sakar, A. & Cheng, Y. Visualizing proteins and macromolecular complexes by negative stain EM: from grid preparation to image acquisition. *J. Vis. Exp.* e3227 (2011) doi:10.3791/3227.

254. Kikumoto, M. & Oosawa, F. Thermodynamic measurements of actin polymerization with various cation species. *Cytoskeleton* **74**, 465–471 (2017).

255. Liu, A., Kage, F., Sapp, G., Aydin, H. & Higgs, H. N. Long-chain fatty acyl-coenzyme A activates the mitochondrial fission factors MiD49 and MiD51 by inducing their oligomerization. *bioRxiv* 2023.07.31.551267 (2023) doi:10.1101/2023.07.31.551267.

256. Chang, C. R. & Blackstone, C. Dynamic regulation of mitochondrial fission through modification of the dynamin-related protein Drp1. in *Annals of the New York Academy of Sciences* vol. 1201 34–39 (John Wiley & Sons, Ltd, 2010).

257. Galvan, D. L. *et al.* Drp1S600 phosphorylation regulates mitochondrial fission and progression of nephropathy in diabetic mice. *J. Clin. Invest.* **129**, 2807–2823 (2019).

258. Warnock, D. E., Hinshaw, J. E. & Schmid, S. L. Dynamin self-assembly stimulates its GTPase activity. *J. Biol. Chem.* **271**, 22310–22314 (1996).

259. Boissan, M. *et al.* Nucleoside diphosphate kinases fuel dynamin superfamily proteins with GTP for membrane remodeling. *Science (80-.).* **344**, 1510–1515 (2014).

260. Honsho, M. *et al.* Mammalian homologue nme3 of dynamo1 regulates peroxisome division. *Int. J. Mol. Sci.* **21**, 1–21 (2020).

261. Abe, Y. *et al.* Genetic defects in peroxisome morphogenesis (Pex11β, dynamin-like protein 1, and nucleoside diphosphate kinase 3) affect docosahexaenoic acid-phospholipid metabolism. *J. Inherit. Metab. Dis.* **46**, 273–285 (2023).